



EXPLAINING EXTREME EVENTS OF 2013

From A Climate Perspective

Special Supplement to the
Bulletin of the American Meteorological Society
Vol. 95, No. 9, September 2014

EXPLAINING EXTREME EVENTS OF 2013 FROM A CLIMATE PERSPECTIVE

Editors

Stephanie C. Herring, Martin P. Hoerling, Thomas C. Peterson, and Peter A. Stott

Special Supplement to the

Bulletin of the American Meteorological Society

Vol. 95, No. 9, September 2014

AMERICAN METEOROLOGICAL SOCIETY

CORRESPONDING EDITOR:

Stephanie C. Herring, PhD
NOAA National Climatic Data Center
325 Broadway, E/CC23, Rm IB-131
Boulder, CO, 80305-3328
E-mail: stephanie.herring@noaa.gov

COVER CREDITS:

FRONT: The final wave of rain storms make their way through Boulder, Colorado, bringing another day of flooding to the already rain swollen area, 15 September 2013. Image by ©Ed Endicott/Demotix/Corbis.

BACK: The city of Boulder, Colorado, experienced substantial flooding for four days that have lasting effects, 18 September 2013. Image by ©Anna M Weaver/Demotix/Corbis.

HOW TO CITE THIS DOCUMENT

Citing the complete report:

Herring, S. C., M. P. Hoerling, T. C. Peterson, and P.A. Stott, Eds., 2014: Explaining Extreme Events of 2013 from a Climate Perspective. *Bull. Amer. Meteor. Soc.*, **95** (9), S1–S96.

Citing a section (example):

Hoerling, M., and Coauthors, 2014: Northeast Colorado extreme rains interpreted in a climate change context [in "Explaining Extremes of 2013 from a Climate Perspective"]. *Bull. Amer. Meteor. Soc.*, **95** (9), S15–S18.

EDITORIAL AND PRODUCTION TEAM

Riddle, Deborah B., Lead Graphics Production, NOAA/NESDIS
National Climatic Data Center, Asheville, NC
Veasey, Sara W., Graphics Team Lead, NOAA/NESDIS
National Climatic Data Center, Asheville, NC
Griffin, Jessica, Graphics Support, CICS-NC, Asheville, NC
Love-Brotak, S. Elizabeth, Graphics Support, NOAA/NESDIS
National Climatic Data Center, Asheville, NC

Misch, Deborah J., Graphics Support, JPS, Inc., NOAA/NESDIS
National Climatic Data Center, Asheville, NC
Osborne, Susan, Copy Editor, JPS, Inc., NOAA/NESDIS
National Climatic Data Center, Asheville, NC
Sprain, Mara, Editorial Support, LAC Group, NOAA/NESDIS
National Climatic Data Center, Asheville, NC
Young, Teresa, Graphics Support, ERT/STG, Inc., NOAA/
NESDIS National Climatic Data Center, Asheville, NC

EDITOR & AUTHOR AFFILIATIONS (ALPHABETICAL BY NAME)

- Abatzoglou, John T.**, Department of Geography, University of Idaho, Moscow, Idaho
- Alexander, Lisa V.**, Australian Research Council Centre of Excellence for Climate System Science, Climate Change Research Centre, University of New South Wales, Sydney, New South Wales, Australia
- Allen, Myles R.**, Environmental Change Institute and Atmospheric, Oceanic, and Planetary Physics, University of Oxford, Oxford, UK
- Añel, Juan A.**, Smith School of Enterprise and the Environment, University of Oxford, Oxford, United Kingdom and EPhys-Lab, Facultad de Ciencias, Universidade de Vigo, Ourense, Spain
- Arblaster, Julie M.**, Centre for Australian Weather and Climate Research, Bureau of Meteorology, Melbourne, Australia and National Center for Atmospheric Research, Boulder, Colorado
- Ashfaq, Moetasim**, Climate Change Science Institute, Oak Ridge National Laboratory, Oak Ridge, Tennessee
- Braganza, Karl**, Climate Information Services, Bureau of Meteorology, Melbourne, Australia
- Buisán, Samuel T.**, Agencia Estatal de Meteorología, Zaragoza, Spain
- Bunkers, Matthew J.**, NOAA's National Weather Service, Rapid City, South Dakota
- Cattiaux, Julien**, Centre National de la Recherche Scientifique, Centre National de Recherches Météorologiques, Groupe d'étude de l'atmosphère Météorologique Toulouse, France
- Charland, Allison**, Department of Environmental Earth System Science and Woods Institute for the Environment, Stanford University, Stanford, California
- Christidis, Nikolaos**, Met Office Hadley Centre, Exeter, United Kingdom
- Ciavarella, Andrew**, Met Office Hadley Centre, Exeter, United Kingdom
- Dean, Sam M.**, National Institute of Water and Atmospheric Research, Wellington, New Zealand
- Diaz, Henry**, University of Colorado, Cooperative Institute for Research in Environmental Sciences, Boulder, Colorado
- Diffenbaugh, Noah S.**, Department of Environmental Earth System Science and Woods Institute for the Environment, Stanford University, Stanford, California
- Dole, Randall**, NOAA's Earth System Research Laboratory, Boulder, Colorado
- Donat, Markus G.**, Australian Research Council Centre of Excellence for Climate System Science, Climate Change Research Centre, University of New South Wales, Sydney, New South Wales, Australia
- Dong, Buwen**, National Centre for Atmospheric Science, Department of Meteorology, University of Reading, Reading, United Kingdom
- Edwards, Laura M.**, South Dakota State University Extension, Aberdeen, South Dakota
- Eischeid, Jon**, University of Colorado, Cooperative Institute for Research in Environmental Sciences, Boulder, Colorado
- Feser, Frauke**, Institute for Coastal Research, Helmholtz-Zentrum Geesthacht, Geesthacht, Germany
- Funk, Chris**, U.S. Geological Survey and Climate Hazard Group, University of California Santa Barbara, Santa Barbara, California
- Haeseler, Susanne**, German Meteorological Service, Hamburg, Germany
- Harrington, Luke**, School of Geography, Environment and Earth Sciences, Victoria University of Wellington, Wellington, New Zealand
- Haugen, Matz**, Department of Statistics and Department of Environmental Earth System Science and Woods Institute for the Environment, Stanford University, Stanford, California
- Hegerl, Gabriele C.**, University of Edinburgh, Edinburgh, Scotland
- Hendon, Harry H.**, Centre for Australian Weather and Climate Research, Bureau of Meteorology, Melbourne, Australia
- Herring, Stephanie C.**, NOAA's National Climatic Data Center, Boulder, Colorado
- Hoell, Andrew**, Climate Hazard Group, University of California Santa Barbara, Santa Barbara, California
- Hoerling, Martin P.**, NOAA's Earth System Research Laboratory, Boulder, Colorado
- Horton, Daniel E.**, Department of Environmental Earth System Science and Woods Institute for the Environment, Stanford University, Stanford, California
- Imada, Yukiko**, Atmosphere and Ocean Research Institute, University of Tokyo, Chiba, Japan
- Ishii, Masayoshi**, Meteorological Research Institute, Japan Meteorological Agency, Ibaraki, Japan
- Johnson, Nathaniel C.**, International Pacific Research Center, University of Hawaii at Manoa, Honolulu, Hawaii and Scripps Institution of Oceanography, University of California—San Diego, La Jolla, California
- Karoly, David J.**, School of Earth Sciences and Australian Research Council Centre of Excellence for Climate System Science, University of Melbourne, Melbourne, Victoria, Australia
- Kim, Maeng-Ki**, Department of Atmospheric Science, Kongju National University, Gongju, Chungnam, Korea
- Kim, Yeon-Hee**, School of Environmental Science and Engineering, Pohang University of Science and Technology, Pohang, Gyeongbuk, Korea
- Kimoto, Masahide**, Atmosphere and Ocean Research Institute, University of Tokyo, Chiba, Japan
- King, Andrew D.**, Australian Research Council Centre of Excellence for Climate System Science, Climate Change Research Centre, University of New South Wales, Sydney, New South Wales, Australia
- Knutson, Thomas R.**, NOAA's Geophysical Fluid Dynamics Laboratory, Princeton, New Jersey
- Lefebvre, Christiana**, German Meteorological Service, Hamburg, Germany
- Lewis, Sophie C.**, Australian Research Council Centre of Excellence for Climate System Science, School of Earth Sciences, University of Melbourne, Melbourne, Victoria, Australia
- Lim, Eun-Pa**, Centre for Australian Weather and Climate Research, Bureau of Meteorology, Melbourne, Australia
- Liu, Guo**, Centre for Australian Weather and Climate Research, Bureau of Meteorology, Melbourne, Australia

- López-Moreno, Juan Ignacio**, Instituto Pirenaico de Ecología, Consejo Superior de Investigaciones Científicas, Zaragoza, Spain
- Ma, Shuangmei**, State Key Laboratory of Numerical Modeling for Atmospheric Sciences and Geophysical Fluid Dynamics (LASG), Institute of Atmospheric Physics, Chinese Academy of Sciences, University of Chinese Academy of Sciences, Beijing, China
- Massey, Neil R.**, Environmental Change Institute, University of Oxford, Oxford, United Kingdom
- Mei, Rui**, Climate Change Science Institute, Oak Ridge National Laboratory, Oak Ridge, Tennessee
- Min, Seung-Ki**, School of Environmental Science and Engineering, Pohang University of Science and Technology, Pohang, Gyeongbuk, Korea
- Mori, Masato**, Atmosphere and Ocean Research Institute, University of Tokyo, Chiba, Japan
- Otto, Friederike E. L.**, Environmental Change Institute, University of Oxford, Oxford, United Kingdom
- Park, Changyong**, School of Environmental Science and Engineering, Pohang University of Science and Technology, Pohang, Gyeongbuk, Korea
- Parker, Lauren E.**, Department of Geography, University of Idaho, Moscow, Idaho
- Perkins, Sarah E.**, Australian Research Council Centre of Excellence for Climate System Science, Climate Change Research Centre, University of New South Wales, Sydney, New South Wales, Australia
- Perlwitz, Judith**, University of Colorado, Cooperative Institute for Research in Environmental Sciences, Boulder, Colorado
- Peterson, Thomas C.**, NOAA's National Climatic Data Center, Asheville, North Carolina
- Quan, Xiaowei**, University of Colorado, Cooperative Institute for Research in Environmental Sciences, Boulder, Colorado
- Rajaratnam, Bala**, Department of Statistics and Department of Environmental Earth System Science and Woods Institute for the Environment, Stanford University, Stanford, California
- Rastogi, Deeksha**, Climate Change Science Institute, Oak Ridge National Laboratory, Oak Ridge, Tennessee
- Rosier, Suzanne**, National Institute of Water and Atmospheric Research, Wellington, New Zealand
- Scahill, Alice**, School of Geography, Environment and Earth Sciences, Victoria University of Wellington, Wellington, New Zealand
- Schaller, Nathalie**, Environmental Change Institute, University of Oxford, Oxford, United Kingdom
- Schubert, Siegfried**, Global Modeling and Assimilation Office, NASA's Goddard Space Flight Center, Greenbelt, Maryland
- Shaffrey, Len**, National Centre for Atmospheric Science, Department of Meteorology, University of Reading, Reading, United Kingdom
- Shiogama, Hideo**, National Institute for Environmental Studies, Ibaraki, Japan
- Singh, Deepti**, Department of Environmental Earth System Science and Woods Institute for the Environment, Stanford University, Stanford, California
- Sparrow, Sarah**, Environmental Change Institute, University of Oxford, Oxford, United Kingdom
- Stendel, Martin**, Danish Climate Centre, Danish Meteorological Institute, Copenhagen, Denmark
- Stone, Dáithí**, Lawrence Berkeley National Laboratory, Berkeley, California
- Stott, Peter A.**, Met Office Hadley Centre, Exeter, United Kingdom
- Stuart, Stephen**, National Institute of Water and Atmospheric Research, Wellington, New Zealand
- Sutton, Rowan**, National Centre for Atmospheric Science, Department of Meteorology, University of Reading, Reading, United Kingdom
- Swain, Daniel L.**, Department of Environmental Earth System Science and Woods Institute for the Environment, Stanford University, Stanford, California
- Todey, Dennis P.**, Department of Agriculture and Biosystems Engineering, South Dakota State University, Brookings, South Dakota
- Trewin, Blair**, Climate Information Services, Bureau of Meteorology, Melbourne, Australia
- Tsiang, Michael**, Department of Statistics and Department of Environmental Earth System Science and Woods Institute for the Environment, Stanford University, Stanford, California
- van Oldenborgh, Geert Jan**, Koninklijk Nederlands Meteorologisch Instituut, De Bilt, Netherlands
- Vicente-Serrano, Sergio**, Instituto Pirenaico de Ecología, Consejo Superior de Investigaciones Científicas, Zaragoza, Spain
- von Storch, Hans**, Institute for Coastal Research, Helmholtz-Zentrum Geesthacht, Geesthacht, Germany
- Wang, Hailan**, Global Modeling and Assimilation Office, NASA's Goddard Space Flight Center, Science Systems and Applications, Inc., Greenbelt, Maryland
- Watanabe, Masahiro**, Atmosphere and Ocean Research Institute, University of Tokyo, Chiba, Japan
- Wheeler, Matthew C.**, Centre for Australian Weather and Climate Research, Bureau of Meteorology, Melbourne, Australia
- Wittenberg, Andrew T.**, NOAA's Geophysical Fluid Dynamics Laboratory, Princeton, New Jersey
- Wolter, Klaus**, University of Colorado, Cooperative Institute for Research in Environmental Sciences, Boulder, Colorado
- Yiou, Pascal**, Laboratoire des Sciences du Climat et de l'Environnement, Institut Pierre Simon Laplace, Gif-sur-Yvette, France
- Zeng, Fanrong**, NOAA's Geophysical Fluid Dynamics Laboratory, Princeton, New Jersey
- Zhang, Xuebin**, Environment Canada, Toronto, Ontario
- Zhou, Tianjun**, State Key Laboratory of Numerical Modeling for Atmospheric Sciences and Geophysical Fluid Dynamics (LASG), Institute of Atmospheric Physics, Climate Change Research Center, Chinese Academy of Sciences, Beijing, China
- Zou, Liwei**, State Key Laboratory of Numerical Modeling for Atmospheric Sciences and Geophysical Fluid Dynamics (LASG), Institute of Atmospheric Physics, Chinese Academy of Sciences, Beijing, China
- Zwiers, Francis W.**, Pacific Climate Impacts Consortium, University of Victoria, Victoria, British Columbia

TABLE OF CONTENTS

LIST OF AUTHORS AND AFFILIATIONS.....	i
ABSTRACT	iv
1. INTRODUCTION TO EXPLAINING EXTREME EVENTS OF 2013 FROM A CLIMATE PERSPECTIVE.....	1
2. THE EXTRAORDINARY CALIFORNIA DROUGHT OF 2013/14: CHARACTER, CONTEXT, AND THE ROLE OF CLIMATE CHANGE.....	3
3. CAUSES OF THE EXTREME DRY CONDITIONS OVER CALIFORNIA DURING EARLY 2013.....	7
4. EXAMINING THE CONTRIBUTION OF THE OBSERVED GLOBAL WARMING TREND TO THE CALIFORNIA DROUGHTS OF 2012/13 AND 2013/14.....	11
5. NORTHEAST COLORADO EXTREME RAINS INTERPRETED IN A CLIMATE CHANGE CONTEXT	15
6. SEASONAL AND ANNUAL MEAN PRECIPITATION EXTREMES OCCURRING DURING 2013: A U.S. FOCUSED ANALYSIS	19
7. OCTOBER 2013 BLIZZARD IN WESTERN SOUTH DAKOTA.....	23
8. MULTIMODEL ASSESSMENT OF EXTREME ANNUAL-MEAN WARM ANOMALIES DURING 2013 OVER REGIONS OF AUSTRALIA AND THE WESTERN TROPICAL PACIFIC.....	26
9. THE ROLE OF ANTHROPOGENIC FORCING IN THE RECORD 2013 AUSTRALIA-WIDE ANNUAL AND SPRING TEMPERATURES	31
10. INCREASED SIMULATED RISK OF THE HOT AUSTRALIAN SUMMER OF 2012/13 DUE TO ANTHROPOGENIC ACTIVITY AS MEASURED BY HEAT WAVE FREQUENCY AND INTENSITY.....	34
11. UNDERSTANDING AUSTRALIA'S HOTTEST SEPTEMBER ON RECORD	37
12. CLIMATE CHANGE TURNS AUSTRALIA'S 2013 BIG DRY INTO A YEAR OF RECORD-BREAKING HEAT.....	41
13. THE ROLE OF ANTHROPOGENIC CLIMATE CHANGE IN THE 2013 DROUGHT OVER NORTH ISLAND, NEW ZEALAND.....	45
14. ASSESSING HUMAN CONTRIBUTION TO THE SUMMER 2013 KOREAN HEAT WAVE.....	48
15. THE CONTRIBUTION OF ANTHROPOGENIC FORCING TO THE JAPANESE HEAT WAVES OF 2013.....	52
16. UNDERSTANDING A HOT SUMMER IN CENTRAL EASTERN CHINA: SUMMER 2013 IN CONTEXT OF MULTIMODEL TREND ANALYSIS.....	54
17. SEVERE PRECIPITATION IN NORTHERN INDIA IN JUNE 2013: CAUSES, HISTORICAL CONTEXT, AND CHANGES IN PROBABILITY.....	58
18. THE 2013 HOT, DRY SUMMER IN WESTERN EUROPE.....	62
19. CONTRIBUTION OF ATMOSPHERIC CIRCULATION TO WET SOUTHERN EUROPEAN WINTER OF 2013	66
20. THE HEAVY PRECIPITATION EVENT OF MAY-JUNE 2013 IN THE UPPER DANUBE AND ELBE BASINS.....	69
21. THE EXTREME SNOW ACCUMULATION IN THE WESTERN SPANISH PYRENEES DURING WINTER AND SPRING 2013.....	73
22. A VIOLENT MIDLATITUDE STORM IN NORTHERN GERMANY AND DENMARK, 28 OCTOBER 2013.....	76
23. THE EFFECT OF ANTHROPOGENIC CLIMATE CHANGE ON THE COLD SPRING OF 2013 IN THE UNITED KINGDOM.....	79
24. SUMMARY AND BROADER CONTEXT.....	82
25. REFERENCES.....	85

ABSTRACT—Stephanie C. Herring, Martin P. Hoerling, Thomas C. Peterson, and Peter A. Stott

Attribution of extreme events is a challenging science and one that is currently undergoing considerable evolution. In this paper, 20 different research groups explored the causes of 16 different events that occurred in 2013. The findings indicate that human-caused climate change greatly increased the risk for the extreme heat waves assessed in this report. How human influence affected other types of events such as droughts, heavy rain events, and storms was less clear, indicating that natural variability likely played a much larger role in these extremes. Multiple groups chose to look at both the Australian heat waves and the California drought, providing an opportu-

nity to compare and contrast the strengths and weaknesses of various methodologies. There was considerable agreement about the role anthropogenic climate change played in the events between the different assessments. This year three analyses were of severe storms and none found an anthropogenic signal. However, attribution assessments of these types of events pose unique challenges due to the often limited observational record. When human-influence for an event is not identified with the scientific tools available to us today, this means that if there is a human contribution, it cannot be distinguished from natural climate variability.

I. INTRODUCTION TO EXPLAINING EXTREME EVENTS OF 2013 FROM A CLIMATE PERSPECTIVE

PETER A. STOTT, GABRIELE C. HEGERL, STEPHANIE C. HERRING, MARTIN P. HOERLING,
THOMAS C. PETERSON, XUEBIN ZHANG, AND FRANCIS W. ZWIERS

Extreme events in recent years have drawn increased attention to the science seeking to understand their causes (Kerr 2013). The Intergovernmental Panel on Climate Change (IPCC) Fifth Assessment Report (Stocker et al. 2014) concluded that strong evidence exists for increases in some extremes worldwide since 1950, especially more frequent hot days and heavy precipitation events. But, with natural variability playing a substantial role in individual events and given the complexities of the weather and climate processes involved, many challenges still need to be overcome to authoritatively assess how climate change has affected the strength and likelihood of individual extremes. These difficulties go beyond the science *per se*. Appreciating the value and applications of such science and how to communicate results effectively also provides a considerable and ongoing challenge.

Every extreme event raises questions about how anthropogenic climate change affected its intensity and its probability of occurrence. This question arises for many reasons, but often it is the implications for the future that is of greatest concern. If anthropogenic influences caused changes in an event's intensity or likelihood, this has implications for the impacts of future events and the actions that may be required to adapt to changes. This demand for information is a challenge for the scientific community, especially when it is requested shortly after an event when planning is underway to lessen the risk from future events (Peterson et al. 2008). It is difficult to quantify the often multiple causal factors among large weather variability. Challenges can be introduced when there is a limited observational record or climate models are not available that fully represent all the relevant physical processes involved in creating the extreme event. Nevertheless, attribution studies of previous events have shown the potential for scientific analyses to provide information on the degree to which anthropogenic climate change affected its likelihood or magnitude. Examples include the 2003 European heatwave (Stott et al. 2004), the 2010 Russian heatwave (Dole et al.

2011; Otto et al. 2012), the UK floods in 2000 (Pall et al. 2011), and the Texas drought and heatwave in 2011 (Hoerling et al. 2013; Rupp et al. 2013).

An important backdrop for the investigation of the causes of individual extreme events is research that is aimed at understanding how and why the frequency and intensity of extremes has changed over time. Globally there is strengthening evidence for changes in some extremes and for links to human influence (Field et al. 2012; Stocker et al. 2014). Moreover, the pause in rising global annual temperatures does not appear to be affecting the continuing intensification of hot temperature extremes (Seneviratne et al. 2014; Sillmann et al. 2014). Over the global land area with sufficient observations to quantify long-term changes, the evidence indicates continued warming of both hot temperature extremes such as the annual maxima of daily temperatures and cold temperature extremes such as annual minimum daily temperature, which have become less cold (Donat et al. 2013). Furthermore, anthropogenic influences were assessed by the IPCC (Stocker et al. 2014) to have contributed to "intensification of heavy precipitation over land regions where data are sufficient."

Observed changes in several metrics of extreme temperature, including the number of warm nights annually and annual maximum and minimum daily temperatures, are consistent with model-simulated anthropogenic influence at the global scale and in many continental and subcontinental regions (Morak et al. 2011, 2013; Min et al. 2013; Christidis et al. 2011; Wen et al. 2013; and Zwiers et al. 2011). Human influence has been detected in observed changes in moderate extremes, i.e., daily maximum temperatures that are greater than their 90th percentile and daily minimum temperatures less than their 10th percentile over the global land and many continental regions (Morak et al. 2011, 2013). Globally, average recurrence times for cold events that, in the 1960s, were expected to recur once every 20 years are now estimated to exceed 35 years. In contrast, average recurrence times for circa 1960s 20-year warm night and warm day

events have decreased to less than 10 and 15 years, respectively (Zwiers et al. 2011).

Over land where sufficient data exist, extreme precipitation, as represented by the annual maxima of one-day precipitation amounts, has increased significantly, with a median increase about 7% per degree Celsius global temperature increase (Westra et al. 2013). The increase since 1951 in these precipitation extremes in the Northern Hemisphere can be partially attributed to human influence on the climate (Zhang et al. 2013). The best estimate suggests that human influence has intensified annual maximum one-day precipitation by 3.3% on average, corresponding to a 5.3% increase per one-degree increase in global mean temperature and consistent with model-simulated changes and the observed intensification when uncertainties are taken into account. Taking this hemispheric perspective into account, extreme one-day precipitation events that were expected to recur once every 20 years in the 1950s are estimated to have become 1-in-15-year events in the early 21st century due to human influence (Zhang et al. 2013).

The evidence from multiple studies, including those mentioned above, indicates that human influence has changed the frequency of high-impact temperature and precipitation extremes on average over land where there are sufficient observational data to make this assessment. At large spatial scales, an attributed reduction in the recurrence time for a defined extreme temperature or precipitation event from 20 years to 15 years over half a century translates into a fraction of attributable risk (FAR) of about 25%. This corresponds to an increase in the frequency of events exceeding the defined threshold that is attributable to anthropogenic causes [note, however, that the contribution by anthropogenic forcing to the *magnitude* of an event may be different (e.g., Dole et al. 2011; Otto et al. 2012)]. This type of finding gives us confidence that there is a basis for studying individual events and for posing, in an operational mode, the question of whether their intensity and likelihood has been affected by human influence on the climate. Individual events considered for such attribution studies are often of longer timescales and larger magnitude than those considered in these global frequency studies. Also, hemispheric-scale changes may average across distinct regional changes associated with changing circulation. Change and variation in circulation are of key importance for climate extremes, yet they are difficult to reliably attribute (Bindoff et al. 2014). Targeted studies, such as those included in this re-

port, are therefore necessary in order to make robust attribution statements about individual events and pose important further scientific challenges.

One of the goals of this report is to foster the development of scientific methods that can be applied operationally to explain the underlying physical processes causing extreme events, including the circulation involved, and to place the event and associated processes in a historical context of climate variability and change. In some cases, scientific methods will be used to evaluate proposed mechanisms for how extreme weather may change in a warming world. For example, a recent theory linked Arctic climate change to extreme weather in mid-latitudes by affecting the circumpolar circulation (Francis and Vavrus 2012), and the question is open whether this theory has explanatory power. For example, one might ask whether the theory explains the occurrence of intense cold waves over the northern United States and severe drought over California in 2013 (Wallace et al. 2014). In this report, case studies of the California drought shed some light on the physical processes involved in that event. Studies like this demonstrate that attribution analyses can go beyond local trends. This is important since anthropogenic and natural factors may be affecting the risk of particular types of events even in the absence of a clearly detectable trend locally.

In three years, the contributors to the report have grown from 6 in the first edition to 22 different contributing groups looking at 16 events in this edition (Figure 1.1). The report has also started to attract attention from outside the scientific community. For example, it has been recognized by *Foreign Policy* magazine in their analysis of the leading global thinkers of 2013. But, with success comes a new set of challenges. With the growth of the breadth of the report has come a greater requirement to synthesize across the disparate contributions involving different methodologies and different teams. Given the subtleties and uncertainties inherent in this work, it can be difficult to accurately summarize the results in a few words. Nevertheless, each author team provided a 30 words or less capsule summary of their work. These short synopses will enable readers to better synthesize across studies, a charge that is also picked up in the conclusions for the entire report. There are groups from many regions of the world. Together they provide a regional perspective on how the global picture outlined by the recent IPCC report (Stocker et al. 2014) interacts with regional variability to influence specific events and their impacts.

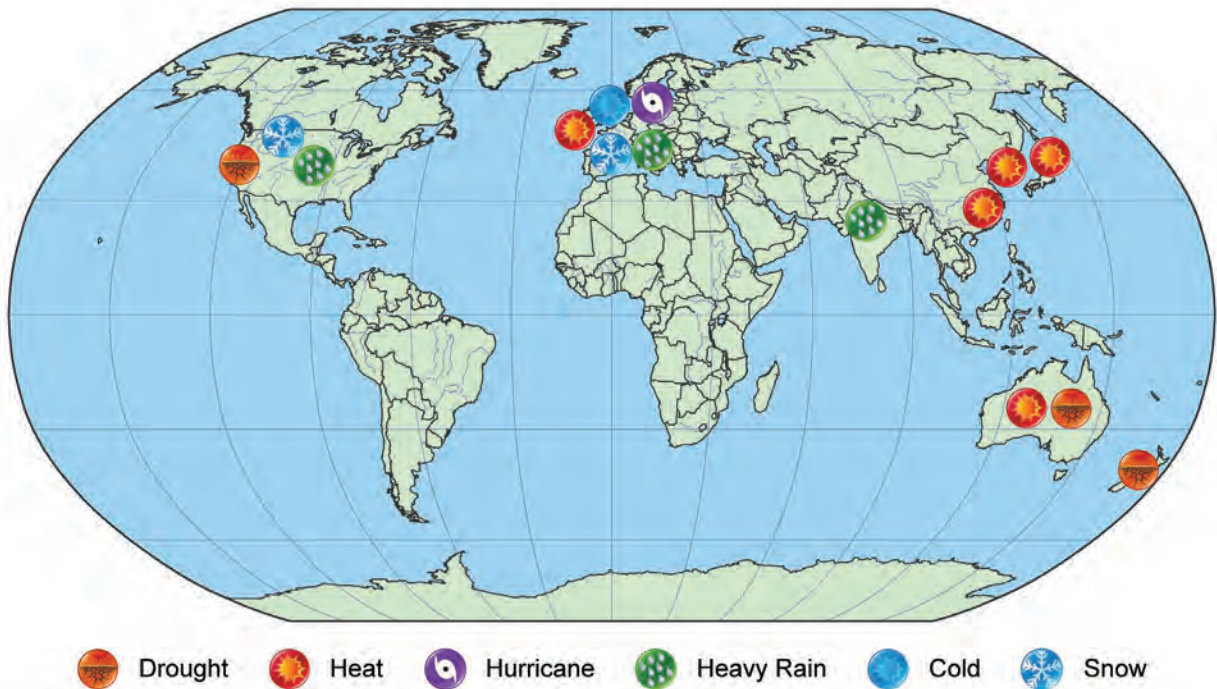


FIG. 1.1. Location and type of events analyzed in this paper.

2. THE EXTRAORDINARY CALIFORNIA DROUGHT OF 2013/2014: CHARACTER, CONTEXT, AND THE ROLE OF CLIMATE CHANGE

DANIEL L. SWAIN, MICHAEL TSIANG, MATZ HAUGEN, DEEPTI SINGH, ALLISON CHARLAND,
BALA RAJARATNAM, AND NOAH S. DIFFENBAUGH

California's driest 12-month period on record occurred during 2013/14, and although global warming has very likely increased the probability of certain large-scale atmospheric conditions, implications for extremely low precipitation in California remain uncertain.

The event: 2013/14 drought in California. Nearly the entire state of California experienced extremely dry conditions during 2013 (Fig. 2.1a). Statewide, 12-month accumulated precipitation was less than 34% of average (Fig. 2.1b), leading to a wide range of impacts. In early 2014, state and federal water agencies announced that agricultural water users in the Central Valley would receive no irrigation water during 2014 (DWR 2014; USBR 2014), and that a number of smaller communities throughout California could run out of water entirely within a 90-day window (USDA

2014a). Low rainfall, unusually warm temperatures, and stable atmospheric conditions affected the health of fisheries and other ecosystems (CDFW 2014), created highly unusual mid-winter wildfire risk (CAL FIRE 2014), and caused exceptionally poor air quality (BAAQMD 2014). Such impacts ultimately resulted in the declaration of a state-level “drought emergency” and the federal designation of all 58 California counties as “natural disaster areas” (USDA 2014b).

The California drought occurred in tandem with a highly persistent region of positive geopotential

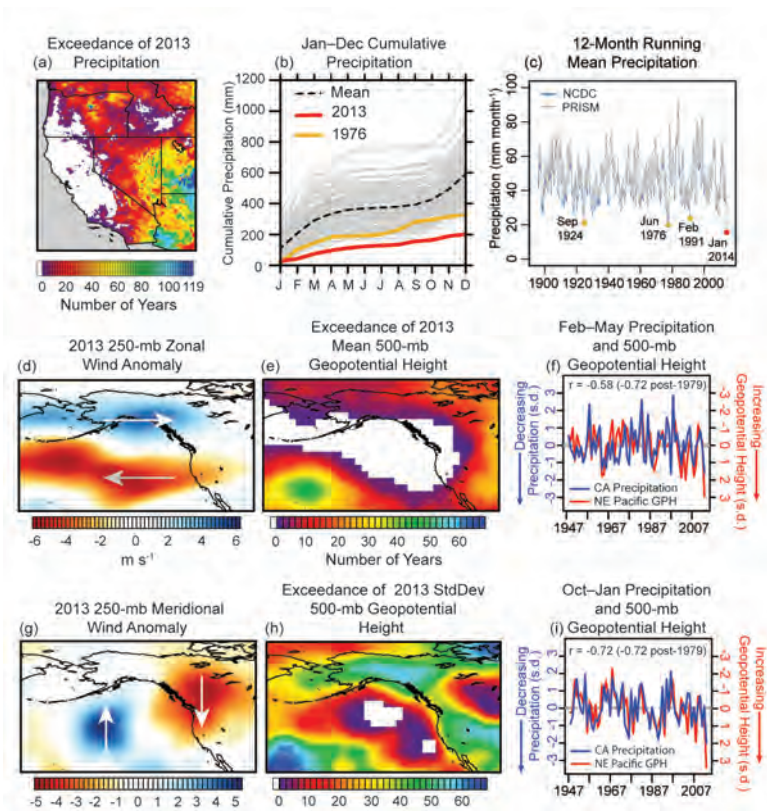


FIG. 2.1. Structure and context of the 2013/14 event. (a) Number of Jan–Dec periods during 1895–2012 in which precipitation was less than the Jan–Dec 2013 value, using the PRISM dataset. (b) Cumulative Jan–Dec precipitation in California for each year in 1895–2013, using the PRISM dataset. (The second-driest calendar year on record, 1976, is shown for reference.) (c) 12-month (one-sided) moving average precipitation in California from 1895 to 2014, using the NCLIMDIV (2014) and PRISM (2014) datasets. 12-month minima experienced during major historical droughts are highlighted. (d) Zonal and (g) meridional wind anomalies during Jan–Dec 2013. Arrows depict the direction of the primary anomaly vectors; the gray arrow in (d) denotes the region where easterly anomalies oppose mean westerly flow. (e) Number of Jan–Dec periods during 1948–2012 in which 500-mb GPH were higher than the Jan–Dec 2013 value. (f) Feb–May and (i) Oct–Jan normalized California precipitation (blue) and sign-reversed northeastern Pacific GPH (red) during 1948–2013 in NCEP reanalysis. (h) As in (e), but for standard deviation of daily 500-mb GPH.

height (GPH) anomalies over the northeastern Pacific Ocean (Fig. 2.1e,h), nicknamed the “Ridiculously Resilient Ridge” in the public discourse. Anomalous geostrophic flow induced by these highly unusual GPH gradients was characterized by weakened westerly zonal winds over the Pacific, strengthened zonal flow over Alaska (Fig. 2.1d), and a couplet of poleward-equatorward meridional wind anomalies centered in the northeastern Pacific around 135°W (Fig. 2.1g). This amplified atmospheric configuration displaced the jet stream well to the north, leading

to greatly reduced storm activity and record-low precipitation in California (Fig. 2.1a,b).

California typically experiences strong seasonality of precipitation, with the vast majority coinciding with the passage of cool-season extratropical cyclones during October–May (e.g., Cayan and Roads 1984). The meteorological conditions that occurred during what would normally be California’s “wet season”—namely, the presence of a quasi-stationary midtropospheric ridge and a northward shift/suppression of the storm track—strongly resembled the conditions during previous California droughts (Namias 1978a,b; Trenberth et al. 1988) and during extremely dry winter months (Mitchell and Blier 1997). The persistence of these meteorological conditions over the second half of the 2012/13 wet season and the first half of the 2013/14 wet season resulted in an extremely dry 12-month period (Fig. 2.1c).

The 2013 event in historical context. The 12-month precipitation and GPH anomalies are both unprecedented in the observational record (Fig. 2.1a,e). We find that a vast geographic region centered in the Gulf of Alaska experienced 500-mb GPH anomalies that exceeded all previous values (Fig. 2.1e) in the 66-year NCEP1 reanalysis (Kalnay et al. 1996). Standard deviation of the daily 500-mb GPH field was also extremely low over much of the northeastern Pacific (Fig. 2.1h), an indication of the profound suppression of

the storm track and of extratropical cyclonic activity induced by persistent ridging.

Likewise, most of California received less precipitation in 2013 than during any previous calendar year in the 119-year observational record (Fig. 2.1a). Observed precipitation over the 12-month period ending on 31 January 2014 was the lowest for any consecutive 12-month period since at least 1895 (Fig. 2.1c). Thus, the one-year precipitation deficit associated with the 2013/14 event was larger than any previous one-year deficit observed during California’s

historical droughts, including the notable events of 1976/77 and 1987–92.

One of the most remarkable aspects of the 2013/14 event was the spatial and temporal coherence of strong midtropospheric ridging and associated wind anomalies over multiple seasons. The spatial structure of observationally unprecedented GPH anomalies during both February–May 2013 and October–January 2013/14 was very similar to that of the 12-month mean (Supplementary Fig. S2.1), as was the structure of the ridging-induced anomalous flow. The coherence of this anomalous large-scale atmospheric pattern preceding and following the canonical June–September dry season was especially unusual. In particular, although high-amplitude meridional flow and positive GPH anomalies over the far northeastern Pacific are often associated with precipitation deficits in California (Carrera et al. 2004; Namias 1978a; Chen and Cayan 1994), the temporal resilience and spatial scale of the GPH anomalies were greater in 2013/14 than during previous droughts in California’s recent past (Fig. 2.1e).

Quantifying the probability of a 2013-magnitude event.

We define a “2013-magnitude event” as the mean January–December 2013 500-mb GPH over the core area of unprecedented annual GPH (35°–60°N and 210°–240°E; Fig. 2.1e). We find a strong negative relationship between northeastern Pacific GPH and California precipitation [for the 1979–2012 period, traditional correlation for February–May (October–January) = -0.72 (-0.72); Spearman’s correlation for February–May (October–January) = -0.66 (-0.73); Fig. 2.1f,i]. We use GPH to characterize the event based on the rarity of the GPH anomalies and the observed strength of the relationship between GPH and precipitation (Mitchell and Blier 1997; Chen and Cayan 1994). Because the 2013 12-month GPH fell far in the upper tail of the observational distribution (Fig. 2.2a), we calculate the likelihood of the 2013 event by fitting a Pareto III-type parametric distribution to the 1979–2012 reanalysis [Fig. 2.2a; Supplementary Materials (SM)]. We select the Pareto-III distribution for parametric fitting because it is characterized by a one-sided heavy tail, which allows for more stable estimates of return periods for extreme events occurring far in the upper tail of observed or simulated distributions (such as a 2013-magnitude event, see SM). We estimate that the return period for the 2013 12-month GPH value “likely” exceeds 285 years ($>66\%$ confidence; Masstrandrea et al. 2011) and “very likely” exceeds 126

years ($>95\%$ confidence), with a median estimate of 421 years (Fig. 2.2b).

We use the CMIP5 global climate models (Taylor et al. 2012) to compare the probability of persistently high GPH in the 20th century (20C) and preindustrial control (P.I.) climates (see SM). The relationship between northeastern Pacific GPH and California precipitation is well represented in the CMIP5 20C simulations (Langford et al. 2014). We select the 12 models for which 20C and P.I. GPH data are available, and for which the Kolmogorov-Smirnov goodness-of-fit test exceeds 0.2 between the climate model and reanalysis distributions (Supplementary Fig. S2.2). We find that the mean change in GPH between the P.I. and 20C simulations is positive for 11 of these 12 models (median change = $+7.96$ m; Fig. 2.2d). We, thus, find large increases in the frequency of occurrence of events exceeding the highest P.I. percentiles in the 20C simulations (Fig. 2.2e). For instance, the median change in occurrence of GPH values exceeding the 99th P.I. percentile is $>670\%$. While the occurrence of events exceeding the P.I. 90–99th percentiles categorically increases in the 20C simulations (which include both natural and anthropogenic forcings), we find no such increase in those CMIP5 simulations which include only natural forcing (Fig. 2.2f; see SM). Thus, we find that anthropogenic forcing—rather than natural external forcing—dominates the simulated response in extreme GPH.

We also use the Pareto-III distribution to calculate the return period of the 2013-magnitude extreme GPH event in the CMIP5 simulations. Here we select the three CMIP5 models for which the Kolmogorov-Smirnov goodness-of-fit test exceeds 0.8 (i.e., the “B3” models; Supplementary Fig. S2.2). For these models, we again fit bootstrapped Pareto-III distributions to the simulated 20C (1979–2005) and P.I. distributions to estimate return periods for a 2013-like extreme GPH value in our index region (see SM). The distribution of ratios between the bootstrapped return periods calculated for the 20C and P.I. simulations suggests that it is “likely” (“very likely”) that the probability of extremely high GPH is at least a factor of 4.02 (2.86) as great in the current climate as in the preindustrial control climate (Fig. 2.2c). Although the trend in GPH during the 20C simulations strongly influences the increase in probability (Supplementary Fig. S2.3), we reiterate that the increased occurrence of extreme GPH does not occur in the absence of human forcing (Fig. 2.2f).

Because the spatial structure of the GPH field—rather than the regional mean value—is the ultimate

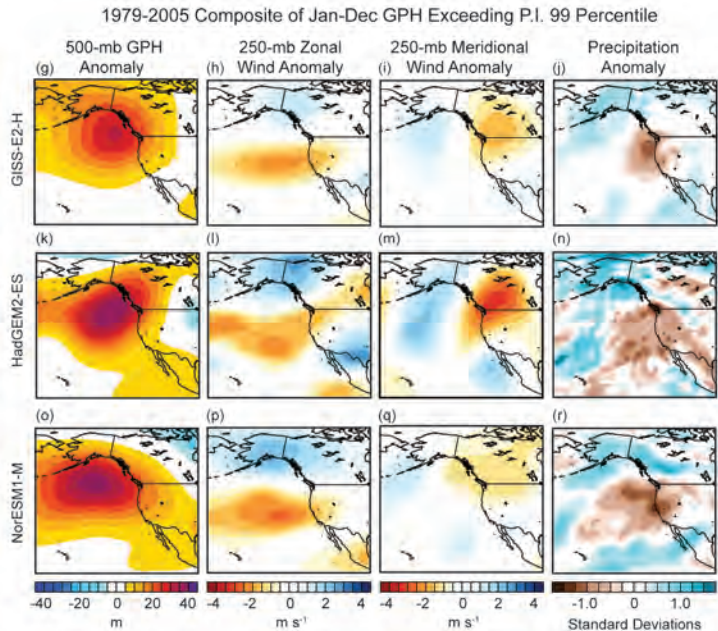
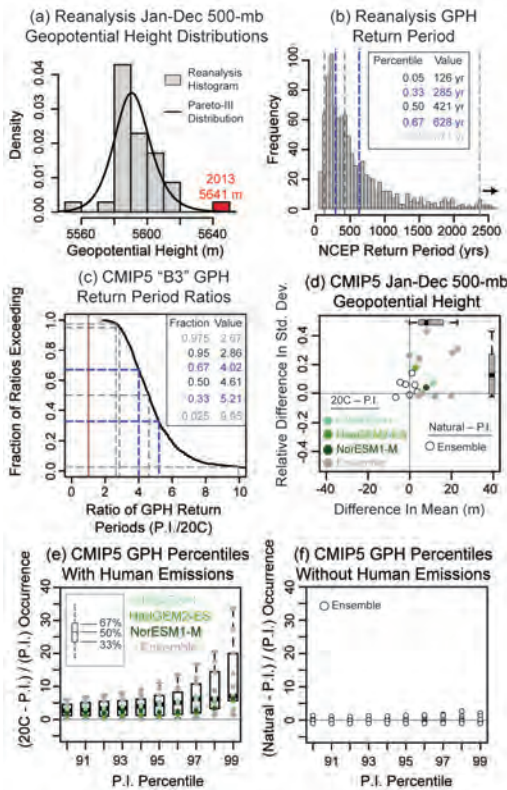


FIG. 2.2. Quantifying the probability of a 2013-magnitude event. (a) Histogram (gray bins) and fitted Pareto-III distribution for NCEP reanalysis 500-mb GPH in the post-satellite period (1979–2013). The fitted distribution—shown for illustrative purposes—is estimated using the actual reanalysis distribution. (b) Distribution of bootstrapped return periods

for a 2013-magnitude Jan–Dec GPH event in the 1979–2012 reanalysis data. (c) Cumulative distribution of bootstrapped return period ratios for the preindustrial control (P.I.) and historical 20th century (20C) simulations in the B3 models, calculated as $(P.I./20C)$. (d) Absolute change in mean and relative change in standard deviation of 500-mb GPH in the historical 20C and natural forcing (“Natural”) CMIP5 simulations relative to P.I. B3 models are highlighted using green colors. (e) Frequency of exceedance of P.I. 0.90–0.99 500-mb GPH quantiles in the 20C simulations. (f) Frequency of exceedance of P.I. 0.90–0.99 500-mb GPH quantiles in the Natural simulations. (g–r) The composite 12-month anomaly fields, calculated for each of the B3 models, of 500-mb GPH (g,k,o), 250-mb zonal winds (h,l,p), 250-mb meridional winds (i,m,q), and total precipitation (j,n,r) from the 20C years in which the GPH in the North Pacific index region exceeds the respective P.I. 99th percentile.

causal factor in rearranging the geostrophic flow field and shifting the midlatitude storm track away from California, we also examine the configuration of the large-scale atmospheric patterns associated with extreme GPH in the B3 models. For each of the B3 models, we composite the 12-month anomaly fields of 500-mb GPH, 250-mb winds, and total precipitation from each 20C year in which the GPH in our index region exceeds the respective P.I. 99th percentile. A zonally asymmetric pattern of positive GPH anomalies is apparent in all three model composites, with a distinct maximum located over the Gulf of Alaska region (Fig. 2.2g,k,o). This perturbation of the GPH field is associated with well-defined anticyclonic circulation anomalies, including weakened westerly flow aloft near and west of California (Fig. 2.2h,l,p) and enhanced equatorward flow aloft near the western coast of North America (Fig. 2.2i,m,q).

This composite spatial pattern strongly resembles the large-scale atmospheric structure that occurred during 2013 (Fig. 2.1d,e,g,h; Supplementary Fig. S2.2), and it is associated with large negative precipitation anomalies in the vicinity of California (Fig. 2.2j,n,r). These composite results thereby confirm that the extreme GPH events identified in our index region are associated with anomalous atmospheric circulation over the northeast Pacific and dry conditions in California.

We note two caveats. First, neither our probability quantification nor our compositing methodology quantifies the amplitude of extreme ridging events. Because we do not explicitly consider geopotential heights outside the North Pacific, it is likely that our inclusion of all years that exceed the 99th percentile P.I. GPH leads to inclusion of some events that have lower amplitude than that associated with either the

99th percentile P.I. GPH or the 2013 event. Thus, our present methodology cannot reject the possibility that the frequency of occurrence of years with anomalous GPH *gradients*—and the risk of extreme drought associated with a perturbed North Pacific storm track—has not changed between the preindustrial period and the present. [However, we note that Wang et al. (2014) do find evidence of increased high-amplitude ridging in this region in response to anthropogenic forcing.] Second, Neelin et al. (2013) report both an increase in long-term mean December–February precipitation over California and strengthened December–February mean westerly flow over the far eastern Pacific at the end of the 21st century under strongly increased greenhouse forcing (RCP8.5). These changes are opposite in sign to those associated with extreme annual GPH events in the 20C simulations relative to the P.I. control (Fig. 2.2).

Conclusions. The 2013/14 California drought was an exceptional climate event. A highly persistent large-scale meteorological pattern over the northeastern Pacific led to observationally unprecedented geopotential height and precipitation anomalies over a broad region. The very strong ridging and highly amplified meridional flow near the West Coast of North America in 2013/14 was structurally similar to—but spatially and temporally more extensive than—atmospheric configurations that have been previously linked to extreme dryness in Califor-

nia (Mitchell and Blier 1997; Namias 1978a,b). We find that extreme geopotential height values in this region, which are a defining metric of this type of atmospheric configuration, occur much more frequently in the present climate than in the absence of human emissions (Fig. 2.2).

The human and environmental impacts of the 2013/14 California drought were amplified by the timing of the event. The event began suddenly in January 2013, abruptly truncating what had initially appeared to be a wet rainy season following very heavy precipitation during November–December 2012 (DWR 2013). By persisting through January 2014, the event also effectively delayed the start of the subsequent rainy season by at least four months. The rapid onset and persistent high intensity of drought conditions presented unique challenges for decision makers tasked with making choices about the allocation of water to urban, agricultural, and environmental interests (USDA 2014a; DWR 2014). Together, the complexity and severity of the observed drought impacts, coupled with our finding that global warming has increased the probability of extreme North Pacific geopotential heights similar to those associated with the 2013/14 drought, suggest that understanding the link between climate change and persistent North Pacific ridging events will be crucial in characterizing the future risk of severe drought in California.

3. CAUSES OF THE EXTREME DRY CONDITIONS OVER CALIFORNIA DURING EARLY 2013

HAILAN WANG AND SIEGFRIED SCHUBERT

The 2013 SST anomalies produced a predilection for California drought, whereas the long-term warming trend appears to make no appreciable contribution because of the counteraction between its dynamical and thermodynamic effects.

Introduction. The state of California experienced extreme dry conditions during early 2013. In particular, January and February received 28% and 15%, respectively, of their normal monthly rainfall. When January and February are combined, January/February 2013 is ranked as the driest of the period 1895–2014. Such large precipitation deficits exerted enormous stress on water resources in an already

high water-demand region. Thus, it is of practical importance to investigate the causes of this extreme climate event so as to assess its predictability.

Climatologically, the winter precipitation over California comes from North Pacific storms that travel eastward under the guidance of the strong North Pacific jet stream. The oceanic storms transport abundant water vapor inland, with heavy

precipitation occurring as the flow encounters the Sierra Nevada mountain range. Given the geographical location of California, likely factors that affect the year-to-year variations of precipitation there include atmospheric internal variability, the Madden–Julian Oscillation, El Niño–Southern Oscillation, decadal-to-multidecadal oscillations, and long-term climate change. This study investigates the specific physical processes that led to the early 2013 California drought.

Data and Methods. This study makes use of various observations, the NASA Modern Era Retrospective-Analysis for Research and Applications (MERRA; Rienecker et al. 2011), and an ensemble of long-term Atmospheric Model Intercomparison Project (AMIP) model simulations performed with the NASA Goddard Earth Observing System Model, Version 5 Atmospheric General Circulation Model (GEOS-5 AGCM; Rienecker et al. 2008; Molod et al. 2012). The observations include HadISST data (Rayner et al. 2003), Global Precipitation Climatology Project (GPCP) precipitation (Adler et al. 2003), and Global Precipitation Climatology Centre (CPCC) land precipitation (Schneider et al. 2014). The GEOS-5 AMIP simulations consist of 12 ensemble members,

forced with observed monthly SST, sea ice, and time-varying greenhouse gases for the period 1871–present (Schubert et al. 2014). The model was run with 72 hybrid-sigma vertical levels extending to 0.01 hPa and with 1° horizontal resolution on a latitude/longitude grid.

Since the extreme precipitation deficit over California during early 2013 mainly occurred during January and February, our analysis focuses on the average of these two months.

Results. a. Effects of SST and atmospheric internal variability. Figure 3.1 portrays the early 2013 California drought in the context of current climate (1980–2013). Figure 3.1a shows that the observed January–February averaged precipitation deficits over northern California are essentially the land extension of a broad precipitation deficit centered over the northeast Pacific. An examination of daily precipitation and atmospheric circulation fields (not shown) reveals that the California precipitation deficit is the result of a substantial reduction in North Pacific storms reaching the West Coast of the United States, due to the blocking by persistent upper-level high pressure anomalies over the northeast Pacific (Fig. 3.1b). Such a high pressure anomaly over the northeast Pacific

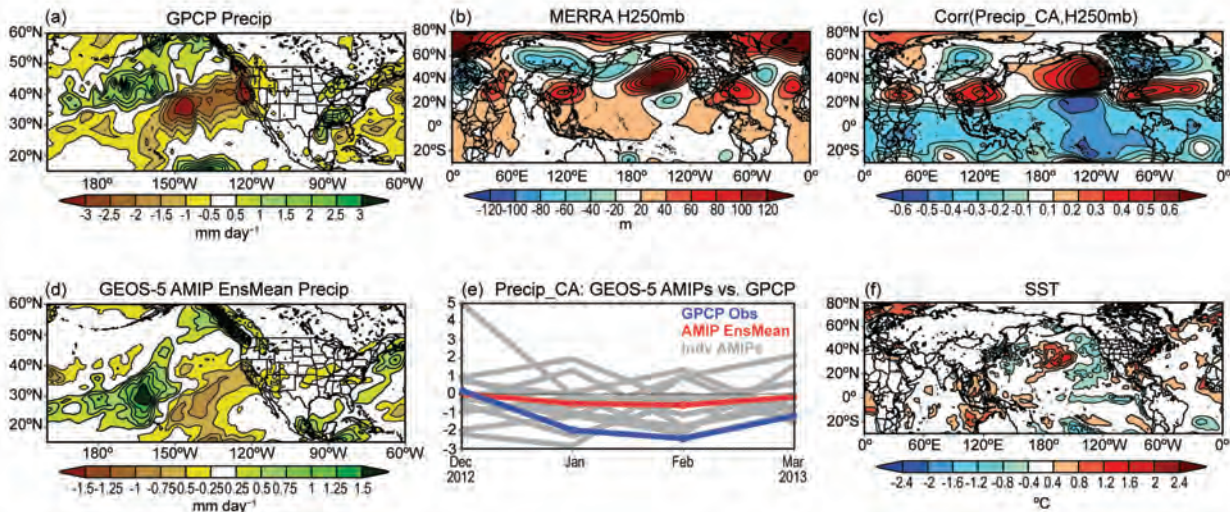


FIG. 3.1. (a) The observed precipitation anomalies (mm day^{-1}) for Jan/Feb 2013 from GPCP. (b) The observed 250-mb geopotential height anomalies (in meters) for Jan/Feb 2013 from MERRA. (c) The temporal correlation between MERRA 250-mb geopotential height and GPCP precipitation averaged over California for Jan/Feb of 1980–2013. A linear trend was removed for each calendar month before computing the correlation. The sign of the correlation is reversed to correspond to precipitation deficit conditions over California. (d) The NASA GEOS-5 AMIP ensemble mean simulation of precipitation anomalies (mm day^{-1}) for Jan/Feb 2013. (e) The comparison between the GPCP (blue), the 12 GEOS-5 AMIP members (gray), and their ensemble mean (red) for monthly precipitation anomalies (mm day^{-1}) averaged over California for Dec 2012–Mar 2013. (f) The observed SST anomalies ($^{\circ}\text{C}$) for Jan/Feb 2013. The above anomalies are obtained as deviations from their climatology over the period 1980–2013.

is rather typical of dry winters over California (Fig. 3.1c). The underlying causes of the high anomaly, however, appear to vary from winter to winter.

To investigate the physical processes for the early 2013 dry event, we turn to the GEOS-5 AMIP simulations. The AMIP ensemble average highlights the forced signals, primarily those by SST anomalies, whereas the spread among the ensemble members reflects the unforced variability or noise generated by processes internal to the atmosphere. The largest SST anomalies during this time occur mainly in the North Pacific, with a warm anomaly in the central North Pacific and cold anomalies to its west and east (Fig. 3.1f). The tropical SST anomalies are weak overall, with indications of warming over the western tropical Pacific and cooling along the central and eastern equatorial Pacific. When forced with the observed SST anomalies, the GEOS-5 AGCM produces a reasonably good simulation of the observed precipitation anomalies over the North Pacific and western North America. While considerably weaker than observed, the ensemble mean, nevertheless, reproduces the basic pattern of a dry response over California as the land extension of a broad oceanic precipitation decrease over the northeast Pacific (Fig. 3.1d). Figure 3.1e further compares the observed monthly precipitation anomalies averaged over California with each of the 12 ensemble members as well as the 12-member ensemble mean. The observations generally fall within the ensemble spread of the 12 members, though they are clearly on the dry edge of the model spread. The ensemble spread is large, with 2 members showing wet anomalies and 10 members producing dry anomalies over California during early 2013, resulting in a weak negative anomaly in the mean. The above results suggest that while the observed SST anomalies have produced a predilection for dryness over California, the large magnitude of the event is primarily an unforced component of the atmospheric internal variability.

b. Role of long-term warming trend. To investigate any long-term changes in the occurrence of extreme dry events over California, we compare two periods: 1871–1970 and 1980–2013. The latter is marked by a period of enhanced global warming. These two periods are chosen because they remove most of the effects of any phase changes of decadal to multidecadal oscillations such as the Pacific decadal oscillation (PDO) and Atlantic multidecadal oscillation (AMO); their contrast, thus, highlights the effect of the long-term warming trend. This is verified in Figure 3.2a,

in which the January/February mean SST differences between the two periods show warming over most of the global ocean, with little indications of PDO and AMO. The differences strongly resemble the global SST trend pattern that is obtained as the leading rotated empirical orthogonal function (REOF) pattern of annual mean SST over the 20th century (Schubert et al. 2009), further supporting that they essentially reflect the long-term warming trend. The change of mean upper-level geopotential height from the early period to the current period (Fig. 3.2b) shows generally positive values, with the main centers of the increase occurring over the North Pacific and eastern United States. The Pacific jet stream also weakens considerably, particularly in the jet exit region at 32°N (not shown). We note that such atmospheric circulation changes resemble the responses of this model and four other AGCMs participating in the U.S. Climate Variability and Predictability Program drought working group (Schubert et al. 2009) to the above-mentioned warm trend pattern, suggesting such circulation changes are indeed a robust response to the warming trend pattern. The implication of the above mean circulation changes is that the weaker westerlies may reduce the number of North Pacific storms reaching California and thereby enhance the risk of dry events over California.

To quantify the effect of the long-term warming trend on the occurrence of dry winters over California, we examine the changes in the probability distribution function (PDF) of the January/February mean precipitation between the early and current periods, again based on the 12 GEOS-5 AMIP simulations. Figure 3.2c shows that the PDF of precipitation over California shows no notable change, consistent with a similar PDF analysis using the GPCC precipitation observations (not shown). We note that, for both the GEOS-5 AMIP simulations and the GPCC observations, the mean precipitation over California does not show any noticeable changes between the two periods either. This suggests that there was no increased risk of drought in California during 2013 as a result of the long-term warming trend. Nevertheless, there are clear indications of an increased probability of warmer surface air temperature over California (Fig. 3.2d), a moister atmosphere over the northeast Pacific off the west coast of California (Fig. 3.2e), and increased height anomalies over the northeast Pacific (Fig. 3.2f)—consistent with the mean height differences found over the North Pacific (Fig. 3.2b). The weakened westerlies on the southern flank of the enhanced northeast Pacific ridge reduces the number

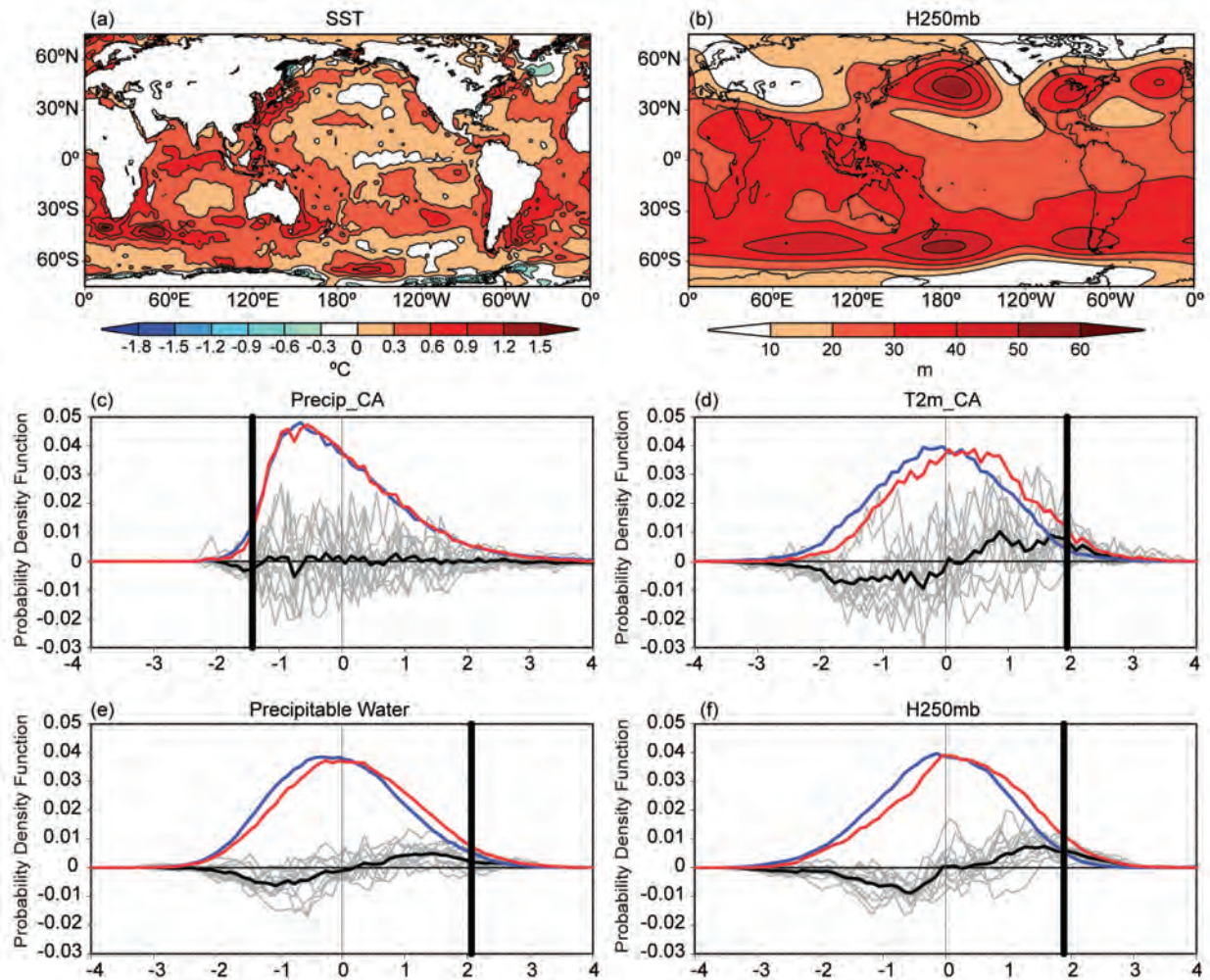


FIG. 3.2. (a) The observed climatology difference of January/February SST ($^{\circ}\text{C}$) between the period 1871–1970 and the period 1980–2013. (b) Same as (a) but for the 250-mb geopotential height (in meters) in the GEOS-5 AMIP ensemble mean simulation. (c) The PDF of precipitation over California for the period 1871–1970 (blue) and for the period 1980–2013 (red) using the 12 GEOS-5 AMIP simulations, the PDF difference between the two time periods using the 12 AMIP simulations (black), and each of the 12 AMIP simulations (gray). (d) Same as (c) but for surface air temperature over California. (e) same as (c) but for total column water vapor over the northeast Pacific just off the west coast of California ($118^{\circ}\text{--}155^{\circ}\text{W}$; $25^{\circ}\text{--}42^{\circ}\text{N}$). (f) Same as (c) but for the 250-mb geopotential height over the northeast Pacific ($120^{\circ}\text{--}155^{\circ}\text{W}$; $30^{\circ}\text{--}54^{\circ}\text{N}$)—the region that has the peak correlation in Figure 2.1c, where the upper-level ridge anomalies exert the strongest dry impact over California. The PDF analysis in (c)–(f) uses data at all grid points in the selected domains. Anomalies used in the PDF analysis are deviations from the climatology over the period 1871–2013. The critical values of 2.5% associated with dryness over California based on the PDF distribution over 1871–2013 are shown using thick black vertical lines.

of North Pacific storms reaching California thereby increasing the chances of dryness over California, whereas the more abundant atmospheric water vapor off the west coast of California enhances the water vapor transport inland and would likely increase the wetness over California. It thus appears that the effects of the above dynamical and thermodynamic processes counteracted each other, contributing to no appreciable change in the PDF of precipitation over California for these two periods. Therefore, dry

climate extremes over California, such as the dry event during early 2013, are unlikely influenced appreciably by the long-term warming trend since the late 19th century.

Conclusions. The extreme precipitation deficits over California during early 2013 resulted from considerably fewer North Pacific storms reaching California, due to the blocking by persistent high anomalies over the northeast Pacific. Our model results show that

the concurrent SST anomalies do force a predilection for dry events over California though considerably weaker than observed, suggesting that atmospheric internal variability accounts for the extreme magnitude of this climate event. An assessment of the role of the long-term warming trend shows that it forces a high anomaly over the northeast Pacific resulting in less North Pacific storms reaching California.

The warming trend, however, also leads to increased atmospheric humidity over the northeast Pacific, thus, facilitating wetter events over California. The above two effects appear to counteract each other, contributing to no appreciable long-term change in the risk for dry climate extremes over California since the late 19th century.

4. EXAMINING THE CONTRIBUTION OF THE OBSERVED GLOBAL WARMING TREND TO THE CALIFORNIA DROUGHTS OF 2012/13 AND 2013/14

CHRIS FUNK, ANDREW HOELL, AND DÁITHÍ STONE

Long-term SST warming trends did not contribute substantially to the 2012/13 and 2013/14 California droughts. North Pacific SSTs were exceptionally warm, however, and coupled models indicate more frequent extreme precipitation.

Introduction. In this study, we examine the November–February California droughts of 2012/13 and 2013/14. During 2013/14, California had its warmest and third driest rainy season on record (1895–2014), while the 2012/13 season registered as the 45th warmest and 38th driest (Vose et al. 2014). The 2013 January–December calendar year was the driest on record (Water CA 2014). These consecutive below-normal seasons conspired with warm temperatures to reduce California’s snowpack to the second lowest level since 1960, when recording began, with snowpack at 24% of normal (Water CA 2014). Between January 2013 and January 2014, satellite observations documented dramatic snowpack-related land cover change (NASA Earth Observatory 2014): in 2014, the Cascade, Sierra Nevada, and Coastal ranges were almost completely devoid of snow. In February and March of 2014, air temperatures were extremely warm (NOAA NCDC 2014; HPRC 2014), and U.S. Geological Survey (USGS) observations indicated extreme or moderate hydrologic drought (USGS 2014) and high levels of vegetation stress (VegDRI 2014). The state declared a drought emergency (NIDIS 2014). While it is too soon to assess the full impact of the 2012/13 and 2013/14 California droughts, they seem likely to substantially impact the state’s ability to generate hydrologic power, support agriculture, reduce

the risk of forest and bush fires, and protect fragile ecosystems (Huffington Post 2014).

While the past three winters have been dry, the 2011–14 precipitation total was slightly higher than totals from the 1973–76 and 1988–91 drought periods, and 1895–2014 California precipitation has exhibited no appreciable downward trend. It is still possible, however, that very warm SSTs, forced by anthropogenic greenhouse gases and aerosols, could increase the probability of 21st century California droughts. We explore this question using two sets of climate model experiments: (a) a 25-member, eight-model, ensemble of Phase 5 Coupled Model Intercomparison Project (CMIP5) historical (Taylor et al. 2012) climate change simulations (Supplemental Table S4.1) and (b) a 21-member ensemble of SST-driven Community Atmospheric Model version 5 (CAM5; Hurrell et al. 2013) driven with the observed and detrended SSTs. We use the CMIP5 simulations to explore SST sensitivities and the CAM5 simulations to formally assess impacts related to the long-term SST global warming pattern. Here, we assess whether SST changes associated with the long-term global warming trend significantly altered California precipitation. Other factors, such as the impact of climate change on the pole-to-equator SST gradient and storm tracks (Favre and Gershunov 2009;

Wang et al. 2014) and changes in sea ice extent (Sewall 2005) are not examined.

CMIP5 sensitivity analysis. We begin by exploring the relationship between California precipitation and SSTs within the CMIP5 ensemble. The selected models have been shown to recreate Pacific-North America climate variations with reasonable levels of realism (Polade et al. 2013). For each ensemble member, we estimate and remove variations associated with ENSO (see Supplementary Materials section). This allows us to focus on the anomalies of SST and precipitation that are not associated with ENSO variability. Since 2012/13 and 2013/14 were ENSO-neutral years, the ENSO-residual relationships are appropriate. Each CMIP5 simulation is initialized in the mid-19th century using preindustrial conditions and then allowed to run through 2005. We have extended these simulations through 2014 using the Representative Concentration Pathway 8.5 experiment. Figure 4.1a shows the ensemble mean composite ENSO-residual SST based on the difference between each simulation's 10 driest and 10 wettest ENSO-residual California winters. In these simulations, California tends to be dry when there is a combination of warm North Pacific SSTs and cool extratropical eastern Pacific SSTs. This pattern bears some similarity to the interdecadal Pacific oscillation (IPO; Dai 2013) and Pacific decadal oscillation (PDO; Mantua et al. 1997), which may drive a substantial portion of decadal precipitation variability in the Southwest (Gershunov and Cayan 2003; Dai 2013) and modulate the strength of ENSO teleconnections (McCabe and Dettinger 1999). Upper-level ridging over the North Pacific tends to reduce precipitation over the southwestern United States (Gershunov and Cayan 2003), and recent research by Wang et al. (2014) has shown a strong connection between anomalous ridging over the North Pacific and the severe 2014 California drought. At present, it is not clear whether the relationship between North Pacific SSTs and North American climate is prognostic or diagnostic. Several studies (Pierce 2002; Kumar et al. 2013) suggest that tropical SST ENSO-related variations are the main driver, with the PDO-signature arising as an atmospheric response.

Figure 4.1b shows running 10-year averages of standardized observed (Vose et al. 2014) California precipitation and the ENSO and ENSO-residual CMIP5 ensemble means. The observed California precipitation exhibits large multiyear swings with no long-term trend. Dividing the CMIP5 precipita-

tion into ENSO and ENSO-residual variations (see Supplementary Materials) suggests conflicting tendencies. The ensemble mean ENSO-related California precipitation time series (blue line, Fig. 4.1b) was estimated by (a) calculating an ENSO time series for each CMIP5 simulation SST field, (b) regressing these time series against the CMIP5 precipitation fields, and (c) taking the ensemble average of the 25 ENSO-related precipitation time series. The ensemble average of the residuals of these time series was also examined. In the ENSO component (blue line, Fig. 4.1b), the CMIP5 trend towards warmer eastern equatorial Pacific SSTs appears associated with more California rainfall. In the component of the CMIP5 precipitation simulations that are not associated with ENSO (red line, Fig. 4.1b), we find an overall precipitation decline beginning in the 1990s. Figure 4.1b also shows the change in the model ensemble standard deviation of standardized precipitation. The models indicate more extreme (more wet and more dry) 21st century California precipitation. This result appears consistent with increasing variance in upper-level geopotential height fields (Wang et al. 2014).

We briefly present time series of observed (Smith et al. 2008) and CMIP5-simulated SST anomalies (deviations from the 1900–2014 mean) averaged over the regions in the North Pacific with anomalous high SSTs during the 2013 (Fig. 4.1c,d) and 2014 (Fig. 4.1e, f) winters. While the SST patterns differ, both winters were characterized by slightly cool, but not La Niña-worthy, temperatures in the eastern equatorial Pacific, warm anomalies in the western equatorial Pacific, and patches of exceptionally warm SST in the North Pacific. Time series of SST from these regions are shown with black lines in Fig. 4.1d and f. The 2012/13 wintertime North Pacific SST anomaly for the rectangle shown in Fig. 4.1c was 0.8°C, the sixth warmest on record. SSTs in this region were warmer in 1943, 1949, 2000, and 2012. This can be contrasted with the 2013/14 wintertime North Pacific SST anomaly for the rectangle shown in Fig. 4.1e. This anomaly was +1.4°C, a three standard deviation warm event, and the warmest on record. The 1900–2014 interannual variations of both of the observed SST time series covary positively (both correlated at $r = 0.44$, $n = 115$, $p = 0.0001$) with the CMIP5 ensemble mean time series (black and dark blue time series in Fig. 4.1b and d), indicating an anthropogenic contribution to recent warming. The seasonal minimum and maximum of the CMIP5 ensembles bracket the observed variations reasonably well (Fig. 4.1d and f). Note that the CMIP5 time series indicate a substantial

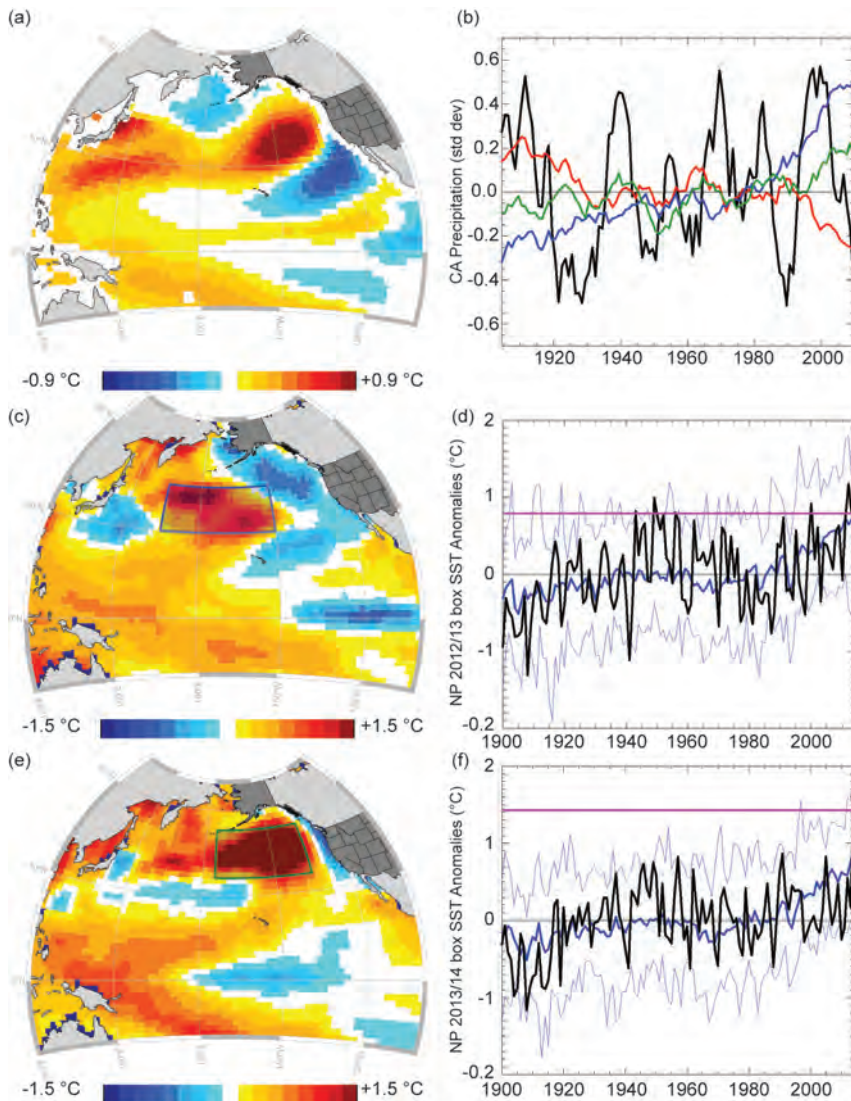


FIG. 4.1. (a) Dry minus wet California CMIP5 SST ensemble averages. (b) Ten-year averages of standardized California precipitation based on observations (black), ensemble mean ENSO CMIP5 precipitation (blue), and ENSO-residual CMIP5 precipitation (red). Also shown is a time series of the intermodel standard deviations (green). (c) Observed 2012/13 SST anomalies. (d) Observed (black) and CMIP5 (blue) time series of SST in box shown in (c). The thick blue line shows the ensemble mean, and the thin blue lines show the ensemble minimum and maximum. A horizontal purple line identifies the 2012/13 extreme. Observed 2013/14 SST anomalies. (e) As in (d) but for the box shown in (e).

post-1980 warming. This warming has contributed to more frequent extremely warm North Pacific SSTs. The purple lines in Fig. 4.1d and f allow us to compare the 2012/13 and 2013/14 extremes to the historical observed and CMIP5 SST distributions. The $+0.8^{\circ}\text{C}$ 2012/13 was rare but not unprecedented. The $+1.4^{\circ}\text{C}$ 2013/14 anomaly was extremely unlikely given either prior observed SST values or the 20th century CMIP5 ensemble. Anthropogenic climate change seems likely

of detrended SST simulations. In these experiments, an empirical estimate of the long-term warming trend (Fig. 4.2a,b; see Supplemental Materials for details) was subtracted from observed SSTs. These estimates were derived by multiplying the 2013 and 2014 trend mode principal component scores (Fig. 4.2a) against the associated trend mode patterns (methods in Supplemental Materials), which are similar to those obtained in recent studies (Compo and Sardeshmukh

to have contributed to these extreme SSTs (Fig. 4.1f) and the associated extreme upper-level height anomalies (Wang et al. 2014).

CAM5 simulations driven with observed and detrended SSTs. We next explore the potential contribution of the long-term warming trend to the recent California droughts. The detection and attribution of climate change is a challenging multifaceted problem (Stone et al. 2009), especially at regional scales (Hegerl and Zwiers 2011). Here, we do not address the general question, “Did climate change increase the chance or severity of the 2013 and 2014 droughts?” We rather address a more constrained hypothesis, “Did the observed global warming trend in SSTs (see Supplemental Materials for a more detailed description) decrease modeled precipitation over California?” We address this hypothesis by contrasting two sets of precipitation simulations using the CAM5 atmospheric general circulation model. In the first “observed” set of simulations, we force CAM5 using observed SST values for 2012/13 and 2013/14. For both years, these simulations exhibited below normal California precipitation (not shown) indicating some SST-forcing for the observed deficits. We then ran a second set

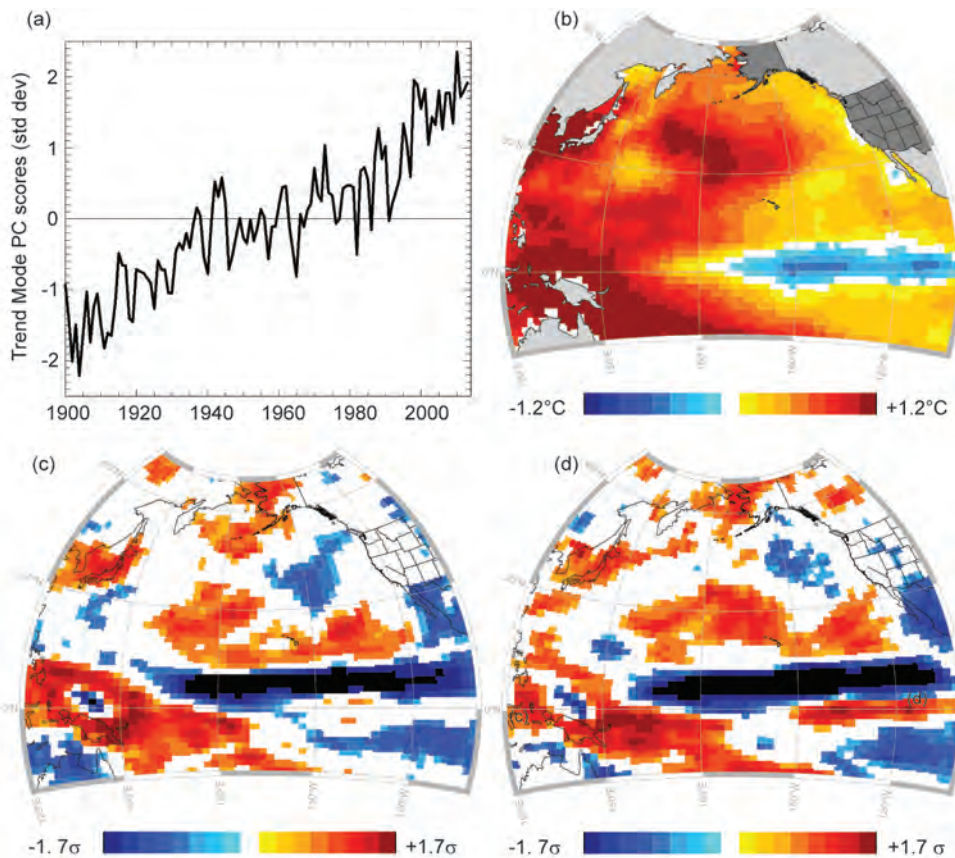


FIG. 4.2. (a) Time series of standardized trend mode principal component scores. (b) The 2012/13 and 2013/14 SST anomalies associated with the observed trend mode. (c) The change in standardized precipitation between the observed and detrended CAM5 SST experiment for 2012/13. Values have been screened for 10% significance using a two-tailed t-test and assuming uncorrelated noise. (d) Same as (c) but for 2013/14.

2010; Dai 2013; Solomon and Newman 2012). The warming associated with the trend mode (Fig. 4.2b) is characterized by substantial ($> +1^{\circ}\text{C}$) warming in the western, northwestern, and north-central Pacific. We postulated that even though California precipitation had not exhibited strong trend-like declines, it was possible that during the 2012/13 and 2013/14 winters, the long-term warming trend (Fig. 4.2b) may have interacted with interannual SST variations to increase California rainfall deficits.

The CAM5 ensemble simulation results did not support this hypothesis. While the differences in the ensemble means (observed ensemble mean minus detrended ensemble mean) in the experiments (Fig. 4.2c,d) do indicate large (more than ± 1 standardized anomaly) changes in precipitation, these changes were largely constrained to the western and central equatorial Pacific. While some modest but statistically significant precipitation declines were identified over Mexico, no statistically significant declines were found over California. This result is based on

climate models, which have difficulties representing the complex California climate (Bacmeister et al. 2014).

Conclusions. While the SST trend mode has resulted in large SST increases (Fig. 4.2b) that appear associated with an equatorial precipitation dipole response contrasting increases over the western Pacific and decreases over the central Pacific (Fig. 4.2c,d), the location of most of this warming is to the west of the key sensitivity areas identified in our CMIP5 composite (Fig. 4.1a). While this trend pattern does resemble SST variations associated with drying in the western United States (Gershunov and Cayan 2003), removing this warming did not increase the CAM5 precipitation over California in a statistically significant manner; thus, our results do not indicate that this long-term warming trend contributed substantially to the 2013 and 2014 drought events. This result appears consistent with the lack of a long-term downward trend in California

precipitation (Fig. 4.1b). California precipitation is, however, sensitive to North Pacific SSTs (Fig. 4.1a; Gershunov and Cayan 2003), and climate change models indicate substantial warming in this region (Fig. 4.1d and f). In 2013/14, the North Pacific SSTs (Fig. 4.1f) and the intensity of the upper troposphere geopotential height gradient (Wang et al. 2014) reached historic maxima. These extremes appear very unlikely without anthropogenic climate change. If SST and ridging events like this become more common, California could experience more frequent droughts (Favre and Gershunov 2009). The impacts of decreased Arctic sea ice may also

contribute to upper-level ridging and dry western U.S. winters (Sewall 2005). In addition, given the strong thermal control on evaporation, snowmelt, and water resources in California, the long-term warming is continuing to exert a growing stress on water availability (Barnett et al. 2008), potentially amplified by both more frequent dry days and more precipitation extremes (Polade et al. 2014). Local air temperature increases in the western United States impact the timing and availability of snowmelt and amplify the demand for water during the summer and fall, exacerbating the impacts of water deficits associated with these droughts.

5. NORTHEAST COLORADO EXTREME RAINS INTERPRETED IN A CLIMATE CHANGE CONTEXT

MARTIN HOERLING, KLAUS WOLTER, JUDITH PERLWITZ, XIAOWEI QUAN, JON EISCHEID, HAILAN WANG,
SIEGFRIED SCHUBERT, HENRY DIAZ, AND RANDALL DOLE

The probability for an extreme five-day September rainfall event over northeast Colorado, as was observed in early September 2013, has likely decreased due to climate change.

Introduction. Welcome rains over northeast Colorado starting on 9 September 2013 turned into a deluge during 11 September and continued through 15 September. Boulder, an epicenter of this regional event (http://www.crh.noaa.gov/bou/?n=stormtotals_092013), almost doubled its daily rainfall record (from 12.2 cm in July 1919 to 23.1 cm on 12 September 2013), with 43.6 cm for the week. Widespread flooding took 10 lives and caused at least \$2 billion in property damage, second only to the June 1965 floods of eastern Colorado (<http://www.reuters.com/article/2013/09/19/us-usa-colorado-flooding-idUSBRE98H1BA20130919>).

Events of similar magnitude are not unprecedented during summer in the Colorado Front Range (Hansen et al. 1978; McKee and Doesken 1997). Some reach that size in a few hours and are more localized (e.g., Big Thompson in late July 1976), while others take longer and have larger footprints as in June 1965 and September 1938. Interestingly, attributes of the 2013 event, including its late-summer occurrence, regional scale, long duration, and slowly

changing atmospheric circulation (see Gochis et al. 2014, manuscript submitted to *Bull. Amer. Meteor. Soc.*) that transported extreme moisture into the Front Range, also characterized the 1938 event.

Does the recent occurrence of this extreme event indicate that its likelihood has increased due to global warming? Globally, the atmosphere has become warmer and moister, with the observed rate of increase since the 1970s broadly consistent with that expected from the Clausius–Clapeyron relation (~7% per °C; Hartmann et al. 2014). Heavy precipitation events have increased over much of the United States since 1901, however, with no significant long-term trends over the northern Great Plains or Southwest (Kunkel et al. 2013). Further, the relationship between heavy precipitation and atmospheric water vapor varies seasonally, with moisture availability rather than moisture-holding capacity being a more dominant factor in summer than winter (Berg et al. 2009). Thus, the answer to our question cannot be readily gleaned from globally and annually averaged statistics but requires careful consideration of place and time.

Datasets and methods. The Global Historical Climatology Network (GHCN)-Daily dataset (Menne et al. 2012) of station observations is used to create a gridded daily analysis at 1° resolution for 1901–2013. Daily column precipitable water (PW) is based on the National Centers for Environmental Prediction–National Center for Atmospheric Research (NCEP–NCAR) reanalysis product for 1948–2013 (Kalnay et al. 1996).

Climate simulations using NASA’s Goddard Earth Observing System (GEOS-5) atmosphere model are diagnosed to determine the effect of time varying forcing on the region’s five-day averaged precipitation and PW. The GEOS-5 model (Rienecker et al. 2008; Molod et al. 2012) employs finite-volume dynamics and moist physics as described in Bacmeister et al. (2006). The simulations consist of 12 ensemble members, forced with observed monthly SST, sea ice, and time-varying greenhouse gases for the period 1871–2013 (Schubert et al. 2014). The model was run at 1° horizontal resolution with 72 hybrid-sigma vertical levels.

The 1° gridded daily observational and model data are spatially averaged over the northeast Colorado study region (Fig. 5.1, box), and they are used to calculate running five-day precipitation and PW for September. A region larger than the scale of the event was selected in part to accommodate model capabilities but also to avoid selection bias. Nonetheless, the 2013 heavy rainfall event was large in spatial scale. Weather predictability of the event per se is not addressed herein (see Hamill 2014), but rather how climate change may have affected the relative likelihood of heavy precipitation in this large region. For this purpose, the modeled statistics of heavy five-day rainfall of the recent 30-year period (1983–2012) are compared to that of the last 30 years of the 19th century.

Results. Model suitability. The footprint of 2013 rains (Fig. 5.1a) was partly organized by the Continental Divide

and the elevation gain from the Great Plains—topographic features pronounced enough to be captured at 1° resolution in GEOS-5, even though smaller scale aspects of the Front Range terrain are not resolved. The rains were also linked to an abundance of atmospheric water vapor in early September 2013 (Fig. 5.1b, blue shading) that was transported principally from source regions over the southern Great Plains and Gulf Coast as implied by the anomalous 700-hPa

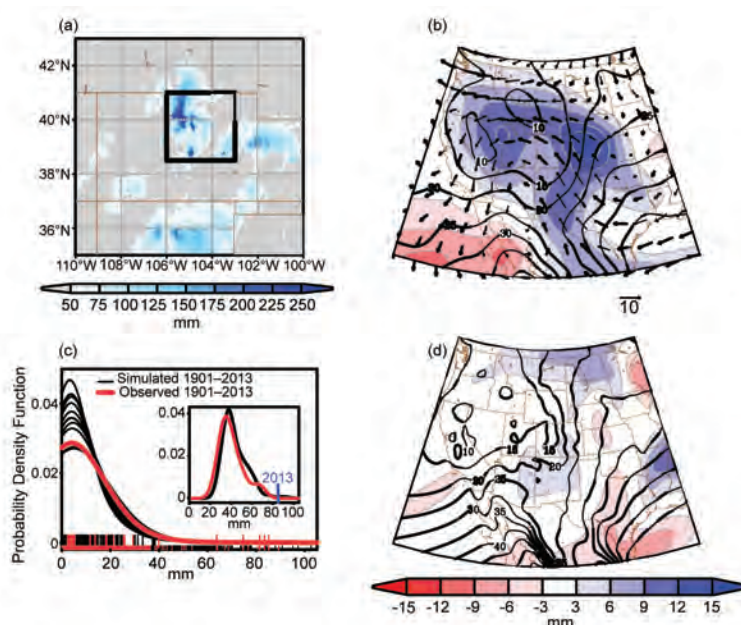


FIG. 5.1. (a) Observed five-day cumulative precipitation totals (mm) during 10–14 Sep 2013 for Colorado and neighboring states at the peak of the extreme event. The box outline denotes the northeast Colorado domain of most extreme precipitation with estimated 84 mm five-day precipitation. (b) Observed five-day average column precipitable water (PW; mm) for 10–14 Sep 2013. Shaded values are departures from a 1948–2013 reference period; the overlain contours indicate the reference period climatology for that five-day period, overlain arrows are 700-hPa wind anomalies. (Data source: NCEP/NCAR Reanalysis.) (c) Frequency distributions (PDFs) of five-day cumulative precipitation during September averaged over the study area shown in Fig. 5.1a for observation (red curve; 3390 values) and for individual ensemble members of climate model simulations (black curves; 3390 values per simulation, 51 480 total) for the period 1901–2013. Individual five-day running totals are shown with tick marks, and the September 2013 values are indicated with taller tick marks. The PDFs are non-parametric curves utilizing kernel density estimation and a Gaussian smoother. Inset shows the frequency distribution of 100-year block maximum values of the wettest five-day rainfall for all consecutive five-day periods in September based on observations (red; 30 samples) and the ensemble of GEOS-5 simulations (black; 360 samples) for the 100-year period 1913–2012. Observed 5-day peak value in September 2013 shown by blue tick mark. (d) As in Fig. 5.1b but for the GEOS-5 climate simulations. The simulated departures (shading) are based on the 12-member ensemble mean and are computed relative to the model climatology (contours).

winds superposed on climatological PW (Fig. 5.1b). Such large-scale PW sources are also realistically simulated in GEOS-5, whose climatology includes a strong gradient separating dry west-central Colorado air from moist air over the Great Plains and Gulf of California (c.f. Fig. 5.1b,d). Most importantly, GEOS-5 generates realistic statistics of five-day September rainfall over the case study region. First, the frequency distribution describing the observed statistics (Fig. 5.1c, red curve) lies within the spread of curves summarizing the five-day rainfall statistics for the 12 model simulations. Second, the statistics of tail events, estimated from 100-year block maxima for any consecutive five-day rainfall total averaged over our northeast Colorado study region, indicate that the model's tail behavior is quite realistic (Fig. 5.1c, inset). The 2013 event is a rare occurrence relative to both model and observed tail behavior, though the model does generate a few stronger cases in its historical simulation.

Simulated long-term change. The ensemble averaged GEOS-5 simulations for September 2013 do not repro-

duce the observed conditions for either the regional precipitation or PW anomalies (c.f. Fig. 5.1b,d). The results can be interpreted to indicate that the specific SST/sea ice boundary forcing and greenhouse gas forcings were not the primary drivers, implying a substantial random component of the event itself. Perhaps model biases were related to its failure to simulate the 2013 event such as an inability to depict the particular pattern of atmospheric circulation and its interaction with complex topography. Yet, this must be weighed against the realistic characterization of the statistics of extreme rainfall events over northeast Colorado (Fig. 5.1c). Ultimately, further analysis using other climate models will be required to clarify these issues.

Nonetheless, the absence of such events in the 12-member September 2013 simulations neither affirms nor refutes a possible effect of long-term change on event likelihood or intensity. To address this issue, we compare five-day rainfall statistics over northeast Colorado between two 30-year periods: one for 1983–2012 that is representative of current climate and the other for 1871–1900 that is representative of preindustrial climate. The model produces realistic global

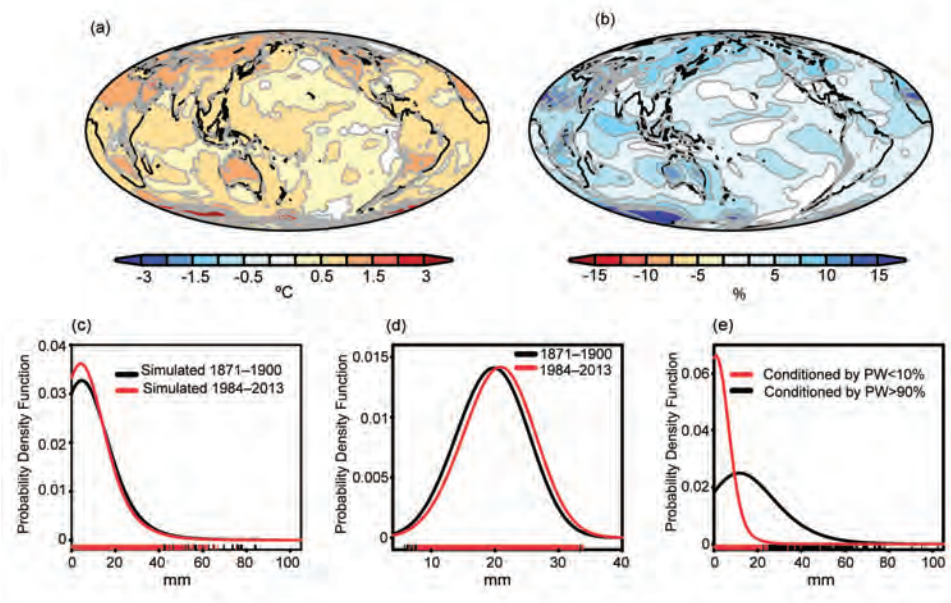


FIG. 5.2. (a) Simulated long-term change in September monthly averaged surface temperature ($^{\circ}\text{C}$) displayed as the difference between 1984–2013 and 1871–1900. (b) As in Fig. 5.2a but for the simulated change in September monthly averaged PW expressed as percent change of the 1871–1900 reference. (c) Climate model simulated frequency distributions of five-day September precipitation totals (mm) over the study area for 1871–1900 (black curve) and the 1984–2013 (red curve) period utilizing 12 GEOS-5 model simulations (10 800 values). Tick marks indicate individual samples. (d) As in Fig. 5.2c but for five-day September PW for 1871–1900 (black) and 1984–2013 (red). (e) Simulated PDFs of September five-day precipitation totals conditioned by the lowest 10% of PW (red curve; $n = 5139$) and the highest 10% PW (black; $n = 5195$) values.

changes between these periods that compare well with observations—global land surface temperature rises 0.9°C (Fig. 5.2a) and global PW rises 5.7% (Fig. 5.2b).

Despite a warmer and moister climate, the frequency of September heavy five-day rain events does not increase in the simulations but substantially declines in northeast Colorado (Fig. 5.2c). Using the model's 95th percentile of five-day rainfall totals, we find a 12% decline in occurrence during recent decades compared to the late 19th century. Using the model's 99th percentile, we find a 44% decline in frequency. The simulated magnitude of September heavy five-day rainfall over northeast Colorado also declines. For the 99th percentile, the threshold value falls from 49 mm in the late 19th century to 45 mm in the recent period.

Conditioning of heavy five-day rain events. To understand the above results we examine the relationship between the probability of heavy five-day rainfall and atmospheric water vapor. Statistics of five-day rainfall are examined for the lower and upper decile of five-day PW (Fig. 5.2e). For dry atmospheric conditions (red curve), very few rainfall occurrences exceed 35 mm (95th percentile) and none exceed 50 mm (99th percentile). For wet atmospheric conditions (black curve), the full range of five-day rainfall amounts is possible. Thus, though a necessary condition for extreme rainfall, high atmospheric water vapor is not sufficient.

Even though the simulated long-term increase in PW over northeast Colorado is small in magnitude (~6%), high five-day PW events increase in frequency (Fig. 5.2d). One would thus expect to also witness an increase rather than a decrease in heavy rain event probabilities over the region in GEOS-5. The contrary behavior suggests changes in other climate features (e.g., atmospheric circulation and vertical stability) act to counter the increase in water vapor over the region in the model.

Conclusion. Our analysis of the GEOS-5 simulations leads to a diagnosis that the occurrence of extreme five-day rainfall over northeast Colorado during September 2013 was not made more likely, or more intense, by the effects of climate change. From an observational perspective, analogous events have occurred before in the Front Range, perhaps most strikingly similar in September 1938, long before appreciable climate change.

Although our model results suggest that the occurrence of this recent extreme has become less probable over northeast Colorado due to climate change, model projections do show an increase in the intensity of maximum five-day precipitation over the globe and for annual averages as a whole by the end of the 21st century (Sillman et al. 2013). Yet, a slight decline in intensity of the maximum five-day precipitation over the central Great Plains during summer is also projected (Sillman et al. 2013), emphasizing that global and annual perspectives of climate change may not always pertain to events at a specific place and time.

A strength of our study is the availability of an ensemble of long-term climate simulations spanning 1871–2013, conducted at 1° spatial resolution, that permits an analysis of statistical properties of the change in extreme events. For the purpose of studying regional five-day rainfall events over northeast Colorado, the GEOS-5 model has the attribute of realistically characterizing the tails of the distribution. A weakness of our study is that results are based on a single model and thus require confirmation using additional models. Also, the physical reasons for the decline in simulated frequency of extreme five-day rainfall over northeast Colorado during September are not addressed. Better understanding of the delivery mechanisms for atmospheric moisture that produce heavy rain events and how those mechanisms respond to global warming will be critical.

6. SEASONAL AND ANNUAL MEAN PRECIPITATION EXTREMES OCCURRING DURING 2013: A U.S. FOCUSED ANALYSIS

THOMAS R. KNUTSON, FANRONG ZENG, AND ANDREW T. WITTENBERG

The Coupled Model Intercomparison Project phase 5 model analyses suggest that seasonal and annual mean precipitation extremes occurring during 2013 in north-central and eastern U.S. regions, while primarily attributable to intrinsic variability, were also partly attributable to anthropogenic and natural forcings combined.

Introduction. We analyze several U.S. regions with seasonal and annual mean precipitation anomalies in 2013 that we classify as “extreme” (i.e., ranked first, second, or third highest or lowest). Our analysis uses the Global Historical Climatology Network (GHCN) monthly precipitation dataset (Vose et al. 1992), covering 1900–2013, on a $5^\circ \times 5^\circ$ grid effectively limited to land regions. The extremes are analyzed in the context of long-term climate change, using trend analysis of historical and control run experiments from 23 Coupled Model Intercomparison Project phase 5 (CMIP5) models (Supplemental Material; Taylor et al. 2012).

Where did seasonal and annual mean precipitation extremes occur in 2013? Figure 6.1a–e identifies several regions of the continental United States that experienced record or near-record seasonal or annual mean precipitation anomalies during 2013. Global maps of seasonal and annual anomalies, and their associated extreme occurrences for 2013 (Supplementary Fig. S6.1), show that record or near-record wet and dry anomalies for 2013 were well dispersed around the globe. Supplementary Fig. S6.2 shows that in recent decades, annual mean rainfall has shown greater areal coverage for record or near-record annual mean wet extremes than dry extremes. In contrast, recent seasonal and annual mean surface temperatures are much more strongly skewed toward warm extremes (e.g., Knutson et al. 2013a).

We focus on six U.S. regions in this study (Fig. 6.1; Supplementary Fig. S6.1) including: the “northern tier—ANN (annual);” “upper Midwest—MAM (March–May);” “Southern Plains—MAM;” “eastern United States—JJA (June–August);” “Northern Plains—SON (September–November);” and “California—ANN.” Each region we analyzed contains multiple grid boxes and stations, which reduces the risk of instrumental or reporting errors at a single

station controlling results for a given “extreme event.” The California region—which in these data did not have annual precipitation anomalies ranked within the lowest three on record during 2013—nonetheless experienced widely publicized drought conditions during 2013, and so is analyzed here.

What is the climate change context for the regional precipitation extremes? Annual or seasonal mean precipitation time series for the focus regions (Fig. 6.1) show some moderate trend-like behavior. For each series, a least squares linear trend (1900–2013) was initially assessed by a standard *t* test (two-sided; $p = 0.10$), assuming that the residual anomalies, after trend removal, were temporally independent. (This assumption is later relaxed for our model-based assessments.) Three of the regions had significant positive trends (1900–2013): northern tier—ANN; upper Midwest—MAM; and Northern Plains—SON. The eastern United States—JJA had a nonsignificant trend over 1900–2013 but had a significant trend over 1950–2013 (discussed later). The significant trends mentioned above remained significant according to the above preliminary tests even if 2013 was excluded. None of the regions had significant negative trends. Previous studies have noted significant annual mean precipitation increases over much of the central and northern United States (Hartmann et al. 2014), and some increases in flood magnitudes over the north-central United States (Hirsch and Ryberg 2012), although these regional changes were not specifically attributed to anthropogenic forcing.

Observed trends for our selected regions were compared to CMIP5 historical and control runs using a “sliding trend” analysis (Fig. 6.2; Supplementary Fig. S6.3), for a range of start years (all trends ending in 2013), following Knutson et al. (2013a). Sensitivity tests were also performed for trends excluding the

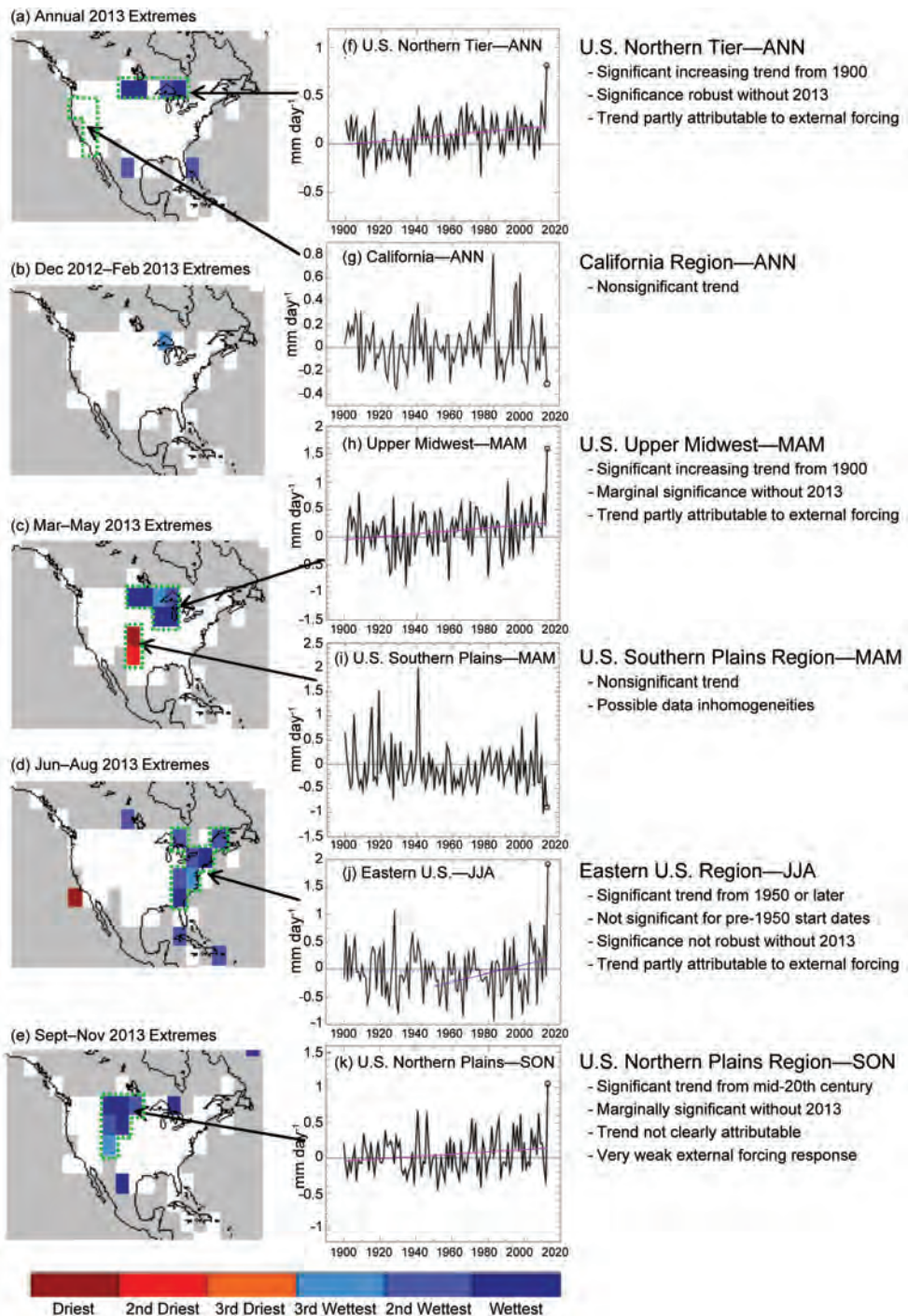


FIG. 6.1. Left column (a–e): Colors identify grid boxes where the annual or seasonal precipitation anomalies for 2013 rank first (dark red), second (red), or third (orange) driest or first (dark blue), second (medium blue) or third (light blue) wettest in the available observed record (see map legend). The seasons are DJF (December 2012–February 2013); MAM (March–May 2013); JJA (June–August 2013); and SON (September–November 2013). The various averaging regions used in the study are shown by the green dashed outlines in (a–e). Gray areas did not have sufficiently long records, defined here as containing at least 100 available annual or seasonal means, with an annual mean requiring at least three of four seasons to be available, and a seasonal mean requiring at least one of three months to be available. Center column (f–k): Time series of precipitation from the extremes regions shown by arrows/green outlines (see also Fig. S6.1 for region definitions). Black: observed anomalies in mm day^{-1} ; purple sloping line: significant linear trends (1900–2013, except 1950–2013 for eastern U.S. region—see text for explanation). The observed anomalies for 2013 are circled for emphasis in (f–k). The overall analysis results of the paper are summarized for each region in the right column.

highly anomalous 2013 observed values (Supplementary Fig. S6.3). Briefly, if observed trends were outside of the 5th–95th percentiles of the control run distribution, they were designated as “detectable” compared to internal variability. Detectable positive trends that lie either within or above the 5th–95th percentile range of the All-Forcing (anthropogenic and natural forcing) distribution are interpreted as at least “partly attributable to external forcing.” For example, the northern tier—ANN plot (Fig. 6.2b) shows that the positive observed trends in this region are detectable compared to internal variability (black curve outside the purple shading) and at least partly attributable to external forcing (inside the pink shading) for start dates from 1900 to about 1940, but are generally not detectable for trend start dates more recent than 1940.

Figure 6.2e, for the upper Midwest—MAM, indicates detectable trends compared to internal variability, except for mid-20th century start dates. For the eastern United States—JJA (Fig. 6.2h), positive trends are detectable for start years of ~1940 and later but not from the early 20th century. The cases of detectable trends for the three regions discussed above are also generally cases where the observed trends are at least partly attributable to external forcing according to the models (i.e., within or above the pink regions on the “sliding trend” graphs). The robustness of these assessments to exclusion of the highly anomalous 2013 value is examined in Supplementary Fig. S6.3. This analysis indicates that the most robust findings are for the northern tier—ANN region, while the detection result for the recent (late 20th century) trends in the eastern United States—JJA region is not very robust to exclusion of 2013. Intermediate robustness results are indicated for the upper Midwest—MAM region. As discussed in the Discussion section and Supplemental Material, insufficient ensemble sizes for the available CMIP5 Natural Forcing experiments have precluded us from robust trend detection compared to the Natural Forcing-only trend distributions, and so our results do not specifically distinguish a detectable *anthropogenic-only* influence on seasonal/annual precipitation trends for any of the focus regions. Some further discussion of trend results for three additional regions: the Southern Plains—MAM, Northern Plains—SON, and California—ANN is contained in the Supplemental Material.

Are the 2013 regional extremes attributable to anthropogenic and natural forcing? We next examine the 2013 anomalies in particular (relative to 1900–40 baseline values) in the three U.S. regions that had both extreme

2013 anomalies *and* long-term increasing trends that were assessed as partly attributable to anthropogenic and natural forcing: northern tier—ANN, upper Midwest—MAM, and eastern United States—JJA. For each of these regions, the CMIP5 multimodel ensemble-mean of the All-Forcing simulations shows a trend toward increasing rainfall but at a rate much smaller than the observed trend (Fig. 6.2a,d,g; Supplementary Fig. S6.4). Because the modeled response series are noisy for estimating a single-year value (even after ensemble-averaging), we apply temporal smoothing to estimate the 2013 All-Forcing anomaly (Supplementary Fig. S6.4; Supplemental Material). Using this estimated 2013 “All-Forcing” anomaly, we then estimate the 2013 All-Forcing distribution via a “rightward displacement” of the CMIP5 multimodel control run variability distribution (Fig. 6.2c,f,i). Using these forced and unforced anomaly distributions for each region, we estimate the influence of “anthropogenic + natural” forcings on the occurrence rate of extreme anomalies, using the “second-ranked year” anomalies (2010, 1991, or 1928) as the threshold values for fraction of attributable risk (FAR) calculations. We tested using the record 2013 values as the thresholds for FAR calculations but found that those values were either extremely rare or unprecedented in the modeled distributions so that the FAR results were very sensitive to our methodology. Therefore, we report here only the calculations based on the second-ranked years.

Note that the ensemble-mean All-Forcing response (shift between red and blue distributions in Fig. 6.2c,f,i) explains just a small fraction of the observed anomalies for 2013, implying a likely dominant role for internal variability in the 2013 rainfall extremes. For northern tier—ANN, the FAR of threshold-exceeding extremes due to anthropogenic and natural forcing combined is estimated as 0.60, based on estimates using the 2010 observed values as the threshold, with an occurrence ratio (All-Forcing vs. Control runs) of 2.5. In other words, the fraction of current risk of events exceeding the threshold that is attributable to external forcing is about 0.6. For the upper Midwest—MAM region, FAR is estimated as 0.49, with an occurrence ratio of 2.0. For the eastern United States—JJA, the FAR is estimated as 0.36 with an occurrence ratio of 1.6. The FAR estimates discussed here are based on the multimodel ensemble-mean All-Forcing response. However, considerable uncertainty remains in the FAR estimates; for example, FAR estimates based on individual models rather than the multimodel ensemble (not shown) can fall below zero or substantially exceed the multimodel estimates.

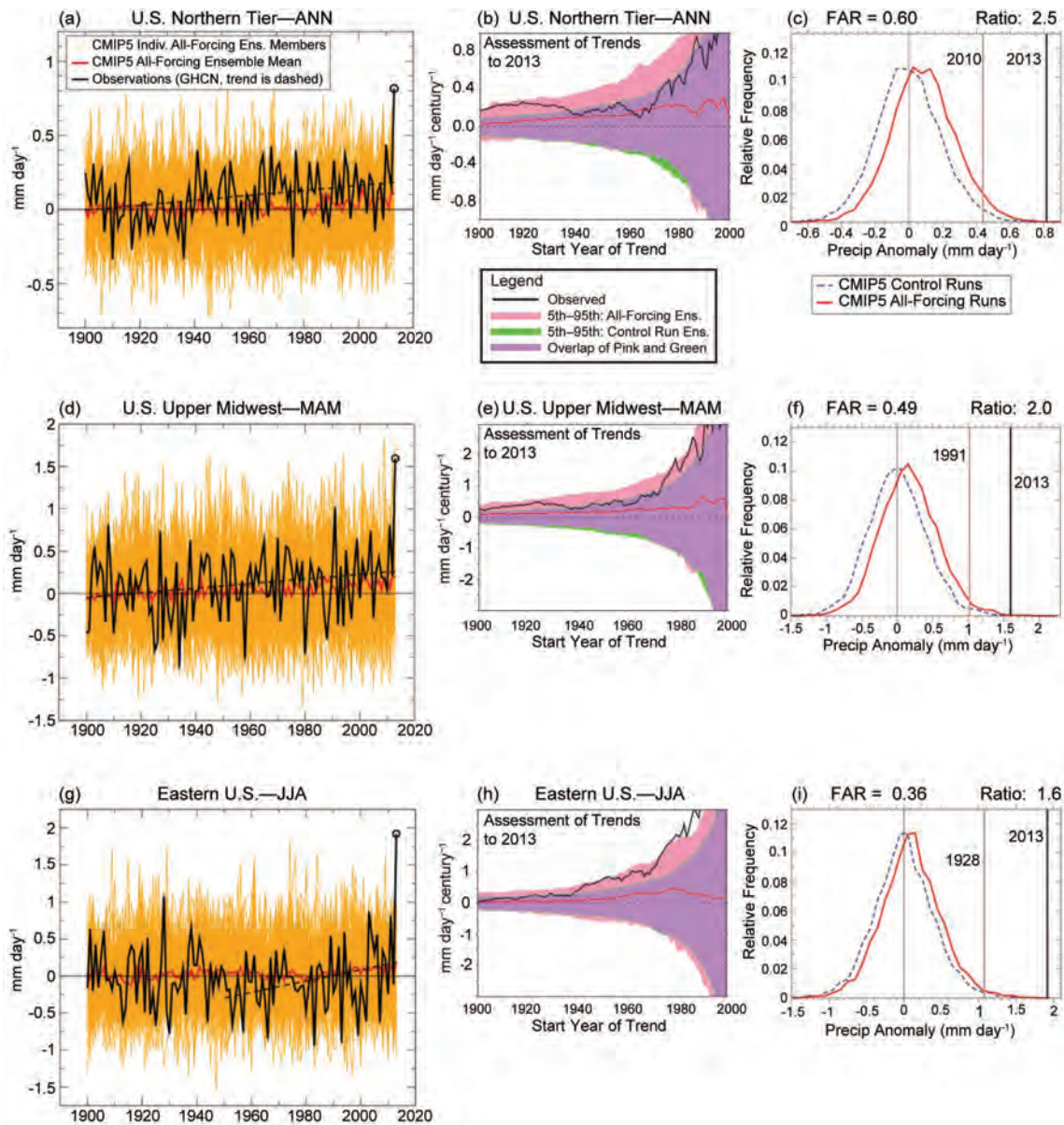


FIG. 6.2. (a,d,g) Rainfall time series averaged over the (a) U.S. northern tier—ANN, (d) U.S. upper Midwest—MAM and (g) eastern U.S.—JJA regions relative to 1900–40 baseline values. Black curves are observations, red curves are CMIP5 ensemble-mean All-Forcing responses, orange curves are individual model ensemble members, and sloping black dashed lines depict significant linear trends for observations. (b,e,h) Sliding trend analysis of precipitation trends for the series in (a,d,g) but for various start years (x-axis) with all trends ending in 2013. Black curves: observed trends; red curves: CMIP5 All-Forcing multimodel ensemble-mean trends; pink shading: 5th–95th percentile range of trends from the CMIP5 All Forcing (anthropogenic + natural forcing) runs, extended to 2013 with RCP4.5 scenarios; green shading: 5th–95th percentile range of internally generated trends from CMIP5 control runs; purple shading: overlap of pink and green regions. (c,f,i) Analysis comparing extreme observed anomalies (relative to 1900–40 baseline) for 2013 or for the next-most extreme year (2010, 1991, 1928) with CMIP5 model-simulated anomaly distributions. Blue histogram: CMIP5 multimodel control run distribution showing model-estimated internal climate variability. Red histogram: All-Forcing distribution obtained by shifting the control run distribution to the right by the estimated All-Forcing ensemble mean response (relative to the 1900–40 baseline) for 2013 (see also Supplemental Material). The black and gray vertical lines in (c,f,i) depict extreme observed anomalies, including the record observed values for 2013 (black) and the second-ranked year (gray), for comparison to the modeled distributions of anomalies. Denoting p_f and p_c as the occurrence rates within the All-Forcing and Control run distributions, respectively, of anomalies exceeding the defined second-ranked-year thresholds shown in the plots, then $FAR = 1 - p_c/p_f$, and the occurrence ratio is p_f/p_c .

Another important potential source of uncertainty is the adequacy of the control run variability, which is compared to “residual” observed variability in the Supplemental Material (Supplementary Figs. S6.5–7). Our basic findings appear robust to this uncertainty, although the simulation or estimate of internal climate variability remains an important topic for further research.

Discussion and conclusions. Three of the focus regions, northern tier—ANN, upper Midwest—MAM, and eastern United States—JJA, had record or near-record seasonal or annual precipitation anomalies during 2013 as well as detectable positive trends that were at least partly attributable to external forcing (anthropogenic and natural forcing combined). However, detection was marginal for the eastern United States. According to the models, external forcing increased the likelihood of rainfall events as extreme as the observed second-ranked year thresholds by factors of 1.6 to 2.5. The climate change detection here is only with respect to control run (intrinsic) climate variability. We have not attempted detection relative to natural forcing and intrinsic variability combined, since (a) the simulated ensemble-mean response to external forcings is generally much smaller than the observed long-term trends, interannual variability, and 2013 anomalies; and (b) too few simulations with only natural forcing were performed to sufficiently delineate the response to that forcing. Thus, while there is some suggestion of increased risk attributable to anthropogenic forcing in our findings (Supplementary Fig. S6.4), this is not emphasized here due to the lack of a sufficiently detectable long-term anthropogenic trend contribution. Extensions of the CMIP5 Natural

Forcing runs through 2013, and larger ensembles of Natural Forcing experiments by various modeling centers, would be particularly useful for further investigations.

Important caveats are that we have not yet systematically analyzed regional precipitation trends globally (which would clarify the large-scale context of our findings), nor have we assessed possible data homogeneity issues, alternative datasets (e.g., Becker et al. 2013), or effects of radiative forcings on precipitation variance. Clearly, it would be much more difficult to detect anthropogenic influences on regional precipitation extremes than on surface temperatures (e.g., Knutson et al. 2013a). This is already evident in other recent analyses of regional precipitation trends (van Oldenborgh et al. 2013; Bhend and Whetton 2013). Nonetheless, some studies have reported detectable anthropogenic influence for zonal-mean precipitation (e.g., Zhang et al. 2007; Marvel and Bonfils 2013), precipitation extremes over large land regions of the Northern Hemisphere (Min et al. 2011), or precipitation changes in the extratropical Southern Hemisphere (Fyfe et al. 2012) or Mediterranean region (Hoerling et al. 2012). We conclude that the 2013 extreme precipitation “events” for three U.S. regions/seasons (northern tier—ANN, upper Midwest—MAM, and eastern United States—JJA) are tentatively attributable in part to external (anthropogenic and natural) forcing, with a likely much larger additional contribution from unforced intrinsic variability. We suggest that these regions be monitored for possible future emergence of anthropogenically forced precipitation increases, including more extreme seasonal or annual mean rainfall.

7. OCTOBER 2013 BLIZZARD IN WESTERN SOUTH DAKOTA

LAURA M. EDWARDS, MATTHEW J. BUNKERS, JOHN T. ABATZOGLOU,
DENNIS P. TODEY, AND LAUREN E. PARKER

An early October blizzard in South Dakota is determined to be climatologically anomalous. Climate models suggest that early autumn extreme snowfall events in western South Dakota are less likely due to anthropogenic climate change.

Introduction. An early season blizzard on 4–5 October 2013 in western South Dakota (SD) and neighboring areas of Wyoming, Nebraska, and North Dakota caused severe infrastructure damage and economic

losses to businesses and agricultural communities. Estimated losses total \$38 million in SD alone.

The blizzard produced 50.8–99.6 cm of snow across the plains and 139.7 cm of snow in the northern

Black Hills (Fig.7.1a). Rapid City, SD, measured 58.4 cm of snowfall during the storm, with 48.3 cm in a 24-hour period. This 24-hour record surpassed the 94-year-old October record by about 22.9 cm and fell just below the all-time 24-hour snowfall record of 50.8 cm set six months earlier on 9 April 2013.

Accumulated precipitation (rainfall plus liquid snowfall water equivalent, SWE) during 4–5 October amounted to as much as 17.1 cm at Lead, SD, with larger totals reported in unofficial observations. The storm total SWE amounted to about 20 percent of the annual average across the northern Black Hills and adjacent plains counties.

Outside of the Black Hills region, agriculture comprises the primary economy and livelihood in western SD. Initial damage assessments include approximately 45 000 livestock that perished in the storm, with 90% loss in some herds. The combination of antecedent soaking rain, large snowfall totals, and blizzard conditions resulted in animal deaths by hypothermia or suffocation due to wind-blown snow. The timing of the blizzard meant livestock were unprepared physiologically for the winter-like conditions and were vulnerable in open pastures. Despite advance notice of the impending storm, there was not sufficient time to move cattle to more sheltered areas. Municipal damage from the blizzard included downed trees and broken utility poles leading to long power outages in rural areas.

Blizzard reporting and recovery efforts were slowed by the unfortunate timing of the U.S. federal government shutdown 1–16 October 2013. Only critical offices were open, such as the National

Weather Service, which issued a blizzard warning 15 hours prior to the onset of the event.

Historical context and synoptic setting. This event occurred in the western portion of the U.S. “blizzard alley” (Schwartz and Schmidlin 2002). A similar blizzard, centered in western North Dakota, occurred on 4–5 October 2005 (NCDC 2005; also see <http://www.crh.noaa.gov/Image/bis/sd2005/October.pdf>)—yielding two October blizzards for parts of the Dakotas just eight years apart. By comparison, only one-to-two October blizzards were reported per

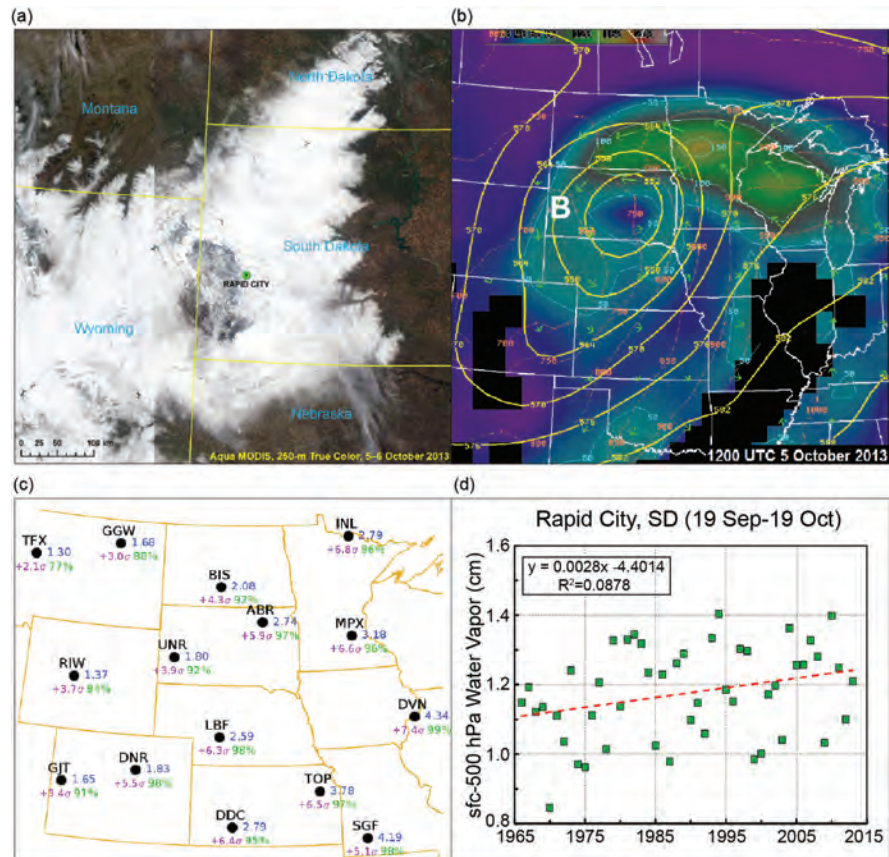


FIG. 7.1. (a) Aqua MODIS true-color 250-m resolution satellite depiction of snow cover centered on the South Dakota Black Hills for 5–6 October 2013 (<http://ge.ssec.wisc.edu/modis-today/index.php>). Two images were stitched together for 5 October (left) and 6 October (right) to avoid cloud contamination. (b) North American Mesoscale (NAM) model zero-hour forecast valid 1200 UTC 5 October 2013 for 500-hPa heights (six-dam yellow contours) and moisture transport vectors (green), moisture transport magnitude ($\text{g kg}^{-1} \text{m s}^{-1}$, shaded with legend at upper left), and pressure (50-hPa orange dashed contours) on the 295-K isentropic surface. The white “B” is centered on the Black Hills. (c) Maximum surface-to-300-hPa column water vapor (cm, blue) from 1200 UTC 3 October 2013 to 0000 UTC 6 October 2013. The corresponding percentiles (green) and standard deviations from the mean (purple) are based on the October observational period of record for each upper-air site (<http://www.crh.noaa.gov/unr/?n=pw>). (d) Average surface-to-500-hPa column water vapor per year for 19 September–19 October from 1966 to 2013 for Rapid City, SD. The linear trend (red dashed) illustrates an increase of 11.9% over 48 years.

county during 1959–99 (Schwartz and Schmidlin 2002), indicating the rarity of October blizzards. Furthermore, snowfall is rare in early autumn (19 September–19 October) across the plains, with only 48 days of measurable snowfall reported during early autumn in Rapid City in 63 years.

The October 2013 blizzard was produced by a strong low-pressure system similar to conditions identified in other heavy snowstorms (e.g., Graves et al. 2003; Jurewicz and Evans 2004; Novak et al. 2004; Moore et al. 2005), with mesoscale to synoptic-scale forcing for ascent aided by jet streak coupling (Uccellini and Kocin 1987), a trough of warm air aloft (trowal; Martin 1999), and low- to midlevel frontogenesis. The mature phase of the synoptic system featured 500-hPa heights of 547 dam over south-central SD (Fig. 7.1b), reaching standardized anomalies (σ) of -2.5 to -3.0 . While these anomalies were significantly less than those associated with other blizzards in the region, they were comparable to 24 major snowstorms in Grumm and Hart (2001). These moderately strong anomalies suggest the storm system was intense, regardless of season, but not unprecedented in terms of 500-hPa heights.

By contrast, precipitable water (PW)—supported by the trowal—concurrent with the blizzard reached $+2.1\sigma$ to $+7.4\sigma$ across the broader region (Fig. 7.1c), reaching the 92nd to 99th percentile for October. The total storm precipitation ranks as a 1-in-10 event for any time of year (NOAA HDSC, http://hdsc.nws.noaa.gov/hdsc/pfds/pfds_map_cont.html?bkmrk=sd). The low-level winds transported this anomalously high water vapor into western SD (Fig. 7.1b). When compared to previous studies, these were highly anomalous water vapor values (e.g., Hart and Grumm 2001; Junker et al. 2008; Mayes et al. 2009; Graham and Grumm 2010), with return periods ranging from 30 days ($+4\sigma$) to 10 years ($+7\sigma$).

Rapid City upper-air soundings for 19 September–19 October from 1966 to 2013 showed an 11.9% increase in water vapor ($\rho = 0.30$, Fig. 7.1d), which is not significant at $\alpha = 0.05$ for the Mann–Kendall test. No trend was found in the number of days with PW above the 95th and 99th percentiles. Thus, we cannot conclude, based on this limited observational dataset, whether the probability of extreme atmospheric water vapor has changed for the Black Hills region.

Role of Anthropogenic Climate Change. We considered the likelihood of such events under the modern climate compared to pre-industrial conditions free of anthropogenic influence using a model ensemble approach.

Data and methods. Daily precipitation rate and maximum and minimum temperature were acquired from eight models participating in the Coupled Model Intercomparison Project Phase 5 (CMIP5) experiments: CCSM4, NorESM1M, CanESM2, CNRM-CM5, CSIRO-MK3-6-0, GFDL-ESM2G, MIROC5, and INMCM4 (Supplementary Table S7.1). PW data for the first four of these models also were acquired. These models were chosen based on overall performance in simulating the climate of North America (Sheffield et al. 2013) and disparate model genealogies (Knutti and Sedláček 2013). Model data were taken from both preindustrial control runs (PI) and from “modern day” runs (MD) encompassing 2013 (2000–29) using historical 20th century runs ending in 2005 and extending these through 2029 using output from the Representative Concentration Pathway 8.5 (RCP85). Over 100 years of daily temperature and precipitation for PI runs were used for the primary analysis of estimating snowfall extremes. Model simulated snowfall flux was not used given potential biases in the joint distribution of simulated precipitation and temperature. Rather, intramodel biases in daily precipitation and temperature were bias-corrected using empirical equidistant quantile mapping (Li et al. 2010a) extended to two dimensions to fit the distribution of daily observations from ERA-Interim reanalysis (Dee et al. 2011). Model output was bias corrected using the common period from 1979–2012 while allowing for differences in the empirical distribution for PI and MD runs post 2012. Daily SWE was estimated using the empirical precipitation phase transformation of Dai (2008).

PW was calculated by vertically integrating specific humidity on isobaric surfaces. Unfortunately, most CMIP5 PI runs only archived ~ 20 years of pressure-level variables at the daily time resolution, thereby limiting a thorough analysis of PW. Instead, projected changes in PW are provided as a supplement to the main analysis.

Three metrics of SWE were considered for the period 19 September–19 October for both PI and MD experiments: (a) annual maxima daily SWE, (b) 90th percentile of annual maxima daily SWE, and (c) average SWE. Statistical significance was assessed by bootstrap resampling with replacement, using 1000 30-year samples from the PI runs. Differences were noted as significant when MD values fall outside the 95% confidence interval of the PI sample.

Results. Differences between the maximum series of daily SWE for early autumn showed a consistent

shift towards a reduction in the magnitude of extremes in MD runs with a multimodel mean decrease of around one-third (Fig. 7.2). Likewise, while two models showed a nonsignificant increase for a 90th percentile early autumn maximum daily SWE, the MD runs primarily tended toward reduced magnitude (mean decrease of 20%) relative to PI runs. However, the changes for both metrics were only significant for a single model and were not considered a robust change. These results largely mirrored projected changes in early autumn SWE that showed intermodel agreement of reduced SWE relative to PI runs (mean decrease of 35%). By contrast, simulated differences in early autumn maximum daily precipitation and the 90th percentile early autumn daily precipitation showed nominal and mixed changes. Increased PW in MD runs relative to PI was found

consistently across the study area and was consistent with overall increases in temperature and potential water holding capacity scaling with the Clausius–Clapeyron relationship.

Conclusions. The record-setting early season blizzard of October 2013 had significant impact on the agriculture, infrastructure, and economy of western SD. This event was associated with highly anomalous

(95th to 99th percentile) atmospheric water vapor for early autumn and anomalous, but not unprecedented, 500-hPa heights for any time of year.

While several climate models are consistent with the observations in showing an increase in PW, there is no apparent model agreement regarding changes in extreme precipitation or snowfall in the early autumn season for western SD under modern conditions relative to preindustrial conditions.

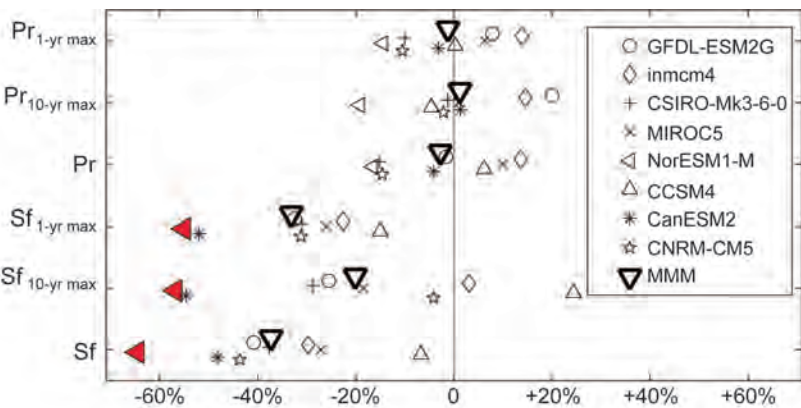


FIG. 7.2. Intramodel differences in the percent change in precipitation (Pr) and snowfall (Sf) between MD and PI in western South Dakota over a 30-day period centered on October 4. Differences are shown for annual extreme (1-yr max), 1-in-10 year annual extreme (10-yr max), and overall means. Statistically significant differences are denoted by red triangles; open triangles denote the eight-model average. A list of the models used is provided in Supplementary Table S7.1. Increased PW in MD runs relative to PI was found consistently across the study area and was consistent with overall increases in temperature and potential water holding capacity scaling with the Clausius–Clapeyron relationship. These findings also held for differences in early autumn maximum series of PW, with a multimodel increase of around 7% for the study area (not shown).

8. MULTIMODEL ASSESSMENT OF EXTREME ANNUAL-MEAN WARM ANOMALIES DURING 2013 OVER REGIONS OF AUSTRALIA AND THE WESTERN TROPICAL PACIFIC

THOMAS R. KNUTSON, FANRONG ZENG, AND ANDREW T. WITTENBERG

CMIP5 simulations suggest that the extremely warm year observed over Australia and the far western Pacific during 2013 was largely attributable to human forcing of the climate system.

Introduction. A global survey of surface temperature anomalies occurring during 2013 (Fig. 8.1a; Supple-

mentary Fig. S8.1) in the HadCRUT4 observations (Morice et al. 2012) reveals pronounced warm an-

nual and seasonal mean anomalies. Two regions with prominent record or near-record annual mean warm anomalies include large regions of Australia and a region in the far western tropical Pacific encompassing the Philippines and part of the Maritime Continent (Fig. 8.1b). The 2013 anomalies appear particularly extreme during austral fall and winter (MAM, JJA) in Australia and during MAM in the far western Pacific (Supplementary Fig. S8.1). Temperatures in these two regions are further assessed in this report for the causes of this extreme warmth. Twenty-three All-Forcing (anthropogenic plus natural) models and control runs and 10 Natural-Forcing models were used from the Coupled Model Intercomparison Project phase 5 (CMIP5; Taylor et al. 2012). See Knutson et al. (2013a,b) for background on our methodology and a global assessment of low-frequency variability and trends.

Global occurrence rates of record or near-record annual mean surface temperatures. Figure 8.1c,d shows the fraction of available global area with record or near-record (ranked in the top/bottom three with at least 100 years of record) annual mean positive or negative anomalies. In 2013, the fraction of area with record or near-record annual anomalies was very skewed toward warm occurrences, with 10.4% of the analyzed area having annual mean warmth that was first, second, or third highest on record, compared with 0% coverage of record or near-record cold. This continues a feature seen in recent decades, with similar rates for positive extreme occurrences since about 2000 and very little analyzed area with annual mean near-record negative temperature anomalies since about 1990. The large occurrence rates of record or near-record annual mean temperature anomalies is high in the early parts of the record as an artifact of the short record lengths, so the focus should be on the latter

parts of the record. Figure 8.1d shows the annual rates using the full record to assess each year, including the early years, and shows the preference for cold mean annual extremes prior to about 1920 and the increasing preference for warm annual mean extremes since about 1990. Although global mean temperature has experienced a “hiatus” or pause since around 2000 (e.g., Fyfe et al. 2013), this pause has occurred at high overall temperature levels relative to the late 1800s, resulting in a much more common occurrence of regional seasonal and annual warm temperature records (or near records) around the globe compared to cold records (Fig. 8.1c,d). Seneviratne

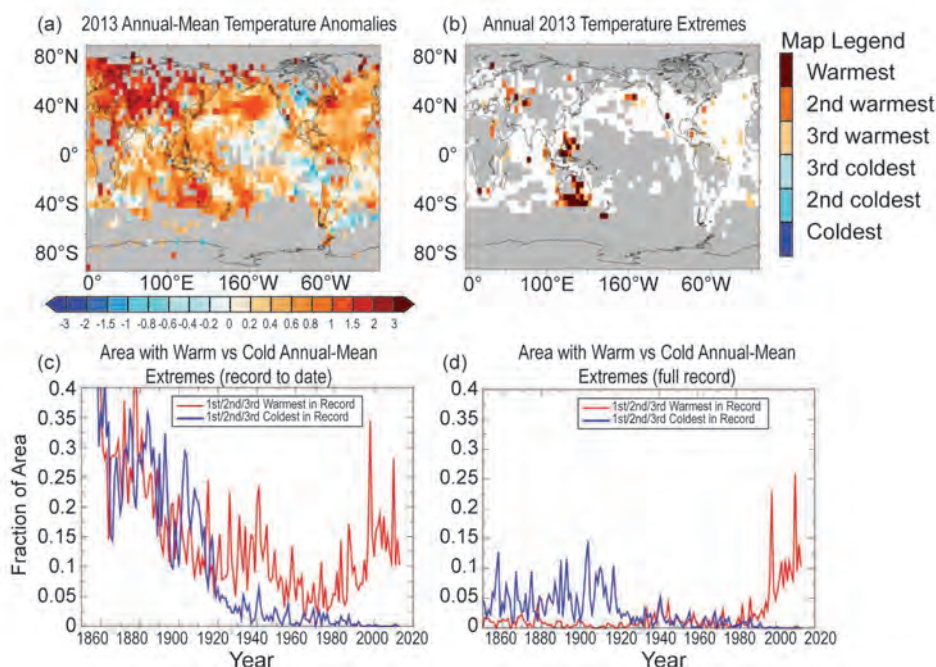


FIG. 8.1. (a) Annual-mean surface air temperature anomalies ($^{\circ}\text{C}$) for 2013 (1961–1990 base period) from the HadCRUT4 data set. (b) Colors identify grid boxes with annual-mean warm anomalies that rank first (dark red), second (orange-red), or third (yellow-orange) in the available observed record. Gray areas did not have sufficiently long records, defined here as containing at least 100 available annual means, with a seasonal mean requiring at least one of three months to be available, and an annual mean requiring at least three of four seasons to be available. (c) Fraction of available global area by year where the given year’s annual mean anomalies for that area rank in the top three highest (red curve) or lowest (blue curve) in the available record to that date. Available area restricted to those regions having at least 100 years of available data through 2013. (d) As in (c) but comparing each year’s annual anomalies to the entire record through 2013 (i.e., at least 100 years of data) for that gridpoint.

et al. (2014) have similarly found that there has been a continued increase in warm daily temperature extremes over global land regions during the “hiatus” period.

Is there a significant long-term anthropogenic warming trend in the Australian and far western Pacific regions? Annual-mean temperature anomaly time series extending back to the late 1800s for Australia and western tropical Pacific regions are shown in Fig. 8.2a,b. Both observed series (black curves) show a pronounced long-term warming, which has been more rapid since ~1970. This general behavior is well captured by the CMIP5 All-Forcing ensemble (red curves), though not by the Natural-Forcing ensemble (blue curves). The western tropical Pacific region has warmed slightly less than the global mean since the 1881–1920 base period, while the Australia region warming has been roughly comparable to that of the global mean (e.g., green curve in Fig. 8.2b).

To assess the causes of the observed long-term warming, we use a “sliding trend” analysis (Knutson et al. 2013a,b), incorporating multimodel samples from CMIP5 control runs and ensemble mean forced trends (Fig. 8.2c,d). The plots compare linear trends in the observations (black lines) with models, for trends ending in 2013 and beginning with a range of start years from the late 1800s to very recent. The pink region represents the “All-Forcing hypothesis”—the 5th–95th percentile range of trends from the All-Forcing runs. It is constructed as an ensemble distribution, aggregating the distributions of trends from the 23 individual CMIP5 models. Each model’s ensemble-mean All-Forcing trend is combined with randomly sampled internally generated trends from that model’s control run. These 23 distributions are aggregated to form the full distribution whose 5th–95th percentile range is depicted by the pink region, which thus reflects uncertainty in both the forced response and the influence of internal variability. The alternative “Internal-Variability-Only hypothesis” is shown by the green region on the plot. For comparison, Supplementary Fig. S8.2 shows an “All-Forcing hypothesis” versus a “Natural Forcing-Only” hypothesis version of the “sliding trend” analysis, in this case, for trends ending in 2012 (as a sensitivity test) and based on a 10-model subset of CMIP5 models with available Natural-Forcing runs through 2012.

The trend assessments in Fig. 8.2c,d and Supplementary Fig. S8.2 show that in both focus regions the observed long-term warming is generally detectable (outside the green band, i.e., significantly larger than

simulated internal or natural climate variability), at least for trends beginning earlier than the 1970s. Moreover, the observed trends are generally consistent with the “All-Forcing” hypothesis (pink region) for trends beginning in these periods. Using the CMIP5 models’ simulated variability and responses to natural forcings to estimate real-world natural variability (see internal variability assessments in Knutson et al. 2013a), we conclude that the long-term observed trends in both regions are very likely inconsistent with natural variability but generally consistent with anthropogenic and natural forcing combined. Therefore, the model results suggest that the long-term observed warming in both regions is very likely attributable in part to anthropogenic forcing.

To what extent are the 2013 extreme annual mean temperatures attributable to anthropogenic forcing? We next assess the 2013 annual mean temperature anomalies in the two regions using All-Forcing and Natural-Forcing scenarios (Fig. 8.2e,f). For the All-Forcing runs (red), the CMIP5 historical runs are extended as necessary through 2013 using the RCP4.5 forcing scenario. However, the Natural-Forcing runs (blue) cannot be extended in this manner, and so the Natural-Forcing ensemble response for 2013 is estimated by using the 2012 ensemble mean of the models along with high and low sensitivity tests (Fig. 8.2a,b; see Supplemental Material). Using the 2012 Natural Forcing estimate, the observed 2013 anomalies (compared to a baseline for 1881–1920) are well outside the range of CMIP5 model-estimated natural climate variability for both regions (Fig. 8.2e,f). We use 1881–1920 as a reference value for the 2013 anomaly, as we are attempting to estimate anthropogenic contributions and so have chosen a relatively early baseline period to be closer to preindustrial conditions. Further discussion of the baseline period and observational uncertainties is contained in the Supplemental Material. According to our analysis, the Australia region 2013 anomaly of 1.72°C had contributions of 0.81°C (anthropogenic forcing), 0.23°C (natural forcing), and 0.68°C (natural internal variability). The observed 1.72°C anomaly was at the 99.3 percentile of the CMIP5 All-Forcing distribution and was much larger than the ensemble mean of the All-Forcing distribution (1.04°C). This suggests that either internal variability played a significant role (in addition to external forcing) in producing the 2013 anomaly (estimated as 0.68°C), or the net climate forcing or the response to climate forcing in the CMIP5 models could be too

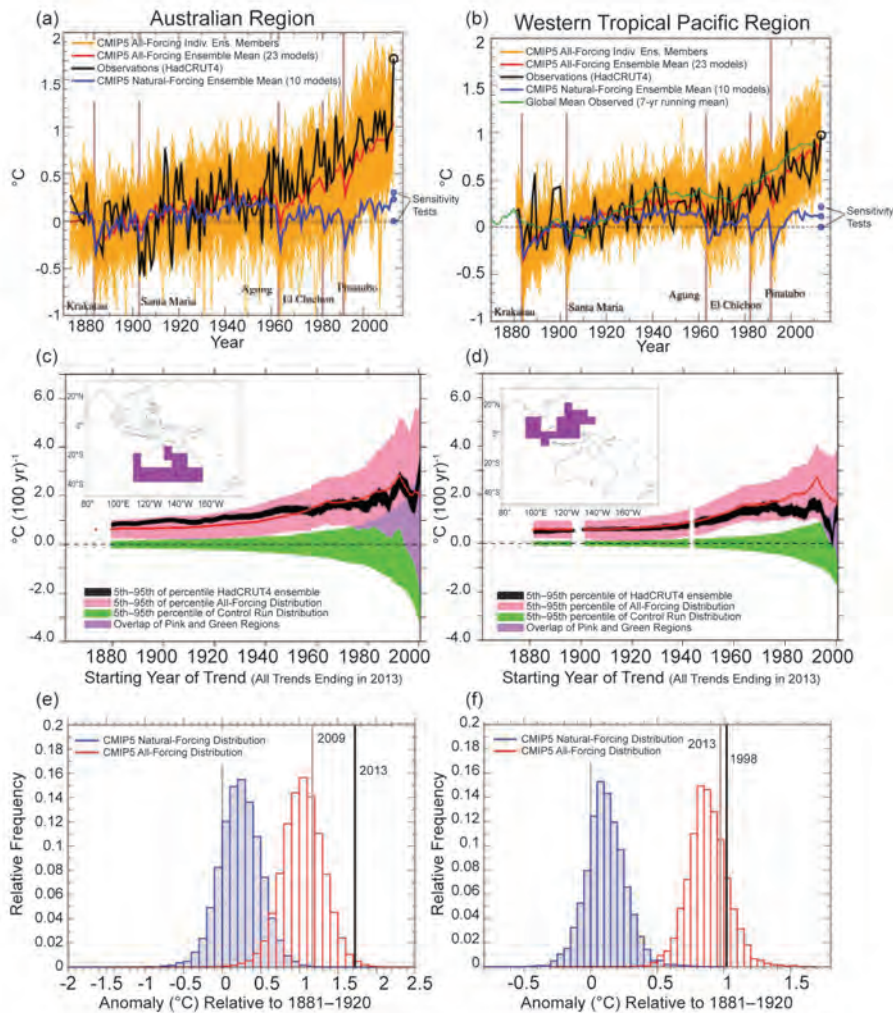


FIG. 8.2. (a,b) Time series of annual averaged surface temperature anomalies ($^{\circ}\text{C}$) averaged over regions of (a) Australia, left column, and (b) the far western tropical Pacific, right column. The black curves depict the observed (HadCRUT4) anomalies; the dark red (dark blue) curves depict the multi-model ensemble anomalies from the CMIP5 All-Forcing (Natural Forcing-only) runs, with each of the 23 (10) available models weighted equally; the orange curves are individual All-Forcing ensemble members. The green curve in (b) is the 7-yr running mean observed global mean temperature anomaly. The three blue circles labelled “Sensitivity Tests” depict low, medium, and high estimates of the Natural Forcing-only response for 2013 (see Supplemental Material). The All-Forcing simulations for these regions included both anthropogenic and natural forcings from about 1860 to the present, with data from RCP4.5 runs used to extend the time series through 2013 where necessary. Only 10 models had Natural Forcing runs available to us through 2012. All time series shown are adjusted to have zero mean over the period 1881–1920. (c,d) Trends [$^{\circ}\text{C}$ (100 yr) $^{-1}$] in the area-averaged annual-mean surface temperature series in (a,b) as a function of starting year, with all trends ending in 2013. The black curves show trends from observations (HadCRUT4), with the black shading depicting the 5th–95th percentile range for the 100-member HadCRUT4 observed ensemble (Morice et al. 2012), giving one indication of the observational uncertainty in these results. The red curves show the inter-model mean of ensemble mean trends from the 23-member CMIP5 All-Forcing ensemble. The pink region represents the ‘All Forcing’ hypothesis—the 5th–95th percentile range of trends from the All-Forcing runs. The green-shaded region shows the 5th to 95th percentile range of the alternative “Internal Variability Only” hypothesis estimated from the pre-industrial control runs. Purple shading indicates where the pink- and green-shaded regions overlap. The white spaces in the curves denote years where the initial “start year” was missing due to inadequate spatial or temporal coverage. Temporal coverage was assessed as in Fig. 8.1, and the spatial coverage was assessed for each year by requiring at least 33% non-missing annual means for the region. (e,f) Distribution of annual mean anomalies in the CMIP5 Natural Forcing-only runs (blue) and for the All Forcing runs (red) for 2013. The observed temperature anomalies for 2013 are depicted as dark black vertical lines, with anomalies for another recent similarly extreme year shown by the gray vertical lines.

weak. Since an anomaly as large as observed was also outside the estimated range of the natural variability (natural forcing plus internal variability) distribution from the CMIP5 models, our analysis shows that the CMIP5 modeled fraction (or percent) of risk of the event that is attributable to anthropogenic forcing is essentially 100%. The second highest anomaly in the Australia region series (1.17°C in 2009) occurs very rarely if at all in the modeled Natural-Forcing distribution, depending on assumptions on the 2012 natural forcing response (Supplementary Table S8.1). We again conclude that the modeled fraction of risk attributable to anthropogenic forcing is near 100% for this alternative threshold value.

Lewis and Karoly (2013) performed a similar analysis on the full Australia region for summer 2013 (December 2012–February 2013). They find a significant anthropogenic contribution to extreme warmth, with about a seven-fold increase in risk of an event like 2013 for an RCP8.5 scenario centered on the year 2013 (2006–20). The increase in risk that we find is even higher than their estimate, presumably because we analyze only that subset of the Australian region having the most unusual 2013 temperatures and we assess annual means rather than summer mean temperatures. Both of these analysis choices would tend to enhance the signal-to-noise ratio for an anthropogenic warming signal (or relative risk); on the other hand, by analyzing the summer season, Lewis and Karoly (2013) were focused on the season with presumably the maximum heat-stress impact. Our findings are also generally consistent with those of two similar analyses of Australian 2013 annual temperature (“The role of anthropogenic forcing in the record 2013 Australia-wide annual and spring temperatures” and “Climate change turns Australia’s 2013 big dry into a year of record-breaking heat” in this report).

For the western tropical Pacific region, the 2013 annual mean anomaly was 0.97°C, or slightly less than the 1998 anomaly of 1.02°C. The estimated contributions to the 2013 anomaly, based on the CMIP5 models, were 0.76°C (anthropogenic forcing), 0.11°C (natural forcing), and 0.09°C (natural internal variability). Both of these observed anomalies (relative to an 1881–1920 baseline) are outside of, or very rarely occurring in, our estimated distribution of natural variability. Thus, the modeled fraction of event risk attributable to anthropogenic forcing is close to 100%. The 2013 anomaly is at the 75.8 percentile of the All-Forcing distribution, indicating either a likely role for natural variability as estimated above

or perhaps an underestimated forcing response in this region.

A simple variance consistency test was also done (Supplemental Material) to assess the adequacy of the control runs’ internal variability as an estimate of the internal variability of the actual climate system. The latter was estimated by subtracting the CMIP5 models’ ensemble-mean All-Forcing response from the observed temperature series. For the Australia region, the residual variability so derived agrees well with the model control run ensemble. For the far western Pacific region, the standard deviation of the observed residual variability is about 16% higher than the control run ensemble, but adjusting the model control run variability upward by over 20% does not impact the main conclusions of our study. Similarly, our attribution conclusions remain robust in light of our assessment of the impact of baseline reference period and other observational uncertainties and related issues as discussed in the Supplemental Material.

Summary. Seasonal and annual temperature anomalies around the globe were highly skewed toward positive (warm) extremes in 2013, as in the recent few decades. Although global warming has been described as “pausing” since 2000, global temperatures remain at anomalously high levels, and warm annual and seasonal temperature extremes continue to far outpace the occurrence of cold annual extremes. Two examples of regions with extreme (record or near-record) annual warmth during 2013 include much of Australia and a region of the far western tropical Pacific. In both regions, a contribution of anthropogenic forcing to an observed long-term warming trend was detected. The annual mean anomalies for 2013 were either completely outside of, or extremely rare in, the distributions of modeled natural variability. Thus, the fraction of risk of these extreme events attributable to anthropogenic forcing was 100% or close to 100%, according to the CMIP5 models. These results reinforce the notion of a potentially high signal-to-noise ratio for anthropogenic warming signals for seasonal and annual anomalies—even at the subcontinental scale in some cases. They further suggest that even if the global warming “hiatus” continues, further extreme (record or near-record) seasonal or annual mean warm anomalies at the regional scale can be anticipated, though the particular regions with such extremes change from year to year (e.g., comparing the present study with our 2012 analysis, Knutson et al. 2013b).

9. THE ROLE OF ANTHROPOGENIC FORCING IN THE RECORD 2013 AUSTRALIA-WIDE ANNUAL AND SPRING TEMPERATURES

SOPHIE C. LEWIS AND DAVID J. KAROLY

Anthropogenic climate change has caused a very large increase in the likelihood of extreme events such as the record Australia-wide average temperatures in September, spring, and the 2013 calendar year.

Introduction. The 2013 Australian calendar year was the hottest in the observational record of over 100 years in terms of area-average mean surface air temperature (Fig. 9.1a). Averaged over Australia, the observed 2013 annual temperature exceeded the 1911–40 mean by 1.53°C (ΔT_{ANN1}), with the previous record anomaly of 1.36°C recorded in 2005 (ΔT_{ANN2}).

In 2013, new Australian area-average mean temperature (Tmean) records were also set for spring ($\Delta T_{\text{SON1}} = 1.83^\circ\text{C}$) and the month of September ($\Delta T_{\text{SEPI}} = 3.01^\circ\text{C}$), when the largest anomaly was recorded for any month since at least 1910 (Bureau of Meteorology 2014).

In this study, we investigate the roles of anthropogenic climate change and natural variability in contributing to the observed 2013 record-breaking temperatures. These contributing factors are assessed using multiple simulations from nine global climate models that participated in phase five of the Coupled Model Intercomparison Project (CMIP5; Taylor et al. 2012), and they were selected using the criteria from Lewis and Karoly (2013) based on data availability and representation of observed Australian temperature variability (see Supplementary Table S9.1 for model list). We consider the observed 2013 annual, spring, and September Australian area-average Tmean anomalies, as these were large record-setting events that have not been investigated previously. We then estimate anthropogenic contributions to 2013 record temperatures using a suite of CMIP5 experiments for the period 1850–2020 with different climate forcing factors imposed [see Supplementary Table S9.2 for experiment description and Lewis and Karoly (2013) for further information].

Data and methods. We investigate changes in area-average Australian annual (January–December, ANN), spring (September–November, SON), and September

(SEP) Tmean distributions from observational and CMIP5 model datasets. We use observed Australian area-average annual Tmean from the high-quality ACORN-SAT dataset for 1911–2013 (Trewin 2012) and then consider 65 realizations of the CMIP5 historical experiment for the period 1911–2005, forced by observed time-evolving changes in anthropogenic (well-mixed greenhouse gases, aerosols, and ozone) and natural forcings (solar irradiance and volcanic aerosols). We also use 35 realizations of the RCP8.5 experiment (representative concentration pathway with high emissions for the 21st century) for 2006–20, centered on 2013, as this is representative of global greenhouse gas emissions from 2005 to present (Peters et al. 2012). Full details of experiment forcings are provided by Taylor et al. (2012).

The probabilities of Australian annual, spring, and September temperatures were calculated for experiments incorporating anthropogenic and natural forcings, and they were compared to a parallel set of experiments including only natural forcings. The long control runs with no changes in external forcing factors (piControl) completed for each participating CMIP5 model provide an estimate of the unforced variability of the climate. The piControl experiment allows a large number of model years to be analyzed (13 realizations from selected models) but provides only an approximation of natural climate variability. Hence, we also utilize 36 realizations of the historicalNat experiment as an additional “natural” climate reference state in which time-evolving solar and volcanic forcings are imposed for the period 1850–2005.

We calculate historical, historicalNat, and RCP8.5 Tmean anomalies relative to the 1911–40 climatology and piControl anomalies relative to the long-term mean. We investigate the frequency of anomalies exceeding the ΔT_{ANN2} threshold observed in 2005. The historical simulations from the nine models

used agree well with the distribution of observed Australian annual average temperatures over the period 1911–2005 (Fig. 9.1b) estimated using a kernel smoothing function, with a two-sided Kolmogorov-Smirnov test indicating that the distributions are statistically indistinguishable ($p = 0.05$).

Results. We compare the occurrence of extreme Australia-wide annual temperatures ($> \Delta T_{ANN2}$) in the CMIP5 experiments (Fig. 9.1c). When anthropogenic forcings are included, there is a clear increase in the likelihood of extreme annual temperatures. The Australia-wide ΔT_{ANN2} temperature anomaly occurs once in six years on average in the RCP8.5 experiments over the period 2006–20 (Fig. 9.1d). Conversely, none of the 5572 historicalNat model years analyzed here exceeds the observed 2005 temperature threshold; it is virtually impossible to reach such a temperature

record due to naturally forced climate variability alone in these model simulations. Furthermore, in the unforced piControl simulations, only one of the 6795 model years analyzed here exceeds the ΔT_{ANN2} threshold set in 2005.

Previous studies investigating anthropogenic contributions to observed extremes have quantified the relative influences on the occurrence of an event using a fraction of attributable risk (FAR) approach (Stott et al. 2004; Stone and Allen 2005) as a quantitative estimate of the fraction of risk of exceeding a particular climatic threshold that can be attributed to a cause. Using CMIP5 experiments, we previously estimated that the probability of extreme Australian summer temperatures, such as observed in 1998 and 2013, very likely increased by at least five-fold (FAR = 0.82) due to anthropogenic forcings (Lewis and Karoly 2013). However, when quantifying anthro-

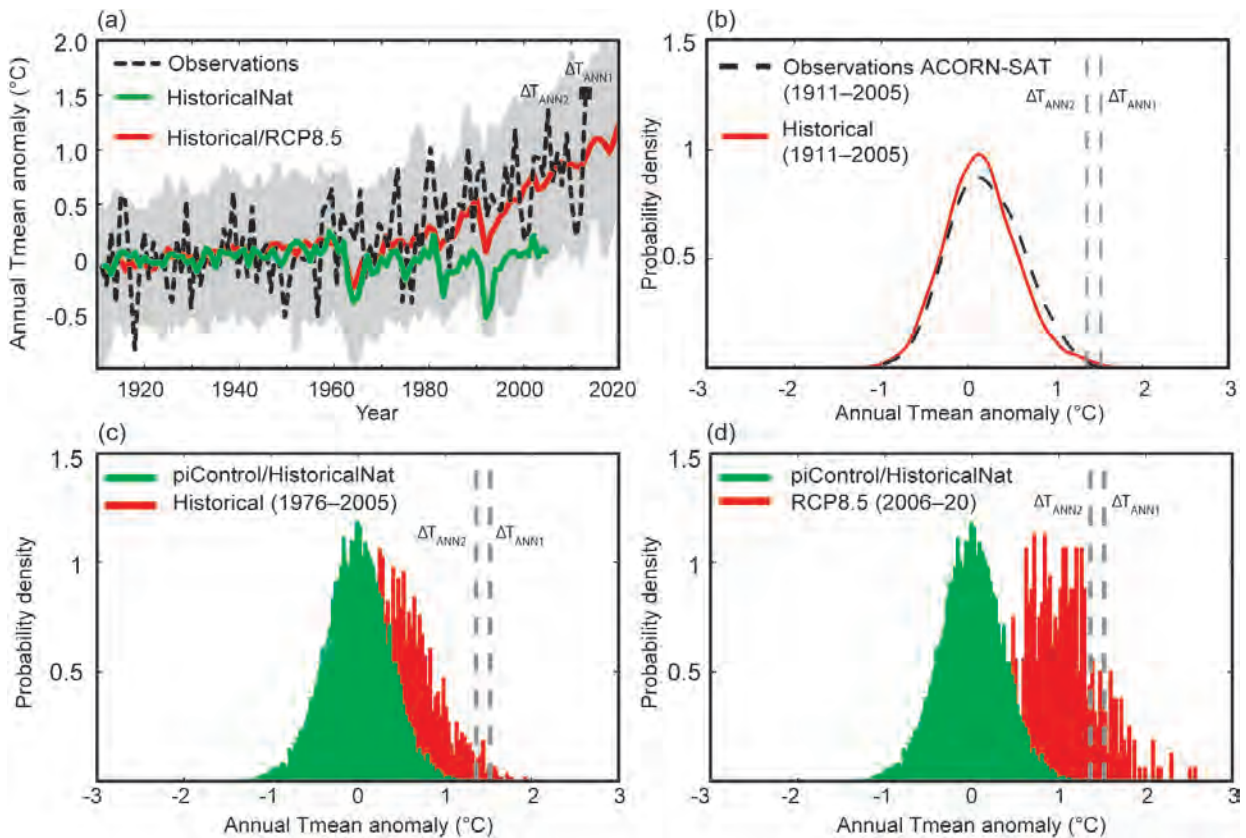


FIG. 9.1. (a) Australian annual average Tmean anomalies (relative to 1911–40) for observations (dashed black) and historicalNat (green) simulations. The historical and RPC8.5 multimodel mean is also shown (red), and gray plumes indicate the 5th and 95th percentile values across the ensemble members. (b) Probability density functions for Australian annual average Tmean anomalies (relative to 1911–40) for observations (dashed black) compared with historical (red) for 1911–2005. (c) Histograms for Australian annual average Tmean anomalies (relative to 1911–40) of historical (red, years 1976–2005) and piControl and historicalNat (green, all years shown). (d) Same as panel (c), but instead showing RCP8.5 Tmean anomalies (red, years 2006–20). In all probability plots, vertical dashed lines show the observed 2013 anomaly ($\Delta T_{ANN1} = 1.53^{\circ}\text{C}$) and threshold of the second hottest year on record ($\Delta T_{ANN2} = 1.36^{\circ}\text{C}$).

pogenic influences on the occurrence of Australian annual average temperatures exceeding ΔT_{ANN2} , the FAR value is effectively equal to one as there is only a single instance in over 12 300 combined model years in which this threshold was exceeded without anthropogenic forcings.

Christidis et al. (2013) investigated the record 2010 Moscow temperatures and found the probability of such an event occurring was near zero in climate simulations without anthropogenic influences. However, as the observed anomalies lie in the far warm tail of both the natural and anthropogenically influenced temperature distributions, this event likely resulted from internal variability. Unlike the Moscow record, 2013 Australian temperature anomalies occur frequently in simulations with anthropogenic factors. A FAR value of one is also obtained by shifting the observed temperature distribution by the modeled mean RCP8.5 temperature changes, demonstrating that the increased likelihood of the Australian annual temperature of 2013 can be explained by the mean warming trend of Australian annual average Tmean having increased by $\sim 0.9^\circ\text{C}$ since 1910 (Bureau of Meteorology 2012). Similarly, although ENSO temperature anomalies are a major driver of Australian temperature variability, the 2013 ENSO conditions were predominantly neutral (observed NINO3.4 anomaly -0.16°C relative to 1981–2010; <http://www.ncdc.noaa.gov/sotc/global/2013/13>, which is typically associated with cooler Australian temperatures (Power et al. 2006; Arblaster and Alexander 2012). ENSO variations alone are also unlikely to explain the record 2013 Australian summer temperature (Lewis and Karoly 2013).

We next compare the probability of spring and September Tmean anomalies in the CMIP5 experiments, using a kernel smoothing function (Fig. 9.2). There is a warm shift in these distributions when anthropogenic forcings are included. As spring and September temperatures exceeding the respective ΔT_2 thresholds occur in natural-only forced simulations, we calculate FAR values by comparing the probability of

extreme ($>\Delta T_2$) mean temperatures in the various model simulations, as determined by the number of times ΔT_2 was exceeded, relative to the total sample size. Using subsamples of only 50% of available data bootstrap resampled 1000 times, a distribution of possible FAR values was calculated. Conservative estimates of the FAR values, which are exceeded by 90% of the values in the FAR distribution determined by bootstrapping, are reported here. The FAR value for Australian SON Tmean anomalies is 0.97 (relative to the historicalNat) for the RCP8.5 experiment for the period 2006–20, indicating a greater than 50-fold in-

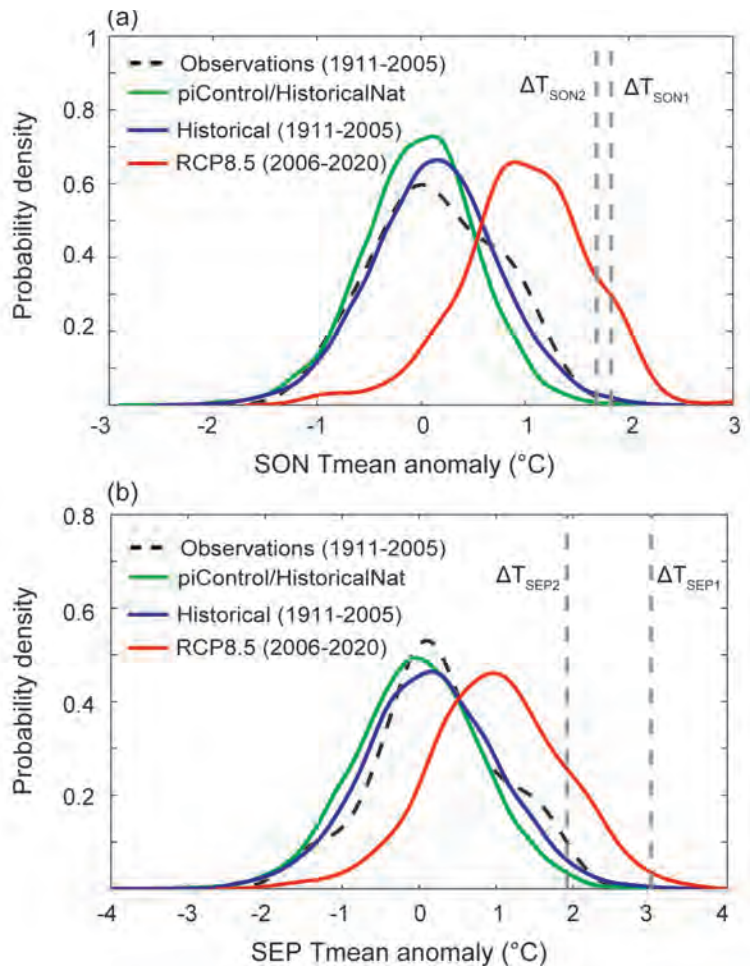


FIG. 9.2. (a) Probability density functions for Australian SON average Tmean anomalies (relative to 1911–40) for observations (dashed black, all years shown) compared with historical (blue, 1911–2005), RCP8.5 (red, years 2006–20), and piControl and historicalNat (green, all years shown), estimated using a kernel smoothing function. Vertical dashed lines show the observed 2013 anomaly ($\Delta T_{SON1} = 1.83^\circ\text{C}$) and threshold of the second hottest spring on record ($\Delta T_{SON2} = 1.62^\circ\text{C}$). (b) Same as panel (a), but showing Australian September average Tmean anomalies for historical (blue), RCP8.5 (red), and piControl and historicalNat (green), with ΔT_{SEP1} (3.01°C) and ΔT_{SEP2} (1.92°C) thresholds indicated.

crease in risk of hot spring temperatures in Australia that can be attributed to anthropogenic forcings. The equivalent FAR value for September Tmean anomalies for Australia is 0.82 (five-fold increase in risk) for the RCP8.5 experiment.

Conclusions. We examined anthropogenic and natural contributions to the record-breaking 2013 Australia-wide annual, spring, and September temperature anomalies. There are substantial increases in the likelihood of hot temperatures occurring ($>\Delta T_2$) that can be attributed to anthropogenic forcings for spring (FAR = 0.97) and September (FAR = 0.82) area-average Australian Tmean anomalies. Annual Tmean anomalies greater than the second hottest year observed for Australia (ΔT_{ANN2}) occur once in six years in the RCP8.5 years investigated here. In the piControl simulations including only natural forcings, only a single year of the 6795 model years analyzed exceeds ΔT_{ANN2} . The ΔT_{ANN2} anomaly falls entirely outside the bounds of natural climate variability simulated in the historicalNat experiment. Hence, temperature anomalies as extreme as those observed in 2005 occur only once in over 12300 years of model simulations without anthropogenic forcings, and the resulting FAR value is essentially equal to one.

These results are derived from a subset of CMIP5 data and encompass only the range of natural variability simulated therein. Model years as warm as or warmer than ΔT_{ANN2} could occur in realizations that were not included. This analysis necessarily assumes that the statistics of the modeled temperature distributions are equivalent to the statistics of observations on long timescales. Additionally, the calculation of meaningful FAR values depends on the validity of the forced response of the models relative to the observed forced response. Nonetheless, it is unlikely that alternative CMIP5 model inclusions or the use of alternative attribution model datasets would result in the attribution of the 2013 Tmean anomalies to a cause other than the anthropogenic factors identified here. Indeed, further analysis of Australia's 2013 record annual Tmean also demonstrates anomalies were largely outside the modeled natural variability, with the attributable risk to anthropogenic forcing essentially 100% (see "Multimodel assessment of extreme annual-mean warm anomalies during 2013 over regions of Australia and the western tropical Pacific" and "Climate change turns Australia's 2013 big dry into a year of record-breaking heat" in this report).

10. INCREASED SIMULATED RISK OF THE HOT AUSTRALIAN SUMMER OF 2012/13 DUE TO ANTHROPOGENIC ACTIVITY AS MEASURED BY HEAT WAVE FREQUENCY AND INTENSITY

SARAH E. PERKINS, SOPHIE. C. LEWIS, ANDREW D. KING, AND LISA V. ALEXANDER

Human activity has increased the risk of experiencing the hot Australian summer of 2012/13, as measured by simulated heat wave frequency and intensity, by two- and three-fold, respectively.

Introduction. The Australian summer of 2012/13 was the warmest since records began in 1910 (Bureau of Meteorology 2013a). The season was characterized by the hottest month on record (January), where the continental mean temperature reached 36.9°C. Averaged nationally, the last four months of 2012 were 1.61°C higher than the long-term mean. Rainfall was below average for much of the country since July 2012. Along with the late onset

of the Australian monsoon, such conditions primed the continent for extremely hot summer weather, including heat waves. Heat waves require detailed focus due to their large impacts (Karoly 2009; Coumou and Rahmstorf 2012), particularly on human health and morbidity (Nitschke et al. 2007). Much of inland Australia experienced extreme temperatures for over three consecutive weeks (Bureau of Meteorology 2013a).

By employing the fraction of attributable risk (FAR) framework (Allen 2003), Lewis and Karoly (2013) demonstrated that the likelihood of the extreme Australian heat during the 2012/13 summer had increased by between 2.5 and 5 times due to human activity. However, this assessment was on the seasonal average temperature anomaly and did not include specific heat wave measures. Here we also undertake an analysis of the summer of 2012/13 but with a metric of two heat wave characteristics (Perkins and Alexander 2013). While focusing specifically on seasonal heat wave measures, such an analysis also allows for the assessment of whether changes in risk are consistent for heat wave magnitude and frequency, thus providing important information for adaptation and impacts groups.

Data and methods. We calculate heat waves using the Excess Heat Factor (EHF) definition (Nairn and Fawcett 2013; Perkins and Alexander 2013) for November–March, where the daily average of minimum and maximum temperature must exceed a separate climatological and monthly threshold for at least three consecutive days. Here the climatological threshold is the calendar day 90th percentile, calculated from a 15-day moving window for 1961–90. Note that EHF units are °C² (see Nairn and Fawcett 2013).

In order to investigate the effects of human activity on heat waves, the preindustrial control (289 years long), historical, and RCP8.5 experiments (Taylor et al. 2012) from the Community Earth System Model (CESM; Fischer et al. 2013) were employed. Here we use a 21-member ensemble of CESM (1.875° × 2.5° resolution; for further model details, see Fischer et al. 2013). The ensemble is generated through perturbations on the order of 10–13 applied to atmospheric temperature initial conditions. We use 1955–2005 of the historical period and merge it with 2006–13 from RCP8.5. A caveat to this study is its dependence on a single model (CESM). However, collectively, the CESM ensemble simulates reasonable changes and variability in observed heat waves over Australia (Perkins and Fischer 2013). Observed heat wave metrics were calculated for austral summers commencing in 1955–2012 using the Australian Water Availability Project (AWAP) temperature dataset (Jones et al. 2009) interpolated onto a two-degree grid. Using AWAP, the observed 2012/13 anomalies of heat wave measures were calculated.

In this study, we investigate the extreme heat of the 2012/13 summer by analyzing two heat wave characteristics (Perkins and Alexander 2013). These

are the total number of heat waves and the peak amplitude (hottest heat wave day). The number of heat waves represents the frequency, and peak heat wave amplitude represents the intensity of the 2012/13 extended summer season (November–March). For each model run and the observations, the characteristics were calculated at the grid box level and expressed as anomalies against the relative 1961–90 average, with the control simulation relative to model years 111–140. The control base period was chosen to be the same length as the historical; however, the start year (111) was selected at random since no significant difference between 30-year windows from the control was detected. All anomalies were area-averaged, and all 21 CESM members were concatenated to form a longer single sample.

We employ the FAR framework to analyze changes in the risk of heat wave attributes due to increases in anthropogenic greenhouse gases. This requires conditions where no anthropogenic emissions are present (the control run) and where greenhouse gas concentrations are prescribed to observed levels to 2005 and projected to 2013, accounting for anthropogenic emissions (the historical/RCP8.5 runs). Three periods are analyzed for summers commencing in 1955–83, 1955–2012, and 1984–2012 to investigate how the risk of each characteristic changes with increasing anthropogenic forcings during the observational period. Per period, we generate 1000 bootstrapped samples, consisting of 50% of the control and historical/RCP8.5 data per heat wave characteristic (i.e., the bootstrapped sample sizes of the control and forced runs are half of the original). Selected years are in two-year blocks to account for time dependence, and using 50% of data accounts for sample size sensitivity. Bootstrapping is employed since a true estimate of FAR cannot be obtained from the original control and forced simulations. Our bootstrapping technique allows the uncertainty in FAR to be estimated. The probability of the respective observed anomaly is calculated, and 1000 FAR values are calculated by:

$$FAR = 1 - \left(\frac{P_{ctrl}}{P_{forced}} \right) \quad (1)$$

We also compute the corresponding changes in risk of the characteristics by:

$$Risk = \frac{1}{(1 - FAR)} \quad (2)$$

Lastly, using the FAR values for each heat wave characteristic, we compare the waiting time of the frequency and intensity of the 2012/13 summer in each of the three periods and the control. This deter-

mines how historical return intervals of the hot 2012/13 summer compare to a world without anthropogenic influence.

Results. Figures 10.1a and 10.1b present the area-averaged probability density functions (PDFs) of anomalies of seasonal heat wave frequency and intensity, respectively. The summer of 2012/13 experienced an unprecedented number of heat waves; however, the peak intensity was not particularly unusual (see Table 10.1). Throughout the periods of the simulations, the right tail of the PDF increases—with greater anthropogenic forcing, more extreme summers, as characterized by heat wave frequency and intensity, are expected (relative to 1961–90).

Figures 10.1c and 10.1d present PDFs of the FAR values per period for heat wave frequency and intensity, respectively. FAR values for intensity (Fig. 10.1b) and frequency (Fig. 10.1a) are very similar. This includes negative median FAR values for 1955–83 (–0.22 and –0.32 for frequency and intensity, respectively). A Kolmogorov–Smirnov test at the 5% level indicates that the 1955–83 and control simulations are not significantly different, indicating that these values hold little meaning and that the impact of human activity on Australian summer intensity and frequency had not yet emerged from natural variability. In the case of this study, this result occurs only when the first 30 years of the historical period (1955–83) is included, that is, when anthropogenic forcings were considerably lower than 2012/13.

It is very likely (>90%) that FAR values are greater than 0.26 and 0.1, respectively, during

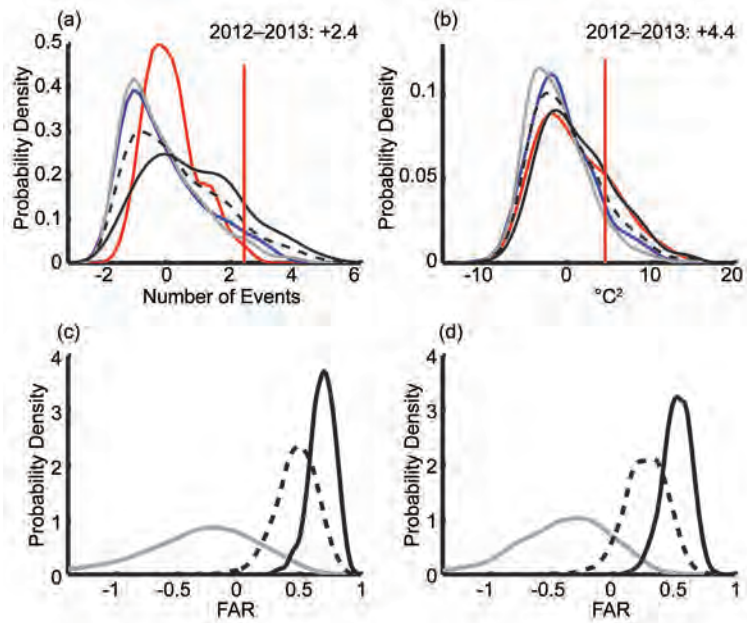


FIG. 10.1. (a), (b) Respective probability density functions (PDFs) of heat wave frequency (number of heat waves) and intensity (peak magnitude) anomalies. Vertical lines reflect the respective anomalies for the 2012/13 Austral summer. (c), (d) Respective PDFs of FAR values from 1000 bootstrapped samples. Red is for the observations, blue is for the control, gray is for 1955–83, black dashed is for 1955–2012, and black solid is for 1984–2012.

1955–2012 (medians 0.49 and 0.27) and very likely that FAR values are greater than 0.55 and 0.37 (medians 0.69 and 0.53), respectively, for 1984–2012. The all-positive FAR values in 1984–2012 indicate that the risk of the intensity and frequency of the 2012/13 summer is always larger due to human activity during the latter decades of the 20th century. Kolmogorov–Smirnov tests on 1955–2012 and 1984–2012 against the control indicate statistical significance for both heat wave frequency and intensity.

Based on the median FAR values, Table 10.1 presents the best estimate changes in the risk of the 2012/13 summer heat wave frequency and intensity during the three time intervals and the

Table 10.1. Changes in the risk of Australian 2012/13 heat wave frequency (number of heat waves) and intensity (peak magnitude) anomalies due to anthropogenic forcings throughout summers commencing in 1955–83, 1955–2012, and 1984–2012, as well as return periods relative to observations for 1955–2012. Note that 1955–83 values are calculated from non-significant FARs.

Characteristic	1955–83		1955–2012		1984–2012		Control	
	Risk	Return period	Risk	Return period	Risk	Return period	Risk	Return period
Frequency	0.78	145.22	1.94	58.00	2.94	32.94	NA	112.64
Intensity	0.73	8.45	1.37	4.46	2.31	2.97	NA	6.12

corresponding return periods. The risk due to human activity is similar for both characteristics during 1955–1983 and is less than zero. However as discussed above, 1955–83 summer heat wave frequencies and intensities are not distinguishable from the control (i.e., cannot be separated from no human influence).

A striking result is that during 1955–2012 and 1984–2012, the risk of the summer of 2012/13 having such a high heat wave frequency anomaly increases faster than heat wave intensity. During the latter period, the risk of experiencing a summer heat wave number (intensity) greater than that of 2012/13 increases by almost three-fold (two-fold) compared to a world with no anthropogenic forcing. This corresponds to a reduction in return periods to ~33 and 3 years, respectively, compared to 1955–2012. It is also an interesting and important result that even though the 2012/13 summer heat wave intensity was much less “extreme” than heat wave frequency (see corresponding return periods in Table 10.1), human activity has clearly increased the risk of both characteristics occurring. Thus, there is a calculable human influence on the hot Australian summer of 2012/13.

Conclusions. Using a 21-member ensemble of the CESM model, we analyzed changes in the risk of the hot Australian 2012/13 summer with respect to heat wave frequency and intensity. Our study found that the risk of both simulated heat wave characteristics has increased due to human activity. The risk of summer heat wave frequency increases faster than heat wave intensity. When isolating 1984–2012, the 2012/13 heat wave frequency increased three-fold due to human activity, while heat wave intensity increased two-fold, compared to a climate with no anthropogenic forcings.

This infers a reduction in return periods when comparing 1955–2012 to 1984–2012—from 58 years to 33 years for frequency and from 4 years to 3 years for intensity. Lastly, even though heat wave intensity of 2012/13 was not the most severe Australia experienced, there is still a calculable influence on this heat wave characteristic on a seasonal scale. Overall, our study shows that the risk of the hot 2012/13 Australian summer with respect to simulated heat wave frequency and intensity increased due to human influences on climate.

II. UNDERSTANDING AUSTRALIA’S HOTTEST SEPTEMBER ON RECORD

JULIE M. ARBLASTER, EUN-PA LIM, HARRY H. HENDON, BLAIR C. TREWIN,
MATTHEW C. WHEELER, GUO LIU, AND KARL BRAGANZA

Record high September maximum temperatures over Australia arose from a combination of a strongly anomalous atmospheric circulation pattern, background warming, and dry and warm antecedent land-surface conditions.

Introduction. September 2013 was Australia’s warmest September since records began in 1910, with anomalous heat across most of the country (Fig. 11.1a). Maximum temperatures, averaged nationally, were 3.32°C above the 1961–90 average—the highest anomaly for any month on record and almost a full degree ahead of the previous September record set in 1980 (Bureau of Meteorology 2013b). September marked the peak of a record warm period for Australia, which commenced in mid-2012. The most unusual heat began from the last week of August 2013 and continued into the first half of September. Temperatures moderated

from 10 September before extreme heat returned to northern and eastern Australia in the final week of the month. Lewis and Karoly (“The role of anthropogenic forcing in the record 2013 Australia-wide annual and spring temperatures” in this report) determine that the attributable risk of such extreme heat in September has increased five-fold due to anthropogenic climate change. Here we take a different attribution approach and use multiple linear regression and experiments with a seasonal forecast system to explain and understand the magnitude of the September 2013 temperatures.

Models to understand the record Australian temperatures. A multiple linear regression model using least squares and assuming normally distributed random errors was built from observed predictors that have historically been used to explain Australia's seasonal climate (e.g., Hendon et al. 2014). These include ENSO, the Indian Ocean dipole (IOD), and the southern annular mode (SAM). Other predictors were global mean temperature, as an indication of the large-scale warming of the climate system, and Australian upper-layer soil moisture from the preceding month, which may be a source of persistence (e.g., Lorenz et al. 2010). All regression calculations were developed using predictors over 1982–2011 using monthly anomalies from the 1982–2011 base period. See the Supplementary Material for details on the predictors and datasets used.

Forecast sensitivity experiments were also performed with the 30-member Predictive Ocean Atmosphere Model for Australia (POAMA) seasonal forecast system (Hudson et al. 2013; see Supplementary Material) to investigate the importance of initial conditions in the ocean, land, and atmosphere for predicting the September record heat. Table 11.1 lists the various sensitivity experiments, all of which were initialized on 21 August 2013, i.e., 10 days prior to the month of interest. Sensitivity experiments consisted of scrambling the atmosphere, land, and ocean initial conditions by sampling the initial conditions for 21 August from the previous 30 years.

Statistically reconstructing September 2013. In calibration, the regression model explains approximately half of the variance in Australian maximum tempera-

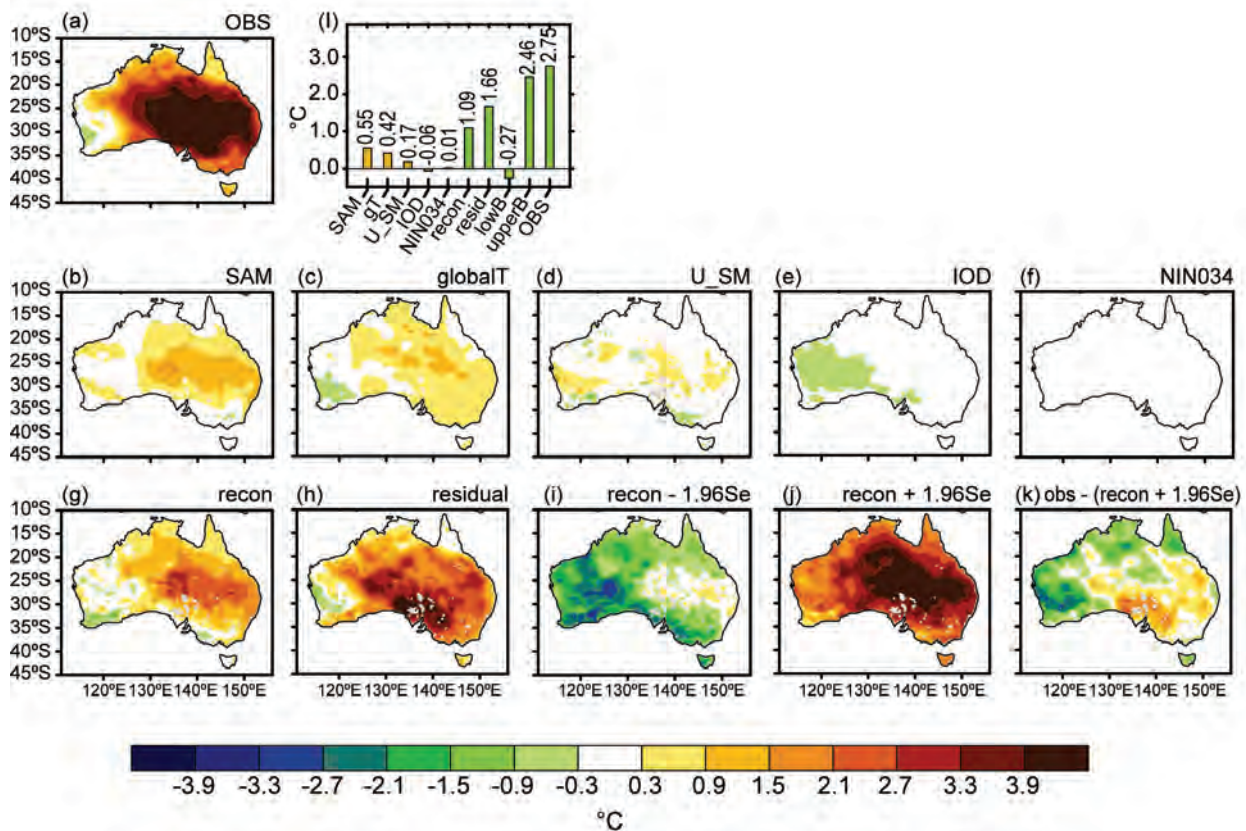


FIG. 11.1. Patterns of September 2013 maximum temperature anomaly (°C) from (a) observations, and the contribution of individual predictors from a multiple linear regression using (b) southern annular mode, (c) global mean temperature, (d) 2013 August upper layer soil moisture, (e) Indian Ocean dipole index, and (f) Niño3.4 SSTs, where each regression map has been multiplied by the size of the predictor in September 2013. The lower row shows (g) the total reconstructed anomaly (sum of panels b–f), (h) the residual, the difference between the observed and reconstructed anomalies, (i) the reconstructed anomaly minus the 95% prediction interval (j) the reconstructed anomaly plus the 95% prediction interval, and (k) difference between (a) and (j). The bar chart (l) displays the observed Australian-average maximum temperature anomaly and the contribution by each of the predictors, the total predicted anomaly, the residual and the predicted anomaly accounting for the 95% prediction interval. Anomalies are relative to the 1982–2011 base period.

Table 11.1. Coupled model seasonal forecast experiments described in the text and their initial conditions for atmosphere (ATM), land surface (LAND), and ocean (OCEAN). See the Supplementary Material for more details on the experimental design. Color shading indicates whether initial conditions for the 30 members are as observed (blue) or scrambled (red).

	Operational seasonal forecast experiment	Scrambled ATM experiment	Scrambled ATM and LAND experiment	Scrambled OCEAN experiment
ATM initial conditions	Observed for 21 August 2013	Selected from 21 August 1981–2010	Selected from 21 August 1981–2010	Observed for 21 August 2013
LAND initial conditions	Observed for 21 August 2013	Observed for 21 August 2013	Selected from 21 August 1981–2010	Observed for 21 August 2013
OCEAN initial conditions	Observed for 21 August 2013	Observed for 21 August 2013	Observed for 21 August 2013	Selected from 21 August 1981–2010

tures during 1982–2011 (Supplementary Fig. S11.1; correlation with observed = 0.73). The contribution from each of the predictors for September 2013 is shown in Figs. 11.1b–f. The SAM, which was the most important predictor of this hot event, contributed 20%, reflecting the second-most negative SAM in the 1982–2013 record (standardized anomaly of -1.5). A negative SAM typically results in higher-than-normal maximum temperatures across much of extratropical Australia in the spring season (Hendon et al. 2007). Note that although the SAM has been trending towards its positive phase in austral summer, there is no significant trend in the September SAM time series. Global mean temperature was the second most important predictor, accounting for 15% of the observed anomaly (using the linear trend as the predictor instead gives a similar result). Both the SAM and global temperature contributions produce similar spatial patterns to the observed. Antecedent soil moisture anomalies had a moderate positive contribution in the interior of the continent, though their contribution to the Australian average anomaly was minor. The IOD and ENSO appear to have played little role in the event. SST anomalies in the Indo-Pacific were indicative of a weak La Niña state (slightly cooler than normal in the eastern Pacific and warmer than normal in the west), which usually drives cooler temperatures over Australia. A negative IOD, which was in its decaying state in September, appears to have mitigated some of the warming in the southwest, contributing to slightly cool anomalies observed there.

The reconstructed Australian September 2013 maximum temperature anomalies are shown in Fig.

11.1g (which is simply the sum of the anomalies from the individual predictors in panels b–f). The reconstruction captures the observed pattern of a warm interior and relatively cooler southwest, though at a weaker magnitude than observed (quantified as the residual in Fig. 11.1h). When averaged over Australia, the mean reconstruction reproduces 40% of the observed anomaly (Fig. 11.1l). The Australian-average anomaly for 2013 also falls outside the 95% prediction interval (which accounts for the uncertainty in the strength of the historical relationships) of the reconstruction (see Supplementary Fig. S11.1). However, 5% of the years are expected to lie outside this interval, and this appears to be, roughly, what occurred for 1982–2013. The inability to reconstruct the full magnitude of the September 2013 warmth could be due to nonlinear processes not accounted for, or it could indicate that a key predictor, not previously identified to be important for September Australian maximum temperatures, is missing. One such possibility is the MJO, which was strong at the beginning and end of the month (based on the diagnostics of Wheeler and Hendon 2004) and has recently been shown to impact weekly and seasonal Australian temperature in certain phases (Marshall et al. 2013). Preliminary analysis suggests that the MJO contributed to the warm anomaly in the first and last week of September.

Analysis of the SST anomaly for 2013 indicates that there was not much similarity with the pattern historically associated with high maximum temperatures over Australia, other than over the western Pacific where the SST warming trend is strong (compare left panels of Supplementary Figs. S11.2 and S11.3). However, the observed mean sea level pressure (MSLP)

anomaly in September 2013 matches well the pattern that is associated with high maximum temperatures over Australia (compare right panels). This pattern has a region of anomalously low pressure immediately to the southwest of the continent and zonally symmetric high pressure farther to the south indicative of a negative SAM. However, while we account for the SAM in our regression model, the strong low pressure to the southwest remains in the pattern of MSLP regressed onto the residual maximum temperature time series (Supplementary Fig. S11.4). The inference is that

the occurrence of this strong low pressure anomaly, unrelated to the occurrence of negative SAM or SST forcing, played a prominent role in the record hot September 2013. We further explore the importance of this inference using sensitivity experiments with the POAMA coupled model forecast system.

Dynamical predictions of the record September 2013 Australian temperature. The ensemble mean POAMA forecast for September 2013, initialized on 21 August using observed atmosphere, land, and ocean

initial states (Hudson et al. 2013), produced warm anomalies across most of the continent (Fig. 11.2a). Though the ensemble mean anomaly is weaker than observed, the histogram of the 2013 Australian maximum temperature forecasts is systematically shifted towards warmer temperatures compared to the hindcast data (Supplementary Fig. S11.5), with, e.g., the likelihood of exceeding a 1.5 standard deviation warm anomaly increasing by a factor of six in 2013.

Rerunning the forecasts using atmospheric initial conditions randomly picked from the previous 30 years for 21 August, which effectively removes any predictability coming from the atmospheric initial state, reduces the ensemble mean temperature anomaly by up to 50% over the interior (Fig. 11.2c). Scrambling the atmosphere and land initial conditions (Fig. 11.2e) further reduces the temperature anomaly, with stippling indicating significant differences to the original forecast across most of the continent. This result suggests that the initial land state was a dominant factor in these

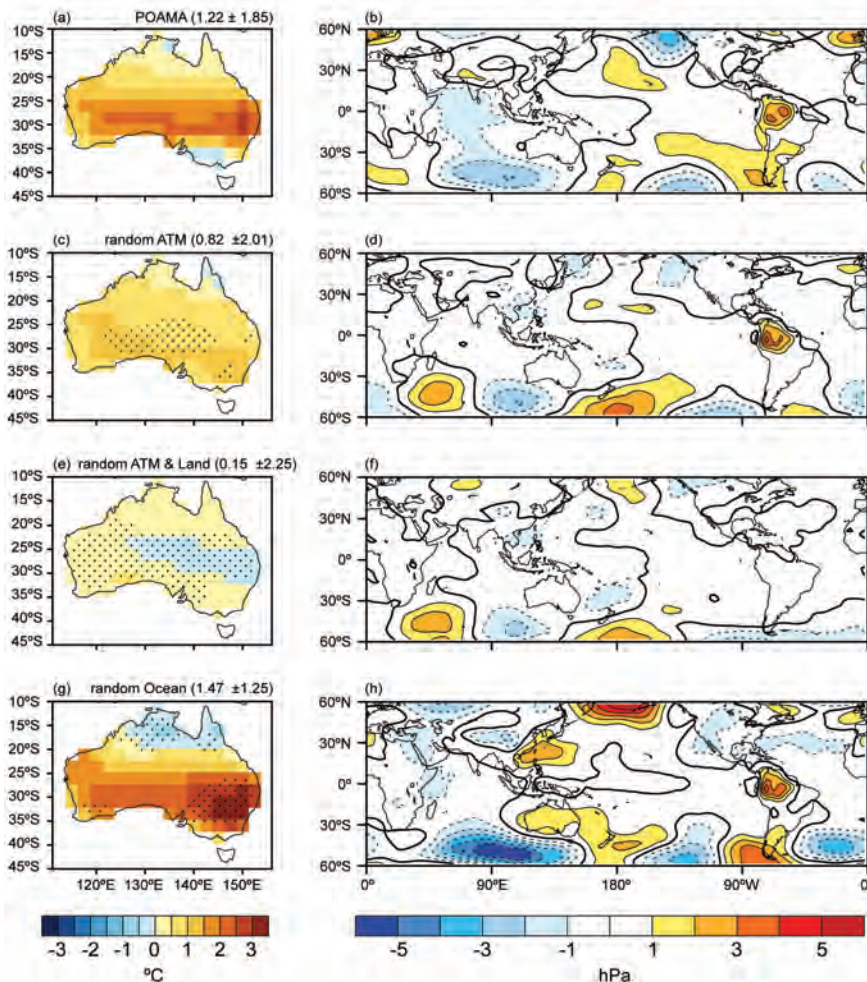


FIG. 11.2. September 2013 30-member ensemble mean (left) maximum temperature ($^{\circ}\text{C}$) and (right) MSLP (hPa) anomalies from the POAMA experiments initialised on 21 August for the prediction with (a,b) 2013 atmosphere, land, and ocean initial conditions; (c,d) atmospheric initial conditions scrambled; (e,f) atmospheric and land initial conditions scrambled; and (g,h) ocean initial conditions scrambled. Stippling in the left panels indicates areas where the temperature differences between the experiment and the operational 2013 POAMA forecasts are statistically significant at the 90% confidence level, based on the 30-member ensemble forecasts used in a two-tailed Student's *t*-test. The predicted Australian average temperature anomaly and 95% prediction interval based on the ensemble members is given in brackets in the left panels.

dynamical predictions and that SST boundary forcing contributed little to the promotion of the record maximum temperatures over Australia. The latter suggestion is confirmed by rerunning the forecasts using observed atmosphere and land initial conditions but scrambled initial ocean states (Fig. 11.2g). In fact, a larger magnitude of predicted warm anomalies is found, suggesting that the ocean had a mitigating impact on temperatures during this extreme event. This is consistent with the weak cooling contribution from tropical SST modes highlighted in the regression analysis.

Note that the low pressure anomaly to the south of Australia is evident in all POAMA experiments (Figs. 11.2b,d,f,h), but with much reduced magnitude compared to observed. The magnitude weakens further when the atmospheric and land initial conditions are scrambled, substantiating the earlier inference of the importance of this mostly unpredictable pressure pattern in the resulting extreme temperatures

Conclusions. Analysis using both multiple linear regression based on historical observational data and sensitivity experiments with a dynamical seasonal prediction system indicates that the record hot September conditions over Australia arose from the

apparently random occurrence of strongly negative SAM together with an anomalously deep low pressure cell situated to the southwest of the continent, the background warming trend, and antecedent dry and warm land surface conditions. SSTs appear to have played little role in promoting the record warm anomaly and, based on the evidence presented, actually acted to mitigate the warming over Australia. The results from the regression model indicate up to 15% of the record temperature anomaly can be explained by the global temperature changes over the 1982–2013 period analyzed. This warming trend is expressed in the seasonal forecast experiments through the trend in ocean and land initial conditions, the latter of which appeared to be the dominant contributor to the September 2013 predicted anomaly over Australia. The sensitivity to the initial land conditions in the POAMA forecasts is thus consistent with the inference from the regression model concerning the substantial role of the upward trend in global temperatures. To the extent that global temperature changes have been attributed to anthropogenic climate change (Bindoff et al. 2014), a multi-step attribution process suggests that anthropogenic climate change played an important role in the record Australian maximum temperatures in September 2013.

12. CLIMATE CHANGE TURNS AUSTRALIA'S 2013 BIG DRY INTO A YEAR OF RECORD-BREAKING HEAT

ANDREW D. KING, DAVID J. KAROLY, MARKUS G. DONAT, AND LISA V. ALEXANDER

The record heat of 2013 across inland eastern Australia was caused by a combination of anthropogenic warming and extreme drought.

Introduction. During 2013, Australia experienced its hottest year on record (23°C on average, 0.17°C above the previous 2005 record) as well as a series of extreme heat wave events (see also “The role of anthropogenic forcing in the record 2013 Australia-wide annual and spring temperatures”, “Multimodel assessment of extreme annual-mean warm anomalies during 2013 over regions of Australia and the western tropical Pacific”, and “Increased risk of the hot Australian summer of 2012/13 due to anthropogenic activity as measured by heat wave frequency and intensity” in this report). Besides being the hottest year in a record dating back to 1910, a drought set in across much of

the east of the country leading the federal government to announce an AUD320 million (~USD 300 million) drought assistance package for affected farmers. The severe lack of water in the region came after the exceptionally wet 2010–12 period, which brought devastating floods to Queensland and New South Wales in particular. Across almost the entirety of Australia, maximum temperatures were warmer than average in 2013 (Fig. 12.1a), and for much of the continent, it was also considerably drier than average (Fig. 12.1b). The area of greatest rainfall deficit, covering inland eastern Australia, coincided with the region where the heat anomalies were strongest. Focusing on the

region of strongest 2013 maximum temperature and rainfall anomalies, an inverse relationship between maximum temperature and precipitation is found with 2013 being the hottest year and one of the driest (Fig. 12.1c). Similar temperature–rainfall relationships have previously been examined for the Murray–Darling Basin (Nicholls 2004) and multiple other regions of Australia (Karoly and Braganza 2005). A shift in the relationship between annual average daily maximum temperature and annual precipitation is observed through time (Fig. 12.1c). In the late 20th century and early 21st century, the temperature–rainfall relationship shifted towards warmer temperatures (an increase of roughly 1°C) associated with the same rainfall anomalies compared to the mid-20th century. This finding is insensitive to the choice of periods analyzed.

Given the relationship between heat and drought, this study examines first whether the risk of hot and dry years has increased due to human-induced climate change. Secondly, the role of the lack of precipitation in the 2013 record-breaking heat is analyzed and discussed.

Data and methods. Observations were obtained from the Australian Water Availability Project (AWAP; Jones et al. 2009) dataset interpolated onto a regular 0.5° grid. These were used to calculate annual anomalies of daily maximum temperature (Fig. 12.1a) and rainfall (Fig. 12.1b) relative to the 1971–2000 climatology, which encompasses both historical dry and wet periods. Anomalies were averaged over our investigation area (18°–30°S, 133°–147°E), which experienced the greatest anomalies in annual average daily maximum temperature and precipitation and covers an important area for agriculture in Australia. The temperature and rainfall anomalies were calculated at individual gridboxes relative to the gridbox mean values. The relationship between annual average daily maximum temperature and rainfall values was studied for the 1930–2013 period.

To examine possible human-induced contributions to the observed heat and drought of the 2013 calendar year, model simulations forced with anthropogenic greenhouse gases were required. Annual average daily maximum temperature and rainfall data derived from the output of single historical (1861–2005) and single RCP4.5 emissions scenario (2006–33) runs from 35 state-of-the-art Coupled Model Intercomparison Project Phase 5 (CMIP5) models were analyzed (see Supplementary Table S12.1; Taylor et al. 2012). The CMIP5 model

outputs were regridded onto a common 2.5° grid. Relationships between maximum temperature and rainfall were examined for a common 1861–2033 period. Combining these model simulations, probability distribution functions (PDFs) of annual average daily maximum temperature and rainfall were compared for two 41-year periods (1861–1901 and 1993–2033), with the latter period centered on 2013, to examine for changes in the risk of very hot or very dry years related to anthropogenic activity. The earlier 41-year period represents a climate with a much smaller influence from anthropogenic factors compared to now. The risk of very hot years occurring with respect to drought conditions was analyzed by considering PDFs of temperature anomalies in wet and dry years separately (where wet and dry years are defined as 33% above and below average annual rainfall respectively for the 1971–2000 period). This is based on the assumption that rainfall and moisture availability are driving temperature variations; although, undoubtedly, there is also a feedback on precipitation from temperature. Comparisons between PDFs were made by calculating the Kolmogorov–Smirnov (KS) test statistic measuring the similarity of the PDFs. Fractional attributable risk (FAR; Allen 2003) statistics may be used to examine whether the likelihood of extreme climate events has changed in relation to a particular aspect of interannual climate variability or anthropogenic warming. FAR statistics were calculated to measure change in likelihood of:

(a) very dry years between 1861–1901 and 1993–2033 (i.e., has anthropogenic activity changed the risk of meteorological drought?),

(b) very hot years between 1861–1901 and 1993–2033 (i.e., has anthropogenic activity changed the risk of extreme hot years?),

(c) the combination of very hot and very dry years between 1861–1901 and 1993–2033 (i.e., has anthropogenic activity changed the risk of very hot dry years?), and

(d) very hot years contrasting between wet and dry years (i.e., do drought conditions change the risk of extreme hot years?).

FAR statistics were calculated based on the 2013 value of rainfall (61% of average; the fifth lowest annual rainfall in the series) and the 2002 value of annual averaged daily maximum temperature (1.52°C above average; the second hottest value). Using the 2002 temperature threshold allows us to examine whether the risk of a hotter year than 2002 (such as 2013) has changed. Since 2013 was not the

driest year in the record, we use the 2013 threshold in our FAR calculations related to precipitation. The PDFs used to calculate the FAR statistics were bootstrapped 1000 times using subsamples of 50% of the models in each case. This allows a range of FAR statistics to be calculated, so uncertainty in the FAR can be assessed. The FAR statistics quoted represent the fifth percentile of the 1000 ranked FAR values calculated through bootstrapping (i.e., 95% of FAR

values are above the quoted value; we may therefore write that the FAR and risk are *extremely likely* to be greater than these stated values).

Note that we also performed this analysis for the shorter January–March and April–December periods to examine if there was a seasonal bias in our calendar year calculations. Generally, results were very similar, although slightly weaker, when considering the shorter periods.

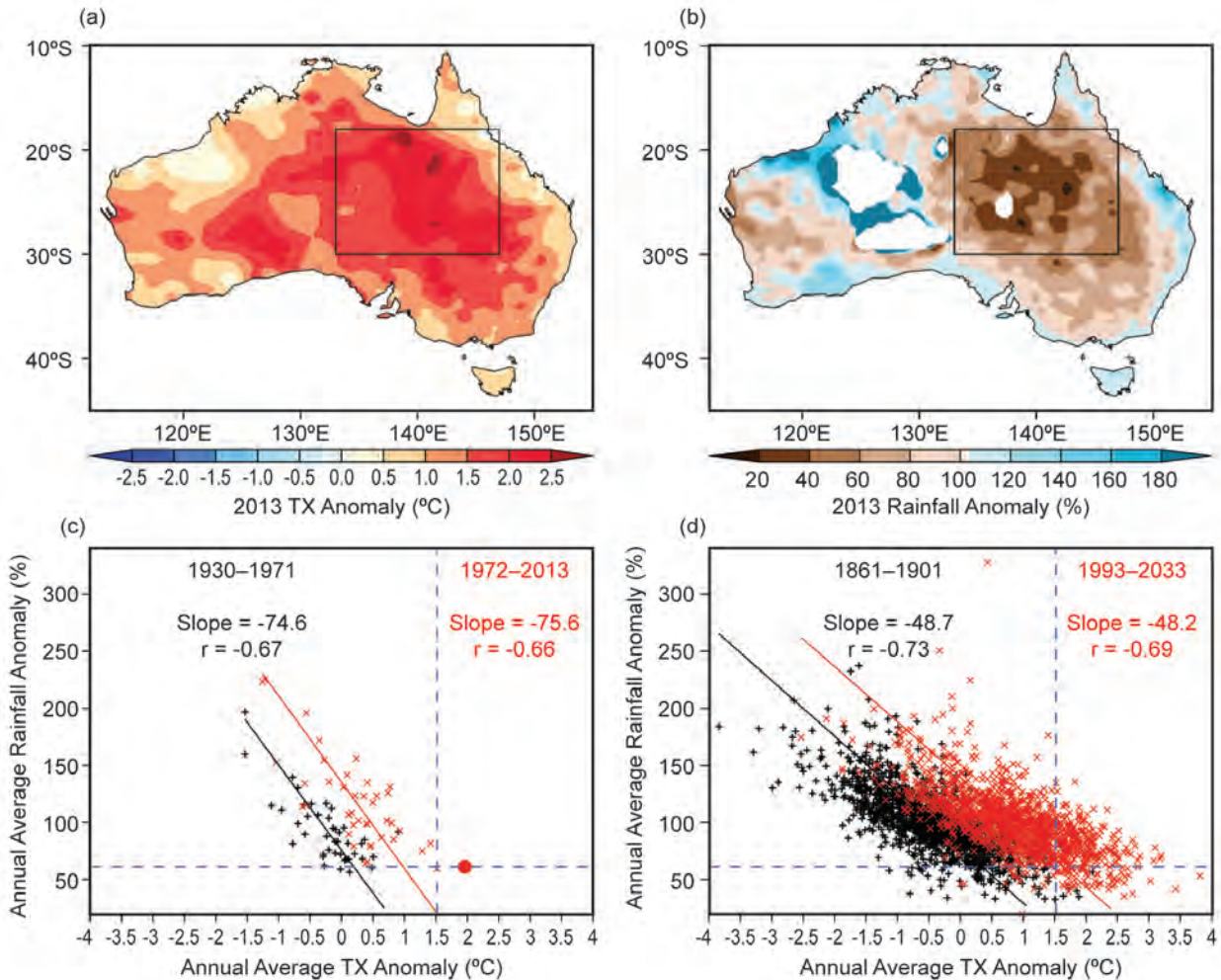


FIG. 12.1. (a) Anomaly of annual average daily maximum temperature (°C) in 2013 relative to the 1971–2000 climatological average. (b) Annual rainfall anomaly of 2013 as a percentage of the 1971–2000 climatological average. Data is incomplete in the unfilled areas. The box marks the region of study for our attribution analysis. (c) Relationship between annual average daily maximum temperature and rainfall anomalies for the investigation area of eastern Australia during 1930–71 (black crosses) and 1972–2013 (red crosses) separately. The large red circle represents 2013. Total least squares regression fits and rank correlations are displayed for 1930–71 and 1972–2013. (d) Relationship in 35 CMIP5 models between annual average daily maximum temperature and rainfall anomalies for eastern Australia investigation area during 1861–1901 (black crosses) and 1993–2033 (red crosses) separately. Total least squares regression fits and rank correlations are displayed for 1861–1901 and 1993–2033. The blue dashed lines in (c) and (d) show maximum temperature and rainfall anomalies used for FAR analyses.

Results. The relationships between annual average daily maximum temperature and annual rainfall were examined in each CMIP5 model separately. All models exhibit strong, statistically significant inverse relationships between maximum temperature and rainfall over the 1861–2033 period. Additionally, there is a shift in this relationship in the models towards warmer temperatures, similar to that which is observed. Later on in the period, the same rainfall totals are associated with warmer temperatures in comparison to the earlier period. The models display a variety of different strengths in the temperature-rainfall relationship; however, the inverse nature of the relationship is captured by every model. The shifting relationship from 1861–1901 to 1993–2033 was also evident when all the model data are plotted together (Fig. 12.1d).

Has anthropogenic activity changed the risk of drought? Using these model data, the change in precipitation between the early and late 41-year periods was investigated. Using a KS test, the PDFs of rainfall in the 1861–1901 and 1993–2033 periods are statistically indistinguishable at the 5% level (Supplementary Fig. S12.1). The risk of a drought worse than the 2013 event is also not significantly different between the two periods (the range of FAR values encompasses zero). Therefore, there has been no significant change in meteorological droughts in this region related to anthropogenic climate change, as simulated by the CMIP5 models. However, in a warming climate, with increasing evaporation and reduced soil moisture, droughts may become more severe (e.g., Seneviratne et al. 2010).

Has anthropogenic activity changed the risk of extreme hot years? The change in average daily maximum temperatures was also examined for the same early and late 41-year periods. The PDFs of maximum temperature for 1861–1901 and 1993–2033 are significantly different (Fig. 12.2a). The FAR value, based on the 2002 threshold, is *extremely likely* to be above 0.96. Thus, the risk of maximum temperatures above the 2002 threshold is *extremely likely* to be 23 times greater now than in the late 19th century. Large increases in the likelihood of extremely hot seasons and years across Australia related to human-induced climate change have been documented previously (Lewis and Karoly 2013).

Has anthropogenic activity changed the combined risk of hot years and dry years? A more interesting question is

to assess whether the risk of extreme heat and drought in combination has increased due to anthropogenic climate change. Therefore, a bivariate FAR analysis was conducted using the same precipitation and maximum temperature thresholds as for the previous univariate FAR analyses. We calculate that the bivariate FAR is extremely likely to be above 0.86. Therefore, between the 1861–1901 and 1993–2033 periods, the risk of extreme heat and drought in combination is extremely likely to have increased by at least seven-fold.

Do drought conditions change the risk of hot years?

The difference in the risk of extreme heat related to whether a year is particularly wet or dry was analyzed. PDFs of annual average daily maximum temperatures were compiled for wet and dry years separately (Fig. 12.2b). These PDFs are also significantly different. The FAR value is extremely likely to be greater than 0.96 and the risk of extreme heat is extremely likely to be 25 times greater in dry years than in wet years. Thus, the heat of 2013 in this region of Australia was strongly related to the lack of rainfall.

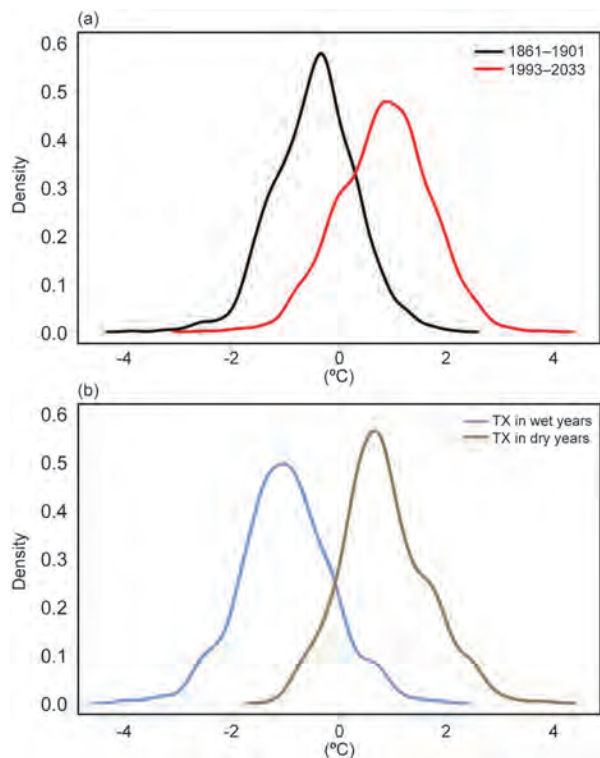


FIG. 12.2. Probability density functions of (a) annual average daily maximum temperature anomalies in model years representing 1861–1901 (black curve) and 1993–2033 (red curve), and (b) annual average daily maximum temperature anomalies in wet (blue curve) and dry (brown curve) model years.

Conclusions. In 2013, much of Australia experienced extreme heat and drought. Using state-of-the-art climate models, this study examines the role of climate change in the heat and drought as well as the relationship between heat and lack of rainfall. We show that the extreme heat was made much more likely by

important contributions from *both* the anthropogenic warming of the climate and the very dry conditions over the inland eastern region of the continent. The combination of these factors increased the probability of 2013 being Australia's hottest year on record.

13. THE ROLE OF ANTHROPOGENIC CLIMATE CHANGE IN THE 2013 DROUGHT OVER NORTH ISLAND, NEW ZEALAND

LUKE HARRINGTON, SUZANNE ROSIER, SAM M. DEAN, STEPHEN STUART, AND ALICE SCAHILL

For the 2013 New Zealand drought, evidence from a number of models suggests that the meteorological drivers were more favorable for drought as a result of anthropogenic climate change.

Introduction. In the latter part of the 2012/13 austral summer season (January–March), the North Island of New Zealand endured its most severe drought in 41 years of widespread measurements of potential evapotranspiration deficit (Porteous and Mullan 2013). For the 2013 drought, 34.2% of the North Island land surface experienced its highest recorded cumulative deficits (Supplementary Fig. S13.1), significantly greater than the 14.3% recorded for the previously severest drought (1997/98). The New Zealand Treasury (2013) estimates reduced agricultural production, attributed to the drought, cost the national economy at least US\$1.3 billion, with continued impacts expected for another two years (Blackham 2013).

Droughts are complex hydrologic phenomena subject to influence by numerous climatological factors, including temperature, wind speed, atmospheric humidity, and precipitation rates (Sheffield et al. 2012; Trenberth et al. 2014). The persistent dryness of the 2013 New Zealand drought has been suggested to be primarily a result of slow-moving (“blocking”) anticyclones over the sector, unrelated to the El Niño–Southern Oscillation (Blackham 2013), with the increase in atmospheric subsidence suppressing precipitation. If true, the meteorological drivers of this drought might, therefore, be characterized using mean sea level pressure (MSLP) and a measure of the absence of precipitation. Using such metrics, the North Island drought was associated with an average February MSLP of 1020 hPa (90th percentile) and a

record total number of dry days of 78.2 for January to March.

Was this event influenced by climate change? Previous studies concerning the attribution of individual drought events to (anthropogenic) climate change have primarily focused on precipitation departures (Rupp et al. 2013; Trigo et al. 2013) and prolonged temperature extremes (Rupp et al. 2012; Hoerling et al. 2013). For a maritime, midlatitude climate like New Zealand's, temperature is not reflective of synoptic-scale drying and, thus, does not perform well as an indicator of drought (Clark et al. 2011; Senviratne 2012). Furthermore, analysis of precipitation rates considers atmospheric processes that operate on small spatial scales and can be poorly constrained in climate models (Trenberth 2011), thereby also failing to capture the synoptic-scale drivers of drought (Sherwood and Fu 2014).

To consider the drought in New Zealand we limit ourselves to the North Island, where extreme drought was ubiquitous, and consider only the distributions for monthly MSLP and dry days per month produced by models that participated in the Coupled Model Intercomparison Project phase 5 (CMIP5; Taylor et al. 2012). Those models for which historical simulations compare well against observations are then quantitatively compared to simulations, which excluded the impact of anthropogenic changes such as greenhouse gases and ozone depletion.

Defining circulation and dryness indices. The North Island pressure index (NIPI) is defined as the average of the monthly MSLP observed at four locations across the North Island, corresponding to weather stations at Auckland, Gisborne, New Plymouth, and Wellington (Supplementary Fig. S13.1). Because the gradients associated with high pressure systems are weak, these stations are spatially representative of the island, and their records are also of sufficient length, with the shortest starting in 1911. Analysis of the NIPI can be used to evaluate systematic changes to atmospheric circulation over the North Island.

In addition to the NIPI, changes in the intensity and frequency of broad-scale subsidence over the North Island sector are evaluated with dry day analysis, defined as less than one millimeter of rain accumulation over a 24-hour period (WMO 2010). Gridded rainfall measurements of daily resolution were available from 1960 to 2013, with individual data points assimilated across the North Island using a spline interpolation technique (Tait et al. 2006).

Can global climate models simulate NZ drought? To determine which global climate models from the CMIP5 archive are reasonable at replicating the two New Zealand drought indices, a validation methodology was applied. Only data from models that contributed to both the historical and natural-forcings only experiments and provided the variables needed for the indices were considered. Gridded data from each model were linearly interpolated onto a $1^\circ \times 1^\circ$ ERA-Interim grid (Dee et al. 2011). If the median of the observed data lay outside the interquartile range of a simulation, that model was excluded from subsequent analysis.

In Fig. 13.1a, the NIPI is compared to observations for 17 different global climate models between 1952 and 2005. Figure 13.1b compares the statistical distribution for the maximum three-month accumulation of dry days (3MDD) in

each extended austral summer (November–April) for 15 climate models between 1952 and 2005. This time span of 54 years is determined by the availability of daily gridded rainfall observations from 1960 to 2013 only. In total, 13 models were deemed appropriate for pressure analysis, while five models were suitable for analysis of extreme dry day totals. It has been verified that the selection of models for 3MDD is unaffected by restricting the comparison to the 45 years of actual overlap from 1960 to 2005 (Supplementary Fig. S13.2).

Is there evidence from global climate models that the North Island drought was influenced by anthropogenic climate change? Figure 13.2a shows the shift in NIPI

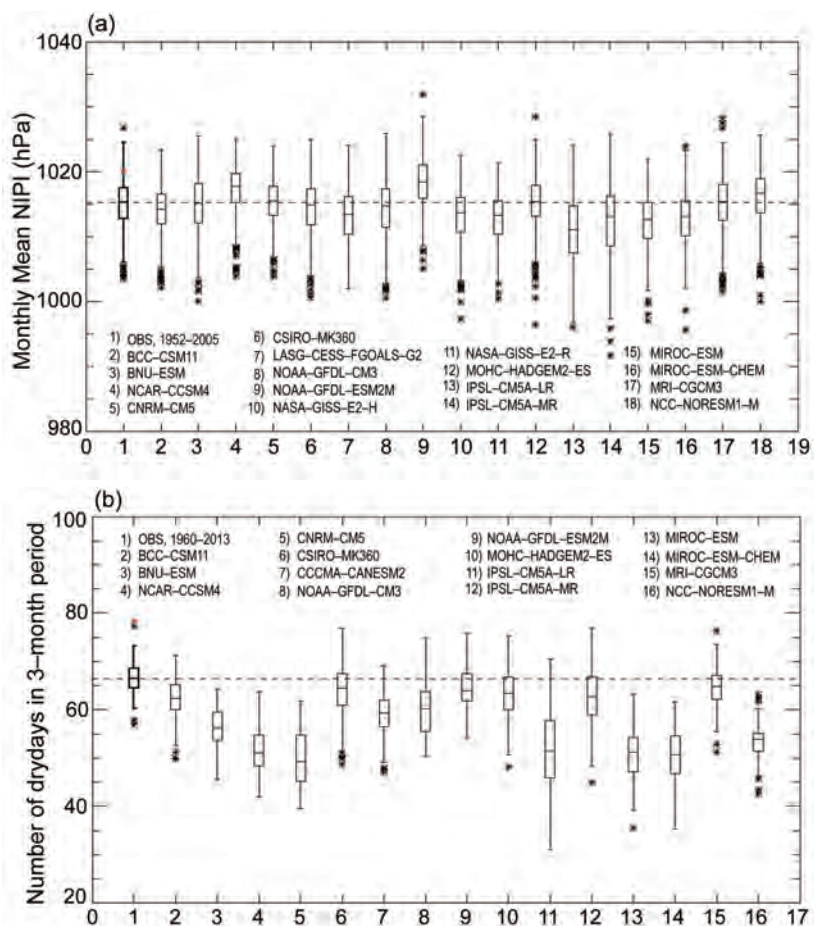


FIG. 13.1. (a) Box plot comparing the observed NIPI distribution (bold) to 17 CMIP5 models, between 1952 and 2005. Each box indicates the median and first and third quartiles, while the whiskers extend to the last values that are 1.5 times the inter-quartile range above or below the quartiles. Models that have an interquartile range outside the median of the observed data (black dashed line) were excluded from subsequent analysis. The red asterisk marks the 2013 drought event. **(b)** Same as in (a), but comparing ended summer three-month dry day (3MDD) maxima over the North Island from 1960 to 2013 with 54 years of model data (1952–2005) for 15 CMIP5 models.

for 13 CMIP5 members (1952–2005), comparing model simulations with all anthropogenic forcings (ALL) to each corresponding run with natural forcings only (NAT). At the observed value for the peak of the 2013 drought, 9 of the 13 models exhibit a shift towards higher NIPI values when anthropogenic emissions are included. The average human-induced shift at the 2013 observation is an increase of 0.39 hPa (significantly different from zero at the 95% confidence level of an applied Student's *t*-test), with a range of -0.24 hPa to 1.09 hPa. Most models in Fig. 13.2a with a NIPI change above zero remain at either a stable or increasing value towards the high-pressure distribution tail.

Figure 13.2b similarly shows the absolute change in the 3MDD summer maxima for model simulations spanning 1952–2005, again comparing the ALL forcing runs to corresponding NAT simulations. Here there are 14 simulations from five different models. The observed 3MDD total for January–March 2013 over the North Island was high enough that no simulation emulated the event over the 54-year period. This may be due in part to a persistent low bias in the dry day distribution common to all models. Regardless, models do demonstrate an anthropogenic-induced shift towards an increased frequency of three-month periods with extreme dry day totals. For example, taking the 90th percentile of observed 3MDD summer maxima as an arbitrary threshold for a drought event, there were 31 simulated extreme events for ALL ensemble members compared to only 18 for the NAT—a 72% increase. At this threshold, there is an average increase in the number of dry days over a three month period of 1.6 (significantly different from zero at the 95% confidence level).

Discussion. Our results are consistent with the broad-scale dynamical changes to the New Zealand sector expected with anthropogenic climate change. A clear poleward shift of the Southern Hemisphere jet stream has been observed for December–February in reanalyses (Swart and Fyfe 2012), with an associated increase in surface pressure over New Zealand (Thompson et al. 2011). This is attributed largely to a trend in the southern annular mode (SAM) driven by ozone depletion

(Thompson et al. 2011). For the three months of January to March 2013, the station-based Marshall Index for the SAM was strongly positive, averaging 1.95. The February value of the SAM index was 2.84, the highest ever for that month. Given that the NIPI index was only at the 90th percentile for this month and lower for the other two, it seems that high pressure induced by the SAM over New Zealand is not a complete explanation for the extreme dryness that occurred. There has also

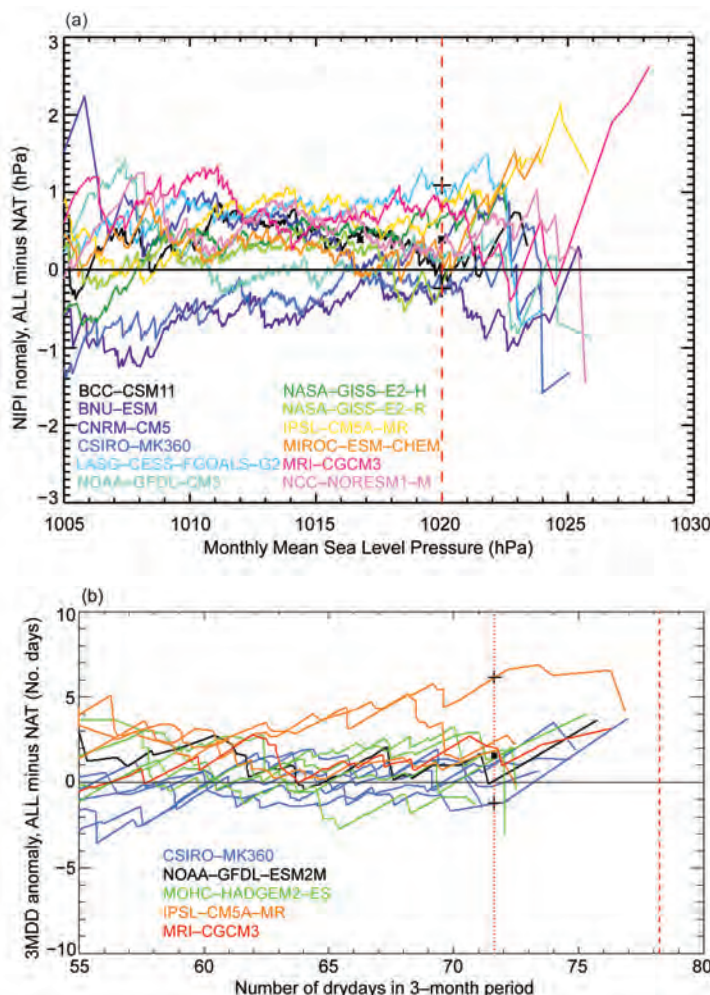


FIG. 13.2. (a) Absolute change in monthly NIPI (hPa), ALL forcings minus NAT, for 13 CMIP5 models between 1952 and 2005. Dashed red line indicates the observed NIPI for Feb 2013—at this point, black cross and black lines indicate, respectively, the mean and range of NIPI anomalies from all models. (b) Absolute shift in 3MDD summer maxima for ALL simulations minus NAT, for 14 simulations of 5 CMIP5 models spanning the period 1952–2005. The red dashed line represents the peak number of dry days in a 3-month period (JFM) for the 2013 New Zealand drought event (78.2). Red dotted line indicates the 90th percentile of observations (71.3)—at this point, black cross and black lines indicate, respectively, the mean and range of 3MDD anomalies from all ensemble members.

been an observed trend towards less precipitation over some midlatitude regions, attributed to the combined effects of anthropogenic greenhouse gases and ozone depletion (Fyfe et al. 2012). It is plausible that these trends in circulation and precipitation conditions have made severe drought more likely.

For the models used in our dry days analysis, we find a strong ($R = 0.95$) positive correlation between the mean shift in NIPI and the corresponding shift in mean number of monthly dry days (Supplementary Fig. S13.3). This indicates that a change in the number of dry days in the models is related to higher pressure over the North Island, with increased subsidence suppressing rainfall. Thus, the models suggest that the anthropogenic contribution to the 2013 drought was mostly through changes in circulation. Since it is also clear that the causes of the 2013 North Island drought were not simply higher pressures, natural internal variability must have played a role in the extremeness of this event.

It is also important to emphasize that quantifying properties of synoptic-scale circulation change over the North Island sector provides only partial understanding of the physical mechanisms contributing to drought formation there; spatial heterogeneity in soil type and topography represent complicating factors (Dai 2011; Seneviratne 2012). There are inherent limi-

tations with only considering 54 years of observations and a limited number of simulations. Future work using a much larger ensemble of simulations, such as the *weather@home* project (Massey et al. 2014), remains critical for more robust attribution statements about changing drought risk.

Conclusions. Results show the monthly pressure anomalies associated with the 2013 drought were higher (0.4 hPa on average) as a result of anthropogenic climate change. No model was able to capture the extremity of the three-month dry day index, likely a combination of bias in the models and the severity of the event relative to the size of the model ensemble. However, using the observed 90th percentile of the dry day index as an (arbitrary) threshold for drought, a 72% increase in the number of events was found, which does suggest a change in drought risk. The human-induced shift in monthly dry days and MSLP were found to be very well correlated ($R = 0.95$), underlining that, in these models, the human-induced contribution to drought over New Zealand occurs through increased high pressure. Since the 2013 drought was not associated with extreme high pressures, natural internal variability in the climate system must have played a role in the underlying causes of its severity.

14. ASSESSING HUMAN CONTRIBUTION TO THE SUMMER 2013 KOREAN HEAT WAVE

SEUNG-KI MIN, YEON-HEE KIM, MAENG-KI KIM, AND CHANGYONG PARK

A comparison of observations and multiple global climate model simulations indicates that extreme hot summer temperatures in Korea have become 10 times more likely due to human influence.

Introduction. East Asia, including Korea, experienced one of its hottest summers in 2013, resulting in severe damage to society and the ecosystems across the region. During summer (June–August, JJA) 2013, South Korea had its hottest summer nights and second hottest summer days since 1954 (Fig. 14.1). The JJA average daily minimum temperature (T_{min}) was 22.7°C (2.2°C warmer than the 1971–2000 climatology), and the average daily maximum temperature (T_{max}) reached 29.9°C (1.9°C warmer than the climatology). New high JJA temperature records have

exerted adverse impacts on the country's economy, health, and infrastructure. In particular, the heat wave increased electricity consumption beyond the forecast level and forced the government to issue several power shortage warnings. In addition to these 2013 extreme events, summer temperatures have been consistently increasing during the past 60 years with statistically significant trends in T_{min} and daily mean temperature (T_{mean} ; Fig. 14.1c).

Here, we assess the Korean heat wave in the context of global warming using recent climate model

datasets available from the Coupled Model Intercomparison Project Phase 5 (CMIP5; Taylor et al. 2012) experiments. Because global climate models (GCMs) like CMIP5 models generally have relatively low horizontal resolutions (typically about 100–200 km), they cannot reproduce the spatiotemporal details of local climate variability and change. Therefore, it would be inappropriate to directly compare raw GCM outputs with station-based observations without utilizing proper downscaling processes. Alternatively, large-scale patterns, very strongly associated with local changes, can be identified, and observed changes in those large-scale patterns can then be compared with model simulations. Despite unavoidable subjectivity in selecting the number of large-scale patterns, variables, and spatial domains, this up-scaling approach can enable causes of local observed changes to be assessed in view of large-scale modeled responses to different external forcing factors, such as greenhouse gas increases. Employing methods similar to multistep attribution approaches (Bindoff et al. 2014), this study analyzes the hot 2013 summer observed in Korea in the context of greenhouse warming.

Data and methods. We use T_{min} , T_{max} , and T_{mean} observations from 12 Korean weather stations for 1954–2013 (from 59 stations for 1973–2013). Monthly SST data from the Extended Reconstruction Sea Surface Temperature (ERSST) version 3 (Smith et al. 2008) dataset are used to find a large-scale SST indicator of Korean summer temperatures. The analysis domain is 15°–50°N and 100°–160°E, where SST exhibits the strongest association with the Korean temperature ($r^2 > 70\%$). For model simulations, we use multimodel datasets available from CMIP5 experiments (see Supplementary Table S14.1) to assess human influence on the observed changes in the large-scale SST pattern. We use the “historical” experiment integrated with natural (due to changes in solar and volcanic activities) and anthropogenic

forcings (due mainly to increases in greenhouse gases and aerosols). We divide it into two 60-year periods, 1860–1919 (ALL_P0) and 1954–2013 (ALL_P1), representing climate conditions without and with human influence respectively. We also use datasets from the “historicalGHG” (greenhouse gas only forcing) and “historicalNat” (natural forcing only) experiments for 1953–2012 to examine the relative contribution of individual forcings (see the Supplementary Material for more details).

To identify a large-scale SST indicator for Korean heat waves in general, we first look for a SST spatial pattern related to the Korean hot summers by regressing SST onto Korean JJA T_{min} using observations from 1954–2013. Here we use T_{min} , which generally better captures Korean heat waves with stronger and more spatially consistent increases (Fig. 14.1; see also Supplementary Fig. S14.1). We then project the observed SST regression field onto the observed JJA SST and also the CMIP5 simulations (referred to as

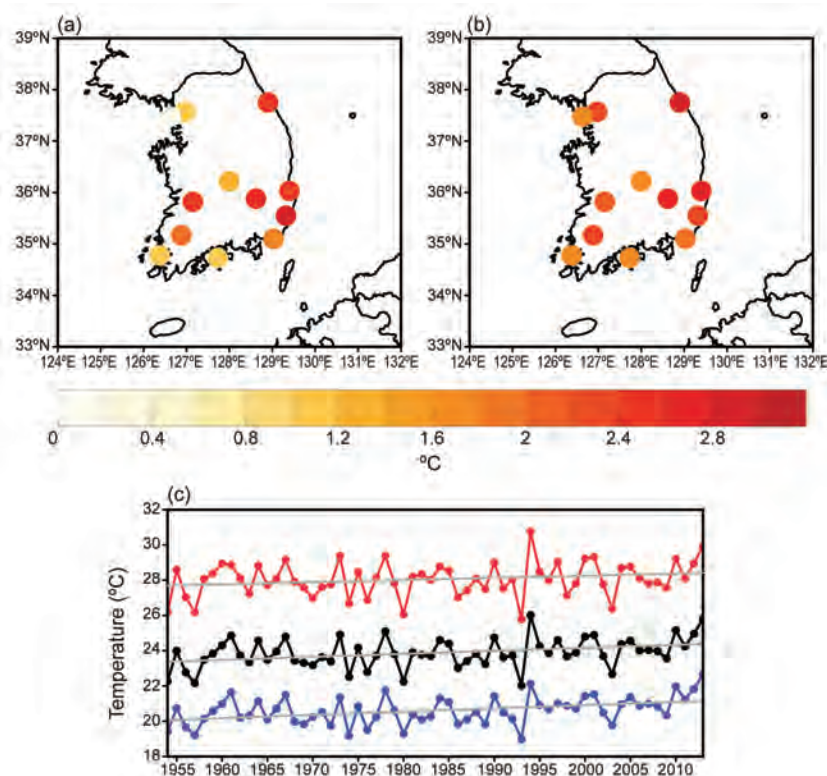


FIG. 14.1. (a) Distribution of JJA 2013 mean daily maximum temperature anomalies observed at 12 South Korean stations. Anomalies are with respect to 1971–2000 mean. (b) Same as (a) but for daily minimum temperature. (c) Time series of JJA mean daily maximum (T_{max} , red), mean (T_{mean} , black), minimum (T_{min} , blue) temperatures averaged over 12 stations. Gray straight lines represent linear trends. Warming trends in T_{min} ($0.18^{\circ}\text{C decade}^{-1}$) and T_{mean} ($0.17^{\circ}\text{C decade}^{-1}$) are statistically significant at the 5% significance level based on the Mann–Kendall test.

“observed projection” and “modeled projection” respectively) for the entire analysis period. The time series of projections represent temporal variations of SST spatial patterns associated with the Korean heat wave (see the Supplementary Material for further details).

By comparing the observed projection with the modeled projections, an attribution analysis of the Korean heat waves can be carried out. To estimate anthropogenic influence in a quantitative manner, we employ the fraction of attributable risk (FAR; Stott et al. 2004) approach in which the probability of extreme events occurring is compared in two hypothetical worlds, without and with human influences. Here, FAR is calculated as $FAR = 1 - (P_N/P_A)$. P_N represents the probability that extremes will occur exceeding the observed strength (trends in SST projection or 2013 projection value) in natural unforced conditions (ALL_P0 or NAT_P1), and P_A represents the same probability estimated in anthropogenic forced conditions (ALL_P1 or GHG_P1). If FAR is 0.5 and 0.67, for example, it means doubled and tripled risk of extreme events due to human influences respectively.

Results. The SST pattern associated with heat waves in Korea is anomalously warm over northern East Asia, north of 30°N, with a maximum over the East Sea (Sea of Japan; Fig. 14.2a). The time series of the observed projection is shown in Fig. 14.2b. The correlation coefficient between Korean T_{min} and the SST projection is 0.79, indicating that this SST projection explains most fluctuations in Korean summer temperature. In-

deed, the observed projection has a record high in 2013 with a value of 82.3 (°C² °C⁻¹). Modeled projection results are illustrated in the same plot for ALL_P0 (blue), ALL_P1 (green), GHG_P1 (red), and NAT_P1 (purple). ALL_P1 reproduces the observed change with very similar trends (Fig. 14.2c). The amplitude of interannual variability is also well simulated by models (The standard deviation of observed de-trended projection series is 36.5. The multimodel mean of standard deviations of the de-trended ALL_P1 series is 39.2 with a 5th–95th percentile range of 27.9–53.0). Trends in ALL_P0 and NAT_P1 are very weak while GHG_P1 possesses stronger positive trends. This implies a

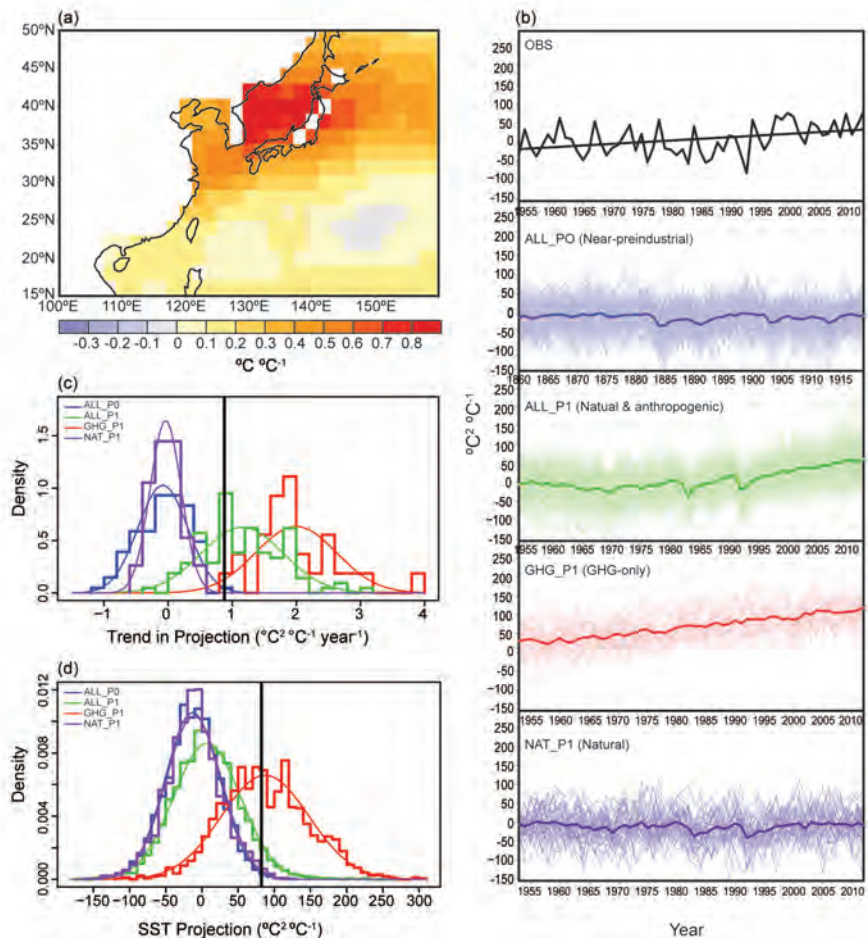


FIG. 14.2. (a) SST pattern regressed onto Korean JJA mean daily minimum temperature. (b) Time series of SST projection from observation, ALL_P0, ALL_P1, GHG_P1, and NAT_P1. The SST projection is an area-weighted sum of the regression coefficient (°C °C⁻¹) multiplied by the SST anomaly (°C), which results in a unit of °C² °C⁻¹. The black straight line represents the observed linear trend. Thick colored lines indicate the ensemble mean of each experiment. (c) Normalized histogram for the trend in SST projection from ALL_P0, ALL_P1, GHG_P1, and NAT_P1 in comparison with the observed trend (vertical black line). (d) Same as (c) but for SST projection values from models and the observed projection value in 2013.

dominant contribution of greenhouse warming to the ALL_P1 trend given overall long-term cooling due to other anthropogenic forcings (see Supplementary Material).

The histogram of trends in observed and modeled projections is compared in Fig. 14.2c. The distributions of ALL_P0 and NAT_P1 trends are centered near zero whereas all runs of GHG_P1 have positive trends, consistent with the time series. The observed trend is positioned near the center of the ALL_P1 distribution, indicating that the observed increasing trend in SST projection, which represents long-term warming of the ocean surface over northern East Asia and the associated intensification of the Korean heat wave, is attributable to natural and anthropogenic forcing. In the FAR analysis (Table 14.1), the trends in SST projection exceeding the observed trend ($0.88 \text{ }^\circ\text{C}^2 \text{ }^\circ\text{C}^{-1} \text{ yr}^{-1}$) are very rarely simulated in ALL_P0 (0.98% probability) and NAT_P1 (0%). However, they are simulated much more frequently in the other model experiments that include anthropogenic forcing (63.8% and 100% probability in ALL_P1 and GHG_P1, respectively). The corresponding FAR values of ALL_P1 and GHG_P1 relative to ALL_P0 (or NAT_P1) are very close to 1, confirming the qualitative comparisons.

Attribution analysis of the 2013 summer event can be done in a similar way. The distributions of all modeled projection values are compared in Fig. 14.2d together with the observed 2013 value. SST projections stronger than the observed 2013 event are extremely rare in ALL_P0 (0.54%) and NAT_P1 (0.88%). The chance of 2013-like extreme events increases to 5.28% and 51.05% in ALL_P1 and GHG_P1, respectively. The corresponding FAR values with respect to ALL_P0 are 0.90 and 0.99. Considering large variability on interannual time scales, this provides very strong evidence that the

risk of extremely hot summers in Korea associated with SST warming is 10 times more likely due to human influence.

Conclusions. This study assesses the possible impacts of greenhouse gas increases on the observed long-term increases in Korean summer temperatures as well as on the 2013 extreme event. A large-scale SST indicator of the Korean summer temperature is identified from observations and then the observed occurrences of the SST patterns are compared with those from CMIP5 model simulations representing climate conditions with and without human influences. We find that a strong long-term increasing trend in the observed SST near northern East Asia during the past 60 years cannot be explained without the inclusion of recent human-induced greenhouse gas forcing. This is because other external forcings, including solar and volcanic activities (natural) and aerosols (anthropogenic), are likely to induce cooling during the latter 20th century (see Supplementary Material). Further, it is implied that extreme hot summers like the 2013 event have become 10 times more probable due to human activities. Our results indicate greenhouse warming contributes significantly to recent warming trends in Korean summer temperature. Although statistical analysis presents strong evidence for human influence, further studies are needed to better understand the physical mechanisms accounting for the large-scale SST indicator. A simple correlation analysis suggests that there may be a weak but statistically significant influence of the Pacific decadal oscillation on Korean summer temperature ($r = -0.37$; Kim et al. 2008) while weaker connections exist with the Pacific–Japan pattern ($r = 0.26$; Wakabayashi and Kawamura 2004) and the western North Pacific subtropical high ($r = -0.11$; Wang et al. 2013).

Table 14.1. Probability of occurrence exceeding the observed trend in SST projection and the observed 2013 projection value. The fraction of attributable risk is calculated as $\text{FAR}_{\text{ALL_P1}} = 1 - P_{\text{ALL_P0}}/P_{\text{ALL_P1}}$ and $\text{FAR}_{\text{GHG_P1}} = 1 - P_{\text{ALL_P0}}/P_{\text{GHG_P1}}$.				
	Obs	ALL_P0	ALL_P1	GHG_P1
Trend in projection (60 years)	0.88 ($^\circ\text{C}^2 \text{ }^\circ\text{C}^{-1} \text{ yr}^{-1}$)	0.98%	63.8% FAR \approx 1	100% FAR \approx 1
2013 summer in SST projection	82.27 ($^\circ\text{C}^2 \text{ }^\circ\text{C}^{-1}$)	0.54%	5.28% FAR = 0.90	51.05% FAR = 0.99

15. THE CONTRIBUTION OF ANTHROPOGENIC FORCING TO THE JAPANESE HEAT WAVES OF 2013

YUKIKO IMADA, HIDEO SHIOGAMA, MASAHIRO WATANABE, MASATO MORI,
MASAYOSHI ISHII, AND MASAHIDE KIMOTO

Anthropogenic climate change played a significant role in increasing the probability of events such as the heat wave in Japan in 2013.

Introduction. During the boreal summer of 2013, Japan experienced extraordinarily high temperatures: record-breaking daily maximum temperatures at 143 sites in the west of the country. Daily mean surface air temperature (SAT) was 1.2°C warmer than normal on average in July and August in western Japan, which was above the 90th percentile for the reference period of 1979–2012.

This heat wave was characterized by the intensification of both the Pacific high and the Tibetan high. Figure 15.1 shows observed anomalies of surface temperature, circulation, and convective activity from July to August 2013. Active convective heating, as indicated by negative anomalies in outgoing longwave radiation, was observed in the Maritime Continent and Southeast Asia (shaded areas in Fig. 15.1b) associated with La Niña-like conditions during this season (Fig. 15.1a). In the upper levels, a divergence flow from the active convective regions converged and descended north and east of the Philippines (arrows in Fig. 15.1b), which intensified the Pacific high (black contours in Fig. 15.1b). Furthermore, the active Asian monsoon resulted in the intensification of the Tibetan high (gray contours in Fig. 15.1b), which extended eastward in the upper troposphere. This double structure of high pressure systems brought a warmer SAT and SST around Japan (Fig. 15.1a).

Although most extreme heat waves might have occurred as part of stochastic atmospheric fluctuations, anthropogenic global warming has the potential to impact the probability of their occurrence (Allen 2003; Stott et al. 2004). In this study, we generated a large ensemble using an atmospheric gen-

eral circulation model (AGCM) under two specific boundary conditions for July and August 2013. We

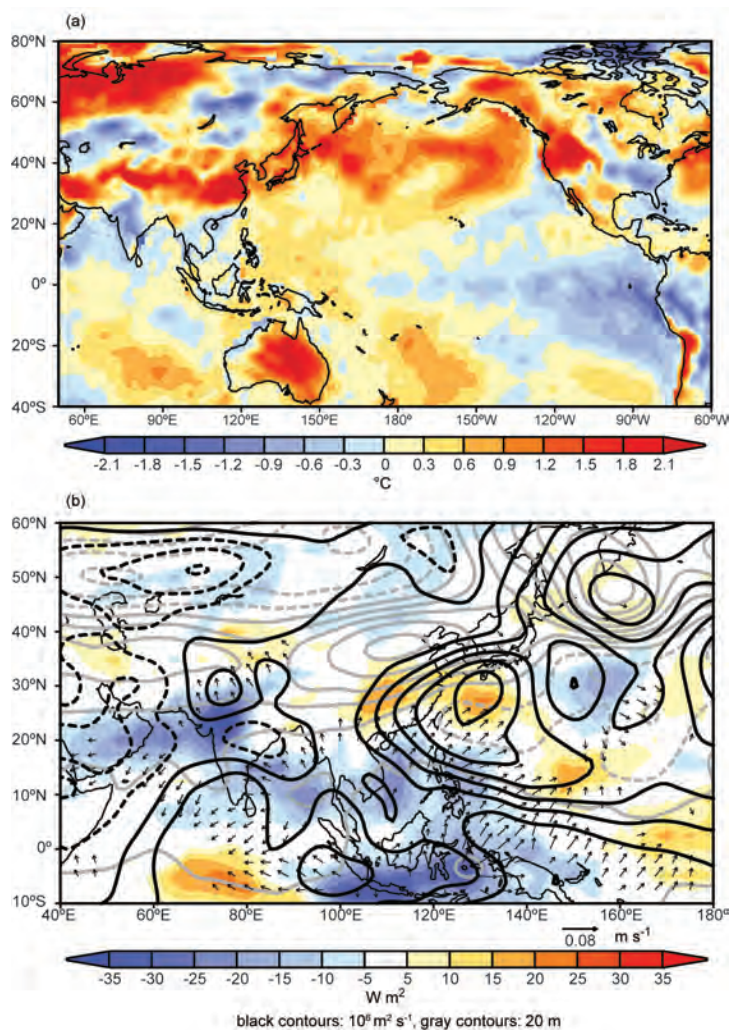


FIG. 15.1. (a) SAT (land) and SST (ocean) anomaly from July to August in 2013 shown by JRA-25 reanalysis (°C). (b) Same as (a) but for outgoing longwave radiation (W m^{-2} , shading), 850-hPa stream function (black contours, $10^6 \text{ m}^2 \text{ s}^{-1}$ interval), 200-hPa geopotential height (gray contours, 20-m interval), and 200-hPa divergence flow (m s^{-1} , arrows).

prepared two scenarios for the boundary conditions: observed conditions for a real-world experiment and those without human-induced long-term changes for an idealized counterfactual experiment. This methodology was first proposed by Pall et al. (2011). We evaluated the probabilistic difference in event occurrence rates due to the contribution of anthropogenic effect through analysis of the sets of AGCM ensemble experiments.

Method. We conducted a 100-member AGCM ensemble experiment (factual run, called the ALL-run) using an atmospheric component model of the Model for Interdisciplinary Research on Climate Version 5 (MIROC5, T85L40; Watanabe et al. 2010). The model was integrated with observed SST and sea ice under the anthropogenic external conditions during the period of the 2013 heat waves. Another 100-member ensemble was constructed under anthropogenic forcing fixed at conditions of the year 1850, with modified SST and sea ice where possible human-induced components were removed (counterfactual run under natural external conditions, called the NAT-run; see Shiogama et al. 2013 for details). We removed two possible patterns of human-induced changes in SST and sea ice: a linear trend based on Hadley Centre sea ice and SST version 1 (HadISST; Rayner et al. 2003) from 1870 to 2012 (NAT1; Christidis and Stott 2014) and changes detected from the multimodel mean of Coupled Model Intercomparison Project phase 5 (CMIP5) historical experiments (NAT2; Daithi 2013). To validate the model's reproducibility of interannual variability, a long-term version of the ALL-run (1949–2011) was replicated with a reduced ensemble size of 10 (ALL-LNG run).

We defined a Japanese SAT index (SATJ index) as SAT averaged from July to August over the land area of western Japan (130°–140°E, 30°–37°N) following the model geography. An ensemble-mean

SATJ time series simulated by the ALL-LNG run reproduces the observed interannual variability with a correlation coefficient of 0.79 from 1979 to 2011, although the model underestimates its variance. In the following analyses of a probability density function (PDF), a Gaussian distribution is assumed and simulated variances in the ALL-run and NAT-runs are corrected with a ratio of variances between the observations (JRA25 reanalysis; Onogi et al. 2007) and the ALL-LNG run.

Results. A PDF for the SATJ index from the ALL-run is shown in Fig. 15.2a (red curve). The ensemble mean of the ALL-run indicated warmer-than-normal conditions in 2013, mainly due to the higher SST around Japan that was given to the model as a boundary condition. Of importance is the fact that the ensemble members are well spread out, covering an observed anomaly of 1.2°C (triangle in Fig. 15.2a). Several heat waves that appeared in the ALL-run (one example of such an extreme case is shown in Supplementary Fig. S15.1) represent the double structure of the intensified Pacific high and Tibetan high associated with the active convection in the western tropical Pacific and in the Asia monsoon regions, akin to observed anomalies.

When the possible anthropogenic components are removed from the boundary conditions, the PDF for the SATJ index shifts toward a normal condition (blue curves in Fig. 15.2a). The difference between the ALL-run and either NAT1 or NAT2 signifies the anthropogenic impact on the occurrence rate of the

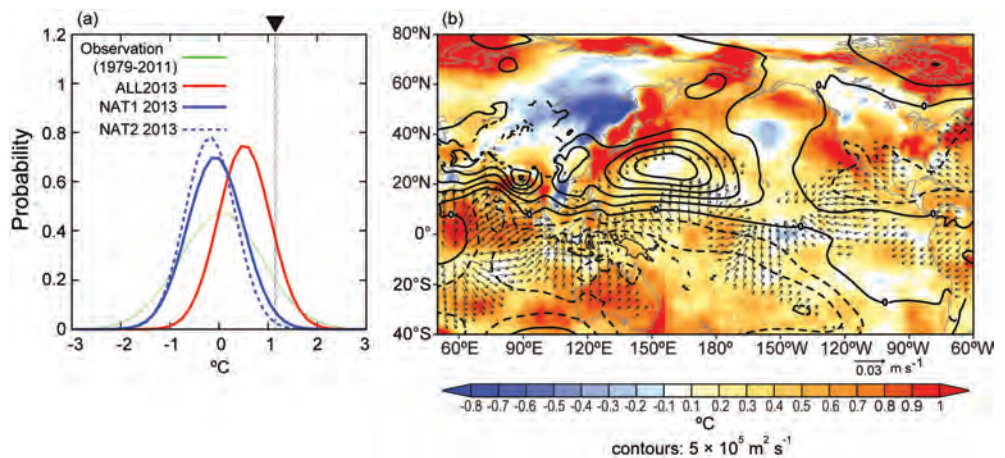


FIG. 15.2. (a) PDF (curve) for the SATJ index: 100-member ALL (red), NAT1 (blue solid), and NAT2 (blue dashed) runs for July–August 2013. For reference, 1979–2011 anomalies based on JRA-25 reanalysis are shown by a green curve. A triangle indicates the observed anomaly in 2013. (b) Difference between the ALL-run and NAT1-run (ALL minus NAT1): SAT (land) and SST (ocean; °C, shading), 850-hPa stream function (black contours, $5 \times 10^5 \text{ m}^2 \text{ s}^{-1}$ interval), and 200-hPa divergent flow (m s^{-1} , arrows).

2013 Japanese heat wave; that is, the anthropogenic effect tends to increase the frequency of extreme warm events. The occurrence rate of extreme warm events that exceed the observed SATJ in 2013 is 12.4% for the ALL-run, 1.73% for the NAT1-run, and 0.50% for the NAT2-run. The estimated percentiles may have some sensitivity to assumed boundary conditions for the NAT-runs, but the difference between the ALL-run and NAT-runs suggests that human activity largely contributed to the increasing probability of heat waves in Japan in 2013.

The PDFs in Fig. 15.2a show an obvious shift of their ensemble mean between the ALL-run and the NAT-runs. The human-induced effect is represented by the difference in their ensemble mean fields between the ALL-run and each of the NAT-runs. Figure 15.2b shows the differences in surface temperature, 850-hPa stream function, and 200-hPa divergence flow between the ALL-run and NAT1-runs. The figure shows a marked warming around Japan (shading in Fig. 15.2b), which is the major cause of the positive shift of the PDF from the NAT1-run to the ALL-run. This enhanced warming around Japan is also detected in the difference from the NAT2-run (Supplementary Fig. S15.2). L. Wu et al. (2012) also found a faster warming rate over the path of global subtropical western boundary currents, including areas surrounding Japan, by analyzing century-long reconstructed SST and reanalysis products. They concluded that the poleward shift of midlatitude westerlies has a role in shifting those currents that contributed to the increase in SST.

In addition to the increase in SST, enhanced upper-level divergent flow (lower-level convergence)

in the central to western equatorial Pacific is visible where surface warming is evident (arrows and shading in Fig. 15.2b). The intensified upper-level divergent flow makes subsidence to the south of Japan and enhances the Pacific high (contours in Fig. 15.2b), which might also have the potential to increase the probability of high temperatures in Japan. On the other hand, there is little change in the Tibetan high (not shown). Deser et al. (2010) reported, however, that there is uncertainty in observed SST warming patterns due to the change in SST measurement technique and to different analysis procedures. They suggested that reconstructed SST datasets, including HadISST, might fail to reproduce the 20th century trends particularly over the equatorial Pacific. Trends in atmospheric responses in AGCMs, thus, may also be subject to the uncertainty in the observed SST warming patterns. Moreover, Christidis and Stott (2014) pointed to a lack of consensus among the CMIP5 models on the magnitude and spatial patterns of the anthropogenic change in SST. There is, hence, a continuing need for longer observations and for reducing model biases and uncertainty.

Conclusions. The 2013 heat wave in Japan was mainly caused by probabilistic atmospheric natural variability, but anthropogenic climate change played a significant role in raising the chance of the heat wave occurring. We emphasize that the increase of heat wave probability in East Asia is not simply a result of an increase in surrounding SST, but it is also potentially affected by atmospheric circulation changes forced remotely by western tropical Pacific warming.

16. UNDERSTANDING A HOT SUMMER IN CENTRAL EASTERN CHINA: SUMMER 2013 IN CONTEXT OF MULTIMODEL TREND ANALYSIS

TIANJUN ZHOU, SHUANGMEI MA, AND LIWEI ZOU

July–August 2013 was the warmest such period in central eastern China since 1951. Comparison based on Coupled Model Intercomparison Project Phase 5 (CMIP5) models suggest a discernible impact of anthropogenic forcing, with internal variability also being important.

The 2013 annual mean temperature in China was the fourth highest since 1961. It was 0.6°C above normal

and 0.8°C higher than 2012 (CMA 2014). Using the observational data of 756 stations provided by China

Meteorological Administration (CMA), we examine both the climate anomalies and the extremes (Fig. 16.1). The strongest heat wave since 1951 occurred in

central eastern China (~24°–33°N, 102.5°–122.5°E), where the July–August average of daily mean temperature was as much as 3.0°C above normal (Fig. 16.1a). Extreme high temperatures broke records at many stations (Fig. 16.1b). The regional average of July–August mean surface temperature was the highest since 1950 (Fig. 16.1c).

An average maximum of 34.4°C contributed to serious summer drought and other societal consequences (CMA 2014) in nine provinces: Shanghai, Zhejiang, Jiangxi, Hunan, Chongqing, Guizhou, Hubei, Anhui, and Jiangsu. The total days with high temperature (the daily maximum temperature $\geq 35^\circ\text{C}$) averaged in these nine provinces was 31 days, more than double the normal average of 14 days and the longest stretch of heat since 1951. Some 344 stations recorded a daily maximum equal to or higher than 40°C, and a highest temperature of 44.1°C was recorded at Xinchang station in Zhejiang province. The total station days in these nine provinces setting maximum daily temperature records was 477, another maximum since 1951. Overall, 144 stations broke records for consecutive high temperature days (CMA 2014). Great public interest necessitates understanding the reason behind the hot summer and detecting the potential effect of anthropogenic forcing.

Did anthropogenic forcing contribute to the heat? To understand the potential contribution of anthropogenic forcing to the seasonal extreme warmth, we based our inquiry on detection and attribution methods by Hegerl et al. (2009) and using the method of Knutson et al. (2013b). We compared the observed trends with model simulations of internal climate variability and model responses to both anthropogenic and natural forcing using 31 models that participated in CMIP5 (Taylor et al. 2012). The models used in the analysis are listed in Supplementary Table S16.1. A preindustrial control simulation, the 20th century historical climate simulation (hereafter “All-forcing”), and part of a climate change projection under Representative Concentration Pathways (RCP) 4.5 scenario are used. The All-forcing simulations included both anthropogenic and natural forcing agents from about 1860 to the present. Note that the preindustrial control simulations are used as an indicator of natural variability without anthropogenic impacts. Since the 20th century historical climate simulation of CMIP5 only covers 1860–2005, as Knutson et al. (2013b), data from RCP4.5 runs are used to extend the time series through 2013 where necessary. Our analysis focuses on the period of 1900–2013.

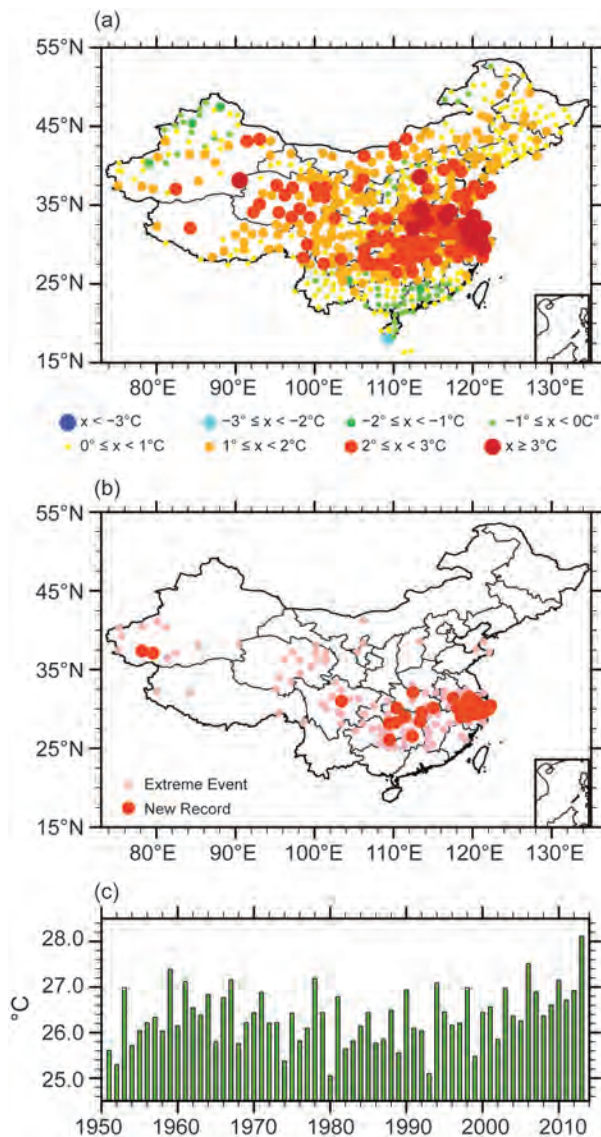


FIG. 16.1. (a) July–August mean surface air temperature anomalies ($^{\circ}\text{C}$) for 2013 (1961–90 base period) from the China Meteorology Administration datasets. (b) Pink color identifies stations with July–August mean warm anomalies that exceed the threshold of extreme temperature, with red color for stations that break the available observed record. The threshold of extreme temperature is defined as the 95th percentile value of the daily maximum temperature for the base period. The little inset in the bottom right represents the South China Sea. (c) Time series of July–August averaged surface air temperature averaged over the region (~24°–33°N, 102.5°–122.5°E) in Fig. 16.1a of record warmth during July–August 2013. The station data are bilinearly interpolated to the resolution of $0.5^{\circ} \times 0.5^{\circ}$ for calculating the regional average.

Figure 16.2a shows the July–August (JA) time series averaged over the region of central eastern China ($\sim 24^{\circ}$ – 33° N, 102.5° – 122.5° E) where the JA 2013 anomalies were the warmest in the record since 1951 (red colors in Fig. 16.1b). The observations operated by CMA show almost no trend before 1980 but a gradual rising trend after the 1980s, with a distinctive warm anomaly in 2013. The regional average surface temperature in 2013 is 1.838°C warmer than normal (base period 1961–90). This observed average is within the range of the 31 CMIP5 ensemble model members but is far higher than the multimodel ensemble mean (an anomaly of 1.838°C versus the simulated value of 0.868°C). The spread among the 31 CMIP5 models is large. Some individual models do reproduce the amplitude of the observed warmth. The weak warming trend prior to 1980 in the observations is related to natural variability of the climate system (Zhou et al. 2009), and it will be discussed in the final section.

Figure 16.2b shows a trend analysis for the JA central eastern China surface air temperature time series given in Fig. 16.2a. The models are compared to the observations. We show the results of both the multimodel ensemble mean and the uncertainties. Following Knutson et al. (2013b), the uncertainties are measured by the 5th–95th percentile range of the distribution of trends, which is obtained by combing random samples from each of the 31 CMIP5 model control runs together with the corresponding model’s ensemble mean forced trends. Thus, a multimodel distribution of total trends is created, and it

reflects uncertainty in both the forcing responses and the influence of internal climate variability. The 31 CMIP5 models used for the analysis contribute equally to the multimodel distribution from which the percentiles are derived in the sense of “one model, one vote.”

The control run internal variability can be used as a surrogate for natural variability in the real

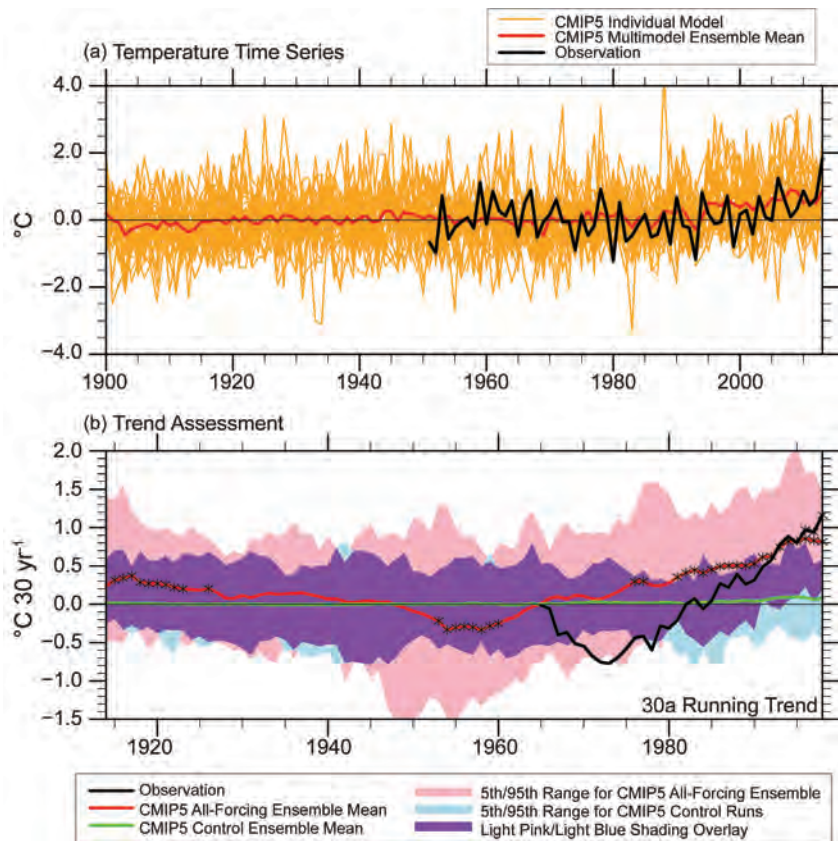


FIG. 16.2. (a) Time series of July–August averaged surface air temperature anomalies ($^{\circ}\text{C}$) averaged over the region in Fig. 16.1a of record summer warmth in central eastern China ($\sim 24^{\circ}$ – 33° N, 102.5° – 122.5° E) during 2013. The black line depicts the observed (CMA data) anomalies; the dark red line depicts the multi-model ensemble anomalies from the CMIP5 All-forcing runs, with each of 31 models weighted equally; and the orange lines are individual ensemble members making up the CMIP5 multi-model ensemble. All time series are anomalies relative to the base period of 1961–90. (b) The 30-year sliding trends [$^{\circ}\text{C} \text{ (30 yr)}^{-1}$] in the area-averaged July–August mean surface temperature series in (a). The trend is marked on the 15th year of the 30-year window. The black curve shows trends from observations. The thick red curve shows the ensemble mean trends from the 31-member CMIP5 ALL-Forcing ensemble. The green curve shows the ensemble mean trend from 31-member CMIP5 preindustrial control run. The pink shading shows the 5th–95th percentile range of the distribution of trends (see text for technical details). The green-shaded regions show the 5th–95th percentile range of the trends from the 31 model control runs. Purple shading indicates where the pink- and green-shaded regions overlap. The trend that is statistically significant at the 1% level is represented as “*” in (b).

world (Knutson et al. 2013b). The observed trends in Fig. 16.2b (black line) generally lie outside of the control run 5th–95th percentile range (green shaded region and the purple shaded region) after about 1990, indicating that the observed trends are inconsistent with internal climate variability alone. The observed trends lie within the pink regions for nearly all starting dates, indicating that the observed JA trends are consistent with the CMIP5 All-forcing model simulations. In particular, after the early 1990s, the observed trends lie outside of the control run 5th–95th percentile range (purple shaded region) but within the All-forcing run 5th–95th percentile range (pink shaded region), indicating the observed JA trends are inconsistent with internal climate variability alone but consistent with the CMIP5 All-forcing model simulations. Based on the comparison, we suggest that the observed warming after the early 1990s over central eastern China is very likely partly attributable to anthropogenic forcings.

Does the anthropogenic forcing contribute to the observed anomalies of JA 2013 over the central eastern China? Based on Fig. 16.2a, the 2013 observed JA surface air temperature anomaly is $\sim 1.838^{\circ}\text{C}$, and the modeled value is $\sim 0.868^{\circ}\text{C}$, a rough estimate of the anthropogenic contribution to the magnitude of the temperature anomaly is 47.23%. If we interpret the difference between the All-forcing and the control run distributions as the anthropogenic influence as Knutson et al. (2013b), the observed $\sim 1.838^{\circ}\text{C}$ warming of JA 2013 was 2.12 times stronger than the expected multimodel ensemble mean contribution of 0.868°C due to anthropogenic forcing in 2013. The difference indicates that internal variability also played a substantial role. Based on the ensemble of 31 CMIP5 models, an event this hot or hotter would occur with a probability of 1.047% in the control run and 2.518% in the forced simulation. Under the forced scenario, the fraction of risk of such an extreme warm event that is attributable to the anthropogenic forcing is $(2.518 - 1.047) / 2.518 = 58.42\%$.

In addition, one may hypothesize that a study focused on maximum temperatures should be more relevant to diagnosing contributions to the anomalies listed in the previous section of the paper. We have assessed the performances of CMIP5 models in reproducing the long-term changes of maximum temperatures over central eastern China. We found that the models are poor in this regard and do not allow us to detect the potential contributions of

anthropogenic forcings to maximum temperature changes over this domain by using CMIP5 models.

Concluding remarks. In this study, seasonal extreme warmth is placed in the context of long-term climate change by analyzing the time series for the region, comparing the observed trends with simulations of 31 CMIP5 models that include both internal variability and responses to anthropogenic and natural forcings. We found that long-term anthropogenic warming in central eastern China is detectable only after the early 1990s. The anthropogenic contribution to the magnitude of the extreme July–August mean warmth over the region is expected to be about 47.23%. Regarding the anthropogenic contribution to the increased probability of the extreme July–August mean warmth, the fraction of attributable risk is estimated to be 58.42%.

Central eastern China is dominated by the monsoon. The strength of the East Asian summer monsoon circulation has exhibited robust interdecadal variability in past decades and resulted in excessive precipitation along the middle and lower reaches of the Yangtze River valley (Yu et al. 2004; Zhou et al. 2009). The excessive precipitation is associated with colder temperatures (Yu and Zhou 2007). This could explain why a warming trend is not evident in Fig. 16.2a in the early decades. In addition, the aerosol emission induced cooling effect also partly slows down the anthropogenic warming trend (Qian et al. 2003, 2009; Song et al. 2014).

The Pacific decadal oscillation (PDO) or interdecadal Pacific oscillation (IPO; Power et al. 1999) is a prominent natural internal variability mode of the coupled climate system. There is increasing evidence that the East Asian summer monsoon circulation is inversely correlated with the phase of the PDO/IPO (Li et al. 2010b; Qian and Zhou 2014); thus, both monsoon precipitation and the associated temperature changes are largely dominated by natural internal variability (Zhou et al. 2009, 2013). The large contribution of internal variability explains why the estimated fraction of attributable risk (58.42%) is lower than that over the eastern United States, which was 92% for the March–May 2012 warm anomaly (Knutson et al. 2013b). Since averaging coupled climate model simulations averages out different phases of the PDO, such variability, for example if it caused the observed cooling during 1960–70, would not be seen in the ensemble mean of CMIP5 historical climate simulations.

17. SEVERE PRECIPITATION IN NORTHERN INDIA IN JUNE 2013: CAUSES, HISTORICAL CONTEXT, AND CHANGES IN PROBABILITY

DEEPTI SINGH, DANIEL E. HORTON, MICHAEL TSIANG, MATZ HAUGEN, MOETASIM ASHFAQ, RUI MEI, DEEKSHA RASTOGI, NATHANIEL C. JOHNSON, ALLISON CHARLAND, BALA RAJARATNAM, AND NOAH S. DIFFENBAUGH

Cumulative precipitation in northern India in June 2013 was a century-scale event, and evidence for increased probability in the present climate compared to the preindustrial climate is equivocal.

The Event: June 2013 Flooding in Northern India. Parts of mountainous northern India—including Himachal Pradesh, Uttarakhand, and Uttar Pradesh—experienced extremely heavy precipitation during 14–17 June 2013 (Fig. 17.1a,b). Landslides, debris flows, and extensive flooding caused catastrophic damage to housing and infrastructure, impacted >100000 people, and resulted in >5800 deaths (Dobhal et al. 2013; Dube et al. 2013; Dubey et al. 2013; Joseph et al. 2014; Mishra and Srinivasan 2013). Subsequent

heavy rains on 24–25 June hampered rescue efforts, ultimately leaving thousands without food or shelter for >10 days (Prakash 2013).

Causes of the mid-June precipitation and associated flooding have been analyzed in detail (Dobhal et al. 2013; Dube et al. 2014; Mishra and Srinivasan 2013; Prakash 2013). Anomalously early arrival of monsoon-like atmospheric circulation over India (Fig. 17.1c, Supplementary Figure S17.1a) brought heavy rains to the mountainous regions where snow

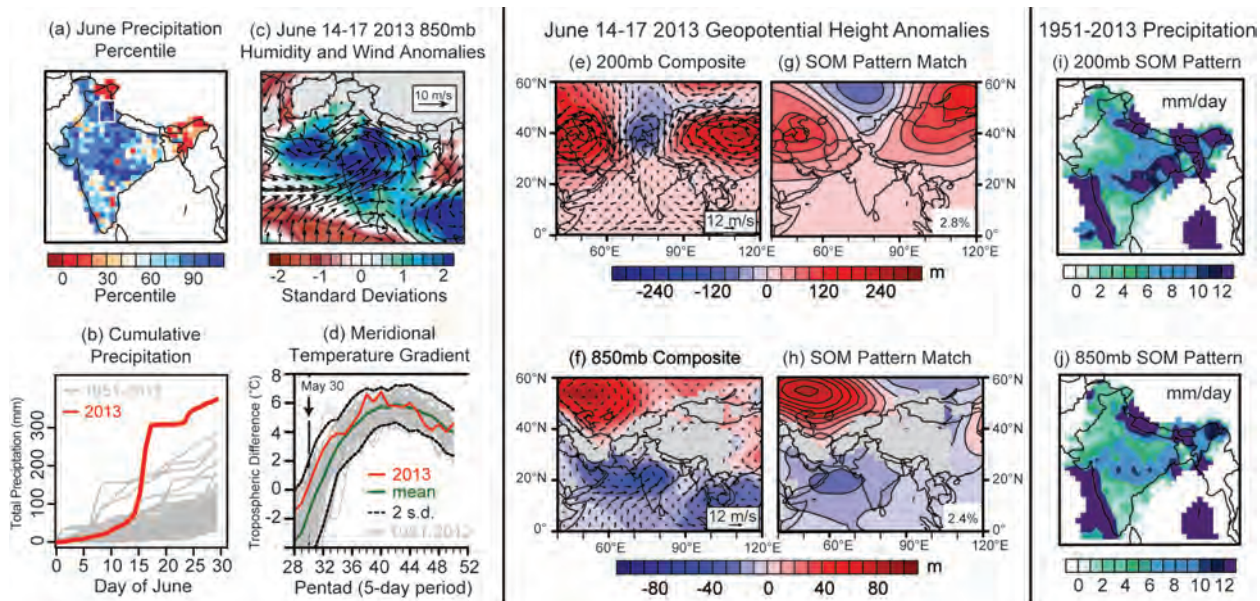


FIG. 17.1. Precipitation characteristics and synoptic environment. (a) June 2013 grid cell cumulative precipitation percentiles relative to June climatology (1951–2012). White box highlights the severe flooding domain (29°–33°N, 77.5°–80°E). (b) Daily cumulative precipitation distribution over the flood domain. (c) 14–17 June 2013 composite lower-level wind and specific humidity anomalies relative to 14–17 June climatology. (d) Climatological and 2013 meridional temperature gradient (MTG), defined as the zonally averaged (52°–85°E) pentad mean tropospheric (200–500 mb) temperature difference between 30°N and 5°N. (e,f) 14–17 June 2013 composite upper- and lower-level wind and geopotential height anomalies relative to the 14–17 June climatology. (g,h) Upper- and lower-atmosphere self-organizing map (SOM) patterns that correspond to 14–17 June 2013. Pattern matches are autonomously selected from 35 SOM nodes, generated from an analysis of all 1951–2013 June days (see Supplemental Materials). (i,j) Composite precipitation for all June days during the 1951–2013 period that were associated with the upper- and lower-level SOM patterns shown in (g) and (h).

cover typically melts prior to monsoon onset (Dube et al. 2014; Joseph et al. 2014). Snow cover in local river basins was ~30% above normal in early June 2013 (Durga Rao et al. 2014). Heavy precipitation led to rapid snowmelt, overwhelming the regional hydrologic system, causing glacial lake outburst floods, and triggering catastrophic mass wastage events (Andermann et al. 2012; Dubey et al. 2013; Durga Rao et al. 2014; Prakash 2013; Siderius et al. 2013).

The upper- and lower-level synoptic conditions in early and mid-June supported the anomalously early monsoon-like circulation (Supplementary Fig. S17.1a) and excessive precipitation in northern India (Fig. 17.1a,b). In the upper atmosphere (200 mb), a persistent anticyclonic anomaly formed over Central Asia (Fig. 17.1e). This upper-level blocking pattern guided mid-to-high-latitude troughs southward, thereby facilitating the advection of relatively cold, dry, high-potential-vorticity air to the upper levels of the atmosphere over northern India (Joseph et al. 2014). In the lower atmosphere (850 mb), low-pressure systems formed over both the northern Bay of Bengal and the northern Arabian Sea (Joseph et al. 2014), with the Bay of Bengal system moving inland over central India and persisting for the duration of the event (Fig. 17.1f). Low-level convergence associated with these systems and a stronger-than-normal Somali Jet facilitated anomalous moisture advection to the Indian subcontinent (Fig. 17.1c). These co-occurring upper- and lower-level dynamics are consistent with a convectively unstable atmosphere (Hong et al. 2011; Ullah and Shouting 2013; Wang et al. 2011), which, when combined with orographic forcing from the surrounding northwestern Himalayan terrain, create an environment ripe for intense mesoscale convection (Houze et al. 2011).

In this study, we analyze the dynamics of this event within the context of the historical and preindustrial climates.

Historical context. We contextualize June 2013 precipitation using the Indian Meteorological Department (IMD) 1951–2013 $1^\circ \times 1^\circ$ gridded dataset (Rajeevan et al. 2010), with the caveat that the rain gauge network in the region could have changed over this period. Cumulative June precipitation exceeded the 80th percentile over much of central and northern India, and it exceeded the maximum quantile over a majority of the flood region (Fig. 17.1a). From 14 to 17 June, this domain (29° – 33° N, 77.5° – 80° E) received four-day total precipitation that was unprecedented in the observed record (Fig. 17.1b), with

the heaviest day (16 June) exceeding the previous one-day June maximum by 105% (Supplementary Fig. S17.2). Consequently, the flood region recorded the highest total accumulated June precipitation in the 1951–2013 record, with the previous maximum June total equaled by 17 June and exceeded by 31% by the end of the month (Fig. 17.1b).

Monsoon dynamics and thermodynamics were also unusual relative to June climatological norms. The monsoon onset date is closely associated with the reversal of the zonally averaged (52° – 85° E) meridional tropospheric (500–200 mb) ocean-to-continent (5° – 30° N) temperature gradient (Ashfaq et al. 2009; Webster et al. 1998), and with the vertical easterly zonal wind shear between 850 mb and 200 mb averaged over 0° – 30° N and 50° – 90° E (Li and Yanai 1996; Webster et al. 1998; G. Wu et al. 2012; Xavier et al. 2007). The 2013 meridional temperature gradient (MTG) reversal dates were among the earliest on record (1951–2013, Fig. 17.1d) and the vertical easterly wind shear was stronger than normal during early-June (Supplementary Fig. S17.1b). The early MTG reversal resulted from anomalously high land temperatures (~2 standard deviations; Supplementary Fig. S17.1c,d), which co-occurred with record-low Eurasian snow cover (NOAA 2013). In addition, as a result of the early monsoon-like circulation, low-level atmospheric humidity exceeded 2 standard deviations above the climatological 14–17 June mean (Fig. 17.1c).

Synoptic conditions were likewise extremely rare for mid-June. We categorize the occurrence of upper- and lower-level daily June atmospheric patterns in the National Centers for Environmental Prediction (NCEP) R1 reanalysis using self-organizing map (SOM) cluster analysis (Borah et al. 2013; Chattopadhyay et al. 2008; Hewitson and Crane 2002; Johnson 2013; Kohonen 2001; see Supplemental Materials). SOM analyses reveal persistent upper-level blocking patterns from 10 to 17 June and lower-level troughing patterns from 11 to 17 June (Supplementary Fig. S17.2). Additionally, the upper- and lower-level patterns (Fig. 17.1g,h) that persisted during the core of the event (14–17 June) are each historically associated with heavy precipitation over northern India (Fig. 17.1i,j). Although occurrence of the core-event upper-level pattern is not rare for June (median frequency of occurrence), the 850-mb pattern is much less common (<6 percentile frequency of occurrence). Further, mid-June 2013 was the only instance that the core-event upper- and lower-level patterns co-occurred in June during the 1951–2013 period. The atmospheric

configuration associated with the unprecedented mid-June extreme precipitation, therefore, appears to also have been unprecedented.

We note that this configuration is not necessarily unprecedented later in the monsoon season. For example, the co-occurrence of upper-level blocking with tropical moisture advection is similar to the conditions identified during the July 2010 Pakistan floods and during heavy precipitation events that occur during the core monsoon season (Hong et al. 2011; Houze et al. 2011; Lau and Kim 2011; Ullah and Shouting 2013; Webster et al. 2011).

Quantifying the probability of a 2013-magnitude event. In quantifying the probability of a 2013-magnitude event, we restrict our focus to the June 2013 total precipitation. We select the monthly scale extreme rather than the daily scale extreme because both the extreme magnitude of this event relative to the observed distribution of four-day June totals and the limited ability of climate models to accurately simulate the daily scale extremes make the problem intractable at the daily scale. Therefore, hereafter, “a 2013-magnitude event” refers to the total June rainfall, which in June 2013 was the most extreme on record (Fig. 17.1b).

Given the rarity of the event in the observed record (Fig. 17.2a), we fit a Pareto (heavy-tailed) distribution to the 1951–2012 observations of spatially averaged (area-weighted average) rainfall over the selected domain (Fig. 17.2a; Supplementary Fig. S17.3a). From the Pareto distribution, we estimate the sample quantile (Q_o) and return period (R_o) of the June 2013 total precipitation in the present climate (see Supplemental Materials). We find that the 2013 event exceeds the 99th percentile in the observed distribution ($Q_o = 99.1$ th quantile), yielding a return period of 111 years (Fig. 17.2a). Because the Pareto is a heavy-tailed distribution, extreme events are less likely to be found anomalous, and, thus, the corresponding return period can be considered a lower bound.

Next, we assess the influence of anthropogenic forcings on the likelihood of extreme June precipitation using the historical (20C) and preindustrial (PI) simulations from the CMIP5 climate model archive (Taylor et al. 2012). We use the Kolmogorov–Smirnov (K-S) goodness-of-fit test to identify the models that most closely simulate the observed distribution of the area-weighted average June total precipitation over the impacted region (Fig. 17.1a). (To control for the mean bias in the models, we first re-center each model’s distribution so that the model mean matches the observed mean.) Because the simulated change in

likelihood of extremes can be heavily influenced by biases in the simulated distribution, we restrict our analyses to 11 models whose K-S value exceeds 0.2 (Supplementary Fig. S17.3b), ensuring a comparatively good fit of the overall distribution, including in the tails. Among these 11 models that pass this goodness-of-fit criterion, 4 show greater mean and variability of June precipitation in the 20C simulations (Fig. 17.2b). However, 7 of the 11 show increased exceedance of the PI 99th percentile value (Fig. 17.2c), suggesting increased probability of extremely high June precipitation in the current climate. This result is consistent with studies that indicate an increase in extremes primarily from increased atmospheric-moisture availability (Allan and Soden 2008; O’Gorman and Schneider 2009).

Next, we use Pareto distributions to estimate the return period of the June 2013 total precipitation in the 20C and PI simulations. To control for the variability-bias in the models, we first determine the magnitude of the 111-year event ($Q_o = 99.1$ th quantile) in the fitted 20C distribution (Pr_H), and then determine the quantile (Q_{PI}) corresponding to Pr_H in the fitted PI distribution (see Supplemental Materials; Supplementary Fig. S17.3c). Further, we quantify the uncertainty in these likelihood estimates (Q_o/Q_{PI}) using the bootstrap (Fig. 17.2d). We find that 5 of the 11 models show >50% likelihood that the extreme June total precipitation has higher probability in the 20C climate. In addition, of the three models that have high p -values from the K-S test (> 0.8) and similar sample sizes in the 20C and PI populations (Fig. 17.2d), two suggest >50% likelihood that the extreme June total precipitation has higher probability in the 20C climate, and the third model suggests ~50% likelihood. Further, the model with the largest 20C ensemble (Centre National de Recherches Meteorologiques Coupled Global Climate Model; CNRM-CM5) demonstrates a ~50% likelihood that the probability of the extreme June total precipitation has at least doubled in the 20C climate. CNRM-CM5 also has the highest skill in simulating the summer monsoon precipitation and lower-level wind climatology (Sperber et al. 2013).

Conclusions. Our statistical analysis, combined with our diagnosis of the atmospheric environment, demonstrates that the extreme June 2013 total precipitation in northern India was at least a century-scale event. Precise quantification of the likelihood of the event in the current and preindustrial climates is limited by the relatively short observational record

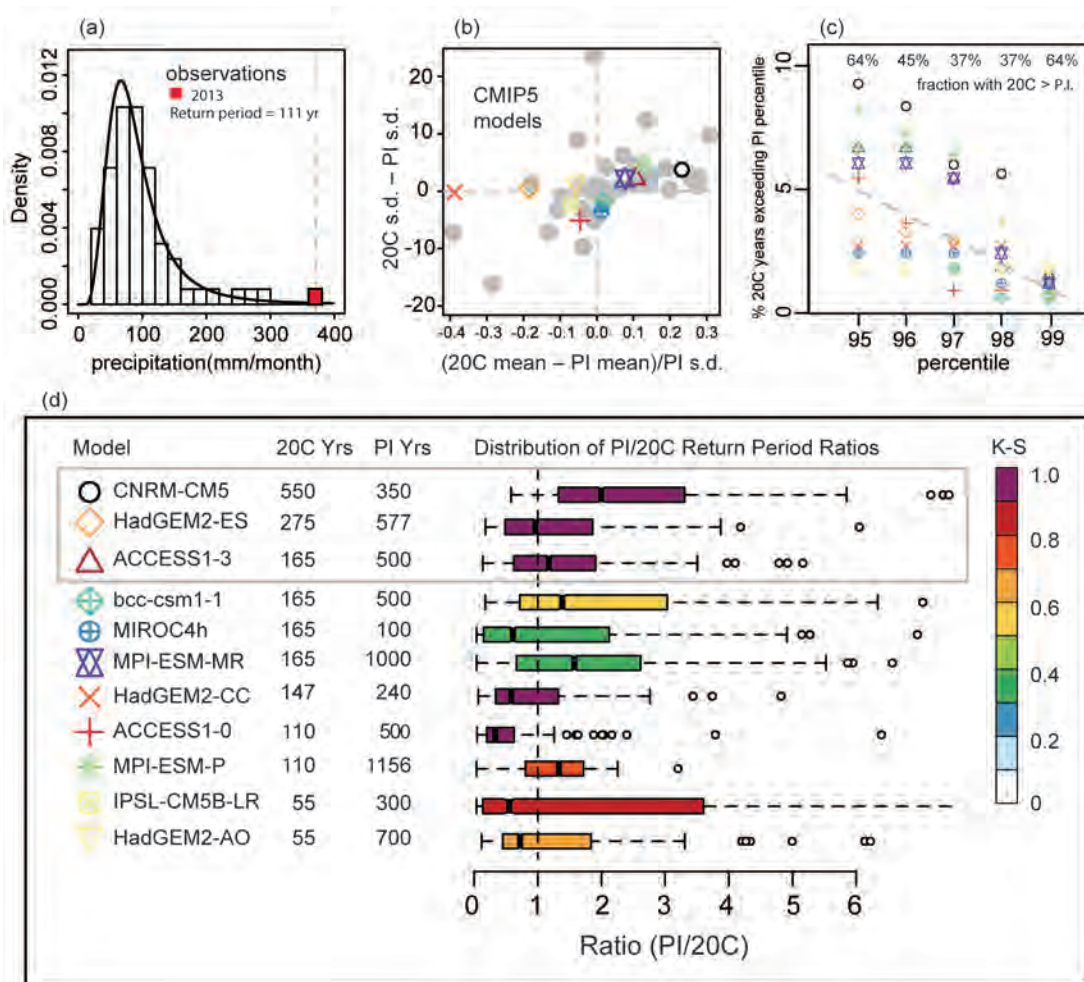


FIG. 17.2. Extreme precipitation statistics in the current and preindustrial climates. (a) Probability density function of the Pareto-fitted observed cumulative-June precipitation distribution (black line; 1951–2012), and probability of occurrence of the June 2013 cumulative precipitation magnitude in this distribution (red). The return period of the June 2013 magnitude in the observed distribution is indicated on the plot. (b) Change in mean and standard deviation of precipitation between the CMIP5 historical (20C) and preindustrial (PI) simulations. Gray dots represent all available CMIP5 models and colored symbols represent AI models that meet the Kolmogorov–Smirnov (K-S) goodness-of-fit test criteria (p value > 0.2). (c) Percent of years in the 20C simulations of AI models that exceed the respective PI quantiles of the AI models. The numbers on the plot indicate the fraction of AI models that exceed the PI quantiles in the 20C simulations. (d) Box plot representing the distribution of ratios of the return period of a June 2013 magnitude event in the PI and 20C simulations, calculated using the bootstrap. The lines in the boxes represent the median of the distribution for each model. The bounds of the boxes represent the 25th and 75th percentiles. The whiskers extend to the edges of 1.5×interquartile range, and points outside of those bounds are shown individually. The number of years indicated for the 20C Yrs and PI Yrs columns are the total years available from all realizations within each scenario. The color bar corresponding to the box plot indicates p values from the Kolmogorov–Smirnov test.

and by the resolution and ensemble size of the small subset of models that credibly simulate the seasonal rainfall distribution over northern India. Indeed, an attempt to quantify the probability of the unprecedented four-day precipitation total would present even greater analytical challenges. However, despite these limitations, our analyses of the observed and

simulated June precipitation provide evidence that anthropogenic forcing of the climate system has increased the likelihood of such an event, a result in agreement with previous studies of trends in rainfall extremes in India (Goswami et al. 2006; Krishnamurthy et al. 2009; Ghosh et al. 2012; Singh et al. 2014).

18. THE 2013 HOT, DRY, SUMMER IN WESTERN EUROPE

BUWEN DONG, ROWAN SUTTON, AND LEN SHAFFREY

Anthropogenic forcing played a substantial part in western Europe's hot, dry summer in 2013. North Atlantic sea surface temperatures were likely a factor in the large contrast with summer 2012.

Observations. Western Europe experienced sweltering high temperatures in summer 2013. On 22 July 2013, the United Kingdom recorded its hottest day since July 2006, with 33.5°C recorded at Heathrow and Northolt in west London (Met Office 2014). Averaged over western Europe (Fig. 18.1c), the seasonal mean (June–August) anomaly in surface air temperature (SAT) was 1.33°C above the mean over the period of 1964–93, which is 3.2 standard deviations of the interannual variability. [HadCRUT4 data (Morice et al. 2012) shows a similar warming of 1.28°C.] This magnitude of warming is slightly less but comparable with the previous hot summers in western Europe, such as 2003 (e.g., Schaer et al. 2004) and 2010 (e.g., Barriopedro et al. 2011) for which summer mean SAT anomalies were 1.46°C and 1.86°C respectively, corresponding to 3.5 and 4.5 standard deviations.

The atmospheric circulation in summer 2013 was characterized by anomalously high sea level pressure (SLP) extending from the United Kingdom into northern Europe and anomalously low SLP over the Arctic (Fig. 18.1a). This pattern projects strongly onto the positive phase of the summer North Atlantic Oscillation (SNAO; Folland et al. 2009). The anomalous SNAO index of 2.7 hPa in 2013 was +1.0 standard deviation of the interannual variability, in stark contrast with the previous summer of 2012 (Dong et al. 2013a) for which the index was –2.7 standard deviations (Supplementary Fig. S18.1b). The circulation pattern in 2013 was associated with a northward shift of summer North Atlantic storm track (Fig. 18.1e and f). The climatology of cyclone track density (Dong et al. 2013b and Fig. 18.1e) shows a split into two preferred cyclone paths at the North Atlantic jet exit region (5°W–5°E): one passing near Iceland at ~71°N and into the Nordic Seas and the other passing across the British Isles at ~56°N and into western Europe. In summer 2013, more storms than usual passed over Iceland and fewer over the United Kingdom and into Western Europe (Fig. 18.1f). This led to dry conditions in the United Kingdom and most of western Europe. The area-averaged precipitation anomaly was –0.35

mm day⁻¹, which is –2.2 standard deviations of the interannual variability (Supplementary Fig. S18.1c). The low rainfall was also in stark contrast to the summer of 2012, which was a record wet summer in the United Kingdom and was last in a series of wet UK summers since 2007, each of which was associated with a negative SNAO index (Allan and Folland 2012; Dong et al. 2013a). [Note that the inhomogeneity of the data in E-OBS precipitation is a potential source of bias (Zolina et al. 2013), but negative precipitation anomalies in Western Europe are consistent with the northward shifted storm track.]

Global SST anomalies for summer 2013 are illustrated in Fig. 18.1d. Warm SSTs (relative to 1964–93) were present in many regions, with a prominent warm anomaly (> 1.0°C) along the Gulf Stream extension in the North Atlantic. Associated with this feature were an enhanced meridional SST gradient to the north and a reduced gradient to the south (Supplementary Fig. S18.2c). These anomalous SST gradients may have played a role in the observed northward shift of the North Atlantic storm track (e.g., Sampe et al. 2010; Ogawa et al. 2012) and influenced the related anomalies in the SNAO and western European climate (Folland et al. 2009; Sutton and Dong 2012; Dong et al. 2013b). Warm anomalies were also observed in the Arctic, consistent with the continuing low sea ice extent (SIE); these SIE anomalies might also have had an influence on the atmospheric circulation (Balmaseda et al. 2010; Petrie et al. 2014, manuscript submitted to *Quart. J. Roy. Meteor. Soc.*).

Relative to the climatological period of 1964–93, by 2012 there were significant increases in anthropogenic greenhouse gas (GHG) concentrations (e.g., WMO 2013) and significant changes in anthropogenic aerosols. European and North American sulphur dioxide emissions had declined while Asian emissions had increased (e.g., Lamarque et al. 2010). In this study, we investigate the roles of changes in SST, SIE, and radiative forcing in shaping the European summer of 2013, as well as possible reasons for the striking contrast between summer 2013 and summer 2012. Our

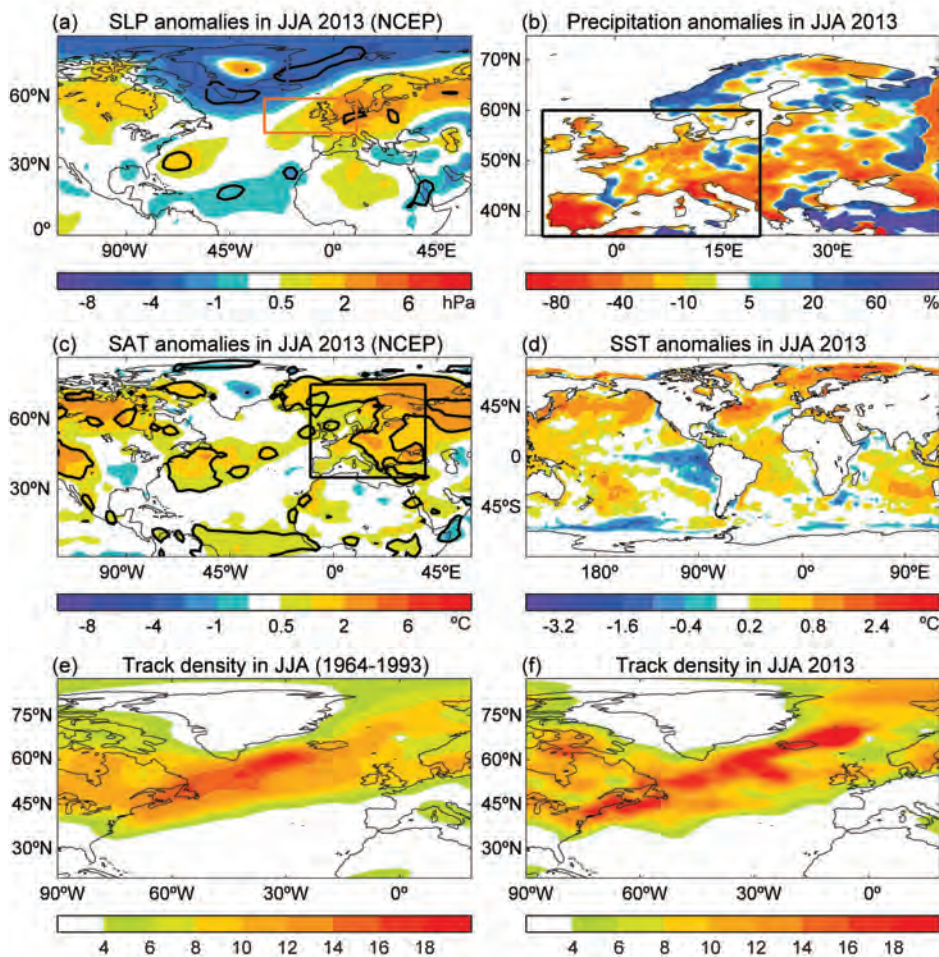


FIG. 18.1. Anomalies for JJA 2013 from the climatological period 1964–93 for (a) SLP (hPa) and (c) SAT (°C) from the NCEP reanalysis (Kalnay et al. 1996), (b) percentage precipitation change (%) from the daily gridded E-OBS precipitation (version 9.0) over Europe (Haylock et al. 2008), and (d) SSTs (°C) from HadISST (Rayner et al. 2003). (e) and (f) Cyclone track density for the climatological period and 2013, respectively, as in Hoskins and Hodges (2002) based on the NCEP reanalysis. Track density is in units of numbers per month per unit area, where the unit area is equivalent to a 5° spherical cap (about 10⁶ km²). Note that this climatological period is dominated by cold AMO conditions and is the period used for the climatological model simulations. Thick lines in (a) and (c) highlight regions where the differences are statistically significant at the 90% confidence level using a two-tailed Student’s t-test.

focus is on seasonal mean conditions rather than on shorter-lived events that occurred within the season. We note that the sign of shorter-lived events can often differ from that of the seasonal mean, so for example, some regions of western Europe experienced floods in summer 2013 even though the seasonal mean precipitation was below average.

Climate model experiments. Climate model experiments have been carried out to identify the roles of changes in: (a) SST/SIE and (b) anthropogenic GHG and aerosol forcing in the European summer climate

anomalies of 2013. In this study, we do not address the anthropogenic contribution to the SST/SIE changes, but rather consider these changes as an independent forcing factor. We use the atmosphere configuration of the Met Office Hadley Centre Global Environment Model version 3 (HadGEM3-A; Hewitt et al. 2011), with a resolution of 1.875° longitude by 1.25° latitude and 85 levels in the vertical. Dong et al. (2013a) used the same model to study the 2012 summer in Europe. A series of experiments was performed, the details of which are summarized in Table 18.1. We use the same control experiment (CONTROL) for the period 1964–93 as Dong et al. (2013a) and perform two other experiments: ALL2013 and SST2013. Both of these experiments use 2013 SST and SIE boundary conditions but they differ in the

specification of anthropogenic GHG and aerosol forcing: ALL2013 uses anthropogenic forcing appropriate for 2013 while SST2013 uses the same anthropogenic forcing as for the CONTROL experiment, appropriate for 1964–93. The last 25 years of each experiment are used for analysis. The CONTROL experiment reproduces realistic climatological SLP and precipitation patterns for summer (Supplemental Fig. S10.2 of Dong et al. 2013a).

The model simulates a significant warming over Europe in summer 2013 in response to changes in SST, SIE, and anthropogenic forcing (i.e., ALL2013–CON-

Table 18.1. Summary of numerical experiments.

Experiments	Boundary Conditions	Length of run
CONTROL	Forced with monthly mean climatological sea surface temperature (SST) and sea ice extent (SIE) averaged over 1964–93 using HadISST data (Rayner et al. 2003) and with anthropogenic greenhouse gases (GHG) concentrations averaged over the same period and anthropogenic aerosols emissions averaged over 1970–93.	32 years
ALL2013	Forced with monthly mean SST and SIE from Dec 2012 to Nov 2013 using HadISST data, with anthropogenic GHG concentration in 2012 (WMO 2013) and anthropogenic aerosol emissions for 2010 (Lamarque et al. 2010), which is the most recent year for which emissions data were available.	27 years
SST2013	As ALL2013, but with anthropogenic GHG concentrations and anthropogenic aerosol emissions the same as in CONTROL.	27 years

TROL, Fig. 18.2a) with an area averaged SAT change of 1.11°C over western Europe. The observed anomaly of 1.33°C is within the ± 1 standard deviation range of the interannual variability of the model response (Supplementary Fig. S18.1a). Changes in SST and SIE explain 63% ($\pm 26\%$) of the area-averaged western European warming response in HadGEM3 (Fig. 18.2d), with the remaining 37% ($\pm 29\%$) explained by the direct impact (without forcing-induced SST and sea ice feedbacks) of changes in radiative forcings from GHG and aerosols (Fig. 18.2g and Supplementary Fig. S18.1a).

The atmospheric circulation anomalies simulated by the model (Fig. 18.2b) show notable similarities to the observed pattern over the North Atlantic and Europe (Fig. 18.1a), including low SLP anomalies over Greenland and an anomalous anticyclone over the United Kingdom. The wave train pattern of SLP anomalies suggests that changes in convection over the Caribbean Sea might be an important factor (e.g., Douville et al. 2011). However, in the model simulation the anomalous anticyclone does not extend as far eastward into central Europe as in the observations. The circulation anomalies correspond to a positive anomaly (mean = 1.2 hPa, which is only 0.5 standard deviations) in the SNAO index relative to the CONTROL, which is smaller than the observed anomaly (2.7 hPa; Supplementary Fig. S18.1b). The pattern of simulated western European precipitation anomalies (Fig. 18.2c) is consistent with the positive phase of the SNAO and is similar to the observations, with anomalously low rainfall over most of western Europe (Fig. 18.1b). As for the circulation anomaly, the magnitude of the mean precipitation anomaly is smaller than observed (Supplementary Fig. S18.1c), although there is substantial interannual variability in the model results.

The additional SST2013 experiment suggests that *both* SST/SIE changes and the direct impact of changes in anthropogenic radiative forcing contributed to the anomalous circulation (Fig. 18.2e and h; Fig. S18.1b) and reduced rainfall over western Europe in summer 2013 (Fig. 18.2f and i; Supplementary Fig. S18.1c). The SST change has the most impact on the low SLP anomalies simulated over Greenland, but GHG and aerosol forcing causes a substantial anticyclonic anomaly over, and north of, the United Kingdom. This anticyclonic circulation anomaly is similar to the summer mean circulation response to an increase in GHG forcing (Bladé et al. 2012) and is presumably due to an increase in the frequency of the positive SNAO-like circulation regimes over the Atlantic sector (Boé et al. 2009).

Changes in GHG and aerosol forcing are unlikely to be a major factor in explaining the striking contrast in circulation and precipitation between the European summers of 2012 and 2013 (Supplementary Fig. S18.2a), as the changes in these forcings between these two years were small. However, the model experiments suggest that changes in SST and SIE in the North Atlantic were a significant factor (Supplementary Fig. S18.2e). In particular, the anomalous meridional SST gradient to the north of the Gulf Stream in 2013, relative to 2012 (Supplementary Fig. S18.2c), may have favored a positive phase of the SNAO and a northward shift of North Atlantic summer storm track (e.g., Folland et al. 2009; Dong et al. 2013b), as was observed (Supplementary Figs. S18.2d and f). The model experiments show some evidence of capturing this shift, although the mean signal (Supplementary Fig. S18.2e) is again much weaker than was observed (Supplementary Fig. S18.2a).

The model results show an encouraging degree of consistency with observations, but it is difficult

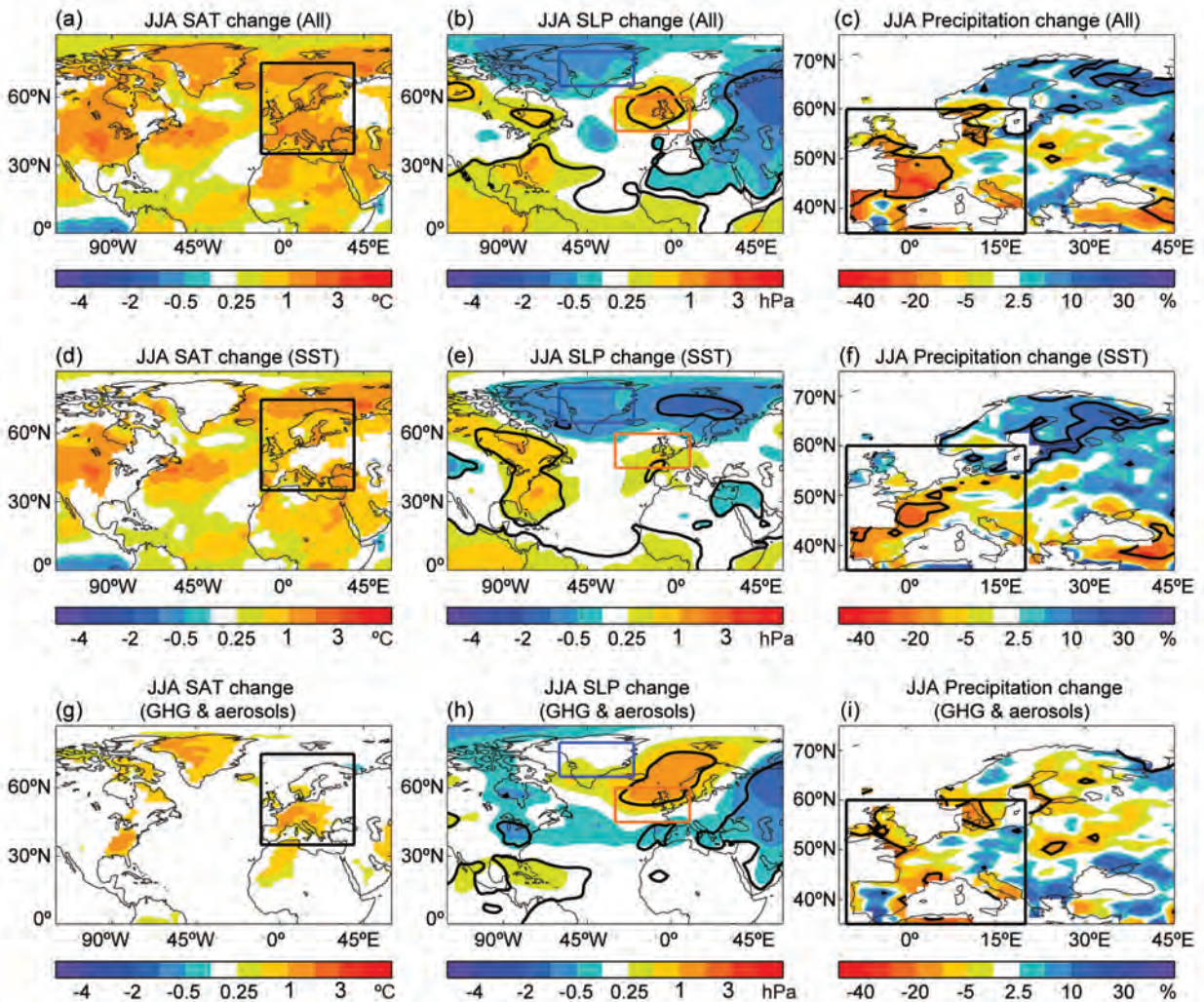


FIG. 18.2. SAT ($^{\circ}\text{C}$; left column), SLP (hPa; middle column) and percentage precipitation changes (%; right column) in the model simulations forced by different configurations of forcings in 2013 relative to the control simulation. (a), (b), and (c) Forced by changes in SST and SIE, GHG concentrations, and aerosols emissions (ALL2013–CONTROL). (d), (e), and (f) Forced by changes in SST and SIE (SST2013–CONTROL). (g), (h), and (i) Forced by changes in GHG and aerosols emissions (ALL2013–SST2013). Only changes that are statistically significant at the 90% confidence level using a two-tailed Student’s *t*-test are plotted in (a), (d), and (g) while thick lines in other panels highlight regions where the differences are statistically significant at the 90% confidence level.

to assess precisely what level of consistency should be expected in view of the high level of internal variability and uncertainty about the true magnitude of forced signals in the real world. It is clear from Supplementary Fig. S18.1 that the signal-to-noise ratio for the changes in SAT is large, which permits more confident conclusions, whereas that for changes in circulation and precipitation is much lower (though it is interesting to note that the model suggests a stronger forced signal in western European summer precipitation than in the SNAO). One limitation of the current experiments, which may well influence the signal-to-noise ratio, is the use of a prescribed

SST boundary condition. Active ocean–atmosphere coupling may modify the response to forcings and is an important area of future work (Sutton and Mathieu 2002; Dong et al. 2013b). Another extension not addressed here is the anthropogenic contribution to the SST/SIE changes.

Conclusions. The European summer of 2013 was marked by hot and dry conditions in western Europe associated with a northward shifted Atlantic storm track and a positive phase of the SNAO. Model results suggest that, relative to a 1964–93 reference period, changes in SST/SIE explain 63% ($\pm 26\%$) of the area-

averaged warming signal over western Europe, with the remaining 37% ($\pm 29\%$) explained by the direct impact of changes in anthropogenic radiative forcings from GHG and aerosols. The results further suggest that the anomalous atmospheric circulation, and associated low rainfall, were also influenced both by changes in SST/SIE and by the direct impact of changes in radiative forcings; however, the magnitude

of the forced signals in these variables is much less, relative to internal variability, than for surface air temperature. Further evidence suggests that changes in North Atlantic SST were likely an important factor in explaining the striking contrast between the European summers of 2013 and that of 2012. A major area for further work is to understand more completely the mechanisms that explain these influences.

19. CONTRIBUTION OF ATMOSPHERIC CIRCULATION TO WET SOUTHERN EUROPEAN WINTER OF 2013

PASCAL YIOU AND JULIEN CATTIAUX

Winter 2013 was the second wettest since 1948 in southern Europe. This is partially explained by the atmospheric circulation. We suspect the warm Atlantic Ocean to have amplified the precipitation extreme.

Introduction. Southern Europe witnessed anomalously high precipitation amounts, associated with anomalously low temperatures, during the winter of 2013. The goal of this paper is to put this regional event into the context of long-term variability. In Europe, studies have highlighted North Atlantic atmospheric dynamics as the main driver of winter precipitation and temperatures on both intra-seasonal and inter-annual time scales (e.g., Cattiaux et al. 2010; Vautard and Yiou 2009). Here, we focus on the contribution of large-scale circulations the winter 2013 precipitation anomalies using the same flow-analogue approach as in the analysis of summer 2012 North European precipitation by Yiou and Cattiaux (2013).

Data. We use in situ measurements provided by the European Climate Assessment dataset at 5231 stations over the period 1948–2013 (Klein-Tank et al. 2002). We compute anomalies relative to a 1971–2000 climatology. The daily climatology is obtained by averaging over each calendar day in 1971–2000, then smoothing by splines. We selected 510 stations on the basis of (a) an altitude lower than 800 m, longitudes between 10°W–40°E, and latitudes between 30°–72°N; (b) the availability of more than 70% of daily values between 1 January 1971 and 31 December 2000 for a reliable estimate of the climatology; and (c) the availability of more than 90% of daily values between 1 January 2013 and 31 December 2013 for a reliable estimate of the 2013

anomalies. We averaged precipitation values over Southern Europe (10°W–20°E; 35°–50°N, see Fig. 19.1) after selecting (d) only one station per 0.5° × 0.5° latitude/longitude box for spatial homogeneity, hence leaving 45 stations in that region. Although we mainly focus on cumulative precipitation, we also computed the precipitation frequency (or fraction of wet days) for each month as in Vautard et al. (2007) and Vautard and Yiou (2009). The precipitation frequency is the empirical probability in a given month of observing a daily precipitation amount larger than 0.5 mm. It provides an indicator of the temporal continuity of precipitation.

Observed rainfall anomaly. Anomalously high precipitation amounts are observed in Southern Europe (e.g., France, Spain, and Italy) in February–March 2013 (Fig. 19.1, upper panels). These anomalously high amounts culminate in March 2013. Those winter wet conditions contrast with drier than usual conditions in Northern Europe (e.g., United Kingdom, Netherlands, Germany, and Scandinavia). The precipitation frequency during winter 2013 (from 1 January to 31 March 2013) also has positive anomalies in Southern Europe, indicating that the rain episodes lasted for prolonged periods of time (Supplementary Fig. S19.1). Therefore, the generally wet conditions mainly concern the southern part of Europe for winter 2013 (mainly February and March). Besides, cold anomalies were observed over

Western Europe during this season (Supplementary Fig. S19.2).

The highest daily precipitation amounts on average over Southern Europe occurred in February and March (Fig. 19.2a), as did the longest winter spells of precipitation (32 days). Part of that precipitation was snow, which caused havoc in French public transportation, especially in the middle of March 2013, and broke local records of snow amounts in the French Pyrenees. On average over Southern Europe during the whole winter season (JFM), 2013 is the second wettest winter since the beginning of our record (1948) behind 1979. This points to the exceptional character of the Southern Europe 2013 winter. The temperatures were also anomalously low in February and March in Southern Europe, contrasting with Eastern Europe, especially in February (Supplementary Fig. S19.2), but the temperature anomaly was close to the median (e.g., 33rd coldest year on record), therefore, justifying our focus on precipitation. The temperature anomalies are not as well reconstructed by the circulation analogues in February 2013, especially over France. This is explained

by the fact that the February cold temperatures were due to persisting snow cover (e.g., in France) rather than the atmospheric circulation itself.

Contribution of the atmospheric circulation. The contribution of large-scale dynamics to the precipitation anomalies of 1948–2013 is estimated from the same flow-analogue approach as used in Cattiaux and Yiou (2012) or Yiou and Cattiaux (2013). For each day, we selected the 20 days with the most correlated sea level pressure (SLP) among days of other years but within a moving window of 60 calendar days to account for seasonality (see Yiou et al. 2007 for details). SLP anomalies are derived from the NCEP–NCAR reanalyses (Kistler et al. 2001) and are considered over the period 1948–2013 and the area (80°W–20°E, 22.5°–70°N).

For each station and each day, we computed the mean of the 20 analogue composites. The mean analogue precipitation of winter 2013 (averaged over 20 analogue days) is higher than usual in Southern Europe, both in terms of precipitation amount (Fig. 19.1) and frequency (Supplementary Fig.

S19.1). Spatial patterns of analogue precipitation follow the observed ones, albeit with lower amplitudes (Fig. 19.1). The spatial correlations are 0.61, 0.64, and 0.79 in January to March, respectively. On a daily time scale over Southern Europe, the precipitation analogues closely follow the observed averages (Fig. 19.2a; temporal correlation $r = 0.57$; p -value $< 5 \times 10^{-3}$). This confirms that the large-scale atmospheric circulation influences the precipitation amounts at the intraseasonal scale.

In order to further describe the circulation patterns of the winter 2013, we used the clustering approach of Michelangeli et al. (1995), and adapted by Yiou

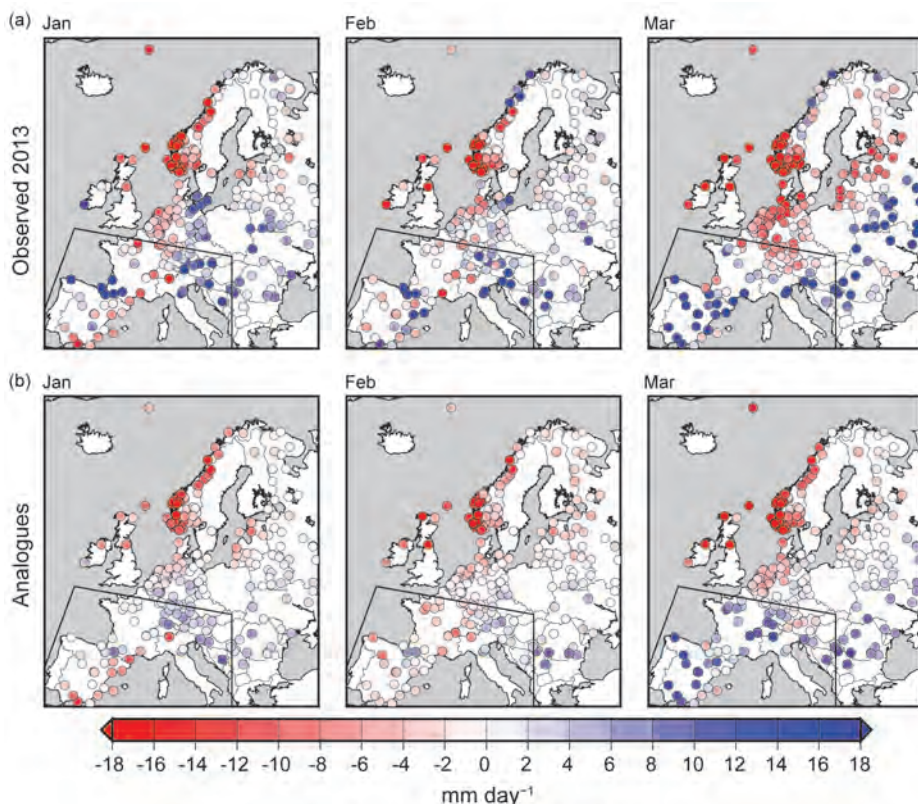


FIG. 19.1. Anomalies of precipitation over Europe (in mm day^{-1}) for the winter months in 2013 (Jan–Mar). The colored points represent the 510 ECA&D stations we retained. The polygon outlines the region over which the averages are computed (10°W–20°E; 35°–49°N). (a) Observed precipitation anomalies. (b) Mean precipitation obtained from 20 analogues of circulation.

et al. (2008), to derive the four preferential winter weather regimes over the North Atlantic region and the period 1948–2013. The rationale for this analysis, which complements the flow-analogue approach, is to visualize the atmospheric circulation temporal variability and associate episodes of high precipitation with circulation patterns (Fig. 19.2a). The weather regimes are computed from SLP anomalies during 1948–2013. These four weather regimes correspond to anomalies in the flow and affect the advection of temperature and humidity (Fig. 19.2c–f). We find that the wet spells over Southern Europe correspond with episodes of the Atlantic Ridge (AR) in February and the negative phase of the North Atlantic Oscillation (NAO–) in March, which yields a weak pressure dipole over Iceland and the Azores (Fig. 19.2d–e). When the circulation yields anticyclonic patterns over Scandinavia (blocking), daily precipitation amounts fall to low values.

Trends of precipitation. We computed the linear trends of the seasonal average precipitation over the outline region (Fig. 19.2b) for the period between 1971 and 2013. The trends for all seasons are not statistically significant (p -values > 0.1). The mean analogue precipitation for winter is well correlated ($r = 0.86$, p -value < 10–15) with the observed average (Fig. 19.2b), and the analogues yield a negative winter trend found in the

observations, although it is not statistically significant (p -value = 0.26). The winter 2013 median analogue

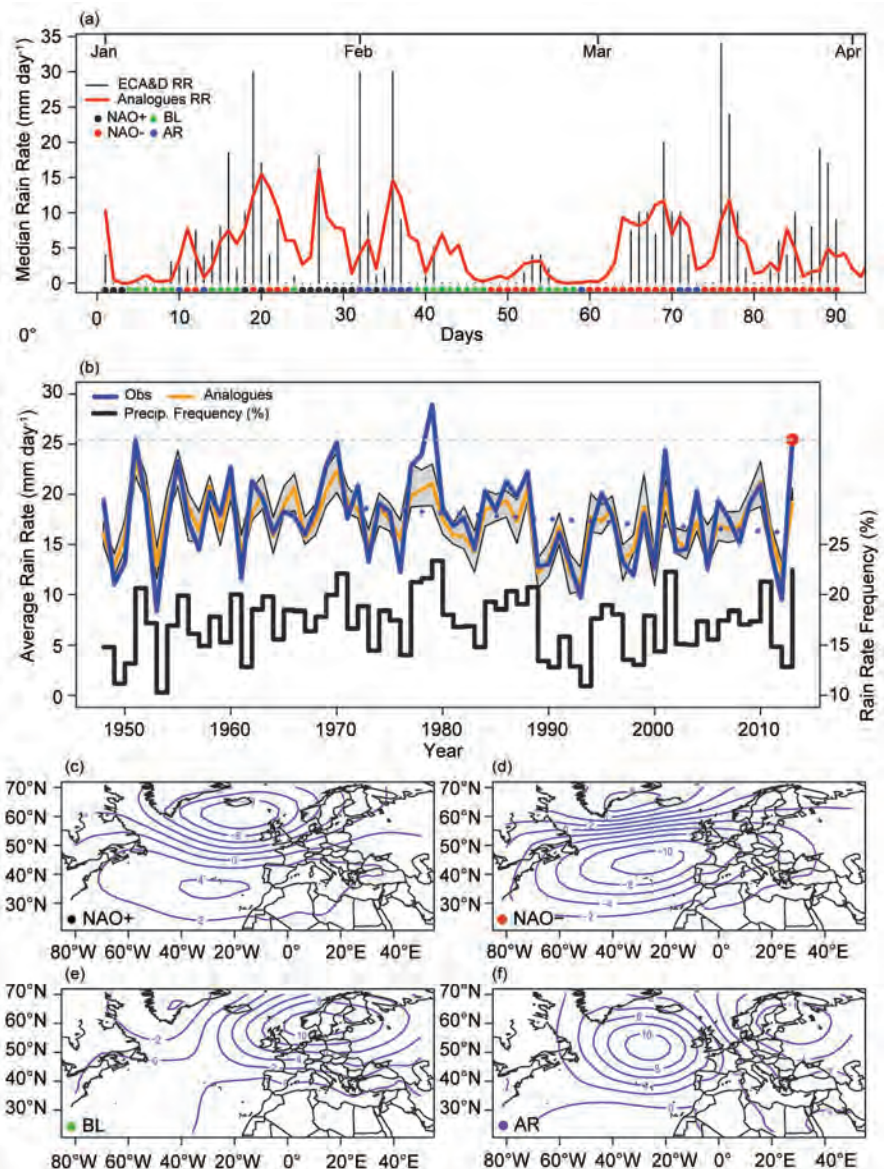


FIG. 19.2. Temporal evolution of precipitation in the outlined Southern Europe region and winter weather regimes. (a) Temporal evolution of precipitation in Jan–Mar 2013 (black vertical lines). The thick red line represents the median of analogue composites across stations and the 20 analogues. The colored points at the bottom of the panel indicate the daily weather regime. (b) Time series of average precipitation for winter (JFM, blue) between 1948 and 2013. A red dot and a horizontal dashed line indicate the value for 2013. Dotted lines are the linear trends between 1971 and 2013. The orange line represents the precipitation mean over Northern Europe stations of the median of analogues (in %). The gray shading is the 10th and 90th percentile of the precipitation analogues. The black line represents the average precipitation frequency (in %) in Jan–Mar. (c–f) Summer weather regimes computed from a classification of NCEP sea level pressure data. We use the terminology of Michelangeli et al. (1995): positive North Atlantic Oscillation (c: NAO+), negative North Atlantic Oscillation (d: NAO–), Scandinavian Blocking (e: BL), and Atlantic Ridge (f: AR). The isolines represent anomalies with respect to a 1971–2000 climatology.

precipitation amount is only the 18th highest of the analogue time series, showing that even if the atmospheric conditions were favorable to wet conditions over Southern Europe, they do not fully explain the exceptional character of the precipitation anomaly. We conjecture that a potential amplifying cause could be that the oceanic air masses carried by regimes of westerly winds were moister than usual due to warmer SSTs in the Northeast Atlantic (between 0.5 and 1.5 K above normal). We performed an additional analysis by searching circulation analogues among the years of warm Northeast Atlantic SST (i.e., above the 1971–2000 average). The mean monthly European precipitation amounts reconstructed from such “filtered” analogues exceed those of “regular” analogues, picked over 1948–2012 (not shown). Although this is not a definite proof, this pleads in favor of this mechanism.

Conclusions. Our analysis suggests that the high precipitation amounts were mainly caused by the cyclonic conditions (NAO– and Atlantic Ridge) that prevailed during the late winter (February and March) over the North Atlantic. Such conditions brought moist air over Southern Europe. This conclusion is drawn from the significant correlations over Europe between the observed and the analogue precipitation, deduced from the North Atlantic atmospheric circulation. The extreme precipitation amounts, not fully explained by the atmospheric circulation, are conjectured to be due to a warmer Northeast Atlantic with more moist air (Trigo et al. 2013).

The trend in winter precipitation over Southern Europe is negative but not statistically significant. The frequency of cyclonic regimes over Scandinavia (NAO– and Atlantic Ridge) has also slightly decreased, albeit not significantly (not shown).

20. THE HEAVY PRECIPITATION EVENT OF MAY–JUNE 2013 IN THE UPPER DANUBE AND ELBE BASINS

NATHALIE SCHALLER, FRIEDERIKE E. L. OTTO, GEERT JAN VAN OLDENBORGH, NEIL R. MASSEY,
SARAH SPARROW, AND MYLES R. ALLEN

An observation-based analysis and large simulation ensembles show no evidence that climate change made heavy precipitation in the upper Danube and Elbe basins in May–June, such as observed in 2013, more likely.

Introduction. After an anomalously cold, cloudy, and rainy spring in central Europe, regions in Germany, Switzerland, Austria, and the Czech Republic received large amounts of precipitation between 30 May and 2 June 2013, with some places receiving the usual monthly precipitation amount within one or two days (CIB 2013). As shown in Fig. 20.1a, the maximum precipitation fell in the upper Danube and Elbe catchments, which led to severe flooding along these rivers in the following weeks. Grams et al. (2014) identified that during the four-day event, three consecutive low pressure systems moved from east to west over central Europe, due to a Rossby wave breaking, with the Alps acting as a wall. Thus, the low pressure systems remained stationary—a rare weather situation that occasionally occurs in summer but is extremely unusual in spring. Hydrological processes, in particular the late snow melt and saturated soils

in some regions in Germany even before the event caused by the unusual spring weather, played an important role in the ensuing Danube and Elbe floods (BfG-DWD 2013). It has been suggested that Arctic warming has increased the chances of flooding on the Elbe and Danube (Petoukhov et al. 2013). However, Hirabayashi et al. (2013) showed that floods in central Europe should decrease with climate change, even as flooding in other parts of Europe has been attributed to anthropogenic warming (Pall et al. 2011). In this study, we analyze whether and to what extent anthropogenic climate change changed the odds of high precipitation in the upper Elbe and Danube catchments in May–June.

Methods. To obtain the very large ensembles of regional climate simulations needed to quantify the role of anthropogenic climate in the heavy precipitation

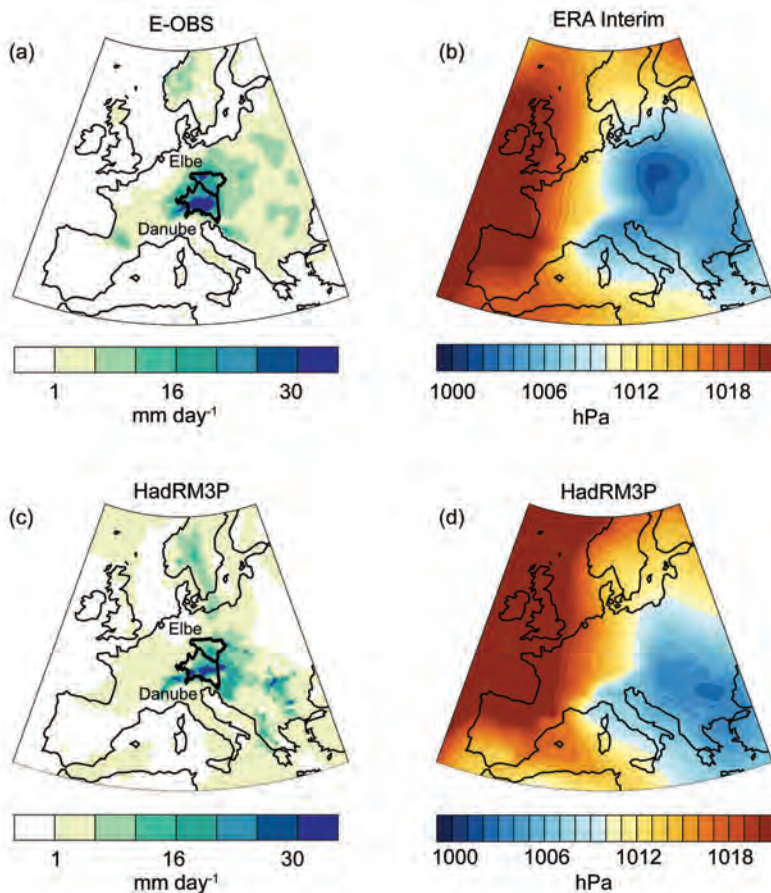


FIG. 20.1. (a) Four-day precipitation average 30 May 2013–02 Jun 2013 in the E-OBS dataset. (b) Mean sea level pressure averaged over the same four-day period in the ERA Interim reanalysis. (c) Average precipitation for the wettest four consecutive days during May–Jun in the all forcings simulations with HadRM3P. (d) Mean sea level pressure averaged over the wettest four consecutive days during May–Jun in the all forcings simulations with HadRM3P. The upper Danube and Elbe catchments are drawn in (a) and (c).

event in central Europe in spring 2013, we make use of the citizen science modeling capability weather@home (Massey et al. 2014). In this study, we perform two types of experiments, the first one simulating the year 2013 under current climate conditions and a second one representing 25 different possible analogous years in a counterfactual world as it might have been without anthropogenic climate change. The Met Office Hadley Centre Atmosphere-only general circulation Model (HadAM3P; Pope et al. 2000), with a nested regional configuration over Europe (HadRM3P), is used to perform these ensemble simulations. Massey et al. (2014) evaluated the ability of the regional climate model (RCM) and showed that the model performs well but tends to underestimate May–June precipitation over central Europe. The first perturbed initial conditions en-

semble representing the year 2013 (“all forcings”) under present day climate conditions is forced with observed aerosols and greenhouse gas composition as well as SST and sea ice fraction values from 2013 obtained from the Operational Sea Surface Temperature and Sea Ice Analysis (OSTIA) dataset (Stark et al. 2007). The 25 perturbed initial conditions ensembles (“natural”) representing the analogous year in the counterfactual experiment are forced with preindustrial atmospheric gas composition and the sea ice extent that corresponds to the year of maximum sea ice extent in each hemisphere of the OSTIA record, which starts in January 1985. The corresponding SSTs are obtained by subtracting 25 estimates of the human influence on SST from the 2013 OSTIA SST values. These 25 SST anomaly patterns are obtained by calculating the difference between nonindustrial and present day simulations for available Coupled Model Intercomparison Project Phase 5 (CMIP5) models (Taylor et al. 2012; see Supplementary Material). Additionally, we also estimate the trend of four-day extremes with the European daily high-resolution (0.25°) gridded (E-OBS version 9.0) precipitation

fields (Haylock et al. 2008). For both the model and observation analyses, we consider maximum four-day average precipitation in the upper Elbe (south of 51°N) and Danube (west of 15°E) catchment areas.

Modeling of the event. A question that arises when using the described setup is whether the model is able to simulate the extreme event considered and the factors affecting it. If the model represents the event accurately, this adds confidence in the resulting attribution statement, bearing in mind that no model is a perfect representation of the real world. Statistically, van Haren et al. (2013a,b) showed that state-of-the-art RCMs represent both the climatology and trends in summer mean and extreme rainfall well; there is no trend in observations or model simulations in the region of study. Regarding the mechanism, Fig. 20.1

shows the four-day precipitation average during the event in the E-OBS dataset and the corresponding mean sea level pressure (MSLP) averaged over these four days in the European Centre for Medium-Range Weather Forecasts Re-Analysis, ERA Interim (Dee et al. 2011). To assess the model's ability to simulate this type of heavy precipitation event, we identified the ensemble member in the all-forcings simulations with the wettest four days in the upper Danube and Elbe catchments. As shown in Fig. 20.1c,d, the model is able to represent a similar event to what occurred in spring 2013 in terms of precipitation and MSLP; although, overall, the model appears to slightly underestimate the extent and intensity of the heavy precipitation event. Comparing the maximum four-day precipitation averages between Fig. 20.2a,b and Fig. 20.2c,d for return times up to 100 years indicates that the model underestimates Danube precipitation by about 20% and overestimates the Elbe precipitation roughly the same amount.

Influence of climate change on the floods. There are several methods to attribute whether the odds of an extreme event occurring have been affected by climate change. Here we compare two of these in order to increase the confidence in the resulting statement. Figure 20.2 shows return times for the maximum four-day average precipitation in the E-OBS dataset and in HadRM3P in May–June. Figure 20.2a,b shows that the 2013 event (purple line) was very unusual in these months, with return times larger than 200 years for the upper Danube and Elbe catchments (in agreement with the observation that none of the six larger floods in Bratislava since 1500 occurred in these months; Pekárová et al. 2013). The time series of the maximum four-day average in May or June 1950–2012 is fitted to a generalized extreme value (GEV) distribution with the position parameter μ and scale parameter σ simultaneously varying exponentially with the global mean temperature (smoothed with

a four-year running mean) as a first approximation of possible effects of global warming (other choices for the trend give very similar results). The 200 years are the lower bound of the 95% confidence interval estimated with a nonparametric bootstrap (upper blue and red lines). There were events in July and August with higher precipitation, but the impact of heavy precipitation events in the summer months is smaller as a higher proportion of precipitation gets absorbed in the soils. The trends in extremes before 2013 have different signs over the two basins; neither is significantly different from zero at $p < 0.1$. This is also shown in Fig. 20.2a,b where the fitted return times are similar in the 1950 climate (blue lines) and the 2013 climate (lines).

Similar figures are produced from the model simulations with and without climate change (Fig. 20.2c,d). Here, each red dot represents the average

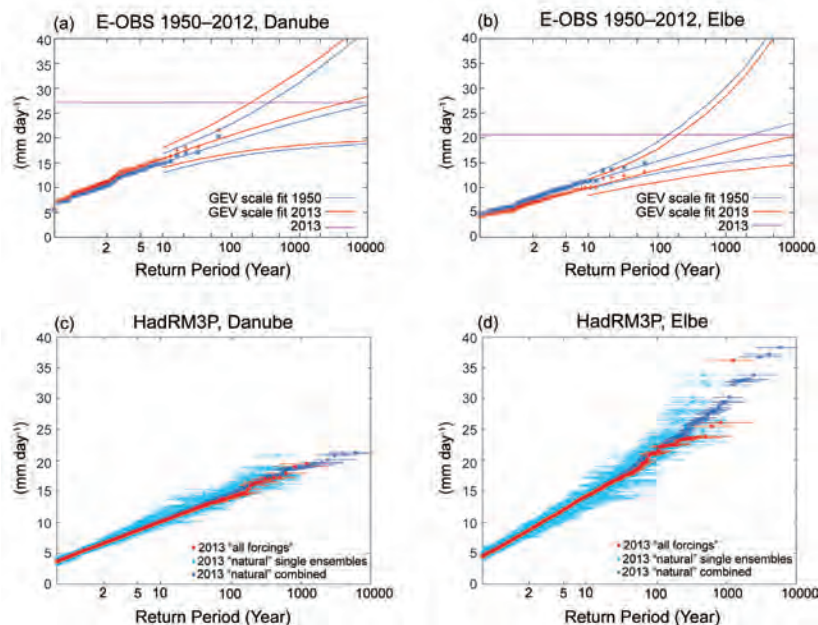


FIG. 20.2. Return time plots for the maximum four-day precipitation average during May–Jun in the E-OBS dataset (a), (b) and in HadRM3P (c), (d) for the upper Danube catchment (left) and the upper Elbe catchment (right). For the E-OBS dataset, red crosses indicate years from 1950 to 2012 after correction for the fitted trend to the year 2013 and the red lines correspond to the 95% confidence interval estimated with a nonparametric bootstrap. Blue crosses and lines represent the same as the red but in the climate of 1950, and the horizontal purple line represents the observed value for May–Jun 2013. For the HadRM3P datasets, the red dots indicate May–Jun possible four-day maximum precipitation events in a large ensemble of HadRM3P simulations of the year 2013, while the light blue dots indicate possible May–Jun four-day maximum precipitation events in 25 different ensemble simulations of the year 2013 as it might have been without climate change. The blue dots represent the 25 natural ensembles aggregated together. The error-bars correspond to the 5%–95% confidence interval estimated with a non-parametric bootstrap.

precipitation over the wettest four-day period in May and June in each of the all forcings simulation ensemble members. Each light blue dot represents the average over the wettest four-day period in May and June in the natural simulations with each of the 25 ensembles forming a separate curve corresponding to the 25 different SST patterns. In addition, all of these 25 natural ensembles have been aggregated and are represented as blue dots. The error bars give the 5%–95% confidence interval of the return periods, derived from bootstrapping several hundred times from the individual ensembles. In the return time plots for the wetter end of the distribution, approximately equal numbers of the 25 different natural simulations (light blue) are found on both sides of the actual conditions curve (red), which is not statistically different from the aggregated natural ensembles (blue). This indicates no evidence that human-induced climate change increased the odds of such an event to occur, nor any evidence that it decreased these odds, in agreement with the E-OBS analysis. Note that this answers a slightly different question from the observational analysis. This analysis considers the odds of an event like the May–June 2013 heavy precipitation happening given the observed SST and sea ice patterns as a function of anthropogenic forcing, whereas the observational analysis only looks at the trend without attribution and without the specific SST and sea ice.

It has been suggested (BfG-DWD 2013) that increased persistence caused by increased CO₂ concentration played a role in the discussed event based on the hypothesis that the decreased meridional temperature gradient would cause more persistent weather patterns at midlatitudes and, consequently, an increased chance of extreme weather like droughts or floods (Francis and Vavrus 2012;

Petoukhov et al. 2013). The fact that polar regions warm faster than lower latitudes under global warming and, hence, the meridional temperature gradient decreases, are well-represented mechanisms in current models and, therefore, the model setup can serve as a valuable check on this hypothesis. Given that no change in return times could be detected between the all forcings and the natural simulations, the results do not support the hypothesis that the Arctic warming increases persistence of a weather type and the associated increase in probability for floods in central Europe, in agreement with Wallace et al. (2014) for example. Analyses of historical floods on the Elbe (Mudelsee et al. 2003) and Danube (Pekárová et al. 2013) also find no change in summer floods.

Conclusions. In this study, we quantify the influence of anthropogenic climate change on the heavy precipitation event in spring 2013 in the upper Danube and Elbe catchments with two methods. Both the model-based analysis, with high statistics but possibly systematic errors, and the observation-based analysis, with lower statistics, consistently show that there was no significant effect of the increased greenhouse gas concentrations on this four-day precipitation event. While this study focuses on precipitation, further analyses should focus on runoff or river flows to conclusively attribute the role of climate change on the floods in the two catchments. Flooding results from interactions between weather events, hydrological processes, and infrastructure. While the heavy precipitation event was rare in itself for the time of year, the weather situation during the previous months and the resulting late snowmelt and saturated soils amplified the magnitude of the Danube and Elbe floods.

21. THE EXTREME SNOW ACCUMULATION IN THE WESTERN SPANISH PYRENEES DURING WINTER AND SPRING 2013

JUAN A. AÑEL, JUAN IGNACIO LÓPEZ-MORENO, FRIEDRIKE E. L. OTTO, SERGIO VICENTE-SERRANO, NATHALIE SCHALLER, NEIL MASSEY, SAMUEL T. BUISÁN, AND MYLES R. ALLEN

Natural climatic variability was apparently the main driver in the extreme cumulative snowfall that fell in the Pyrenees in 2013.

Introduction. Snow accumulation in the Pyrenees has shown a statistically significant negative trend since 1950 (López-Moreno 2005) in a similar way to other European mountain areas (Marty 2008). In the Pyrenees, the reduction in snow cover has mostly been associated with decreasing winter precipitation, which in turn has been related to a positive trend of the North Atlantic Oscillation index (NAOi, López-Moreno and Vicente-Serrano 2007; López-Moreno et al. 2010). However, this long-term trend is superimposed upon a high interannual variability, which leads to frequent changes between snow-poor and snow-rich years (Buisán et al. 2014). In the last decade the Pyrenees have recorded 5 years that have clearly exceeded the long-term average (above 75th percentile) winter precipitation, leading to deeper than normal snow-cover. This has been associated with a continuing trend of negative NAO conditions (Vicente-Serrano et al. 2011). Thus we investigate whether a different driver, anthropogenic emissions, played a role in changing the frequency of occurrence of deep and extensive snow cover using the example of the wet and snow rich winter and spring 2013. This year, despite having temperatures close to the long-term average for winter and spring, recorded far above normal precipitation from January to June over the Atlantic coast of the Iberian Peninsula and western Pyrenees. This wet anomaly was a consequence of an above average frequency of advections from the north and north-west, leading to the January–June precipitation events exceeding 100–200 year return periods (considering a reference period of only 33 years, 1980–2012, and using a generalized Pareto distribution). In the case of the Pyrenees, the anomaly of recorded precipitation was less extreme in the east than in the west (Fig. 21.1a).

Empirical evidence. The accumulated precipitation in this very wet winter and spring (January to June, both included) exceeded by far the 95th percentile in the western Pyrenees with only slightly above average snow cover in the central and eastern Pyrenees (Fig. 21.1b). In terms of snowfall days (snow precipitating within 24 hours), the anomaly was only measured at stations in the western Pyrenees at mid- and high elevation, where they exceeded the 95th percentile by a large margin. In contrast, low elevation stations in the western Pyrenees (i.e., Valcarlos) and inland stations (Torla and Eriste) observed values consistent with the normal long-term interannual variability (Fig. 21.1c). At Linza station (1330 m a.s.l.), at which a continuous snowpack is not guaranteed (López-Moreno et al. 2007), snow cover remained from early January to late April, recording a snow depth of 235 cm in only 31 days and a snow net accumulation of 554 cm between January and April. In Izas station (2080 m a.s.l.) snow lasted until early July and the snowpack exceeded 4 meters depth, accumulating 355 net cm in 35 days from mid-January to mid-February, and maintained a thickness above 300 cm until mid-June (Fig. 21.1d). Table 21.1 shows the values of the total snow water equivalent (SWE) and estimated snowfall computed from SWE for some stations where it was available. SWE was measured with GMON3 sensors from Campbell Scientific operated by the Ebro Basin District Authority. The snow data (both precipitation and number of days) were provided by the Spanish national weather service (Agencia Estatal de Meteorología; AEMET) except for Izas, a station operated by the Instituto Pirenaico de Ecología-Spanish national research council (IPE-CSIC).

The hydrological consequence of this extremely wet and snow-rich year was that the river flow of

the Ebro in Zaragoza, where the river has collected the main tributaries that drain headwaters of western Pyrenees, exceeded the 90th percentile of average flow from January to June. This is clear from the analysis of the data provided by the Ebro Basin District Authority (Fig. 21.1e). The largest anomalies occurred in February as a consequence of heavy rains at low elevation, and in June in response to the melting of the anomalously deep snowpack, which lasted

until late in the season in the mid and high elevated areas of the Pyrenees.

The anomalous snow accumulation in 2013 is of great interest if it suggests that, despite a clear warming trend occurring in the region since the early 20th century (El-Kenawy et al. 2012), it is still possible to observe snow-record years. However, at low and mid-elevation accumulation of snow in wet years is expected to decrease with increasing regional temperatures in a globally warming world.

Evaluation of the impact of climate change. In order to assess whether and to what extent anthropogenic climate change has played a role in the chances of occurrence of such an extreme event, we performed a series of climate simulations using the ClimatePrediction.net (Allen 1999) / weather@home system (Massey et al. 2014). We used the same model and configuration as the study by Schaller et al. ("The heavy precipitation event of May–June 2013 in the upper Danube and Elbe basins" in this report). We used the atmosphere only general circulation model HadAM3P to drive the regional version of the same model, HadRM3P, over Europe at 50-km resolution. The region considered for the evaluation of cumulative precipitated snow from the model was 2°W–3.5°E and 41.5°–44°N, covering the full Pyrenees with 49 grid points from the model (see Fig. 21.2). The variable from the model is the amount of snow, computed for each time step in kg m^{-2} . Two different ensembles of possible weather in the relevant seasons in the Pyrenees were simulated: one using observed greenhouse gases, sea surface temperatures (SSTs) and sea ice to drive the model, the other one using preindustrial values of aerosols and greenhouse gases, 14 small ensembles with different SST patterns of warming removed and a sea ice fraction equivalent to observed values in 1985 (see "The heavy precipitation event of May–June 2013 in the upper Danube and Elbe basins" in this report). Given that we have no method or metric of deciding within

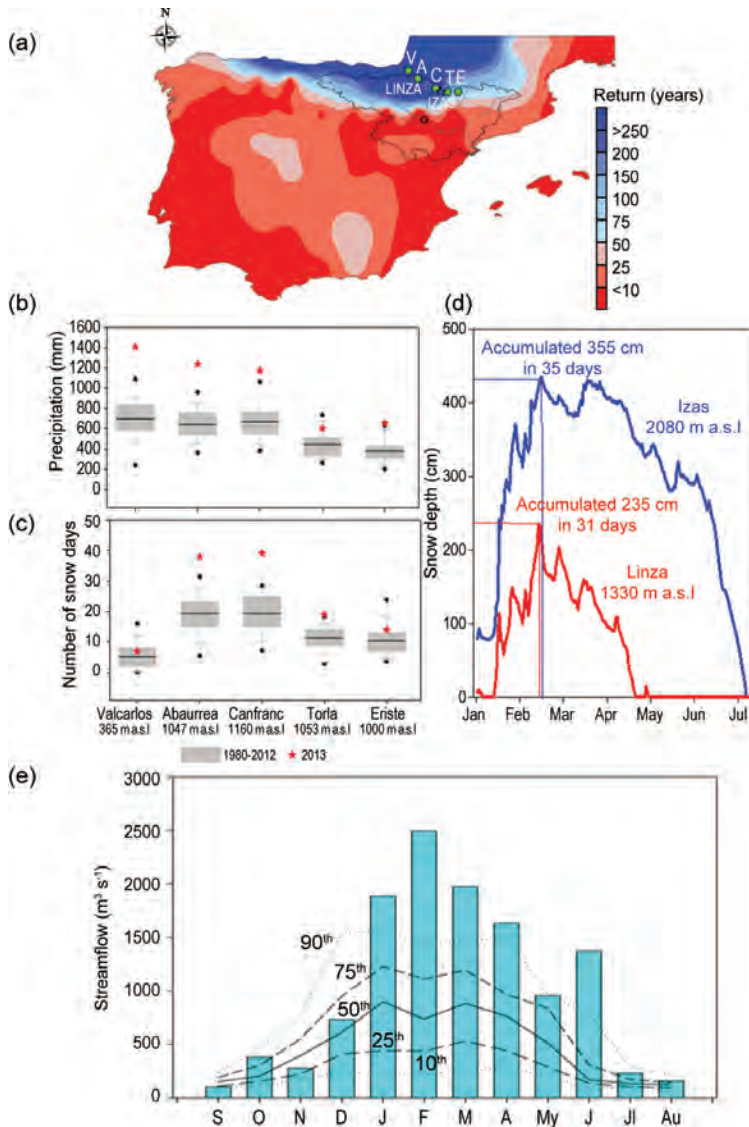


FIG. 21.1. (a) Return period of accumulated precipitation from January to June in the Iberian Peninsula; (b) Box plots showing the median, 5th, 25th, 75th, and 95th percentiles of precipitation in selected observatories [Valcarlos (V), Abaurrea (A), Canfranc (C), Torla (T) and Eriste (E)] during the period 1980–2012; red stars indicate the value for 2013; (c) Same as (b) for snow days; (d) daily snow accumulation in Linza (1330 m a.s.l.) and Izas (2080 m a.s.l.) observatories; (e) Monthly average river flow in the Ebro river at Zaragoza, and the long-term (1980–2012) average, 10th, 25th, 75th, and 90th percentiles.

the warming-removed ensemble which pattern of warming is closer to the truth, we treat them as equally likely and thus increase the robustness of the statements we can make by increasing the sample size to one large ensemble instead of 14 small ones. The number of members in each ensemble were 261 and 583 respectively. They were all the members available.

We verified that both data distributions (“all forcings” and “natural forcings”) are statistical independent using a Kolmogorov-Smirnov two-sample test (Wilks 2006). Figure 21.2 shows the return times (chances of exceeding the threshold of snow cover on the vertical axis in a given year) for the two different ensembles. These model simulations suggest that return times (a measure of the probability of occurrence) for a given snowfall value over the Pyrenees have slightly increased with climate change but the two curves representing the different ensembles are not statistically significant for return times above 10 years.

As pointed out for most of the stations the snow accumulated was above the 95th percentile. Therefore to assess such an extreme event we should look for a return time exceeding this value in the simulations. In the all-forcings ensemble the 95th percentile corresponds to 1687 mm with a return time of 18.8 years. The equivalent in the natural has a return time of 16.8 years. As said, the return time has increased in comparison to a scenario without climate change effects. When comparing the observations and the model results, several issues need to be taken into account. First, the mean climatological value of cumulative SWE for January–June over the period 1980–2012 for the five stations of Figure 21.1a is 565 mm but for the all-forcings simulations from Fig. 21.2b it is 287 mm. This implies the existence of a dry bias in the model (Pope et al. 2000). Elevation affects the amount of snow precipitation but comparing the extreme values from Table 21.1 with the median values in Fig. 21.1b we can see that the differences are similar for all the cases. Therefore to use a comparison of the percentile seems to be enough to assess potential changes in the return time. However the size of the horizontal grid probably has an effect reducing the maximum height represented in the region and therefore prevents getting the extreme snow values observed in the highest locations.

Table 21.1. Snow water equivalent for nine stations in the Pyrenees from January to June 2013.

Station	Altitude (m above sea level)	Snow Water Equivalent (mm)
Quimboa	1810	2033.7
Izas	2080	2431.5
Canal Roya	1971	1963.1
Bachimaña	2220	2349.8
Lapazosa	2140	2604.0
Ordiceto	2380	2235.8
Renclusa	2180	1971.6
Salenques	2600	2023.4
Eriste-2	2350	1645.1

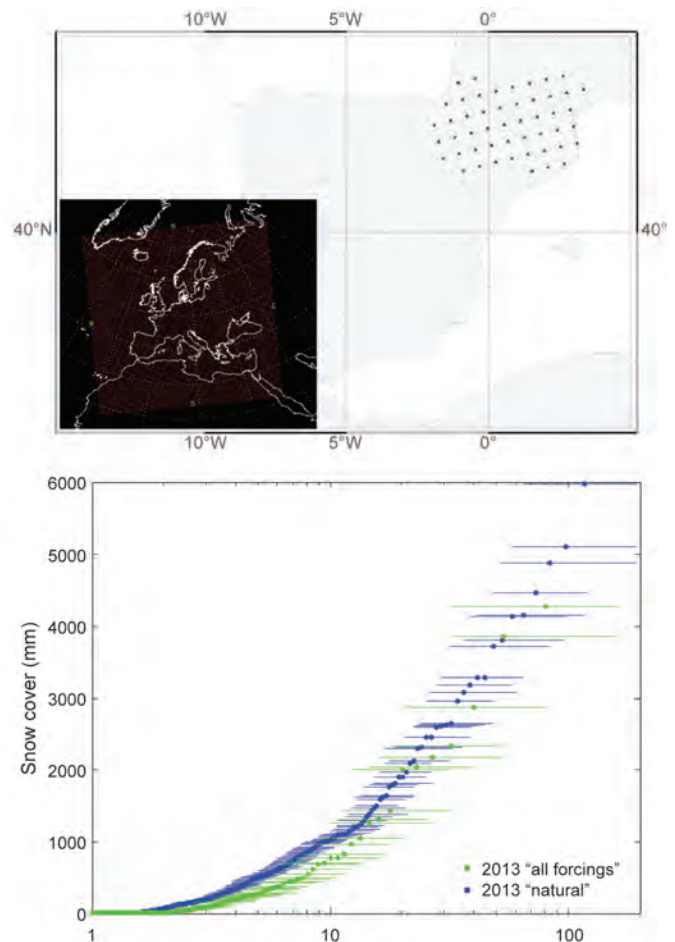


Fig. 21.2. (Upper) Grid points from the model used for the study. The map in the lower corner shows the grid of the regional model for Europe. (Lower) Return time plot for the accumulated snow for January to June 2013. Blue dots correspond to the simulations having into account preindustrial atmospheric conditions and green dots correspond to the simulations with 2013 values of CO₂, sea surface temperature and sea ice fraction. The horizontal error bars represent 5%–95% confidence intervals obtained by non-parametric bootstrapping (resampling with replacement) on the two ensembles.

Conclusion. The empirical evidence shows that the snowfall over the Pyrenees from January to June of 2013 was a rare weather event. Despite five winters in the last decade clearly exceeding the long-term average (above the 75th percentile), we have not been able to find a link between the recent increase in greater-than-normal snowfall seasons and anthropogenic forcing of climate in our model simulations.

On the contrary, simulating precipitation and snow cover in the Pyrenees with and without the influence of anthropogenic greenhouse gas emissions shows a decrease in the occurrence probability of the event, although the result is not statistically significant for rare phenomena. In this assessment we find no evidence of a significant influence of anthropogenic emissions on this event.

22. A VIOLENT MIDLATITUDE STORM IN NORTHERN GERMANY AND DENMARK, 28 OCTOBER 2013

HANS VON STORCH, FRAUKE FESER, SUSANNE HAESELER, CHRISTIANA LEFEBVRE, AND MARTIN STENDEL

A strong storm on 28 October 2013 over northern Germany and southern Denmark fits a slight increase in storminess during recent decades. However, the increase constitutes part of multidecadal variability.

Introduction. In late October 2013, a strong cyclone moved across northern Europe causing massive damages and interruptions. In Germany, the storm was named “Christian”, in Denmark, “Allan”.

The impact of the storm was considerable. At least 15 people perished, a large number of trees were blown down, power supply broke down, train connections were interrupted, streets were impassable, and the Øresund Bridge between Denmark and Sweden had to be closed (Haeseler et al. 2013).

Synoptic analysis. The cyclone formed off the coast of Newfoundland, favored by large temperature differences between cold air behind a previous storm there and warm air related to the remnants of a former tropical storm. At 18 UTC on Sunday, 27 October, the storm was located southwest of Ireland; then, it crossed the southern part of the United Kingdom, moved across the North Sea, and made landfall in northern Denmark. In northern Germany, the first storm gusts were observed at about 1100 UTC. The storm moved on northeastward across

southern Sweden and Finland towards Russia, where it weakened considerably on 29 October.

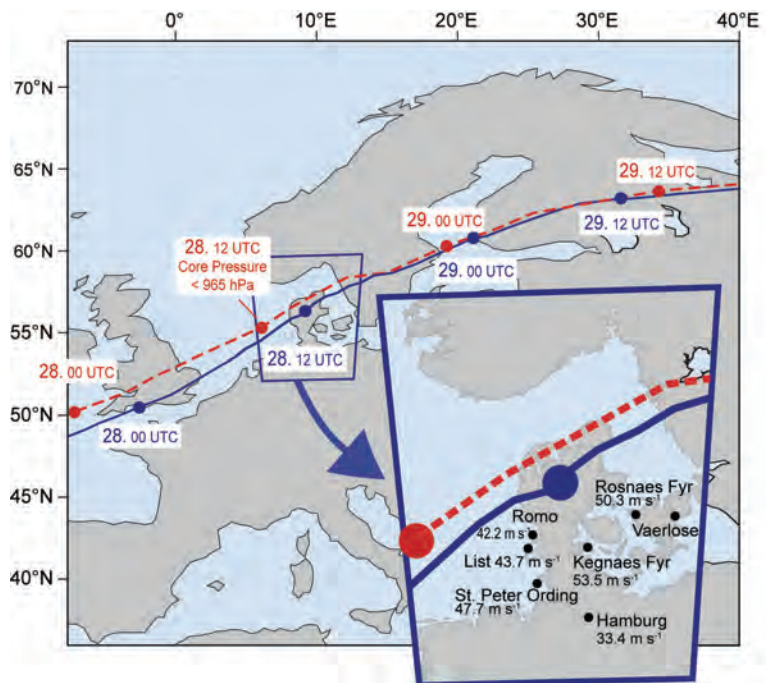


FIG. 22.1. Track of the Christian/Allan storm according to an analysis by Deutscher Wetterdienst [(German National Meteorological Service (red, dashed))] and to the reconstruction in CoastDat (blue, continuous). The box, showing the mentioned stations with measured peak gusts, marks the area for the storm statistics.

In Germany, peak wind speeds ranking 11 ($28.5\text{--}32.6\text{ m s}^{-1}$) and 12 ($\geq 32.7\text{ m s}^{-1}$) on the Beaufort scale (Bft) were observed at many stations along the North and Baltic Seas coasts as well as further inland, with a maximum of 47.7 m s^{-1} at St Peter Ording, a location facing the North Sea. Even 10-minute sustained winds reached Bft 12, which is a rare event. Very high wind speeds were also observed in Denmark, even far away from the North Sea. The maximum 10-minute sustained wind was observed at Røsnæs Fyr (39.5 m s^{-1}), on a peninsula in the Great Belt, and the strongest gust was observed at Kegsnæs Fyr (53.5 m s^{-1}) in the Flensburg Firth. Both are the highest wind speeds that have ever been recorded in Denmark. Station locations as well as the analyzed track are shown in Fig. 22.1.

Climatological assessment: Local observations. Storms can be ranked by many factors, including by maximum sustained wind or by strongest gust. Of course, such rankings depend on the homogeneity of the data. This not only has to take into account local effects, such as changes in the surroundings of the meteorological station (for example, trees growing over time or new buildings, c.f. Lindenberget al. 2012) and modifications in instrumentation or the definition of “sustained wind speed”, but also inhomogeneities that relate to the violent wind as such cases where the anemometers were blown away. The series by Hamburg airport, starting in the mid-1930s, seems to be less affected by inhomogeneities. Therefore, observations from this station are useful for assessing the Christian/Allan event. Here, we find a peak gust of 33.4 m s^{-1} , which makes it the eighth strongest since 1951 compared to the maximum value of 39.1 m s^{-1} in January 1990 (Haeseler et al. 2013).

The 2013 event’s impact can be regarded as highly unusual, but there have been stronger events before. While the storm reached the highest wind speed ever recorded in Denmark, its peak gust ranks among the top five of the previous 30 years at German weather stations (altitude below 600 m). However, what makes the storm a rare event is the timing. In Germany and Denmark, hurricane force winds in October are very unusual.

Climatological assessment: Reanalysis. When assessing whether an event or its statistics are outside the range of normal, a long homogeneous reference is needed, i.e., historical observations covering several decades. This is often not available for wind speeds. Ways to overcome this limitation are to use either more robust

proxies, such as geostrophic winds calculated from pressure differences (Alexandersson et al. 1998), or to dynamically downscale reanalyses, that are as homogeneous as possible in terms of large-scale patterns (c.f. Feser et al. 2001). The CoastDat dataset describes storms in the region of the northeast Atlantic and northern Europe, obtained by downscaling NCEP/NCAR Reanalysis 1 with the large-scale constrained regional atmospheric model COSMO-CLM (Geyer 2014). It, thus, constitutes a near-real-time homogeneous dataset, beginning in the late 1950s (Weisse et al. 2005). The dataset is of limited accuracy, but the error characteristics are homogeneous.

In this simulation, the storm of 28 October 2013 compares favorably with the operational analyses. It is associated with a maximum (instantaneous) wind speed of 26.7 m s^{-1} , derived for grid boxes of about $50 \times 50\text{ km}^2$. The homogeneous dataset allows for the analysis of changes in storm frequency and intensity over time.

Considering strong winter storms, defined by a minimum core pressure of 970 hPa or less, we find 74 events since 1948 that have passed over a region covering northern Germany, Denmark, and the Skagerrak/Kattegat region ($52^{\circ}\text{--}60^{\circ}\text{N}$, $6^{\circ}\text{--}13^{\circ}\text{E}$). Of these, 52 are weaker than Christian/Allen in terms of maximum wind speeds, and 22 are stronger in the downscaled reanalysis. We conclude that the Christian/Allan storm of 28 October 2013 was, indeed, a very strong and unusual one. Storms of this strength have crossed the region of interest about once every one or two years, however, rarely in October. Interestingly, a few weeks later (5–7 December 2013) another storm, named “Xaver” in Germany (Deutschländer et al. 2013) and “Bodil” in Denmark, passed over the region. It was stronger in parts of Denmark and in the Baltic Sea area. Its storm field was more extended and slower, so it caused severe storm surges in the North Sea and the Kattegat region.

Another question is, “Have such storms clustered in recent years?” An answer to this question is provided by Fig. 22.2, which displays the number of storms weaker or stronger than Christian/Allen for all years from 1948 to 2013 in the CoastDat dataset. We note that a strong storm event occasionally is followed by another one a few days or even weeks later, as the general circulation may still be favorable for storm development. This was recently shown by Pinto et al. (2013).

Figure 22.2 describes not a clear change, but rather a slight tendency towards more intense storms in the last decades. This is in accordance with the

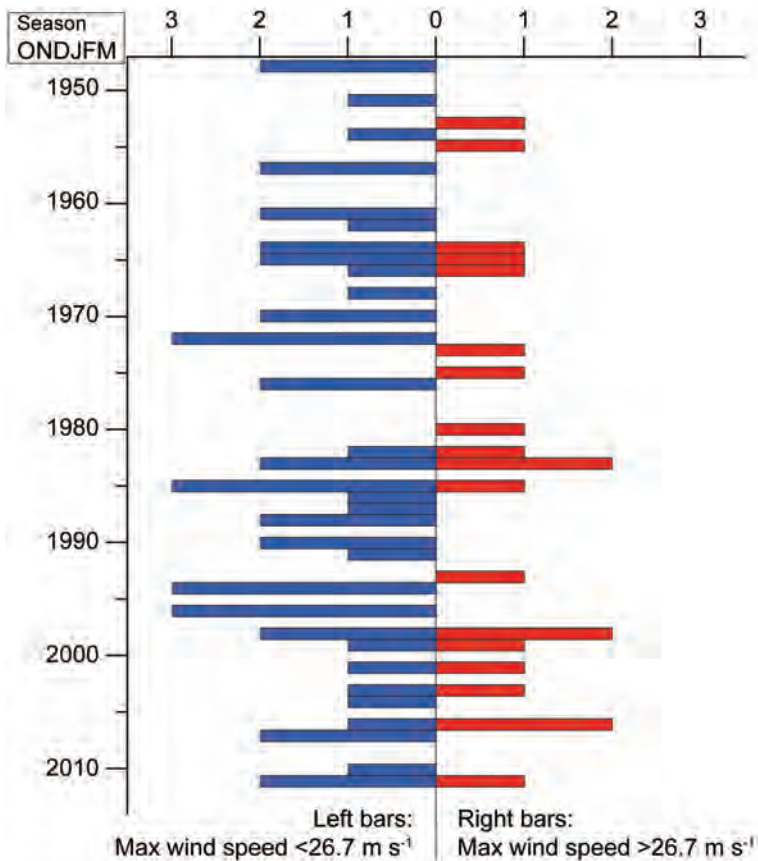


FIG. 22.2. Number of heavy storms (with minimum pressure ≤ 970 hPa) crossing the Jutland area during winter (ONDJFM) seasons according to the CoastDat data set (using $50 \text{ km} \times 50 \text{ km}$ grid boxes). Left: Storms with maximum wind speeds smaller than Christian/Allan (26.7 m s^{-1}); right: storms with larger maximum wind speeds.

latest IPCC Fifth Assessment Report (Stocker et al. 2014), which states that it is “virtually certain” that the frequency and intensity of storms over the North Atlantic have increased since the 1970s. An eastward extension of the North Atlantic storm track towards Europe may have contributed to higher intense storm counts. An increase in storm numbers over the last decades is consistent with trends found in other reanalyses (e.g., Feser et al. 2014), while studies of long-term proxy data, in particular geostrophic winds (Alexandersson et al. 1998; Matulla et al. 2007; Schmidt and von Storch 1993) and storm surge records (e.g., Dangendorf et al. 2014), describe the trend as part of multidecadal variability. Since the 1880s, a decrease in storm numbers over the North Atlantic and western Europe was found until the mid-1960s, followed by an increase until the mid-1990s (Alexandersson et al. 1998, 2000). These decadal trends are also reflected in the number of low pressure systems (≤ 950 hPa)

levels. Studies (e.g., Stocker et al. 2014) have demonstrated that a trend beyond the range of natural variations and possible drivers cannot be detected at this time. Instead, we explore if the considered event is outside the range of normal storms and if such storms cluster in recent times. Doing this as a formal hypothesis test is difficult given the multidecadal variability, as is demonstrated by proxy reconstructions (Alexandersson et al. 1998; Matulla et al. 2007; Schmidt and von Storch 1993). Thus, instead of falsely suggesting statistical rigor, we prefer to only demonstrate that such events took place throughout the documented past, albeit rarely so. For the time being, the simplest answer—the 2013 event is a realization that cannot be distinguished from those drawn out of a climate undisturbed by anthropogenic influence—cannot be rejected. However, ongoing monitoring may reveal more storms at a later time, which may then possibly be explained only by assuming an external forcing.

over the North Atlantic (Franke 2009). They peaked during the 1990s and reached the highest number since the first records in 1956/57 between November 2013 and March 2014. Ensembles of regional climate change scenarios, as available from Norddeutscher Klimaatlas (<http://www.norddeutscher-klimaatlas.de>), do not envisage a well-defined change, as some of the scenarios point towards higher maximum wind speeds and others to smaller. It should be emphasized that extreme wind statistics differ from extreme temperature and precipitation statistics in this respect.

Conclusions. When analyzing the Christian/Allan storm, we used an approach similar to van Oldenborgh et al. (2012), who examined both limited recorded data as well as model output. Within the framework of classical detection of climate change and attribution of plausible cases (Hasselmann 1979), there is no robust evidence for supporting claims that the intensity of the Christian/Allan storm would be beyond historical occurrences and that the recent clustering of storms should be related to the recently elevated greenhouse gas

23. THE EFFECT OF ANTHROPOGENIC CLIMATE CHANGE ON THE COLD SPRING OF 2013 IN THE UNITED KINGDOM

NIKOLAOS CHRISTIDIS, PETER A. STOTT, AND ANDREW CIAVARELLA

Anthropogenic climate change reduced the odds of an extremely cold UK spring in 2013 at least 30 times, as estimated from ensembles of simulations with and without human influences.

The event. Spring 2013 in the United Kingdom was characterised by prolonged cold spells with strong northeasterly winds drawn from Siberia and heavy, unseasonal snowstorms. March 2013 was the coldest after 1962 in the national record dating back to 1910 and colder than the preceding winter months (according to the Met Office, National Climate Information Centre). While the season as a whole was exceptionally cold, it was by no means unprecedented (Fig. 23.1a). However, the associated impacts widely covered in the national and local press make the event an interesting case for an attribution study. Most notably, snowdrifts topping 5 m in places killed thousands of newborn lambs and cost the UK government £250,000 (~\$420,000 US dollars) in reimbursements to livestock farmers (DEFRA 2013). According to the press, frozen soil stunted the growth of cereal crop, snow-damaged power cables left thousands of homes and businesses in Northern Ireland without power, and the electricity network infrastructure in Scotland was significantly damaged. Here we employ the Hadley Centre system for Attribution of extreme weather and Climate Events (ACE; Christidis et al. 2013) to investigate the effect of anthropogenic climatic forcings on the cold spring in the context of internal climate variability.

Possible drivers. The North Atlantic Oscillation (NAO) is the dominant mode of winter variability in the North Atlantic. The prominence of northeasterly winds during the event is a characteristic mark of its negative phase, typically associated with cold winters in the United Kingdom and likely to explain

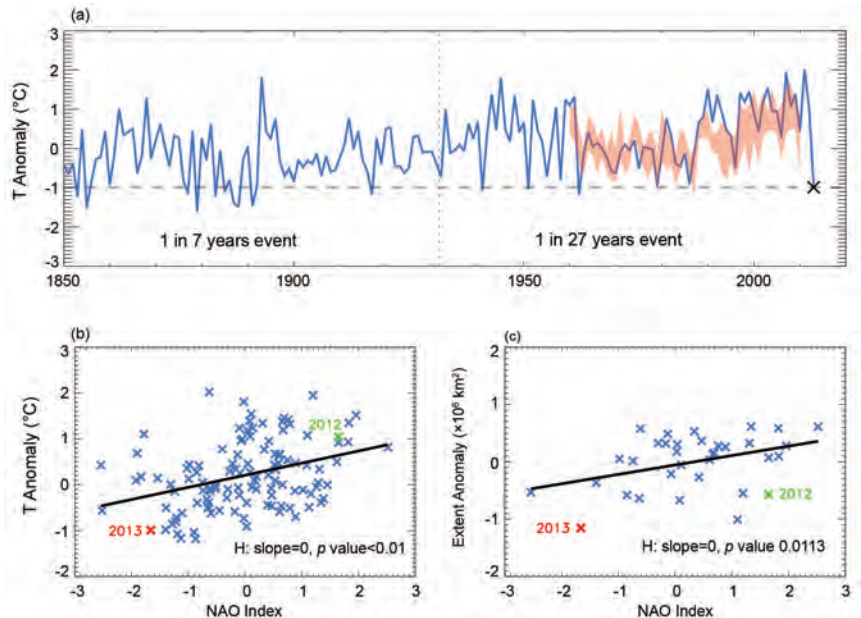


FIG. 23.1. Spring temperature in the UK region (10°E–5°W, 48°–60°N). (a) Observed timeseries of the regional MAM temperature estimated with the CRUTEM4 dataset (Jones et al. 2012). Temperature anomalies are relative to 1961–90. The red area highlights the temperature range from five HadGEM3-A simulations over period 1960–2010. The horizontal dashed line marks the temperature anomaly of -0.99°C observed in 2013. Estimates of the return time of seasons colder than 2013 (derived using the generalized Pareto distribution) are shown for the two halves of the observational record. (b) The relationship between observed spring UK temperature and the NAO index (from <https://climatedataguide.ucar.edu/climate-data/hurrell-north-atlantic-oscillation-nao-index-pc-based>). NAO is found to explain 13% of the MAM temperature variability. (c) The relationship between the Northern Hemisphere sea-ice extent anomaly estimated with HadISST and the NAO index. In panels (b) and (c), year 2013 is highlighted in red and year 2012 (which had a positive NAO) is highlighted in green for comparison. The p -values shown on the panels refer to testing of the hypothesis that the least square fit (black line) has a zero trend.

the cold start of spring (Visbeck et al. 2001). A significant relationship between the NAO and spring (March–May or MAM) temperature in the United Kingdom is illustrated in Fig. 23.1b. We use the principle component-based NAO index corresponding to the leading EOF of the December to March (DJFM) sea level pressure anomalies over the North Atlantic (Hurrell and Deser 2009). The strong negative phase of the NAO in 2013 could be expected to have set the scene for cold extremes; the index had its seventh most negative value since 1899. Moreover, several factors may have predisposed the Atlantic winter circulation to a negative NAO state (Slingo 2013), including the influence of the MJO (Cassou 2008) and of stratospheric warming events (Omrani et al. 2014). The record-low sea ice extent in the Arctic may also have favored a negative NAO regime (Petoukhov and Semenov 2010). Although we find a significant relationship between the NAO and the autumn and winter mean sea ice extent (Fig. 23.1c), a clear link between the two has not yet been established (Screen et al. 2013), and the distance of the 2013 point from the best-fit line in Fig. 23.1c indicates that variability also played an important role.

While the negative NAO phase provided favorable conditions for the cold UK spring, warming due to anthropogenic climate change (Bindoff et al. 2014) would be expected to reduce the frequency of such cold events. Given the underlying observed warming trend of 0.07 °C per decade since 1850 in the UK spring temperature, the 2013 anomaly would have been almost four times more likely to occur during the first half of the observational record (Fig. 23.1a). It should be noted that this warming trend has not yet formally been attributed to human influence, though seasonal warming over the whole of Europe in recent decades has been shown to be mainly anthropogenic (Christidis et al. 2012). In this study, we aim to quantify how anthropogenic forcings influenced the odds of the cold spring of 2013 given the prevailing NAO conditions. We first examine the relative impact of the NAO phase on the event and subsequently investigate the anthropogenic influence on its frequency under negative NAO conditions. Thus, the relative contributions of these two factors can be effectively compared.

Method. Our ACE system has been employed in several studies to assess the human influence on extreme events like heat waves, cold spells, floods, and droughts (e.g., Christidis et al. 2013; Lott et al. 2013). Ensembles of simulations are generated with the HadGEM3-A global atmospheric model that

represent the actual climate as well as a hypothetical “natural” climate without the effect of human influence (see Supplemental Material). Simulations of the actual world include all the main external climatic forcings and use prescribed values of observed SST and sea ice data from the HadISST dataset (Rayner et al. 2003) as boundary conditions. Simulations of the natural world include natural forcings only and use (a) SSTs produced by subtracting an estimate of the anthropogenic warming from the HadISST data and (b) adjusted estimates of the sea ice based on simple empirical relationships (Pall et al. 2011).

For this study, we produced three ensembles, with 600 simulations each, spanning the period September 2012–August 2013. We have one ensemble for the actual climate influenced by all external forcings (ALL) and two for the natural climate (NAT) produced with different sets of boundary conditions. The first version of NAT employs boundary conditions constructed from observations (Christidis and Stott 2014), whereas the second uses model-based estimates from seven atmosphere–ocean coupled models (see Supplemental Material). Details of the experimental setup are given in Christidis et al. (2013). We also performed model evaluation tests to ensure the model is fit for purpose by comparing five multidecadal simulations of the actual climate against observations. We found that HadGEM3-A provides a good statistical representation of spring temperatures in the UK region and has good skill in reproducing cold springs as indicated by reliability diagrams (see Supplemental Material).

The NAO effect. We first investigate how the NAO influences the odds of the cold event. In order to partition the ACE simulations between the two phases of the NAO, we constructed the leading EOF of DJFM sea level pressure anomalies with data from five model simulations over 1960–2010. We then projected the 2012/13 pressure anomalies from each ensemble member of the ALL and NAT experiments onto the EOF and computed the NAO index. About half (40%–60%) ensemble members produce a positive and half a negative index, i.e., the boundary conditions do not strongly force the observed negative phase. Figure 23.2a–c shows a comparison between simulations of the actual climate (ALL) that produce positive and negative phases. There is a significant shift towards colder spring temperatures when the NAO index is negative, as inferred from a Kolmogorov–Smirnov test applied to the distributions of the two phases (Fig. 23.2a).

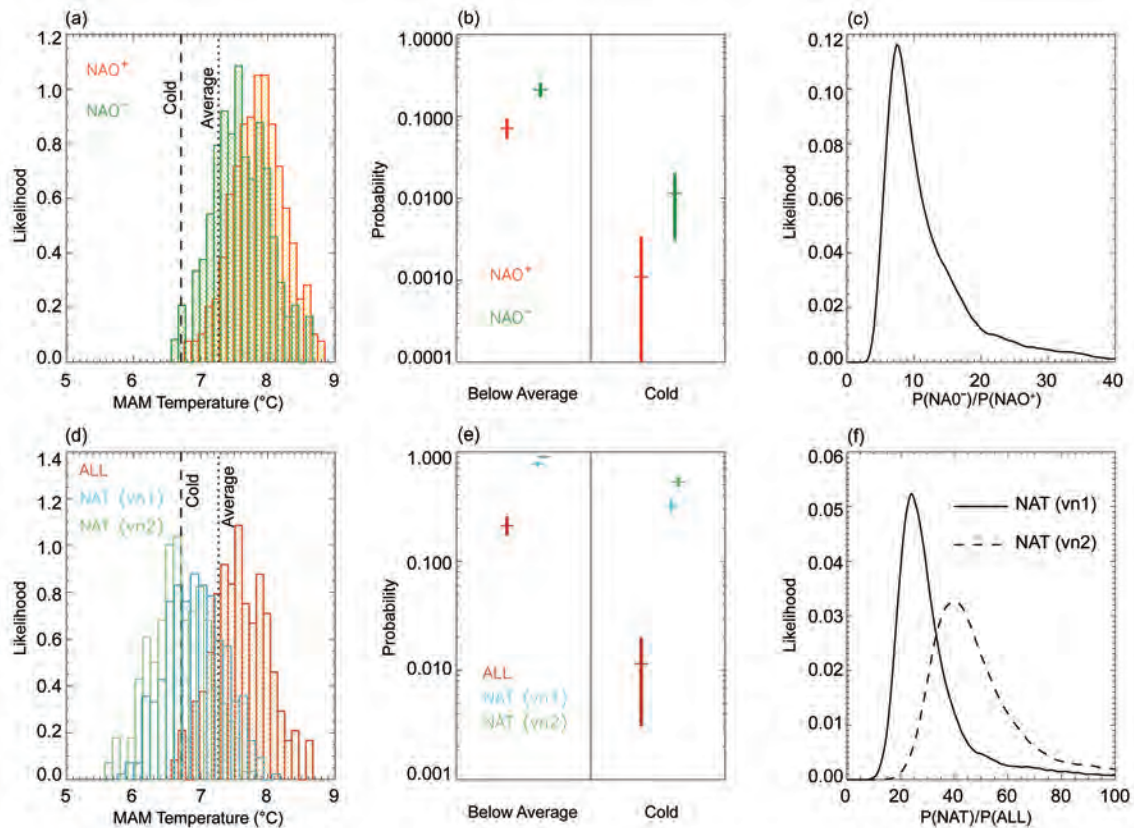


FIG. 23.2. Results from the ACE analysis. Panels (a), (b), and (c) illustrate the NAO influence on the cold UK spring in 2013. (a) Normalized distributions of the regional MAM temperature from members of the ALL ensemble with positive (orange) and negative (green) NAO indices. The thresholds for cool seasons (temperature below the climatological mean of period 1960–2010) and cold seasons (temperature at least a standard deviation below the climatological mean) are marked by the vertical dotted and dashed lines respectively. (Note that the temperature in 2013 was 1.8 standard deviations below the climatological mean). (b) Probabilities of a cool and cold spring under positive (orange) and negative (green) NAO conditions. The vertical bars around the best estimate (50th percentile of the distribution) correspond to the 5%–95% uncertainty range. (c) Normalized distribution of the change in the odds of a cold event in 2013 due to the NAO effect. Panels (d), (e), and (f) provide similar illustrations as panels a, b and c but for the anthropogenic influence on the event: (d) Distributions as in panel (a), but for the ALL ensemble (red) and the two NAT ensembles (blue and green). Only members with a negative NAO index are kept in the analysis of the anthropogenic effect. (e) Probabilities of a cool and cold spring from the ALL (red) and the two NAT ensembles (blue and green). (f) Distributions similar to panel (c), produced with the two NAT versions (solid and dashed lines).

We also examine the probabilities of MAM 2013 being a cool or a cold season using the threshold definitions given in the caption of Fig. 23.2. The probabilities are estimated with the generalized Pareto distribution if the threshold lies at the tails and the uncertainties are derived using a Monte Carlo bootstrap procedure as in previous work (Christidis et al. 2013; see Supplemental Material). An increase in the odds of a cool and cold spring is evident when the NAO state is negative. However, as the cold temperature threshold lies in the tail of both distributions, the odds of a cold spring are small, even for the negative NAO phase (return time of 50–1000 years).

In relative terms, negative NAO conditions make the occurrence of a cold spring 10 times more likely (best estimate corresponding to the 50th percentile of the distribution in Fig. 23.2c), though the probability of the event remains small.

The anthropogenic effect. We next compare the ALL and NAT ensembles to assess the impact of human influence. To minimise the NAO influence, we only keep simulations with a negative NAO index. The anthropogenic effect leads to a wider separation of the temperature distributions (Fig. 23.2d) compared to the NAO effect. There is a marked increase in the

odds of cool and cold events in the colder natural world (Fig. 23.2e) with the chances of a cold spring rising from less than 2% to 30%–60% in the absence of human influence. The two versions of the NAT experiment give qualitatively similar results, though the precise estimates of the probabilities differ. The odds of a cold spring in the natural world are estimated to increase by a factor of 30–50 (best estimates of the two NAT versions are shown in Fig. 23.2f). We repeated the analysis keeping only the most negative NAO years and found little impact on the best estimate of the probabilities, but an increase in their uncertainty was found as the sample size decreases (see Supplemental Material). Finally, using the MAM instead of the

DJFM NAO index was found to have no influence on the main analysis results (see Supplemental Material).

Conclusions. Cold springs in the United Kingdom are expected to become rarer in a warming climate. Had there been no anthropogenic influence on the climate, the chances of a cold spring in 2013 would sharply increase from less than 2% to 30%–60%, and the event would not be deemed as extreme. Negative NAO conditions led to an estimated 10-fold increase in the odds of a cold spring. However, the MAM temperature is too low to be solely explained by the NAO effect and can thus be mainly attributed to other components of internal climate variability.

24. SUMMARY AND BROADER CONTEXT

STEPHANIE C. HERRING, MARTIN P. HOERLING, THOMAS C. PETERSON, AND PETER A. STOTT

This report contributes to the growing body of evidence that human influences on climate have changed the risk of some extreme events and that scientists are increasingly able to detect these changes. A failure to find anthropogenic signals for several events examined in this report does not prove anthropogenic climate change had no role to play. Rather, an anthropogenic contribution to these events that is distinguishable from natural climate variability could not be detected by these analyses. Thus, there may have been an anthropogenic role, but these particular analyses did not find one. This year, the number of events analyzed in this report has again increased, and the range of event types analyzed has expanded to include a blizzard, snowfall, and a midlatitude cyclone.

We acknowledge that these reports represent a small and nonrandom sampling of extreme events from around the world. However, with 22 studies looking at 16 events, a few interesting patterns emerge. Examining Table 24.1 reveals that the nine analyses of extreme heat events overwhelmingly showed that human-caused climate change is having an influence. In some cases, events have become as much as 10 times more likely due to the current cumulative effects of human-induced climate change, as found for the Korean heat wave of summer 2013. These individual examples are consistent with the broader trends captured in the latest IPCC (Stocker et al. 2014) statement, “it is likely that the frequency of heat waves has increased in large parts of Europe, Asia and Australia.” At the other end of the temperature distribution, the one analysis of a cold event found that such events were becoming much less likely.

In contrast, the role of human influences on extreme precipitation events observed in 2013 is decidedly mixed (Table 24.1). The analysis of the extreme

June monthly averaged precipitation in northern India found evidence suggesting an increase of the event probability in the present climate compared to preindustrial climate (see “Severe Precipitation in Northern India in June 2013: Causes, Historical Context, and Changes in Probability” in this report), whereas analyses of seasonal and annual precipitation extreme values over the north-central and eastern United States (see “Seasonal and Annual Mean Precipitation Extremes Occurring During 2013: A U.S. Focused Analysis” in this report) showed an anthropogenic contribution. The high profile and high impact extreme rainfall event in northeast Colorado in early September happened despite global warming making the event *less likely* according to this analysis (see “Northeast Colorado Extreme Rains Interpreted in a Climate Change Context” in this report). Two additional heavy precipitation analyses did not find anthropogenic influences.

Of the four analyses of drought, the one focused on New Zealand drought found global warming contrib-

Table 24.1. Summary of results for *Explaining Extreme Events of 2013 from a Climate Perspective*, with the role of anthropogenic climate change (increased, decreased, no evidence) noted for each event. Specific papers examining the event are noted in parenthesis.

	Summary Statement	Anthropogenic Influence Increased Event Likelihood or Strength	Anthropogenic Influence Decreased Event Likelihood or Strength	Anthropogenic Influence Not Found or Uncertain	Total # of Papers
Heat	Long duration heat waves during the summer and prevailing warmth for annual conditions are becoming increasingly likely due to a warming planet, as much as 10 times more likely due to the current cumulative effects of human-induced climate change, as found for the Korean heat wave of summer 2013.	Australia Heat [Arblaster et al., King et al. Knutson et al. (a), Lewis et al., Perkins et al.] Europe Heat (Dong et al.) China Heat (Zhou et al.) Japan Heat (Imada et al.) Korea Heat (Min et al.)			9
Cold	Prolonged cold waves have become much less likely, such that the severely cold 2013 winter over the United Kingdom was perhaps the most remarkable event of all those studied in 2013—its probability of occurrence may have fallen 30-fold due to global warming.		UK Cold Spring (Christidis et al.)		1
Heavy Precipitation	Extreme precipitation events of 2013 were found to have been much less influenced by human-induced climate change than extreme temperature events.	U.S. Seasonal Precip [Knutson et al. (b)] India Precip (Singh et al.)	U.S. Northern Colorado Precip (Hoerling et al.)	Southern Europe Precip (Yiou and Cattiaux) Central Europe Precip (Schaller et al.)	5
Drought	Droughts are highly complex meteorological events, and research groups analyzed different factors that influence droughts such as sea surface temperature, heat, or precipitation.	New Zealand Drought (Harrington et al.)		U.S. California Drought* (Funk et al., Wang and Schubert**)	3
	Swain et al. found evidence that atmospheric pressure patterns increased, but the influence on the California drought remains uncertain.	Large-scale atmospheric conditions linked to the U.S. California drought (Swain et al.***)			1
Storms	There was no clear evidence for human influence on any of the three very intense storms examined, which included a surprising winter-like storm during autumn in the Pyrenees, an extreme blizzard across the U.S. High Plains, and Cyclone 'Christian' that delivered damaging winds across northern Germany and southern Denmark.			Cyclone Christian (von Storch et al.) Pyrenees Snow (Anel et al.) U.S. South Dakota Blizzard (Edwards et al.)	3
		13	2	7	22

* Some elements of factors that contributed to California drought were found to be affected by long-term climate change.
 ** Wang and Schubert found that global warming would increase risk in some ways but decrease it in others, showing no NET change to risk.
 *** Swain et al. found a strong influence of global warming upon the large-scale atmospheric conditions linked to the drought but do not make an explicit attribution claim regarding extremely low precipitation.

uted to the severity of that event. However, the three papers that looked at the California drought did not find a clear anthropogenic influence. “Examining the Contribution of the Observed Global Warming Trend to the California Droughts of 2012/13 and 2013/14” and “Causes of the Extreme Dry Conditions Over California During Early 2013” looked directly at the precipitation deficits associated with the California drought and their link to SSTs and found no appreciable effect from long-term SST warming. “The Extraordinary California Drought of 2013/14: Character, Context, and the Role of Climate Change” took a different approach and focused on particular circulation patterns that contributed to the drought, rather than examining precipitation directly. While they found global warming to increase the probability of certain large-scale atmospheric circulations, the implications for extremely low precipitation over California were found to be uncertain. This comparison of three studies for the same extreme event, each using different methods and metrics, strengthened the attribution evidence (in this case, against a substantial effect of global warming on the severe precipitation deficits), and revealed the sources of uncertainty more deeply than might have been evident from a single study alone.

This year, we also had a few very exciting additions that looked at different types of extreme events: an assessment of a blizzard that hit South Dakota, Cyclone “Christian” that caused significant damage in northwestern Europe, and an extreme snowfall event in the Pyrenees Mountains. None of these analyses found an anthropogenic signal, in part because attribution assessments of storm events such as these pose unique challenges due to the often limited observational record. As stated earlier, this failure to find anthropogenic signals does not prove anthropogenic climate change had no role to play in these events. Rather, a substantial anthropogenic contribution to these events cannot be supported by these analyses.

Broader context of attribution research. As we conclude our third annual report on explaining extreme events, the dialog around the value of attribution science is intensifying (Kerr 2013). Perhaps the most evident and widely applicable value of event attribution is to interpret what an event occurrence means for the future. The annual *State of the Climate* report (Blunden and Arndt 2014) puts current conditions into historical perspective, while our report also seeks to explain the events in the context of the future as well by identifying how our changing climate system is currently influencing events.

In addition to interpreting how the risk of an extreme event may be changing, event attribution is also valuable to the overall scientific enterprise of improving predictions and projections. As stated in the World Climate Research Program Grand Challenges white paper for Science Underpinning the Prediction and Attribution of Extreme Events, “There are strong links between the development of routine event attribution methods and those used to make sub-seasonal to interannual predictions” (Karoly et al. 2012). The physical understanding of extreme events is valuable in determining if models are capable of representing and simulating those processes and events realistically. Assessments of extremes can, therefore, elucidate strengths and limitations of models. The ultimate goal is to develop new prediction products relating to extremes that better meet the needs of the public and decision makers, who must make choices about how to prepare for extremes.

Beyond the science, there is an ongoing public dialog around climate change and its impacts. It is clear that extreme events capture the public’s attention. And, indeed, they should because “people, plants and animals tend to be more impacted by changes in extremes compared to changes in average climate” (Peterson et al. 2008). And, with or without the availability of a robust scientific analysis, the public often associates extreme events such as these with climate change. Scientific event attribution can help inform the public’s understanding of our changing environment.

The challenges in event attribution are high both from a technological perspective of improving scientific knowledge and from a communication perspective of explaining what that science knowledge means. Observed events, such as those analyzed in this report, demonstrate the vulnerabilities of societies to extremes of weather and climate. In the face of such vulnerabilities, citizens are faced with decisions in the presence of uncertainty, for instance whether climate change may be increasing their exposure to drought or flooding. Enhancing scientific knowledge through attribution helps build environmental intelligence, thereby enabling better decisions than would be possible without such understanding.

It remains that after an extreme event there is a window of opportunity to engage the public on climate change impacts and science more broadly (Peterson et al. 2008). Being able to deliver scientifically robust attribution statements about the event in a timely manner is an important first step in this dialog.

REFERENCES

- Adler, R. F., and Coauthors, 2003: The Version 2 Global Precipitation Climatology Project (GPCP) monthly precipitation analysis (1979-Present). *J. Hydrometeorol.*, **4**, 1147–1167.
- Alexandersson, H., T. Schmith, K. Iden, and H. Tuomenvirta, 1998: Long-term variations of the storm climate over NW Europe. *Global Atmos. Ocean Sys.*, **6**, 97–120.
- , H. Tuomenvirta, T. Schmith, and K. Iden, 2000: Trends of storms in NW Europe derived from an updated pressure data set. *Climate Res.*, **14**, 71–73.
- Allan, R., and C. K. Folland, 2012: [Global climate] Atmospheric circulation: Mean sea level pressure [in “State of the Climate 2011”]. *Bull. Amer. Meteor. Soc.*, **93** (7), S35–S36.
- , and B. J. Soden, 2008: Atmospheric warming and the amplification of precipitation extremes. *Science*, **321**, 1484.
- Allen, M., 1999: Do-it-yourself climate prediction. *Nature*, **401**, 642.
- , 2003: Liability for climate change. *Nature*, **421**, 891–892.
- Andermann, C., L. Longueuevigne, S. Bonnet, A. Crave, P. Davy, and R. Gloaguen, 2012: Impact of transient groundwater storage on the discharge of Himalayan rivers. *Nature Geosci.*, **5**, 127–132.
- Arblaster, J. M., and L. V. Alexander, 2012: The impact of the El Niño–Southern Oscillation on maximum temperature extremes. *Geophys. Res. Lett.*, **39**, L20702, doi:10.1029/2012GL053409.
- Ashfaq, M., Y. Shi, W.-W. Tung, R. J. Trapp, X. Gao, J. S. Pal, and N. S. Diffenbaugh, 2009: Suppression of south Asian summer monsoon precipitation in the 21st century. *Geophys. Res. Lett.*, **36**, L01704, doi:10.1029/2008GL036500.
- BAAQMD, 2014: Challenging “Winter Spare the Air” season comes to a close. Bay Area Air Quality Management District, press release, 4 March 2014. [Available online at <http://www.baaqmd.gov/~media/Files/Communications%20and%20Outreach/Publications/News%20Releases/2014/2014-019-WSTA-SEASON-ENDS-030414.ashx?la=en>.]
- Bacmeister, J. T., M. J. Suarez, and F. R. Robertson, 2006: Rain reevaporation, boundary layer–convection interactions, and Pacific rainfall patterns in an AGCM. *J. Atmos. Sci.*, **63**, 3383–3403.
- , M. F. Wehner, R. B. Neale, A. Gettelman, C. Hannay, P. H. Lauritzen, J. M. Caron, and J. E. Truesdale, 2014: Exploratory high-resolution climate simulations using the Community Atmosphere Model (CAM). *J. Climate*, **27**, 3073–3099.
- Balmaseda, M. A., L. Ferranti, F. Molteni, and T. N. Palmer, 2010: Impact of 2007 and 2008 Arctic ice anomalies on the atmospheric circulation: Implications for long-range predictions. *Quart. J. Roy. Meteor. Soc.*, **136**, 1655–1664.
- Barnett, T. P., and Coauthors, 2008: Human-induced changes in the hydrology of the western United States. *Science*, **319**, 1080–1083.
- Barriopedro, D., E. M. Fischer, J. Lutenbacher, R. M. Trigo, and R. Garcia-Herrera, 2011: The hot summer of 2010: redrawing the temperature record map of Europe. *Science*, **332**, 220–224.
- Becker, A., P. Finger, A. Meyer-Christoffer, B. Rudolf, K. Schamm, U. Schneider, and M. Ziese, 2013: A description of the global land-surface precipitation data products of the Global Precipitation Climatology Centre with sample applications including centennial (trend) analysis from 1901 to present. *Earth Syst. Sci. Data*, **5**, 71–99.
- Berg, P., J. O. Haerter, P. Thejll, C. Piani, S. Hagemann, and J. H. Christensen, 2009: Seasonal characteristics of the relationship between daily precipitation intensity and surface temperature. *J. Geophys. Res.*, **114**, D18102, doi:10.1029/2009JD012008.
- BfG-DWD, 2013: Länderübergreifende Analyse des Juni-Hochwassers 2013. Bundesanstalt für Gewässerkunde, 69 pp. [Available online at http://www.vhw.de/fileadmin/user_upload/Themenfelder/Umweltrecht/2013_09_04_pm_bfg-bericht.pdf.]
- Bhend, J., and P. Whetton, 2013: Consistency of simulated and observed regional changes in temperature, sea level pressure and precipitation. *Climatic Change*, **118**, 799–810, doi:10.1007/s10584-012-0691-2.
- Bindoff, N. L., and Coauthors, 2014: Detection and attribution of climate change: From global to regional. *Climate Change 2013: The Physical Science Basis*, T. F. Stocker et al., Eds., Cambridge University Press, 867–952.
- Blackham, M., 2013: Dust bowled. *Water Atmos.*, **8**, 12–21.
- Bladé, I., B. Liebmann, D. Fortuny, and G. J. Oldenborgh, 2012: Observed and simulated impacts of the summer NAO in Europe: Implications for projected drying in the Mediterranean region. *Climate Dyn.*, **39**, 709–727, doi:10.1007/s00382-011-1195-x.
- Blunden, J., and D. S. Arndt, Eds., 2014: State of the Climate in 2013. *Bull. Amer. Meteor. Soc.*, **95** (7), S1–S257.
- Boé, J., L. Terray, C. Cassou, and J. Najac, 2009: Uncertainties in European summer precipitation changes: Role of large scale circulation. *Climate Dyn.*, **33**, 265–276, doi:10.1007/s00382-008-0474-7.
- Borah, N., A. K. Sahai, R. Chattopadhyay, S. Joseph, S. Abhilash, and B. N. Goswami, 2013: A self-organizing map–based ensemble forecast system for extended range prediction of active/break cycles of Indian summer monsoon. *J. Geophys. Res. Atmos.*, **118**, 9022–9034, doi:10.1002/jgrd.50688.

- Buisán, S. T., M. A. Sanz, and J. I. López-Moreno, 2014: Spatial and temporal variability of winter snow and precipitation days in the western and central Spanish Pyrenees. *Int. J. Climatol.*, in press, doi:10.1002/joc.3978.
- Bureau of Meteorology, 2012: State of the Climate 2012. [Available online at <http://www.csiro.au/Outcomes/Climate/Understanding/State-of-the-Climate-2012.aspx>.]
- , 2013a: Extreme heat in January 2013. Bureau of Meteorology Special Climate Statement 43, 19 pp. [Available online at <http://www.bom.gov.au/climate/current/statements/scs43e.pdf>.]
- , 2013b: Australia's warmest September on record. Bureau of Meteorology Special Climate Statement 46, 26 pp. [Available online at <http://www.bom.gov.au/climate/current/statements/scs46.pdf>.]
- , 2014: Annual Climate Report 2013. Bureau of Meteorology (Australia), 31 pp. [Available online at http://www.bom.gov.au/climate/annual_sum/2013/index.shtml.]
- CAL FIRE, 2014: Drought prompts CAL FIRE to increase statewide staffing: Expected prolonged, elevated threat of wildfire due to dry conditions. CAL FIRE, news release, 28 January 2014. [Available online at http://www.fire.ca.gov/communications/downloads/newsreleases/2014/2014_Drought_Staffing.pdf.]
- Carrera, M., R. Higgins, and V. Kousky, 2004: Downstream weather impacts associated with atmospheric blocking over the northeast Pacific. *J. Climate*, **17**, 4823–4840.
- Cassou, C., 2008: Intraseasonal interaction between the Madden-Julian Oscillation and the North Atlantic Oscillation. *Nature*, **455**, 523–527.
- Cattiaux, J., and P. Yiou, 2012: Contribution of atmospheric circulation to remarkable European temperatures of 2011. *Bull. Amer. Meteor. Soc.*, **93**, 1054–1057.
- , R. Vautard, C. Cassou, P. Yiou, V. Masson-Delmotte, and F. Codron, 2010: Winter 2010 in Europe: A cold extreme in a warming climate. *Geophys. Res. Lett.*, **37**, L20704, doi:10.1029/2010gl044613.
- Cayan, D., and J. Roads, 1984: Local relationships between United States West Coast precipitation and monthly mean circulation parameters. *Mon. Wea. Rev.*, **112**, 1276–1282.
- CDFW, 2014: CDFW puts closures in effect on some rivers, recommends further changes to the Fish and Game Commission. *California Department of Fish and Wildlife News*, 29 January 2014. [Available online at <http://cdfgnews.wordpress.com/2014/01/29/cdfw-puts-closures-in-effect-on-some-rivers-recommends-further-changes-to-the-fish-and-game-commission/>.]
- Chattopadhyay, R., A. K. Sahai, and B. N. Goswami, 2008: Objective identification of nonlinear convectively coupled phases of monsoon intraseasonal oscillation: Implications for prediction. *J. Atmos. Sci.*, **65**, 1549–1569.
- Chen, S., and D. Cayan, 1994: Low-frequency aspects of the large-scale circulation and West Coast United States temperature/precipitation fluctuations in a simplified general circulation model. *J. Climate*, **7**, 1668–1683.
- Christidis, N., and P. A. Stott, 2014: Change in the odds of warm years and seasons due to anthropogenic influence on the climate. *J. Climate*, **27**, 2607–2621.
- , —, and S. J. Brown, 2011: The role of human activity in the recent warming of extremely warm daytime temperatures. *J. Climate*, **24**, 1922–1930.
- , —, G. S. Jones, H. Shiogama, T. Nozawa, and J. Luterbacher, 2012: Human activity and warm seasons in Europe. *Int. J. Climatol.*, **32**, 225–239.
- , —, A. A. Scaife, A. Arribas, G. S. Jones, D. Copsey, J. R. Knight, and W. J. Tennant, 2013: A new HadGEM3-A-based system for attribution of weather- and climate-related extreme events. *J. Climate*, **26**, 2756–2783.
- CIB, cited 2013: Central European flooding 2013. EURO4M Climate Indicator Bulletin. [Available online at http://cib.knmi.nl/mediawiki/index.php/Central_European_flooding_2013.]
- Clark, A., B. Mullan, and A. Porteous, 2011: Scenarios of regional drought under climate change. National Institute of Water & Atmospheric Research, 135 pp. [Available online at http://www.niwa.co.nz/sites/niwa.co.nz/files/slmacc_drought_slidr093_june2011.pdf.]
- CMA, 2014: *China Climate Bulletin for 2013*. China Meteorological Administration, 50 pp.
- Compo, G. P., and P. D. Sardeshmukh, 2010: Removing ENSO-related variations from the climate record. *J. Climate*, **23**, 1597–1978.
- Coumou, D., and S. Rahmstorf, 2012: A decade of weather extremes. *Nature Climate Change*, **2**, 491–496, doi:10.1038/NCLIMATE1452.
- Dai, A., 2008: Temperature and pressure dependence of the rain-snow phase transition over land and ocean. *Geophys. Res. Lett.*, **35**, L12802, doi:10.1029/2008GL033295.
- , 2011: Drought under global warming: a review. *Wiley Interdiscip. Rev.: Climate Change*, **2**, 45–65.
- , 2013: The influence of the Inter-decadal Pacific Oscillation on US precipitation during 1923–2010. *Climate Dyn.*, **41**, 633–646.
- Daithi, S., 2013: Boundary conditions for the C20C Detection and Attribution project: The ALL-Hist/est1 and NAT-Hist/CMIP5-est1 scenarios. International CLIVAR C20C+ Detection and Attribution Project, 18 pp. [Available online at http://portal.nersc.gov/c20c/input_data/C20C-DandA_dSSTs_All-Hist-est1_Nat-Hist-CMIP5-est1.pdf.]
- Dangendorf, S., S. Müller-Navarra, J. Jensen, F. Schenk, T. Wahl, and R. Weisse, 2014: North Sea storminess from a novel storm surge record since AD 1843. *J. Climate*, **27**, 3582–3595.

- Dee, D. P., and Coauthors, 2011: The ERA-Interim reanalysis: Configuration and performance of the data assimilation system. *Quart. J. Roy. Meteor. Soc.*, **137**, 553–597, doi:10.1002/qj.828.
- DEFRA, 2013: Defra to meet the cost of removing sheep killed in snow, Department for Environment, Food & Rural Affairs, press release, 15 May 2013. [Available online at <https://www.gov.uk/government/news/defra-to-meet-the-cost-of-removing-sheep-killed-in-snow>.]
- Deser, C., A. S. Phillips, and M. A. Alexander, 2010: Twentieth century tropical sea surface temperature trends revisited. *Geophys. Res. Lett.*, **37**, L10701, doi:10.1029/2010GL043321.
- Deutschlander, T., K. Friedrich, S. Haeseler, and C. Lefebvre, 2013: Severe storm XAVER across northern Europe from 5 to 7 December 2013. Deutscher Wetterdienst, 19 pp. [Available online at http://www.dwd.de/bvbw/generator/DWDWWW/Content/Oeffentlichkeit/KU/KU2/KU24/besondere__ereignisse__global/stuerme/englischeberichte/201312__XAVER__europa,templateId=raw,property=publicationFile.pdf/201312__XAVER__europa.pdf.]
- Dobhal, D. P., A. K. Gupta, M. Mehta, and D. D. Khandelwal, 2013: Kedarnath disaster: Facts and plausible causes. *Current Sci.*, **105**, 171–174.
- Dole, R., J. Perlwitz, J. Eischeid, P. Pegion, T. Zhang, X. W. Quan, T. Xu, and D. Murray, 2011: Was there a basis for anticipating the 2010 Russian heat wave? *Geophys. Res. Lett.*, **38**, L06702, doi:10.1029/2010GL046582.
- Donat, M. G., and Coauthors, 2013: Updated analyses of temperature and precipitation extreme indices since the beginning of the twentieth century: The HadEX2 dataset. *J. Geophys. Res. Atmos.*, **118**, 2098–2118, doi:10.1002/jgrd.50150.
- Dong, B.-W., R. T. Sutton, and T. Woollings, 2013a: The extreme European summer 2012 (in “Explaining Extreme Events of 2012 from a Climate Perspective”). *Bull. Amer. Meteor. Soc.*, **94** (9), S28–S32.
- , —, —, and K. Hodges, 2013b: Variability of the North Atlantic summer stormtrack: Mechanisms and impacts. *Environ. Res. Lett.*, **8**, 034037, doi:10.1088/1748-9326/8/3/034037.
- Douville, H., S. Bielli, C. Cassou, M. Deque, N. M. J. Hall, S. Tyteca, and A. Voldoire, 2011: Tropical influence on boreal summer mid-latitude stationary waves. *Climate Dyn.*, **38**, 1783–1798.
- Dube, A., R. Ashrit, A. Ashish, K. Sharma, G. R. Iyengar, E. N. Rajagopal, and S. Basu, 2013: Performance of NCMRWF forecast models in predicting the Uttarakhand heavy rainfall event during 17–18 June 2013. [India] National Centre for Medium Range Weather Forecasting Research Report NMRF/RR/08/2013, 35 pp. [Available online at http://www.ncmrwf.gov.in/ncmrwf/KEDARNATH_REPORT_FINAL.pdf.]
- , —, —, —, —, —, and —, 2014: Forecasting the heavy rainfall during Himalayan flooding - June 2013. *Wea. Climate Extremes*, **4**, 22–34, doi:10.1016/j.wace.2014.03.004.
- Dubey, C. S., D. P. Shukla, A. S. Ningreihon, and A. L. Usham, 2013: Orographic control of the Kedarnath disaster. *Current Sci.*, **105**, 1474–1476.
- Durga Rao, K. H. V., V. Venkateshwar Rao, V. K. Dadhwal, and P. G. Diwakar, 2014: Kedarnath flash floods: A hydrological and hydraulic simulation study. *Current Sci.*, **106**, 598–603.
- DWR, 2013: DWR experimental winter outlook for water year 2014: Sees mostly dry conditions for California. California Department of Water Resources, news release, 27 November 2013. [Available online at <http://www.water.ca.gov/news/newsreleases/2013/112513.pdf>.]
- , 2014: DWR drops state water project allocation to zero, seeks to preserve remaining supplies. California Department of Water Resources, news release, 31 January 2014. [Available online at <http://www.water.ca.gov/news/newsreleases/2014/013114pressrelease.pdf>.]
- El Kenawy, A., J. I. Lopez-Moreno, and S. M. Vicente-Serrano, 2012: Trend and variability of surface air temperature in northeastern Spain (1920–2006): Linkage to atmospheric circulation. *Atmos. Res.*, **106**, 159–180.
- Favre, A., and A. Gershunov, 2009: North Pacific cyclonic and anticyclonic transients in a global warming context: Possible consequences for Western North American daily precipitation and temperature extremes. *Climate Dyn.*, **32**, 969–987.
- Feser, F., R. Weisse, and H. von Storch, 2001: Multi-decadal atmospheric modeling for Europe yields multi-purpose data. *Eos, Trans. Amer. Geophys. Union*, **82**, 305–310.
- , M. Barcikowska, O. Krueger, F. Schenk, R. Weisse, and L. Xia, 2014: Storminess over the North Atlantic and northwestern Europe - A review. *Quart. J. Roy. Meteor. Soc.*, in press, doi:10.1002/qj.2364.
- Field, C. B., and Coauthors, Eds., 2012: *Managing the Risks of Extreme Events and Disasters to Advance Climate Change Adaptation*. Cambridge University Press, 582 pp.
- Fischer, E. M., U. Beyerle, and R. Knutti, 2013: Spatial aggregation reveals robust projections in climate extremes. *Nature Climate Change*, **3**, 1033–1038, doi:10.1038/NCLIMATE2051.
- Folland, C. K., J. Knight, H. W. Linderholm, D. Fereday, S. Ineson, and J. W. Hurrell, 2009: The summer North Atlantic oscillation: Past, present, and future. *J. Climate*, **22**, 1082–1103.
- Francis, J. A., and S. J. Vavrus, 2012: Evidence linking Arctic amplification to extreme weather in mid-latitudes. *Geophys. Res. Lett.*, **39**, L06801, doi:10.1029/2012GL051000.
- Franke, R., 2009: Die nordatlantischen Orkantiefs seit 1956. *Naturwiss. Rundsch.*, **62**, 349–356, updated.

- Fyfe, J. C., N. P. Gillett, and G. J. Marshall, 2012: Human influence on extratropical southern hemisphere summer precipitation. *Geophys. Res. Lett.*, **39**, L23711, doi:10.1029/2012GL054199.
- , —, and F. W. Zwiers, 2013: Overestimated global warming over the past 20 years. *Nature Climate Change*, **3**, 767–769.
- Gershunov, A., and D. Cayan, 2003: Heavy daily precipitation frequency over the contiguous United States: Sources of climatic variability and seasonal predictability. *J. Climate*, **16**, 2752–2765.
- Geyer, B., 2014: High-resolution atmospheric reconstruction for Europe 1948–2012: coastDat2. *Earth Sys. Sci. Data*, **6**, 147–164, doi:10.5194/essd-6-147-2014.
- Ghosh, S., D. Das, S.-C. Kao, and A. R. Ganguly, 2012: Lack of uniform trends but increasing spatial variability in observed Indian rainfall extremes. *Nature Climate Change*, **2**, 86–91.
- Goswami, B. N., V. Venugopal, D. Sengupta, M. S. Madhusoodanan, and P. K. Xavier, 2006: Increasing trend of extreme rain events over India in a warming environment. *Science*, **314**, 1442–1445.
- Graham, R. A., and R. H. Grumm, 2010: Utilizing normalized anomalies to assess synoptic-scale weather events in the western United States. *Wea. Forecasting*, **25**, 428–445.
- Grams, C. M., H. Binder, S. Pfahl, N. Piaget, and H. Wernli, 2014: Atmospheric processes triggering the central European floods in June 2013. *Nat. Hazards Earth Syst. Sci.*, **14**, 1691–1702, doi:10.5194/nhess-14-1691-2014.
- Graves, C. E., J. T. Moore, M. J. Singer, and S. Ng, 2003: Band on the run - Chasing the physical processes associated with heavy snowfall. *Bull. Amer. Meteor. Soc.*, **84**, 990–994.
- Grumm, R. H., and R. Hart, 2001: Standardized anomalies applied to significant cold season weather events: Preliminary findings. *Wea. Forecasting*, **16**, 736–754.
- Haeseler, S., and Coauthors, 2013: Heavy storm CHRISTIAN on 28 October 2013. Deutscher Wetterdienst, 20 pp. [Available online at http://www.dwd.de/bvbw/generator/DWDWW/Content/Oeffentlichkeit/KU/KU2/KU24/besondere__ereignisse__global/stuerme/englisch/berichte/20131028__CHRISTIAN__europa,templateId=raw,property=publicationFile.pdf/20131028__CHRISTIAN_europa.pdf.]
- Hamill, T., 2014: Performance of operational model precipitation forecast guidance during the 2013 Colorado Front-Range floods. *Mon. Wea. Rev.*, **142**, 2609–2618.
- Hansen, W. R., B. J. Chronic, and J. Matlock, 1978: Climatology of the Front Range urban corridor and vicinity, Colorado. USGS Professional Paper 1019, 59 pp. [Available online at <http://pubs.usgs.gov/pp/1019/report.pdf>.]
- Hart, R. E., and R. H. Grumm, 2001: Using normalized climatological anomalies to rank synoptic-scale events objectively. *Mon. Wea. Rev.*, **129**, 2426–2442.
- Hartmann, D. L., and Coauthors, 2014: Observations: Atmosphere and surface. *Climate Change 2013: The Physical Science Basis*, T. F. Stocker et al., Eds., Cambridge University Press, 159–254.
- Hasselmann, K., 1979: On the signal-to-noise problem in atmospheric response studies. *Meteorology over the Tropical Oceans*, B. D. Shaw, Ed., Royal Meteorological Society, 251–259.
- Haylock, M. R., N. Hofstra, A. M. G. Klein Tank, E. J. Klok, P. D. Jones, and M. New, 2008: A European daily high-resolution gridded dataset of surface temperature and precipitation for 1950–2006. *J. Geophys. Res.*, **113**, D20119, doi:10.1029/2008JD010201.
- Hegerl, G., and F. Zwiers, 2011: Use of models in detection and attribution of climate change. *Wiley Interdiscip. Rev.: Climate Change*, **2**, 570–591.
- , O. Hoegh-Guldberg, G. Casassa, M. P. Hoerling, R. S. Kovats, C. Parmesan, D. W. Pierce, and P. A. Stott, 2009: Good practice guidance paper on detection and attribution related to anthropogenic climate change. IPCC Expert Meeting on Detection and Attribution Related to Anthropogenic Climate Change, T. F. Stocker et al., Eds., University of Bern, Switzerland, 1–8. [Available online at https://www.ipcc-wg1.unibe.ch/guidancepaper/IPCC_D&A_GoodPracticeGuidancePaper.pdf.]
- Hendon, H. H., D. W. J. Thompson, and M. C. Wheeler, 2007: Australian rainfall and surface temperature variations associated with the Southern Hemisphere annular mode. *J. Climate*, **20**, 2452–2467.
- , E.-P. Lim, J. M. Arblaster, and D. T. L. Anderson 2014: Causes and predictability of the record wet spring over Australia in 2010. *Climate Dyn.*, **42**, 1155–1174.
- Hewitson, B. C., and R. G. Crane, 2002: Self-organizing maps: Applications to synoptic climatology. *Climate Res.*, **22**, 13–26.
- Hewitt, H. T., D. Copey, I. D. Culverwell, C. M. Harris, R. S. R. Hill, A. B. Keen, A. J. McLaren, and E. C. Hunke, 2011: Design and implementation of the infrastructure of HadGEM3: The next-generation Met Office climate modelling system. *Geosci. Model Dev.*, **4**, 223–253.
- Hirabayashi, Y., R. Mahendran, S. Koirala, L. Konoshima, D. Yamazaki, S. Watanabe, H. Kim, and S. Kanaes, 2013: Global flood risk under climate change. *Nature Climate Change*, **3**, 816–821.
- Hirsch, R. M., and K. R. Ryberg, 2012: Has the magnitude of floods across the USA changed with global CO₂ levels? *Hydrolog. Sci. J.*, **57**, 1–9, doi:10.1080/02626667.2011.621895.

- Hoerling, M., J. Eischeid, J. Perlwitz, X. Quan, T. Zhang, and P. Pegion, 2012: On the increased frequency of Mediterranean drought. *J. Climate*, **25**, 2146–2161.
- , and Coauthors, 2013: Anatomy of an extreme event. *J. Climate*, **26**, 2811–2832.
- Hong, C.-C., H.-H. Hsu, N.-H. Lin, and H. Chiu, 2011: Roles of European blocking and tropical-extratropical interaction in the 2010 Pakistan flooding. *Geophys. Res. Lett.*, **38**, L13806, doi:10.1029/2011GL047583.
- Hoskins, B. J., and K. I. Hodges, 2002: New perspectives on the Northern Hemisphere winter storm tracks. *J. Atmos. Sci.*, **59**, 1041–1061.
- Houze, R. A., K. L. Rasmussen, S. Medina, S. R. Brodzik, and U. Romatschke, 2011: Anomalous atmospheric events Leading to the summer 2010 floods in Pakistan. *Bull. Amer. Meteor. Soc.*, **92**, 291–298.
- HPRC, cited 2014: High Plains Regional Center - Current climate summary maps. [Available online at <http://www.hprcc.unl.edu/>.]
- Hudson, D., A. G. Marshall, Y. Yin, O. Alves, and H. H. Hendon, 2013: Improving intraseasonal prediction with a new ensemble generation strategy. *Mon. Wea. Rev.*, **141**, 4429–4449.
- Huffington Post, 2014: The costs of California's bellwether drought: What can we expect? [Available online at http://www.huffingtonpost.com/peter-h-gleick/the-costs-of-californias_b_4747043.html.]
- Hurrell, J. W., and C. Deser, 2009: North Atlantic climate variability: The role of the North Atlantic Oscillation. *J. Marine Sys.*, **79**, 231–244.
- , and Coauthors, 2013: The Community Earth System Model: A framework for collaborative research. *Bull. Amer. Meteor. Soc.*, **94**, 1339–1360.
- Johnson, N. C., 2013: How many ENSO flavors can we distinguish? *J. Climate*, **26**, 4816–4827.
- Jones, D. A., W. Wang, and R. Fawcett, 2009: High-quality spatial climate data-sets for Australia. *Aust. Meteor. Oceanogr. J.*, **58**, 233–248.
- Jones, P. D., D. H. Lister, T. J. Osborn, C. Harpham, M. Salmon, and C. P. Morice, 2012: Hemispheric and large-scale land surface air temperature variations: An extensive revision and an update to 2010. *J. Geophys. Res.*, **117**, D05127, doi:10.1029/2011JD017139.
- Joseph, S., and Coauthors, 2014: North Indian heavy rainfall event during June 2013: Diagnostics and extended range prediction. *Climate Dyn.*, in press, doi:10.1007/s00382-014-2291-5.
- Junker, N. W., R. H. Grumm, R. Hart, L. F. Bosart, K. M. Bell, and F. J. Pereira, 2008: Use of normalized anomaly fields to anticipate extreme rainfall in the mountains of northern California. *Wea. Forecasting*, **23**, 336–356.
- Jurewicz, M. L., and M. S. Evans, 2004: A comparison of two banded, heavy snowstorms with very different synoptic settings. *Wea. Forecasting*, **19**, 1011–1028.
- Kalnay, E., and Coauthors, 1996: The NCEP/NCAR 40-Year Reanalysis Project. *Bull. Amer. Meteor. Soc.*, **77**, 437–471.
- Karoly, D. J., 2009: The recent bushfires and extreme heat wave in southeast Australia. *Bull. Aust. Meteor. Oceanogr. Soc.*, **22**, 10–13.
- , and K. Braganza, 2005: A new approach to detection of anthropogenic temperature changes in the Australian region. *Meteor. Atmos. Phys.*, **89**, 57–67.
- , and Coauthors, 2012: Science underpinning the prediction and attribution of extreme events. WCRP Grand Challenge white paper, 5 pp. [Available online at http://www.wcrp-climate.org/documents/GC_Extremes.pdf.]
- Kerr, R., 2013: In the hot seat. *Science*, **342**, 688–689.
- Kim, Y. H., M.-K. Kim, and W.-S. Lee, 2008: An investigation of large-scale climate indices with the influence of temperature and precipitation variation in Korea. *Atmosphere*, **18**, 83–95. (In Korean with English abstract.)
- Kistler, R., and Coauthors, 2001: The NCEP-NCAR 50-year reanalysis: Monthly means CD-ROM and documentation. *Bull. Amer. Meteor. Soc.*, **82**, 247–267.
- Klein-Tank, A. M. G., and Coauthors, 2002: Daily dataset of 20th-century surface air temperature and precipitation series for the European Climate Assessment. *Int. J. Climatol.*, **22**, 1441–1453.
- Knutson, T. R., F. Zeng, and A. T. Wittenberg, 2013a: Multi-model assessment of regional surface temperature trends: CMIP3 and CMIP5 Twentieth Century simulations. *J. Climate*, **26**, 8709–8743.
- , —, and —, 2013b: The extreme March 2012 warm anomaly over the eastern United States: Global context and multimodel trend analysis [in “Explaining Extreme Events of 2012 from a Climate Perspective”]. *Bull. Amer. Meteor. Soc.*, **94** (9), S13–S17.
- Knutti, R., and J. Sedláček, 2013: Robustness and uncertainties in the new CMIP5 climate model projections. *Nature Climate Change*, **3**, 369–373.
- Kohonen, T., 2001: *Self-Organizing Maps*. 3rd ed. Springer Series in Information Sciences, Vol. 30, Springer, 501 pp.
- Krishnamurthy, C. K. B., U. Lall, and H.-H. Kwon, 2009: Changing frequency and intensity of rainfall extremes over India from 1951 to 2003. *J. Climate*, **22**, 4737–4746.
- Kumar, A., H. Wang, W. Wang, Y. Xue, and Z.-Z. Hu, 2013: Does knowing the oceanic PDO phase help predict the atmospheric anomalies in subsequent months? *J. Climate*, **26**, 1268–1285.
- Kunkel, K. E., and Coauthors, 2013: Monitoring and understanding trends in extreme storms: State of knowledge. *Bull. Amer. Meteor. Soc.*, **94**, 499–514.

- Lamarque, J.-F., and Coauthors, 2010: Historical (1850–2000) gridded anthropogenic and biomass burning emissions of reactive gases and aerosols: Methodology and application. *Atmos. Chem. Phys.*, **10**, 7017–7039, doi:10.5194/acp-10-7017-2010.
- Langford, S., S. Stevenson, and D. Noone, 2014: Analysis of low-frequency precipitation variability in CMIP5 historical simulations for southwestern North America. *J. Climate*, **27**, 2735–2756.
- Lau, W. K. M., and K.-M. Kim, 2011: The 2010 Pakistan flood and Russian heat wave: Teleconnection of hydrometeorological extremes. *J. Hydrometeorol.*, **13**, 392–403.
- Lewis, S. C., and D. J. Karoly, 2013: Anthropogenic contributions to Australia’s record summer temperatures of 2013. *Geophys. Res. Lett.*, **40**, 3705–3709, doi:10.1002/grl.50673.
- Li, C., and M. Yanai, 1996: The onset and interannual variability of the Asian summer monsoon in relation to land–sea thermal contrast. *J. Climate*, **9**, 358–375.
- Li, H., J. Sheffield, and E. F. Wood, 2010a: Bias correction of monthly precipitation and temperature fields from Intergovernmental Panel on Climate Change AR4 models using equidistant quantile matching. *J. Geophys. Res.*, **115**, D10101, doi:10.1029/2009JD012882.
- , A. Dai, T. Zhou, and J. Lu, 2010b: Responses of East Asian summer monsoon to historical SST and atmospheric forcing during 1950–2000. *Climate Dyn.*, **34**, 501–514.
- Lindenberg, J., H.-T. Mengelkamp, and G. Rosenhagen, 2012: Representativity of near surface wind measurements from coastal stations at the German Bight. *Meteor. Z.*, **21**, 99–106.
- López-Moreno, J. I., 2005: Recent variations of snowpack depth in the Central Spanish Pyrenees. *Arct. Antarct. Alp. Res.*, **37**, 253–260.
- , and S. M. Serrano-Vicente, 2007: Atmospheric circulation influence on the interannual variability of snowpack in the Spanish Pyrenees during the second half of the twentieth century. *Nordic Hydrol.*, **38**, 38–44.
- , —, and S. Lanjeri, 2007: Mapping of snowpack distribution over large areas using GIS and interpolation techniques. *Climate Res.*, **33**, 257–270.
- , —, S. Beguería, A. M. El Kenawy, and M. Angulo, 2010: Trends in daily precipitation on the north-eastern Iberian Peninsula, 1955–2006. *Int. J. Climatol.*, **120**, 248–257.
- Lorenz, R., E. B. Jaeger, and S. I. Seneviratne, 2010: Persistence of heat waves and its link to soil moisture memory. *Geophys. Res. Lett.*, **37**, L09703, doi:10.1029/2010GL042764.
- Lott, F. C., N. Christidis, and P. A. Stott, 2013: Can the 2011 East African drought be attributed to human-induced climate change? *Geophys. Res. Lett.*, **40**, 1177–1181.
- Mantua, N. J., S. R. Hare, Y. Zhang, J. M. Wallace, and R. C. Francis, 1997: A Pacific interdecadal climate oscillation with impacts on salmon production. *Bull. Amer. Meteor. Soc.*, **78**, 1069–1079.
- Marshall, A. G., D. Hudson, M. C. Wheeler, O. Alves, H. H. Hendon, M. J. Pook, and J. S. Risbey, 2013: Intra-seasonal drivers of extreme heat over Australia in observations and POAMA-2. *Climate Dyn.*, doi:10.1007/s00382-013-2016-1.
- Martin, J. E., 1999: Quasigeostrophic forcing of ascent in the occluded sector of cyclones and the trowal airstream. *Mon. Wea. Rev.*, **127**, 70–88.
- Marty, C., 2008: Regime shift of snow days in Switzerland. *Geophys. Res. Lett.*, **35**, L12501, doi:10.1029/2008GL033998.
- Marvel, K., and C. Bonfils, 2013: Identifying external influences on global precipitation. *Proc. Natl. Acad. Sci. USA*, **110**, 19301–19306.
- Massey, N., and Coauthors, 2014: weather@home – development and validation of a very large ensemble modelling system for probabilistic event attribution. *Quart. J. Roy. Meteor. Soc.*, in press, doi:10.1002/qj.2455.
- Mastrandrea, M. D., K. J. Mach, G.-K. Plattner, O. Edenhofer, T. F. Stocker, C. B. Field, K. L. Ebi, and P. R. Matschoss, 2011: The IPCC AR5 guidance note on consistent treatment of uncertainties: a common approach across the working groups. *Climate Change*, **108**, 675–691.
- Matulla, C., W. Schönner, H. Alexandersson, H. von Storch, and X. Wang, 2007: European storminess: Late nineteenth century to present. *Climate Dyn.*, **31**, 125–130.
- Mayes, B. E., J. M. Boustead, M. O’Malley, S. M. Fortin, and R. H. Grumm, 2009: Utilizing standardized anomalies to assess synoptic scale weather events in the central United States. Preprints, *23rd Conf. on Weather Analysis and Forecasting*, Omaha, NE, Amer. Meteor. Soc., 16B.3. [Available online at <http://ams.confex.com/ams/pdfpapers/154217.pdf>.]
- McCabe, G. J., and M. D. Dettinger, 1999: Decadal variations in the strength of ENSO teleconnections with precipitation in the western United States. *Int. J. Climatol.*, **19**, 1399–1410.
- McKee, T. B., and N. J. Doesken, 1997: Colorado Extreme Storm Precipitation Data Study. Climatology Rep. 97-1, Colorado Climate Center, Colorado State University, 109 pp. [Available online at http://climate.colostate.edu/pdfs/Climo_97-1_Extreme_ppt.pdf.]
- Menne, M., I. Durre, R. Vose, B. Gleason, and T. Houston, 2012: An overview of the Global Historical Climatology Network-Daily database. *J. Atmos. Oceanic Technol.*, **29**, 897–910.
- Met Office, cited 2014: Hot dry spell July 2013. [Available online at <http://www.metoffice.gov.uk/climate/uk/interesting/2013-heatwave>.]

- Michelangeli, P.-A., R. Vautard, and B. Legras, 1995: Weather regimes: Recurrence and quasi-stationarity. *J. Atmos. Sci.*, **52**, 1237–1256.
- Min, S.-K., X. Zhang, F. W. Zwiers, and G. C. Hegerl, 2011: Human contribution to more-intense precipitation extremes. *Nature*, **470**, 378–381, doi:10.1038/nature09763.
- , —, —, H. Shiogama, Y.-S. Tung, and M. Wehner, 2013: Multi-model detection and attribution of extreme temperature changes. *J. Climate*, **26**, 7430–7451.
- Mishra, A., and J. Srinivasan, 2013: Did a cloud burst occur in Kedarnath during 16 and 17 June 2013. *Current Sci.*, **105**, 1351–1352.
- Mitchell, T., and W. Blier, 1997: The variability of wintertime precipitation in the region of California. *J. Climate*, **10**, 2261–2276.
- Molod, A., L. Takacs, M. Suarez, J. Bacmeister, I.-S. Song, and A. Eichmann, 2012: The GEOS-5 Atmospheric General Circulation Model: Mean climate and development from MERRA to Fortuna. NASA Tech. Rep. Series on Global Modeling and Data Assimilation, NASA TM—2012-104606, Vol. 28, 117 pp.
- Moore, J. T., C. E. Graves, S. Ng, and J. L. Smith, 2005: A process-oriented methodology toward understanding the organization of an extensive mesoscale snowband: A diagnostic case study of 4–5 December 1999. *Wea. Forecasting*, **20**, 35–50.
- Morak, S., G. C. Hegerl, and J. Kenyon, 2011: Detectable regional changes in the number of warm nights. *Geophys. Res. Lett.*, **38**, L17703, doi:10.1029/2011GL048531.
- , —, and N. Christidis, 2013: Detectable changes in the frequency of temperature extremes. *J. Climate*, **26**, 1561–1574.
- Morice, C. P., J. J. Kennedy, N. A. Rayner, and P. D. Jones, 2012: Quantifying uncertainties in global and regional temperature change using an ensemble of observational estimates: The HadCRUT4 dataset. *J. Geophys. Res.*, **117**, D08101, doi:10.1029/2011JD017187.
- Mudelsee, M., M. Börngen, G. Tetzlaff, and U. Grunewald, 2003: No upward trends in the occurrence of extreme floods in central Europe. *Nature*, **425**, 166–169.
- Nairn, J., and R. Fawcett, 2013: Defining heatwaves: Heatwave defined as a heat impact event servicing all community and business sectors in Australia. CAWCR Technical Report No. 060, 84 pp. [Available online at http://www.cawcr.gov.au/publications/technicalreports/CTR_060.pdf.]
- Namias, J., 1978a: Recent drought in California and western Europe. *Rev. Geophys.*, **16**, 435–458.
- , 1978b: Multiple causes of the North American abnormal winter 1976–1977. *Mon. Wea. Rev.*, **106**, 279–295.
- NASA Earth Observatory, cited 2014: MODIS TERRA imagery. [Available online at <http://earthobservatory.nasa.gov/IOTD/view.php?id=82910>.]
- NCDC, 2005: *Storm Data*. NOAA/NESDIS National Climatic Data Center, **47** (10), 132 pp. [Available online at <http://www.ncdc.noaa.gov/IPS/sd/sd.html>.]
- NCLIMDIV, 2014: NOAA's gridded climate divisional dataset. National Climatic Data Center, Asheville, NC, digital media, retrieved 05 June 2014. [Available online at <http://www.ncdc.noaa.gov/cag/>.]
- Neelin, J. D., B. Langenbrunner, J. E. Meyerson, A. Hall, and N. Berg, 2013: California winter precipitation change under global warming in the Coupled Model Intercomparison Project Phase 5 ensemble. *J. Climate*, **26**, 6238–6256.
- New Zealand Treasury, 2013: Budget economic and fiscal update 2013. New Zealand Treasury, 176 pp. [Available online at <http://www.treasury.govt.nz/budget/forecasts/befu2013/befu13-whole.pdf>.]
- Nicholls, N., 2004: The changing nature of Australian droughts. *Climatic Change*, **63**, 323–336.
- NIDIS, cited 2014: National Integrated Drought Information System drought portal. [Available online at <http://www.drought.gov/drought/news/ca-governor-signs-687-million-drought-plan>.]
- Nitschke, M., G. R. Tucker, and P. Bi, 2007: Morbidity and mortality during heatwaves in metropolitan Adelaide. *Med. J. Aust.*, **187**, 662–665.
- NOAA, 2013: State of the climate: Global analysis for May 2013. [Available online at <http://www.ncdc.noaa.gov/sotc/global/2013/5>.]
- NOAA NCDC, 2014: National overview: February 2014. [Available online at <https://www.ncdc.noaa.gov/sotc/national/2014/2>.]
- Novak, D. R., L. F. Bosart, D. Keyser, and J. S. Waldstreicher, 2004: An observational study of cold season–banded precipitation in northeast U.S. cyclones. *Wea. Forecasting*, **19**, 993–1010.
- Ogawa, F., H. Nakamura, K. Nishii, T. Miyasaka, and A. Kuwano-Yoshida, 2012: Dependence of the climatological axial latitudes of the tropospheric westerlies and storm tracks on the latitude of an extratropical oceanic front. *Geophys. Res. Lett.*, **39**, L05804, doi:10.1029/2011GL049922.
- O’Gorman, P. A., and T. Schneider, 2009: The physical basis for increases in precipitation extremes in simulations of 21st-century climate change. *Proc. Natl. Acad. Sci. USA*, **106**, 14773–14777.
- Omrani, N.-E., N. S. Keenlyside, J. Bader, and E. Manzini, 2014: Stratosphere key for wintertime atmospheric response to warm Atlantic decadal conditions. *Climate Dyn.*, **42**, 649–663.
- Onogi, K., and Coauthors, 2007: The JRA-25 reanalysis. *J. Meteor. Soc. Japan*, **85**, 369–432.

- Otto, F. E. L., N. Massey, G. J. van Oldenborgh, R. G. Jones, and M. R. Allen, 2012: Reconciling two approaches to attribution of the 2010 Russian heat wave. *Geophys. Res. Lett.*, **39**, L04702, doi:10.1029/2011GL050422.
- Pall, P., T. Aina, D. A. Stone, P. A. Stott, T. Nozawa, A. G. J. Hilberts, D. Lohmann, and M. R. Allen, 2011: Anthropogenic greenhouse gas contribution to flood risk in England and Wales in autumn 2000. *Nature*, **470**, 382–385, doi:10.1038/nature09762.
- Pekárová, P., D. Halmová, V. B. Mitková, P. Miklánek, J. Pekár, and P. Škoda, 2013: Historic flood marks and flood frequency analysis of the Danube River at Bratislava, Slovakia. *J. Hydrol. Hydromech.*, **61**, 326–333.
- Perkins, S. E., and L. V. Alexander, 2013: On the measurement of heat waves. *J. Climate*, **26**, 4500–4517.
- , and E. M. Fischer, 2013: The usefulness of different realizations from the model evaluation of regional trends in heat waves. *Geophys. Res. Lett.*, **40**, 5793–5797, doi:10.1002/2013GL057833.
- Peters, G. P., and Coauthors, 2012: The challenge to keep global warming below 2°C. *Nature Climate Change*, **3**, 4–6, doi:10.1038/nclimate1783.
- Peterson, T. C., and Coauthors, 2008: Why weather and climate extremes matter. *Weather and Climate Extremes in a Changing Climate. Regions of Focus: North America, Hawaii, Caribbean, and U.S. Pacific Islands*. T. R. Karl et al., Eds., U.S. Climate Change Science Program and the Subcommittee on Global Change Research, 11–33.
- Petoukhov, V., and V. Semenov, 2010: A link between reduced Barents-Kara sea ice and cold winter extremes over northern continents. *J. Geophys. Res.*, **115**, D21111, doi:10.1029/2009JD013568.
- , S. Rahmstorf, S. Petri, and H. J. Schellnhuber, 2013: Quasiresonant amplification of planetary waves and recent Northern Hemisphere weather extremes. *Proc. Natl. Acad. Sci. USA*, **110**, 5336–5341.
- Pierce, D. W., 2002: The role of sea surface temperatures in interactions between ENSO and the North Pacific oscillation. *J. Climate*, **15**, 1295–1308.
- Pinto, J. G., N. Bellenbaum, M. K. Karremann, and P. M. Della-Marta, 2013: Serial clustering of extratropical cyclones over the North Atlantic and Europe under recent and future climate conditions. *J. Geophys. Res. Atmos.*, **118**, 12476–12485, doi:10.1002/2013JD020564.
- Polade, S. D., A. Gershunov, D. R. Cayan, M. D. Dettinger, and D. W. Pierce, 2013: Natural climate variability and teleconnections to precipitation over the Pacific-North American region in CMIP3 and CMIP5 models. *Geophys. Res. Lett.*, **40**, 2296–2301.
- , D. W. Pierce, D. R. Cayan, A. Gershunov, and M. D. Dettinger, 2014: The key role of dry days in changing regional climate and precipitation regimes. *Sci. Rep.*, **4**, 4364, doi:10.1038/srep04364.
- Pope, V. D., M. L. Gallani, P. R. Rowntree, and R. A. Stratton, 2000: The impact of new physical parametrizations in the Hadley Centre climate model: HadAM3. *Climate Dyn.*, **16**, 123–146, doi:10.1007/s003820050009.
- Porteous, A., and B. Mullan, 2013: The 2012–13 drought: An assessment and historical perspective. MPI Tech. Paper No. 2012/18. Ministry for Primary Industries/National Institute of Water & Atmospheric Research, 57 pp. [Available online at <http://www.niwa.co.nz/sites/niwa.co.nz/files/2013-18-The%202012-13%20drought%20an%20assessment%20and%20historical%20perspective.pdf>.]
- Power, S., T. Casey, C. Folland, A. Colman, and V. Mehta, 1999: Inter-decadal modulation of the impact of ENSO on Australia. *Climate Dyn.*, **15**, 319–324.
- , M. Haylock, R. Colman, and X. Wang, 2006: The predictability of interdecadal changes in ENSO activity and ENSO teleconnections. *J. Climate*, **19**, 4755–4771.
- Prakash, S., 2013: Brief Report on visit to Alaknanda Valley, Uttarakhand Himalaya during 22–24 June 2013. [India] National Institute of Disaster Management, [12 pp.] [Available online at <http://www.nidm.gov.in/pdf/Uttarakhand%20Disaster.pdf>.]
- PRISM, 2014: PRISM climate data. PRISM Climate Group, Oregon State University, Corvallis, OR, digital media, retrieved 10 Feb 2014. [Available online at <http://prism.oregonstate.edu/>.]
- Qian, C., and T. Zhou, 2014: Multidecadal variability of North China aridity and its relationship to PDO during 1900–2010. *J. Climate*, **27**, 1210–1222.
- Qian, Y., L. Leung, S. Ghan, and F. Giorgi, 2003: Regional climate effects of aerosols over China: Modeling and observation. *Tellus*, **55B**, 914–934.
- , D. Gong, J. Fan, L. Leung, R. Bennartz, D. Chen, and W. Wang, 2009: Heavy pollution suppresses light rain in China: Observations and modeling. *J. Geophys. Res.*, **114**, D00K02, doi:10.1029/2008JD011575.
- Rajeevan, M., S. Gadgil, and J. Bhate, 2010: Active and break spells of the Indian summer monsoon. *J. Earth Sys. Sci.*, **119**, 229–247.
- Rayner, N. A., D. E. Parker, E. B. Horton, C. K. Folland, L. V. Alexander, D. P. Rowell, E. C. Kent, and A. Kaplan, 2003: Global analyses of sea surface temperature, sea ice, and night marine air temperature since the late nineteenth century. *J. Geophys. Res.*, **108** (D14), 4407, doi:10.1029/2002JD002670.
- Rienecker, M. M., and Coauthors, 2008: The GEOS-5 data assimilation system—Documentation of versions 5.0.1, 5.1.0, and 5.2.0. NASA Tech. Rep. Series on Global Modeling and Data Assimilation, NASA/TM-2007-104606, Vol. 27, 95 pp.
- , and Coauthors, 2011: MERRA: NASA's Modern-Era Retrospective Analysis for Research and Applications. *J. Climate*, **24**, 3624–3648.

- Rupp, D. E., P. W. Mote, N. Massey, C. J. Rye, R. Jones, and M. R. Allen, 2012: Did human influence on climate make the 2011 Texas drought more probable? [in “Explaining Extreme Events of 2011 from a Climate Perspective”]. *Bull. Amer. Meteor. Soc.*, **93**, 1052–1067.
- , —, —, F. E. L. Otto, and M. R. Allen, 2013: Human influence on the probability of low precipitation in the Central United States in 2012 [in “Explaining Extreme Events of 2012 from a Climate Perspective”]. *Bull. Amer. Meteor. Soc.*, **94** (9), S2–S6.
- Sampe, T., H. Nakamura, A. Goto, and W. Ohfuchi, 2010: Significance of a midlatitude SST frontal zone in the formation of a storm track and an eddy-driven westerly jet. *J. Climate*, **23**, 1793–1814.
- Schaer, C., P. L. Vidale, D. Luethi, C. Frei, C. Haeberli, M. A. Liniger, and C. Appenzeller, 2004: The role of increasing temperature variability in European summer heatwaves. *Nature*, **427**, 332–336.
- Schmidt, H., and H. von Storch, 1993: German Bight storms analysed. *Nature*, **365**, 791–791.
- Schneider, U., A. Becker, P. Finger, A. Meyer-Christoffer, M. Ziese, and B. Rudolf, 2014: GPCP’s new land surface precipitation climatology based on quality-controlled in situ data and its role in quantifying the global water cycle. *Theor. Appl. Climatol.*, **115**, 15–40, doi:10.1007/s00704-013-0860-x.
- Schubert, S., and Coauthors, 2009: A U.S. CLIVAR project to assess and compare the responses of global climate models to drought-related SST forcing patterns: Overview and results. *J. Climate*, **22**, 5251–5272.
- , H. Wang, R. Koster, M. Suarez, and P. Groisman, 2014: Northern Eurasian heat waves and droughts. *J. Climate*, **27**, 3169–3207.
- Schwartz, R. M., and T. W. Schmidlin, 2002: Climatology of blizzards in the conterminous United States, 1959–2000. *J. Climate*, **15**, 1765–1772.
- Screen, J. A., I. Simmonds, C. Deser, and R. Tomas, 2013: The atmospheric response to three decades of observed Arctic sea ice loss. *J. Climate*, **26**, 1230–1248.
- Seneviratne, S. I., 2012: Climate science: Historical drought trends revisited. *Nature*, **491**, 338–339.
- , T. Corti, E. L. Davin, M. Hirschi, E. B. Jaeger, I. Lehner, B. Orlowsky, and A. J. Teuling, 2010: Investigating soil moisture-climate interactions in a changing climate: A review. *Earth-Sci. Rev.*, **99**, 125–161.
- , M. G. Donat, B. Mueller, and L. V. Alexander, 2014: No pause in the increase of hot temperature extremes. *Nature Climate Change*, **4**, 161–163, doi:10.1038/nclimate2145.
- Sewall, J. O., 2005: Precipitation shifts over western North America as a result of declining Arctic sea ice cover: The coupled system response. *Earth Interact.*, **9**, 1–23, doi:10.1175/EI171.1.
- Sheffield, J., E. F. Wood, and M. L. Roderick, 2012: Little change in global drought over the past 60 years. *Nature*, **491**, 435–438.
- , and Coauthors, 2013: North American climate in CMIP5 experiments. Part I: Evaluation of historical simulations of continental and regional climatology. *J. Climate*, **26**, 9209–9245.
- Sherwood, S., and Q. Fu, 2014: A drier future? *Science*, **343**, 737–738.
- Shiogama, H., M. Watanabe, Y. Imada, M. Mori, M. Ishii, and M. Kimoto, 2013: An event attribution of the 2010 drought in the south Amazon region using the MIROC5 model. *Atmos. Sci. Lett.*, **14**, 170–175.
- Siderius, C., and Coauthors, 2013: Snowmelt contributions to discharge of the Ganges. *Sci. Total Environ.*, **468–469** (Suppl.), S93–S101, doi:10.1016/j.scitotenv.2013.05.084.
- Sillmann, J., V. V. Kaharin, F. W. Zwiers, X. Zhang, and D. Bronaugh, 2013: Climate extreme indices in the CMIP5 multimodel ensemble: Part 2. Future climate projections. *J. Geophys. Res. Atmos.*, **118**, 2473–2493, doi:10.1002/jgrd.50188.
- , M. G. Donat, J. C. Fyfe, and F. W. Zwiers, 2014: Observed and simulated temperature extremes during the recent warming hiatus. *Environ. Res. Lett.*, **9**, 064023, doi:10.1088/1748-9326/9/6/064023.
- Singh, D., M. Tsiang, B. Rajaratnam, and N. S. Diffenbaugh, 2014: Observed changes in extreme wet and dry spells during the South Asian summer monsoon season. *Nature Climate Change*, **4**, 456–461.
- Slingo, J., 2013: Why was the start to spring 2013 so cold? Met Office briefing note, April 2013. [Available online at <http://www.metoffice.gov.uk/research/news/cold-spring-2013>.]
- Smith, T. M., R. W. Reynolds, T. C. Peterson, and J. Lawrimore, 2008: Improvements to NOAA’s historical merged land-ocean surface temperature analysis (1880–2006). *J. Climate*, **21**, 2283–2296.
- Solomon, A., and M. Newman, 2012: Reconciling disparate twentieth-century Indo-Pacific Ocean temperature trends in the instrumental record. *Nature Climate Change*, **2**, 691–699.
- Song, F., T. Zhou, and Y. Qian, 2014: Responses of East Asian summer monsoon to natural and anthropogenic forcings in the 17 latest CMIP5 models. *Geophys. Res. Lett.*, **41**, 596–603, doi:10.1002/2013GL058705.
- Sperber, K. R., H. Annamalai, I.-S. Kang, A. Kitoh, A. Moise, A. Turner, B. Wang, and T. Zhou, 2013: The Asian summer monsoon: An intercomparison of CMIP5 vs. CMIP3 simulations of the late 20th century. *Climate Dyn.*, **41**, 2711–2744.

- Stark, J. D., C. J. Donlon, M. J. Martin, and M. E. McCulloch, 2007: OSTIA: An operational, high resolution, real time, global sea surface temperature analysis system. *Oceans 2007 - Europe*, Aberdeen, Scotland, IEEE, Vols. 1–3, 331–334, doi:10.1109/OCEANSE.2007.4302251.
- Stocker, T. F., and Coauthors, Eds., 2014: *Climate Change 2013: The Physical Science Basis*. Cambridge University Press, 1535 pp.
- Stone, D. A., and M. R. Allen, 2005: Attribution of global surface warming without dynamical models. *Geophys. Res. Lett.*, **32**, L18711, doi:10.1029/2005GL023682.
- , —, P. A. Stott, P. Pall, S.-K. Min, T. Nozawa, and S. Yukimoto, 2009: The detection and attribution of human influence on climate. *Ann. Rev. Environ. Res.*, **34**, 1–16.
- Stott, P. A., D. A. Stone, and M. R. Allen, 2004: Human contribution to the European heatwave of 2003. *Nature*, **432**, 610–614, doi:10.1038/nature03089.
- Sutton, R. T., and B.-W. Dong, 2012: Atlantic Ocean influence on a shift in European climate in the 1990s. *Nature Geosci.*, **5**, 788–792, doi:10.1038/ngeo1595.
- , and P. P. Mathieu, 2002: Response of the atmosphere–ocean mixed-layer system to anomalous ocean heat-flux convergence. *Quart. J. Roy. Meteor. Soc.*, **128**, 1259–1275.
- Swart, N. C., and J. C. Fyfe, 2012: Observed and simulated changes in the Southern Hemisphere surface westerly wind-stress. *Geophys. Res. Lett.*, **39**, L16711, doi:10.1029/2012GL052810.
- Tait, A., R. Henderson, R. Turner, and X. Zheng, 2006: Thin plate smoothing spline interpolation of daily rainfall for New Zealand using a climatological rainfall surface. *Int. J. Climatol.*, **26**, 2097–2115.
- Taylor, K. E., R. J. Stouffer, and G. A. Meehl, 2012: An overview of CMIP5 and the experiment design. *Bull. Amer. Meteor. Soc.*, **93**, 485–498.
- Thompson, D. W. J., S. Solomon, P. J. Kushner, M. H. England, K. M. Grise, and D. J. Karoly, 2011: Signatures of the Antarctic ozone hole in Southern Hemisphere surface climate change. *Nature Geosci.*, **4**, 741–749, doi:10.1038/ngeo1296.
- Trenberth, K. E., 2011: Changes in precipitation with climate change. *Climate Res.*, **47**, 123–138.
- , G. Branstator, and P. Arkin, 1988: Origins of the 1988 American drought. *Science*, **242**, 1640–1645.
- , A. Dai, G. van der Schrier, P. D. Jones, J. Barichivich, K. R. Briffa, and J. Sheffield, 2014: Global warming and changes in drought. *Nature Climate Change*, **4**, 17–22.
- Trewin, B., 2012: A daily homogenized temperature data set for Australia. *Int. J. Climatol.*, **33**, 1510–1529, doi:10.1002/joc.3530.
- Trigo, R. M., and Coauthors, 2013: The record winter drought of 2011–12 in the Iberian Peninsula [in “Explaining Extreme Events of 2012 from a Climate Perspective”]. *Bull. Amer. Meteor. Soc.*, **94** (9), S41–S45.
- Uccellini, L. W., and P. J. Kocin, 1987: The interaction of jet streak circulations during heavy snow events along the East Coast of the United States. *Wea. Forecasting*, **2**, 289–308.
- Ullah, K., and G. Shouting, 2013: A diagnostic study of convective environment leading to heavy rainfall during the summer monsoon 2010 over Pakistan. *Atmos. Res.*, **120–121**, 226–239.
- USBR, 2014: Reclamation announces initial 2014 Central Valley Project water supply allocation. United States Bureau of Reclamation, news release, 21 February 2014. [Available online at <http://www.usbr.gov/newsroom/newsrelease/detail.cfm?RecordID=46045>.]
- USDA, 2014a: Obama Administration announces additional assistance to Californians impacted by drought. United States Department of Agriculture, news release, 0022.14. [Available online at <http://www.usda.gov/wps/portal/usda/usdamediafb?contentid=2014/02/0022.xml&printable=true&contentidonly=true>.]
- , 2014b: Secretarial Disaster Designations - 2014 Crop Year. All Crop - Total Counties by State (updated 9/3/2014). United States Department of Agriculture. [Available online at <http://www.usda.gov/documents/2014-all-crop-list-counties.pdf>.]
- USGS, cited 2014: California Water Science Center. [Available online at <http://ca.water.usgs.gov/data/drought/drought-impact.html>.]
- van Haren, R., G. J. van Oldenborgh, G. Lenderink, and W. Hazeleger, 2013a: Evaluation of modeled changes in extreme precipitation in Europe and the Rhine basin. *Environ. Res. Lett.*, **8**, 014053, doi:10.1088/1748-9326/8/1/014053.
- , —, —, M. Collins, and W. Hazeleger, 2013b: SST and circulation trend biases cause an underestimation of European precipitation trends. *Climate Dyn.*, **40**, 1–20.
- van Oldenborgh, G. J., A. van Urk, and M. Allen, 2012: The absence of a role of climate change in the 2011 Thailand floods. *Bull. Amer. Meteor. Soc.*, **93**, 1047–1049.
- , F. J. Doublas Reyes, S. S. Dirjfhout, and E. Hawkins, 2013: Reliability of regional climate model trends. *Environ. Res. Lett.*, **8**, 014055, doi:10.1088/1748-9326/8/1/014055.
- Vautard, R., and P. Yiou, 2009: Control of recent European surface climate change by atmospheric flow. *Geophys. Res. Lett.*, **36**, L22702, doi:10.1029/2009GL040480.
- , and Coauthors, 2007: Summertime European heat and drought waves induced by wintertime Mediterranean rainfall deficit. *Geophys. Res. Lett.*, **34**, L07711, doi:10.1029/2006GL028001.
- VegDRI, cited 2014: Vegetation drought response index. [Available online at <http://vegdroi.unl.edu/>.]

- Vicente-Serrano, S. M., R. M. Trigo, J. I. López-Moreno, M. L. R. Liberato, J. Lorenzo-LaCruz, S. Beguería, E. Morán-Tejada, and A. El Kenawy, 2011: Extreme winter precipitation in the Iberian Peninsula in 2010: Anomalies, driving mechanisms and future projections. *Climate Res.*, **46**, 51–65.
- Visbeck, M. H., J. W. Hurrell, L. Polvani, and H. M. Cullen, 2001: The North Atlantic Oscillation: Past, present, and future. *Proc. Natl. Acad. Sci. USA*, **98**, 12876–12877.
- Vose, R. S., R. L. Schmoyer, P. M. Steurer, T. C. Peterson, R. Heim, T. R. Karl, and J. K. Eischeid, 1992: The Global Historical Climatology Network: Long-term monthly temperature, precipitation, sea level pressure, and station pressure data. ORNL/CDIAC-53, NCDP-041, 325 pp.
- , and Coauthors, 2014: Improved historical temperature and precipitation time series for U.S. climate divisions. *J. App. Meteor. Climatol.*, **53**, 1232–1251.
- Wakabayashi, S., and R. Kawamura, 2004: Extraction of major teleconnection patterns possibly associated with the anomalous summer climate in Japan. *J. Meteor. Soc. Japan*, **82**, 1577–1588.
- Wallace, J. M., I. M. Held, D. W. J. Thompson, K. E. Trenberth, and J. E. Walsh, 2014: Global warming and winter weather. *Science*, **343**, 729–730, doi:10.1126/science.343.6172.729.
- Wang, B., B. Xiang, and J.-Y. Lee, 2013: Subtropical high predictability establishes a promising way for monsoon and tropical storm predictions. *Proc. Natl. Acad. Sci. USA*, **110**, 2718–2722.
- Wang, S.-Y., R. E. Davies, W.-R. Huang, and R. R. Gillies, 2011: Pakistan's two-stage monsoon and links with the recent climate change. *J. Geophys. Res.*, **116**, D16114, doi:10.1029/2011JD015760.
- , L. Hipps, R. R. Gillies, and J.-H. Yoon, 2014: Probable causes of the abnormal ridge accompanying the 2013–2014 California drought: ENSO precursor and anthropogenic warming footprint. *Geophys. Res. Lett.*, **41**, 3220–3226, doi:10.1002/2014GL059748.
- Watanabe, M., and Coauthors, 2010: Improved climate simulation by MIROC5: Mean states, variability, and climate sensitivity. *J. Climate*, **23**, 6312–6335.
- Water CA, cited 2014: California Department of Water Resources. [Available online at <http://www.water.ca.gov/waterconditions/>]
- Webster, P. J., V. O. Magaña, T. N. Palmer, J. Shukla, R. A. Tomas, M. Yanai, and T. Yasunari, 1998: Monsoons: Processes, predictability, and the prospects for prediction. *J. Geophys. Res.*, **103** (C7), 14451–14510, doi:10.1029/97JC02719.
- , V. E. Toma, and H.-M. Kim, 2011: Were the 2010 Pakistan floods predictable? *Geophys. Res. Lett.*, **38**, L04806, doi:10.1029/2010GL046346.
- Weisse, R., H. von Storch, and F. Feser, 2005: Northeast Atlantic and North Sea storminess as simulated by a regional climate model during 1958–2001 and comparison with observations. *J. Climate*, **18**, 465–479.
- Wen, Q. H., X. Zhang, Y. Xu, and B. Wang, 2013: Detecting human influence on extreme temperatures in China. *Geophys. Res. Lett.*, **40**, 1171–1176, doi:10.1002/grl.50285.
- Westra, S., L. V. Alexander, and F. W. Zwiers, 2013: Global increasing trends in annual maximum daily precipitation. *J. Climate*, **26**, 3904–3918.
- Wheeler, M. C., and H. H. Hendon, 2004: An all season real-time multivariate MJO index: Development of an index for monitoring and prediction. *Mon. Wea. Rev.*, **132**, 1917–1932.
- Wilks, D. S. 2006: *Statistical Methods in the Atmospheric Sciences*. International Geophysics Series, Vol. 91, Elsevier Academic Press, 627 pp.
- WMO, 2010: Guide to meteorological instruments and methods of observation. WMO No. 8. World Meteorological Society, 437 pp. [Available online at <http://www.wmo.int/pages/prog/www/IMOP/CIMO-Guide.html>.]
- , 2013: The state of greenhouse gases in the atmosphere based on global observations through 2012. *WMO Greenhouse Gas Bulletin*, No. 9, 4 pp.
- Wu, G., Y. Liu, B. He, Q. Bao, A. Duan, and F.-F. Jin, 2012: Thermal controls on the Asian summer monsoon. *Sci. Rep.*, **2**, Article 404, doi:10.1038/srep00404.
- Wu, L., and Coauthors, 2012: Enhanced warming over the global subtropical western boundary currents. *Nature Climate Change*, **29**, 161–166.
- Xavier, P. K., C. Marzin, and B. N. Goswami, 2007: An objective definition of the Indian summer monsoon season and a new perspective on the ENSO–monsoon relationship. *Quart. J. Roy. Meteor. Soc.*, **133**, 749–764.
- Yiou, P., and J. Cattiaux, 2013: Contribution of atmospheric circulation to wet north European summer precipitation of 2012[in “Explaining Extreme Events of 2012 from a Climate Perspective”]. *Bull. Amer. Meteor. Soc.*, **94** (9), S39–S41.
- , R. Vautard, P. Naveau, and C. Cassou, 2007: Inconsistency between atmospheric dynamics and temperatures during the exceptional 2006/2007 fall/winter and recent warming in Europe. *Geophys. Res. Lett.*, **34**, L21808, doi:10.1029/2007GL031981.
- , K. Goubanova, Z. X. Li, and M. Nogaj, 2008: Weather regime dependence of extreme value statistics for summer temperature and precipitation. *Nonlin. Processes Geophys.*, **15**, 365–378, doi:10.5194/npg-15-365-2008.
- Yu, R., and T. Zhou, 2007: Seasonality and three-dimensional structure of the interdecadal change in East Asian monsoon. *J. Climate*, **20**, 5344–5355.

- , B. Wang, and T. Zhou, 2004: Tropospheric cooling and summer monsoon weakening trend over East Asia. *Geophys. Res. Lett.*, **31**, L22212, doi:10.1029/2004GL021270.
- Zhang, X., F. W. Zwiers, G. C. Hegerl, F. H. Lambert, N. P. Gillett, S. Solomon, P. A. Stott, and T. Nozawa, 2007: Detection of human influence on twentieth-century precipitation trends. *Nature*, **448**, 461–465.
- , H. Wan, F. W. Zwiers, G. C. Hegerl, and S.-K. Min, 2013: Attributing intensification of precipitation extremes to human influence. *Geophys. Res. Lett.*, **40**, 5252–5257, doi:10.1002/grl.51010.
- Zhou, T., D. Gong, J. Li, and B. Li, 2009: Detecting and understanding the multi-decadal variability of the East Asian Summer Monsoon - Recent progress and state of affairs. *Meteor. Z.*, **18**, 455–467.
- , F. Song, R. Lin, X. Chen, and X. Chen, 2013: The 2012 North China floods: Explaining an extreme rainfall event in the context of a long-term drying tendency [in “Explaining Extreme Events of 2012 from a Climate Perspective”]. *Bull. Amer. Meteor. Soc.*, **94** (9), S49–S51.
- Zolina, O., C. Simmer, A. Kapala, P. Shabanov, P. Becker, H. Mächel, S. Gulev, and P. Groisman, 2013: New view on precipitation variability and extremes in Central Europe from a German high resolution daily precipitation dataset: Results from STAMMEX project *Bull. Amer. Meteor. Soc.*, **95**, 995–1002.
- Zwiers, F. W., X. Zhang, and Y. Feng, 2011: Anthropogenic influence on long return period daily temperature extremes at regional scales. *J. Climate*, **24**, 881–892.

